Quality of as-cast ingots with extreme large shapes

Von der Fakutät für Georessourcen und Materialtechnik

der Rheinisch-Westfälische Technische Hochschule Aachen

Zur Erlangung des akademischen Grades einer

Doktorin der Ingenieruwissenschaften

genehmigte Dissertation

vorgelgt von **Master of Science**

Zhiye Chen

aus Anhui, China

Berichter: Univ.-Prof. Professor h.c. (CN) Dr.-Ing. Dr. h.c. (CZ) Dieter Senk

Univ. -Prof. Dr.-Ing. Andreas Bührig-Polaczek

Prof. Dr.-Ing. Yanping Bao

Tag der mündlichen Prüfung: 09.Dezember 2014

Diese Dissertation ist auf den Intenetseiten der Universitätsbibliothek online verfügbar

Danksagung

Meinen Eltern danke ich sehr für die finanzielle Hilfe während meines Studiums, und mein liebster Dank gilt meinem Mann Lei Hu für seine Geduld, Verständnis, moralische und fachliche Unterstützung während der gesamten Zeit meiner Promotion!

Abstract

The quality of as-cast ingots and continuous cast products are controlled by solidification process mainly. Regarding to this, investigation on casting and solidification process of ingots and continuous cast products is considerable important in control of the quality of as-cast products especially for products with extremely heavy weight like several hundred tons. The present work focuses on the solidification process of large ingots. The complex solidification phenomena in large ingots have been investigated by means of three modelling methods, namely hot modelling, cold modelling and numerical modelling.

In hot modelling, two series of ingot casting experiments has been performed for ingots with weight of 100 kg and 500 kg with various parameter combinations. The large ingots with weight of 500 kg solidify slowly in a specially designed isolating mould with the solidification time over several hours, and this slow solidification process simulates the solidification of industrial scale large ingots with weight between 3 to 6 t. Cooling curves have been measured by thermocouples during solidification, and as-cast structure and macrosegregation of solutes have been quantified. Based on this, solidification in large ingots has been investigated and three solidification regimes have been suggested and discussed. A-type Segregations could be produced in the laboratory for detailed studies.

Meanwhile, water modelling (cold modelling) by using NH_4Cl solution has been conducted with different cool conditions and initial solution temperature. A quasi 2-D water model has been built up with glass and aluminium, where hot saturated NH_4Cl solution are poured in and crystallized subjected to cooling conditions. During precipitation of solid NH_4Cl, phenomena such as dendritic growth and sedimentation of crystals are similar to those in ingots solidification, therefore NH_4Cl solution is used as transparent analog to provide information of the solidification process in large ingots.

Besides the experimental work, numerical modelling of ingot solidification has been performed as well. A two-phase solidification model based on volume-averaging-technique has been developed. This solidification model has been applied for the ingots with weight of 100 kg and 500 kg, and the simulation results have been compared with the experimental results regarding as-cast structure and macrosegregation. Furthermore, a channel-segregation model has been developed for the determination of the A-type segregation formation. The effects of carbon concentration and flow velocity of the solute enriched melt on the widening and closing of the potential channel have been investigated.

Overall, solidification in large ingots has been investigated experimentally and numerically. The

relationship among as-cast structure, local solidification driving force and solidification sequence in large ingots has been intensively studied, and the formation mechanism of A-segregation has also been explored.

Zusammenfassung

Die Qualität von gegossenen Blöcken und Stranggussprodukten werden vor allem vom Erstarrungsprozess gesteuert. Dazu ist die Untersuchung von Gießen und Erstarrung der Blöcke und Stranggussprodukte bei der Steuerung der Qualität der Gussprodukte, insbesondere Produkte mit extrem großer Maße von großer Bedeutung. Die vorliegende Arbeit konzentriert sich auf den Erstarrungsprozess von großen Blöcken. Die komplexen Erstarrungsphänomene in großen Blöcken wurden mit Hilfe von drei Modellierungsmethoden, nämlich mit Heiß-, Kalt- und numerischem Modell, untersucht.

Als Heißmodelle wurden zwei Reihe der Gießversuche für Blöcken mit Gewicht von 100 kg und 500 kg mit verschiedenen Parameterkombinationen durchgeführt. Die großen Blöcke mit einem Gewicht von 500 kg erstarrten langsam in einer spezieller isolierende Kokille mit Erstarrungszeiten von über mehreren Stunden; diese langsame Erstarrungsprozess kann die Erstarrung von großen Blöcken mit einem Gewicht zwischen 3 t und 6 t simulieren. Die Kühlkurven der Böcke wurden während der Erstarrung durch Thermoelemente gemessen und das Erstarrungsgefüge und Makroseigerung von gelösten Stoffen wurden ebenfalls quantifiziert. Auf dieser Basis wurde die Erstarrung von großen Blöcken untersucht, und drei Erstarrungsregime wurden vorgeschlagen und diskutiert. Im Metallurgischen Labor konnten deutliche A-Seigerungen erzeugt werden.

Weiterhin werden eine Wassermodellierung (Kaltmodelle) mit NH_4Cl-Lösung unter verschiedenen Kühlungsbdingungen und Lösungstemperaturen durchgeführt. Ein quasi 2-D-Wassermodell wurde mit Glas und Aluminium aufgebaut, wobei heiße gesättigte NH_4Cl-Lösung eingegossen, gekühlt und dort kristallisiert wurde. Phänomene wie dendritisches Wachstum und Sedimentation der Kristalle stellen ähnliche Phänomene wie in großen Blöcken dar. Die NH_4Cl-Lösung wurde als transparentes Analogon verwendet, um Informationen des Blockerstarrungsprozesses bereitzustellen.

Ergänzend zu dem den experimentellen Arbeiten wurde die numerische Modellierung der Blockerstarrung durchgeführt. Ein Zwei-Phasen-Erstarrungsmodells wurde auf Basis von Volume-Averaging-Technik entwickelt. Das Modell wurde für die Erstarrung der Blöcke mit einem Gewicht von 100 kg und 500 kg aufgebracht, und die Simulationsergebnisse in Bezug auf Erstarrungsgefüge und Makrosegregation wurden mit den Versuchsergebnissen verglichen. Außerdem wurde ein Kanalseigerungsmodell zur Bestimmung der A-Seigerungsbildung entwickelt. Die Einflüsse des Kohlenstoffgehaltes und der Strömungsgeschwindigkeit der angereicherten Schmelze auf die Verbreiterung und das Schließen der Strömungskanäle wurden untersucht.

Zusammenfassend wurde die Erstarrung von großen Blöcken experimentell und numerisch untersucht. Die Beziehung zwischen Erstarrungsgefüge, lokaler Erstarrungstriebkraft und Erstarrungsablauf großer Blöcken wurde intensiv untersucht, unter besonderer Berücksichtigung des Bildungsmechanismus der A-Seigerung.

Contents

1 Introduction

Ingot casting is a conventional casting process for steel, which possesses about 5% of the total steel production today. Despite of the low percentage, ingot casting plays important role in production of special steel grades and products with large dimension, high quality or small lot size.

Nowadays there is a tendency of producing extreme large ingots over 600 t and continuous cast strands with thickness over 450 mm and round with dimension over 800 mm, which are mainly applied for retaining components such as reaction vessels for nuclear power plant and rotating components like drive shafts of gas turbines and generator rotors [1]. These high value products demand high quality of the as-cast semi-products, and the production of the heavy steel semi-products with adequate control of the quality become one of the great concern for steelmakers worldwide. During the last few years, customer requirement of the large as-cast products have been concentrated mainly on low levels of macrosegregation and macroscopic cleanliness [2].

In control of solidification in large continuous cast strands and ingots, although numerous experimental study on heavy ingot casting have been started since 1960's, fundamental knowledge and deep understanding of some basic macroscopic casting phenomena are still missing, such as A-segregation, sedimentation of free crystals, convective fluid flow during solidification as well as macrosegregation. Meanwhile, numerical simulation on solidification has been widely applied for the prediction and control of macrosegregation as well as the as-cast structure. However, quantitative prediction remains difficult attributed to the complexity of solidification in multiple scales and the interaction with the microstructure. As the multiple scale solidification models are based on a couple of macroscopic and microscopic mathematic models, the deeper the understanding on the physical phenomena is, the more accurate the prediction could be.

The current research aims to investigate the complex macroscopic solidification phenomena and to optimize the quality of as-cast semi-products with regard to macrosegregation and as-cast structure of large ingots. On one hand, series of ingot casting experiments, the so-called hot modelling are performed with different ingot weights; cooling curves have been measured during solidification; as-cast structure and macrosegregation pattern have been quantitative characterized. On the other hand, numerical simulation of solidification in heavy ingots has been performed; a two-phase solidification model based on volume-average-method has been developed with consideration of certain solidification details; ingots geometry and casting parameters of the casting experiments have been utilized as input data for the numerical model, and the experimental measurements are used for the

validation of the model. Furthermore, water modelling experiments (cold models) have been conducted, using NH$_4$Cl solution as transparent analog in order to gain insight of the solidification process and to study a few macroscopic phenomena.

The hot models compare the solidification in both small ingots and in large ingots. A special isolating mould have been built up with isolation materials and refractory bricks for ingots with weight of 500 kg, in order to prolongate the solidification time of the 500 kg ingots and to simulate the slow solidification behaviour of industrial scale large ingots with the weight of several tons. By means of this ingot casting simulation, several phenomena which are typically found in large ingots such as A-segregation can be reproduced in small ingots, and the expenses for experiments and analysis are considerably reduced. Meanwhile, small ingot casting experiments with the weight of 100 kg have been conducted as well to compare with the solidification in large ingots. Solidification in the two cases has been compared in terms of cooling curves, as-cast structure, macrosegregation as well as the solidification driving force. Suggestions for enhancement of quality of the both types of ingots have been given with regard to the suppression of A- and V-segregation, macrosegregation and improvement of dendritic structure.

The numerical simulation has also been applied to the 100 kg ingots and the 500 kg ingots. Movement of solid grains is taken into account for the 500 kg ingot, whereas for the 100 kg ingot is ignored. The predicted macrosegregation fields have been compared with the experimental results, and the deviation of the model to reality has been analyzed, limitations of the model have been discussed, and future possibilities for model modification have been listed. Furthermore, based on the two-phase solidification model and the experimental work, a one dimensional channel-segregation model has been developed to simulate the widening and closing behaviour of the potential channels in the mushy zone. With consideration of effects of fluid flow and carbon content of the segregated melt which flows through the potential channels, the solidification and remelting inside the potential channels can be modelled.

Water modelling using NH$_4$Cl solution provides an easy method for the observation of the dynamic process of some solidification phenomena, as great similarity exists between NH$_4$Cl crystallization and metal solidification regarding dendritic growth, sedimentation of free crystals and convective flow. These solidification phenomena have been quantitatively characterized, similarities between NH$_4$Cl crystallization and ingot solidification have been analyzed, and the application of NH$_4$Cl-water modelling on numerical simulation has been further discussed.

The aim of this work is to prepare a comprehensive set of models for the solidification of steel ingots by laboratory experiments and mathematical computation.

2   Fundamentals

Controlled solidification is one of the oldest processes for producing complex shapes for applications ranging from conventional process like foundry, ingot casting and continuous casting etc. to the modern technologies like directional crystal growth or laser processing, and remains as one of the most important commercial processes for many materials [3].

2.1   Solidification and as-cast structure

Solidification is a type of phase transformation during which liquid phase is transferred into solid phase, where the atom arrangement is an eternal repeating lattice. The driving force of solidification is the free Gibbs energy difference between the liquid and solid phase, and is usually achieved by cooling down the melt. A typical cooling curve of steel with high carbon content is shown in Fig. 2.1, where the liquidus temperature, solidus temperature of the steel grade can be determined from thermal analysis of the curve.
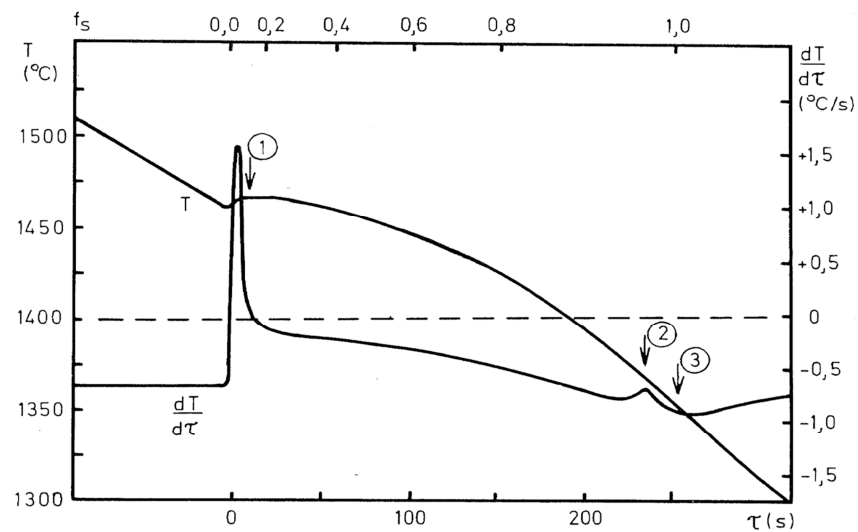
Fig. 2.1: Cooling curve of a steel grade with 0.69wt.-% carbon, ①: liquidus temperature, ②: temperature of eutectic formation, ③: solidus temperature [4]

The general macrostructure that is often seen in castings and ingot can be divided into three distinct zones: the outer chill zone with small crystals of approximately equal size, the intermediate columnar zone with elongated columnar dendrites, and the central equiaxed zone with relatively large equiaxed, Fig. 2.2.
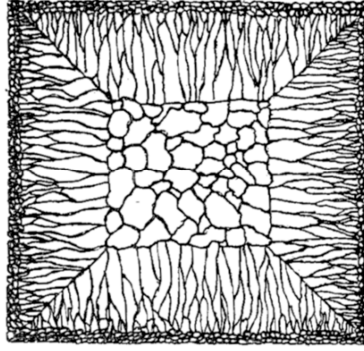
Fig. 2.2: Schematic sketch of ingot structure showing chill zone, columnar zone, equiaxed zone [5]

Besides the referred three zones, a region where the outer columnar dendritic structure transfers to the inner equiaxed grain structure is commonly observed in steel casting, named as the Columnar-to-Equiaxed Transition (CET) zone. Numerous mechanisms for CET have been proposed, and can be mainly divided into two types: mechanical blocking (hard blocking) [6] and solutal blocking (soft blocking) [7]. Mechanical blocking mechanism considers the blocking effect of the equiaxed grains on columnar grains that if the equiaxed grains are large enough or their volume fraction is large enough, CET will occur; whereas solutal blocking mechanism takes the solutal interaction into account that if the solute rejected from the equiaxed grains is sufficient to dissipate the undercooling at the columnar front, CET can take place.

2.2   Microsegregation

During solidification of a dendritic alloy, solute redistribution happens in the liquid and solid phase. Solute is rejected at the solid-liquid interface at the local scale of the secondary dendrite arm spacing by mass diffusion or convection [8, 9]. This process causes progressive enrichment of the interdendritic liquid with solutes and results in progressive increase of solute concentration in the dendrite from the core to its periphery [10]. This concentration inhomogeneity between the secondary dendrite arms is referred as microsegregation.

If the dendrites are small in size, the interdendritic liquid in the mushy zone may be assumed to be completely mixed. In such a situation, Guliver-Scheil model has been employed as the basis of quantitative analysis [11, 12] with the assumption of complete mixing in the liquid and no diffusion in the solid, as given in Equation 2.1

$$\frac{c_l}{c_0} = (1 - f_s)^{k-1} \qquad\qquad \text{Equation 2.1}$$

where k is the distribution coefficient and fs is the fraction of solid. This is known as the Gulliver-Scheil equation. $\frac{c_l}{c_0}$ is a measure of solute segregation (i.e. enrichment) of the liquid with progressive solidification.

Brody and Flemings [13, 14] took diffusion in solid dendrites into account and have modified the Gulliver-Scheil equation as follows:

$$C_s^* = k \cdot C_l = k \cdot C_0 (1 - \frac{f_s}{1+a \cdot k})^{k-1}$$

Equation 2.2

where $a = \frac{4D_s \cdot t_f}{\lambda^2}$, D_s is diffusivity of the solute in solid, t_f is solidification time, λ is the dendrite arm spacing.

2.3   Macrosegregation

Macrosegregation is a composition inhomogeneity in the scale from several millimeters to centimeters or even meters. These compositional variations have a detrimental impact on the properties of steel ingots and are not possible to eliminate by thermo-mechanical post-treatments because of the low diffusivity of the solutes in the solid state and the large distances involved. Therefore, it is one of the most well-known casting defects and remains a demanding challenge of scientific and technological importance in the field of solidification and casting [15, 16].

Commonly found macrosegregation patterns in steel ingots are a positively segregated zone at the top, negative segregation near the bottom in the equiaxed zone, inverse segregation near the ingot surface, V-segregation along the centerline, and A-segregation in the columnar zone [17, 18], as illustrated in Fig. 2.3. These inhomogeneities can seriously restrict the yield in the ingot casting and at the same time leads to the problems in the subsequent processing and final steel properties.

It is generally believed that macrosegregation results from the relative movement of solute enriched liquid or solute poor solid phase during solidification, e.g. thermal-/solutal-driven natural convection of the melt in the mushy zone, flow due to solidification contraction and the sedimentation of free equiaxed crystals over the scale of the whole cast [19, 20]. Accordingly, efforts to prevent macrosegregation are all aimed at controlling fluid flow and movement of solid, including adjustments of the alloy composition or thermal gradients to induce a stable density stratification in the liquid; application of nozzles, baffles, porous materials, or electromagnetic fields to redistribute the flow; and modifications to the grain structure to change the resistance to flow through the solid network or the prevalence of equiaxed grains [16].

Pool of solute-rich
buoyant liquid

Rising plumes of
buoyant liquid

Channels dissolved
through columnar
dendrite zone

Dendrite fragments
falling like snow from
emerging streams

Heap of heavy
equiaxed crystals

(a) Partially solidified ingot

Primary
pipe

Secondary
pipe

Positive
segregation

'A'
channel
segregates

'V'
channel
segregates

Cone of
negative
segregation

(b) Solid ingot

Fig. 2.3 Development of macrosegregation in a killed steel ingot [21]

2.4   Liquid motion and solid sedimentation

Movement of the melt flow and grains happens in the different stage of the whole ingot casting process. During mould filling, strong turbulence flow occurs, and it flushes the chilled grains on the mould wall down to the melt and thereby creates numerous nuclei. After a while it is attenuated, but the melt flow which inherits the turbulence pattern from filling still influences the solidification in terms of thermal and solute convection. During solidification melt flow is driven by buoyancy force due to density differences. Natural convection happens not only in front of the columnar dendrites, but also in the mushy zone. Interdendritic flow is driven primarily by thermal and solute buoyancy force and partly by the forced convection due to suction by shrinkage cavity formation etc. [22]. Meanwhile, globulitic or equiaxed grains can move along with the melt due to the drag force, or they can sink down on account of the density differences. The behaviour of the grains in terms of sinking or ascending depends on the size, morphology of the grains, and also on the volume fraction of solid inside the envelope of single or agglomerated grains. Besides the buoyancy force, other forces owing to motion of gas bubbles, applied magnetic fields, stirring, rotation and vibration also cause fluid flow and solid movement.

3   Bibliographic review

3.1   Ingots production

Since 1960's, top pouring casting was gradually replaced by bottom teeming with advanced refractory materials and casting fluxes, and the quality, surface and inner cleanliness of ingots is also constantly improved in order to keep pace with the increasing requirements [2]. Therefore production of steel ingots with adequate control of the quality of as-cast semi-products is of great concern for steelmakers today.

Typical application for conventional ingot casting includes the power engineering industry (e.g. shafts for power generation plants, turbine blades), the oil and gas industry (conveying equipment, seamless tubes), the aerospace industry (shafts, turbines, engine parts), medical engineering, ship building (shafts for engines and drives), tool making and mechanical engineering (heavy forgings, cold, hot and high-speed steels, bearing, drive gears) as well as automotive engineering (shafts, axes) [2].

3.1.1   Current situation of ingot production

The word wide production of crude steel in 2012 was 1518.3 million tonnes, 1438.3 million tonnes were cast by continuously, and 71.4 million tonnes were produced by ingot casting, which is 4.7% of the whole steel production [23]. Fig. 3.1 and 3.2 show the distribution of total steel production from 2002 to 2012 worldwide and in Germany, respectively. In Germany, 44.28 million tonnes of steel were produced in 2012, and 1.63 million tonnes of them were cast into ingots, which is 3.69% of the total domestic steel production. Most of the cast ingots were used in the rolling industry and the rest were forged. In 2011, 46% of the steel ingots were further process in forging industry, and 54% were used as rolling stock. Fig. 3.3 shows the distribution of steel ingot production for rolling and for forging from 2001 to 2011 in Germany.
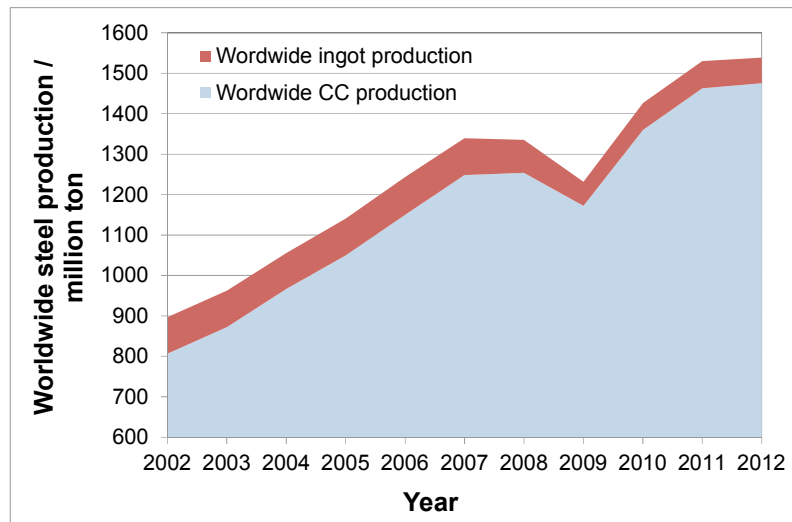
Fig. 3.1: Distribution of total steel production from 2002 to 2012 worldwide [23]
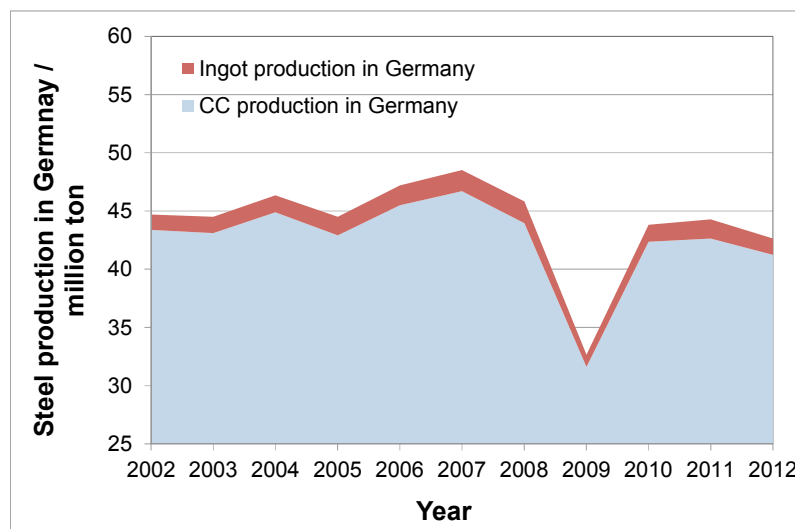
Fig. 3.2: Distribution of total steel production from 2002 to 2012 in Germany [23]
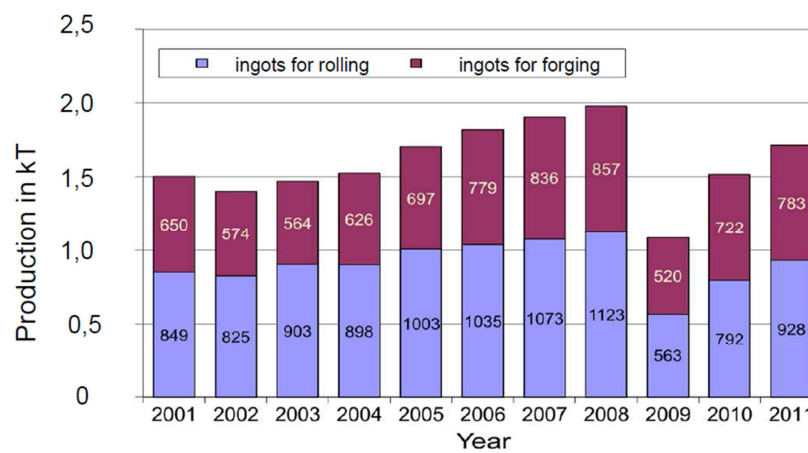
Fig. 3.3: Distribution of steel ingot production for rolling and for forging from 2001 to 2011 in Germany [24]

In Germany, ingot casting was practiced in 19 steel works in 2012, and in addition, 9 remelting shops produce high quality steel ingots as well, as given in Fig. 3.4.

a)   b)
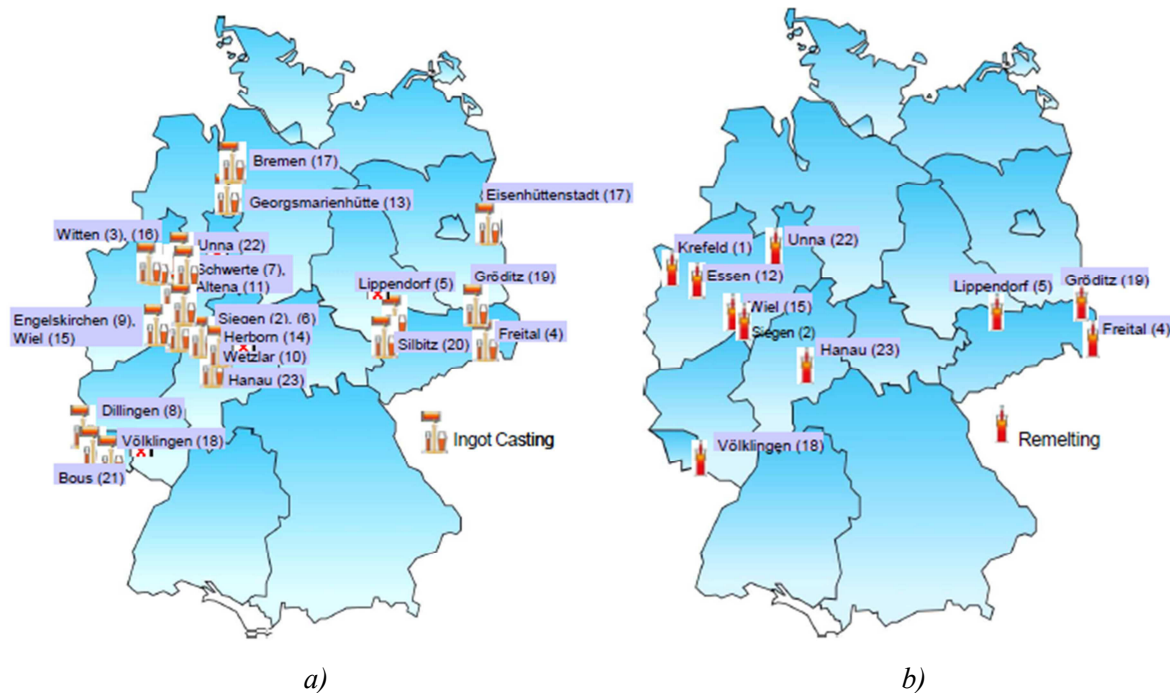
Fig. 3.4: a) Ingot casting shops in Germany, b) remelting shops in Germany [24]

(1)DEW, Krefeld, (2) DEW Siegen, (3) DEW Witten, (4) BGH Freital, (5) BGH Lippendorf, (6) BGH Siegen, (7) Deutsche Nickel, (8) Dillinger Hüttenwerke, (9) Dörrenberg Edelstahl, (10) Edelstahlwerke Buderus, (11) Edelstahlwerke W. Ossenberg, (12) Energietechnik Essen, (13) Georgsmarienhütte, (14) Isabellenhütte, (15) Kind & Co. Edelstahlwerke, (16) Friedrich. Lohmann, (17) Bremen, Eisenhüttenstadt / Brach (18) Saarschmiede, (19) Schmiedewerke Gröditz, (20) Silbitz Guss, (21) Stahlwerk Bous, (22) ThyssenKrupp VDM, (23) Vacuumschmelze Hanau.

As the demand of heavy ingot increases nowadays, especially from the power engineering industry and ship industry, there is a tendency of producing extreme large ingots over 600 t and continuous cast strands with thickness over 450 mm and rounds with diameter up to 800 mm [1], which are mainly applied for pressure retaining components such as reaction vessels for nuclear power plant and rotating components like drive shafts of gas turbines and generator rotors.

The very heavy casting capacity in operation today is in Japan (Japan Steel Works), China China (China First Heavy Industries and China Erzhong) and Russia (OMZ Izhora). Till August 2013, the maximum weight of ingot produced today is around 650 t with the press up to 14 000 t in the world largest supplier of heavy forgings Japan Steel Works (JSW). New capacity is being built by JSW and JCFC in Japan, Shanghai Electric Group (SEC) and subsidiaries in China, and in South Korea (Doosan), France (Le Creusot), Czech Rep (Pilsen) and Russia (OMZ Izhora and ZiO-Podolsk). New capacity is planned in UK (Sheffield Forgemasters) and India (Larsen & Toubro, Bharat Heavy Electricals, Bharat Forge Ltd). In China the Harbin Boiler Co. and SEC subsidiary SENPE are increasing capacity [26]. Table 3.1 gives the major heavy ingot manufacturers and the corresponding

capacities in the world.

Country	Company	Max. Ingot (t)	Press(t)
Japan	Japan Steel works	600 (650)	14 000
	JCFC		
China	Erzhong + Dongfang	600	12 700 / 16000
	Shanghai (SEC)	600	16 500
	China First Heavy Industries (CFHI)	580	15 000 / 12 500
South Korea	Doosan	540	10 000
Russia	OMZ Izhora	600	12 000
India	Larsen & Toubro	600	15 000
UK	Sheffield Forgemasters	500	10 000
Italy	ThyssenKrupp Acciai Speciali Terni	500	12 600
France	Creusot	250	11 300
	Areva, SFA Rsteel	250	11 300
Czech	Pilsen Steel	250	10 200
Germany	Saarschmiede	370	8670

Table 3.1: World major heavy ingot manufacturers [24, 26]

Since the application of the heavy ingots is mostly high value products, high quality of the as-cast ingots is demanded. Main issues related to production of these heavy ingot are: optimization of metallurgical process; geometrical design of the ingot; control of the composition, temperature and casting speed; simulation of solidification, minimization of inclusions, impurities and segregation; optimization of refractory materials, etc.

3.1.2   Ingot quality

Typical ingot casting defects are cavities, porosities, macrosegregation, inclusions, cracks, and other surface defects. Among these defects, macrosegregations are the most serious ones since it is far difficult to be reduced by thermo-mechanical post-treatment.

Many studies suggested that the ingot size has effects on macrosegregation. Delorme et al. have examined the macrostructures of 30-300 t steel ingots produced by conventional casting processes and reported that by that as the ingot diameter increases, the macrosegregation degree of the ingot increases [27]. Fig. 3.5 shows the dependency of macrosegregation degree of carbon on the diameter of ingots.
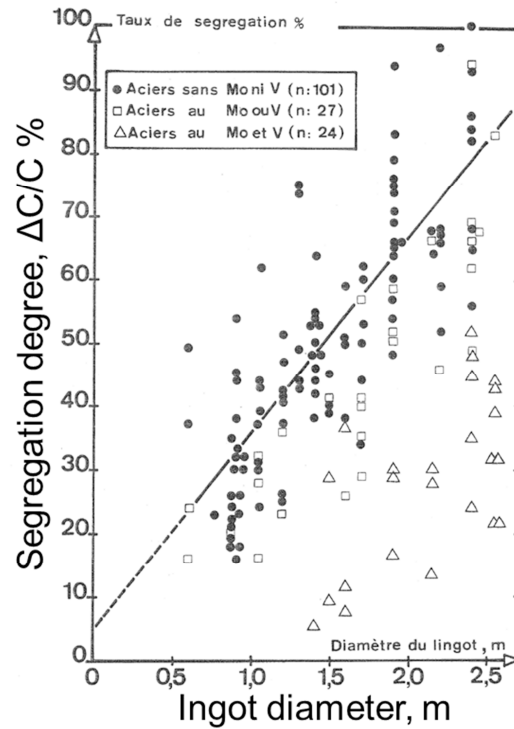
Fig. 3.5: Dependency of macrosegregation degree of carbon on ingot diameter [27]

From 1970's till present, plenty studies on ingot macrosegregation with various different sizes and weight have been conducted and reported, mainly in terms of the carbon segregation degree along the centerline of the ingot [28- 31, 19, 32]. Data of the ingots with weight from 5 t to 90 t from literature have been extracted and summarized as a distribution of segregation index $\Delta C/C_0$ (see also Equation 5.2 in page 60) along the longitudinal direction, i.e. $\Delta C/C_0$ versus H/Hmax, as shown in Fig. 3.6.

It seems that the maximum segregation index always happens at the top, and the heavier the ingot is, the larger the segregation index is. For the ingot with the weight of 90 t, the maximum segregation index is up to 1.5. However, the effect of ingot size does not seem to be very pronounced on the macrosegregation degree for manganese [33].

Besides the segregation degree, it was also found that macrosegregation pattern in terms of the position and contour of A- and V-lines varies. Fig. 3.7 shows sulfur prints of a few ingots with weight from 30 t to 300 t.
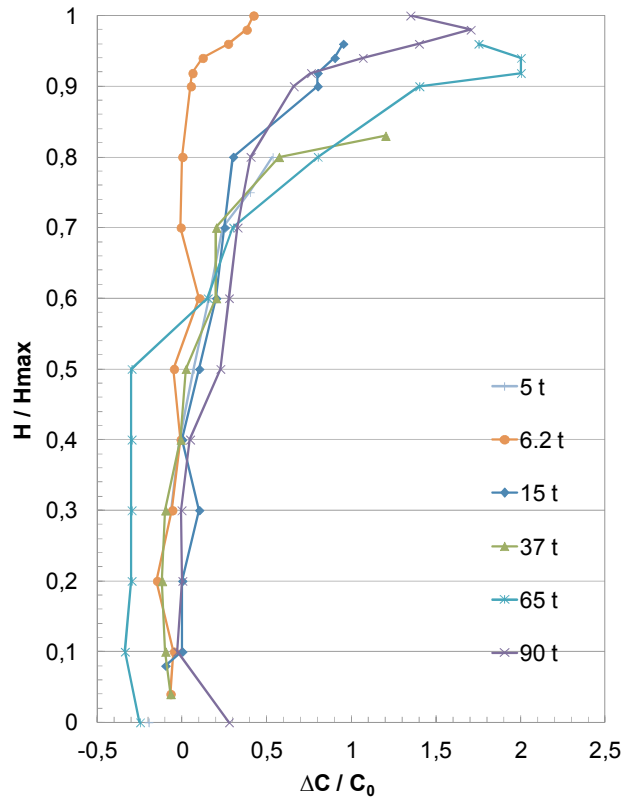
Fig. 3.6: Distribution of segregation index of carbon ($\Delta C/C_0$) along the centerlines of 5t, 6.2t, 15t, 37t, 65t and 90t steel ingots [28- 31, 19, 32]

a) *H/D=2.0*   b) *H/D=2.1*   c)*H/D=1.8*   d)*H/D=1.39*
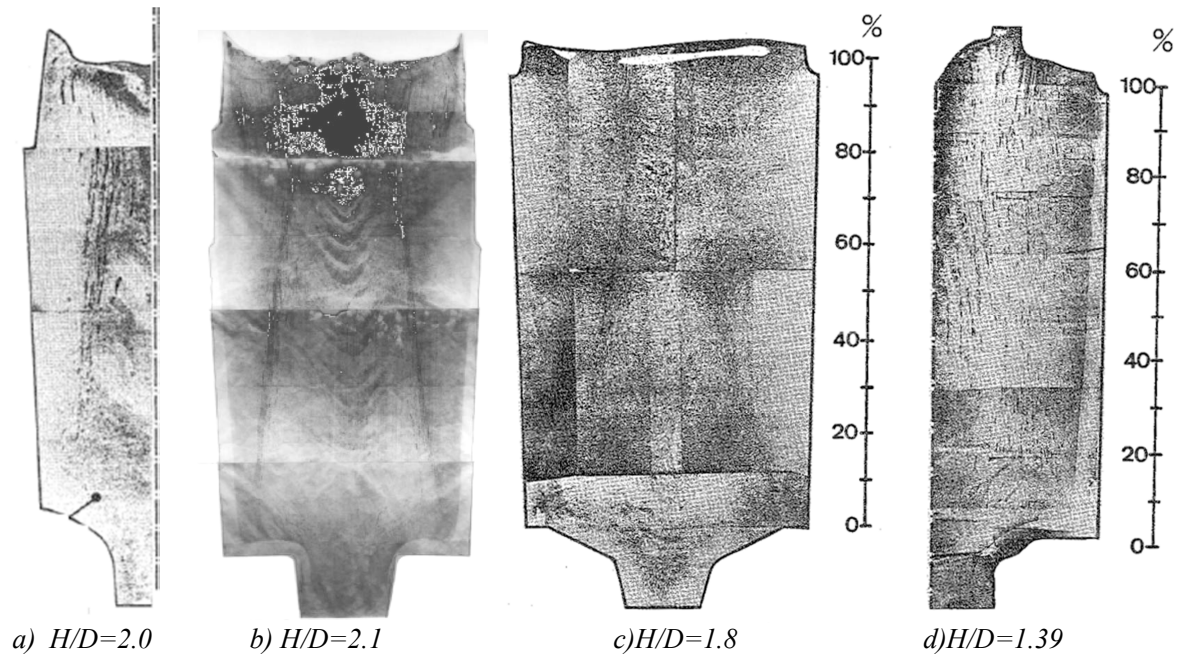
Fig. 3.7: (a) 30t carbon steel ingot; (b) 65t steel ingot with 0.2wt.-% C; (c) 105t 22NiMoCr3.7; (d) 300t 25NiCrMoV14.5, b)[34], a)c)d) [27]

Generally all the sulfur prints in Fig. 3.7 show the form of A-lines at the half radius position of the

ingots and V-lines in ingot center. The 30 t and 65 t carbon ingots have more obvious alternation in the form of V-lines, whereas in the 105 t and 300 t ingots the periodic occurrence of V-lines is not very apparent. The region of A-lines for the 30 t to 65 t ingots are relative narrow are near the ingot center line, whereas for the 105 t ingot there is a wide region of A-lines from the side to ingot center where A-lines are distributed loosely. The 105-t ingot shows an accentuated segregation border in the form of a cone directed from the bottom to the top. The 300 t ingot doesn't show such form, instead, it shows vertical lines which are arranged in annular zones. The inclined angle of the A-lines to gravity is also different at different part of the ingots, as shown in Fig. 3.7, at the lower portion and outer region of the ingot, the A-inclined angle seems to be larger and at upper portion and inner region of the ingot, the A-lines are more vertical.

Table 3.2 summarized the solidification time of different ingots which have been reported in the past, with mass from 37 t ton 600 t and different shapes. The H/D ratio has been calculated from the ingot geometry for each ingot, and it seems that the H/D ratio decreases as ingot mass increases. The solidification constant has been calculated based on the width D and the solidification time according to the square root law:

$$x = k \sqrt{t} \qquad \qquad \text{Equation 3.1}$$

$$k = \frac{D/2}{\sqrt{t}} \qquad \qquad \text{Equation 3.2}$$

From Table 3.2 it can be seen that for ingots with round shape, the solidification constant is between 26 to 31.8 mm/min$^{0.5}$, and with ingot mass over 300 t the solidification constant is over 30 mm/min$^{0.5}$, whereas for ingot with the mass from 65 t to 230 t the solidification constant is from 26 to 28.3 mm/min$^{0.5}$. For the slab ingot is seems that the solidification constant is lower with the value of 21.8 mm/min$^{0.5}$. This might be due to the fact that the heat transfer in slab is mainly one dimensional from beginning to end of solidification, whereas the heat transfer in round ingots is two dimensional especially at the late stage of solidification, and this leads to a faster solidification rate in the end and therefore a higher averaged solidification constant for the whole solidification process in round ingots.

Ingot mass / t	H / mm	D / mm	B / mm	Shape	H/D	Solidification time	Solidification constant / (mm/min$^{0.5}$)
37	2819	1016	2083	slab	2.78	≤ 9 h	21.8
65	3800	1800	--	round	2.11	20 h	26.0
100	3760	2150	--	round	1.75	24 h	28.3
230	4500	2737	--	round	1.64	45.8 h	26.1
360	5320	3640	--	round	1.46	60 h	30.3
600	6313	4072	--	round	1.55	68.4 h	31.8

Table 3.2: Ingot geometry, solidification time and calculated solidification constant [19, 35, 31, 36, 37, 38]

The solidification constants were reported to be 22 mm/min$^{0.5}$ for slab ingots with the width/thickness

ratio larger than 1.7 [39-40], and for round/square shaped ingots with the width/thickness ratio smaller than 1.7, the solidification constants were found to be higher, for example for a square ingot with the thickness of 400 mm the solidification constant is 31 mm/min$^{0.5}$ [41-43].

Although ingot casting is a highly mature technique, there is still potential for further improvement with regard to quality and processing. During the last few years, customer requirement of the ingot products have been concentrated mainly on low levels of segregation and macroscopic cleanliness of the ingots. Simulations on solidification and fluid flow have been widely applied for the prediction and control of segregation and inclusions distribution. Casting fluxes such as granulated products are more often used not only to reduce the dust at the work place but also to benefits the feeding and distribution of the casting fluxes, in order to prevent re-oxidation during teeming, especially for ingots with large cross-sections. Robots are more often used to automate the manufacturing processes [2].

Besides the conventional ingot casting, other special technologies such as vacuum casting (VC), electroslag remelting (ESR) and vacuum arc remelting (VAR) and Plasma Treatment Casting (PTC) are applied for production of ingots of high quality. During the last few decades, through ESR process it is possible to produce ingots with the weight up to 250 t, and the demand for ESR-ingots with the weight over 100 t is still increasing.

3.2   Prediction of macrosegregation

Many simulation and experimental works have been performed on the prediction of macrosegregation and validation of the models since 1960's [44-47, 20]. Today, quantitative prediction of macrosegregation remains to be difficult due to its complexity that species are transported in multiple scales and has interaction with the microstructure. In order to model the solidification process, consideration of many solidification phenomena such as heat transfer, phase transformation, fluid flow, and the movement of the residual liquid and equiaxed grains is required, meanwhile the understanding of nucleation, growth kinetics, and species redistribution on interfacial scale is also demanded [19, 48]. In the following chapters, macrosegregation models and commercial software packages for ingot casting are introduced with highlights and shortcomings, and the current techniques for the characterization of marosegregation are presented.

3.2.1   Macrosegregation models

LSRE-models

In 1960's, the macrosegregation models have been developed by Fleming and co-workers [44] that has indicated macrosegragtion results from interdendritic flow. In their model, they considered planer

isotherm that isotherms move with a velocity R_x describe by

$$G_x = \frac{dT}{dx} \, . \qquad\qquad\qquad \text{Equation 3.3}$$

$$R_x = \frac{\dot{T}}{G_x} \qquad\qquad\qquad \text{Equation 3.4}$$

where G_x is the thermal gradient in x-direction, dT is the change of temperature, and $\dot{T}$ is the cooling rate. The interdendritic flow (no diffusion) is driven by the solidification shrinkage, and the local solute redistribution equation (LSRE) is influenced by the fluid flow and the solidification progress, as given in Equation 3.5.

$$\frac{\partial f_l}{\partial C_l} = -\left(\frac{1-\beta}{1-k}\right) \cdot \left(1 + \frac{\vec{v} \cdot \nabla T}{\dot{T}}\right) \cdot \frac{f_l}{C_l} \qquad\qquad \text{Equation 3.5}$$

where f_l is the fraction of liquid within the volume element (a small volume with the order of dendritic arm spacing), C_l is the liquid concentration in the volume element, β is the solidification shrinkage, and $\beta = \frac{\rho_s - \rho_l}{\rho_s}$, $\vec{v}$ is the local velocity of interdendritic liquid relative to solid, ∇T is the temperature gradient. With no shrinkage and no interdendritic flow, Eqation 3.3 is reduced to the Scheil equation.

Mehrabian et al. [49] modified the LSRE model with consideration of the effect of thermal buoyancy force to fluid flow. The change of liquid density is calculated through a temperature gradient ∇T within the mushy zone, given in Equation 3.6.

$$\nabla \rho_l = -\frac{1}{\dot{T}} \cdot \frac{\partial \rho_l}{\partial t} \cdot \nabla T \qquad\qquad \text{Equation 3.6}$$

They also take into account the drag force in the mushy zone to the liquid flow, and Darcy's law have been applied to calcualte the velocity of the interdendritic liquid, as given in Equation 3.7.

$$\vec{v} = -\frac{K}{\mu \cdot f_l}(\nabla P + \rho_l \cdot g) \qquad\qquad \text{Equation 3.7}$$

where μ is the dynamic viscosity of the interdendritic liquid, K is the permeability of the mushy zone, P is the pressure, ρ_l is the liquid density, and g is the acceleration due to gravity.

By recognising that isotherm velocity $R = \frac{\dot{T}}{\nabla T}$, Equation 3.7 can be re-written:

$$\frac{\partial f_l}{\partial C_l} = -\left(\frac{1-\beta}{1-k}\right) \cdot \left(1 + \frac{\vec{v}}{R}\right) \cdot \frac{f_l}{C_l} \qquad\qquad \text{Equation 3.8}$$

Based on the expression in Equation 3.8, Mehrabian and Flemings. have proposed a criteria of flow instability. If the flow velocity $\vec{v}$ in the opposite direction of isotherm movement is larger the isotherm velocitye R, $-\left(1 + \frac{\vec{v}}{R}\right)$ is positive, meaning that $\frac{\partial f_l}{\partial C_l}$ is also positive, i.e. the liuid fraction is increasing, remelting will occur.

In 1986 Ohnaka [50] has presented a numerical model for predicting macrosegregations with modified microsegregation model which considers diffusion in solid state, and he suggested that the diffusion path through the primary and secondary dendrites could influence the solute redistribution. The liquid concentration is calculated with consideration of the dendritic structure, as given in Equation 3.9.

$$\frac{c_l}{c_0} = (1 - \varphi \cdot f_s)^{(k-1)/\varphi} \qquad\qquad \text{Equation 3.9}$$

where $\varphi = 1 - \beta \cdot k/(1 + \beta)$, $\beta = 2\alpha$, $\alpha = 4D_s \cdot t_f/\lambda^2$, k is the distribution coefficient.

In the same year, Olsson have reported a simple macrosegragtion models which considers the effect of settling of the equiaxed grains and the A-segregates on macrosegregation. In his work he calculated the macrosegregation degree for carbon (C/C_0) along the center line of the ingot and compared the simulation results with a 170 kg steel ingot [20].

Most of the models appearing in 1970's and 1980's are solely concerned with heat transfer based on simplifications such as steady state thermal condition with a given temperature gradient as an input instead of calculation by using the energy conservation equations to find the transient values. Another limitation is that fluid flow in the bulk liquid and coupled flows between the bulk and mushy regions are not included. Since the appearance of the multi-domain models and later the continnum models these simplifications and limitations were gradually removed [51].

Multi-domain models

As the first attempt of multi-domain models, Fuji et al. [52] developed a model in 1979 which couples energy and momentum conservation in the mushy zone. In their model a modified LSRE model which accounts for complete solid diffusion of interstitials and limited solid diffusion of substitutionals has been applied, and the prediction of the transient temperature field and velocity field have been accomplished.

In 1981 Riddel et al. reported the first multi-domain model which treated with two calculation domains in terms of the mushy zone and the fully liquid metal pool ahead of the liquidus isotherm [53]. Velocity and pressure are coupled and calculated in each domain and also across the moving boundaries between them. In the mushy zone the interdendritic flow which is driven by solidification shrinkage is calculated by using Darcy's law and whereas in the pure liquid zone the fluid motion due to natural convection is calculated by solving Navier-Stock equations for laminar convective flow. The temperature field in the liquid zone was calculated by coupling with the momentum equation and in mushy zone no temperature field was predicted. This model has been validated experimentally with Sn-Pb alloys.

It needs to be noticed that unlike the former models that melt densities were fixed, in this model the change of melt density caused by thermal and solutal expansion is calculated as a function of both local concentration and temperature. Ridder et al. were the first to investigate the effect of natural convection flows in the bulk liquid on interdendritic flows in the mushy zone [53].

The main limitation of the multi-domain models is that the border between the mushy zone and the bulk liquid needs to be tracked. For solidification in steady state where the liquidus isotherm is fixed, the border is not movable and no tracking is necessary; for non-steady solidification where the liquidus isotherm moves during solidification, it is difficult to track the border and re-mesh the calculation domain especially for complex border morphologies [54].

Continuum models based on mixture theory

In order to solve the problem of border tracking of the multi-domain approach, the continuum models with single calculation domain have been developed [55-57] based on mixture theory. The first single domain continuum model has been reported by Bennon and Incropera for a binary solid-liquid system [55]. In this model, by assuming level-rule equilibrium solidification and usage of semi-empirical laws, the microscopic transport behavior have been integrated with principles of classical mixture theory, and a set of continuum conservation equations for the solid-liquid phase change system have been applied. The momentum equations are for laminar Newtonian flow and are based on the Navier-Stroke equations, and with consideration of the drag force in the mushy zone, Darcian term has been added. The thermal/solutal buoyancy force has also been taken into account by using Boussinesq approximation [59].

Bennon and Incropera have applied this model to the "solidification" of a binary, aqueous ammonium chloride solution in a rectangular cavity [58]. The study indicated that advective transport of water enriched interdendritic fluids across the permeable liquidus interface is the primary mechanism for macroscopic species redistribution, and the extent of this penetration is governed by the relative strengths of solutally driven mushy region flows and thermally driven flows in the bulk liquid. What is remarkable is that they have examined the local unstable remelting and flucturating bulk fluid transport behavior, and for the first time, A-segregation has been numerically predicted.

One drawback of the continuum models is that the interfacial exchange of solute, enthalpy, momentum is not included in the governing equations since these conservation equations describe only the macroscopic behavior of the mixture of the solid-liquid phase as one phase, in other words, the microscopic relations between the phases are missing. Another drawback is that since the local solid concentration is simply averaged over the whole phase or not calculated, the negative segregation due to grain sedimentation cannot be predicted by the continuum models. To solve these problems, a volume-averaging approach which couples microscopic and macroscopic solidification behavior has been developed.

Volume averaged models

The volume averaged method separate the conservation equations for each phases (e.g. solid and liquid phase), and by adding the interfacial exchange term, the microscopic interaction between different phases are embedded into the macroscopic system and the both are strongly couple. This method introduces a representative elementary volume (REV). A REV is defined as a volume element that is large enough to include a representative sampling of the microscopic structures and meanwhile small enough to enable a continuum description of the variables averaged over the REV on the macroscopic scale [60]. The solid and liquid phases in a (REV are treated separately and the field properties are averaged.

The first volume averaged model was proposed by Ni and Beckermann [61] in early 1990's. The model is formulated by viewing the solid and liquid phase separately and averaging the field properties of each phase over a representative elementary volume. Two set of governing equations are used to describe the conservation and transport of mass, momentum, energy and species transport in a solidifying system. The solid velocity is calculated by using an effective solid viscosity which varies between zero and infinity according to the solid fraction. This model succeeded in prediction of the double-diffusive convection during dendritic solidification in a binary-phase system (solid and liquid). Besides Ni and Beckermann, various volume averaged models were proposed by other researchers with the similar volume-averaged formulations [57, 62-63].

The advantage of the volume averaged approach is that the transfer of momentum, species and enthalpy between the liquid and solid phase are already accounted in the governing equations for both phases, and phenomena such as sinking of equiaxed grains can be modeled, and the interfacial composition and temperature can be calculated, therefore interfacial grain growth as well as nucleation are able to be incorporated [64-67]. Due to the power of the volume average model, it was widely accepted and further developed in the next two decades till present [68-70].

The volume averaged models proposed by Ni and Beckermann contains many simplifications such as immobile solid phase and simple feature of the grains, and is applied to a binary Fe-C alloy system. Wang and Bckermann [71-73] developed a two phase model which considers the morphology of the equiaxed dendritic structure and settling of the equiaxed grains. They have introduced a grain envelope consist of solid dendritic skeleton and interdendritic liquid, and the contour of the envelope is the boundary between the interdendritic and extradendritic liquid, as shown in Fig. 3.8. The phase change rate (Γs) is calculated through interfacial species balance between the dendritic skeleton, interdendritic and extradendritic liquid, as given in Equation 3.10.

$$\frac{c_l}{c_0} = (1 - \varphi \cdot f_s)^{(k-1)/\varphi}$$ Equation 3.10

where φ is an envelope shape factor defined as $\varphi = A_{equivalent}/A_{actual}$. The microscopic

concentration profile at the two interfaces from dendritic skeleton to extradendritic liquid is illustrated in Fig. 3.9.
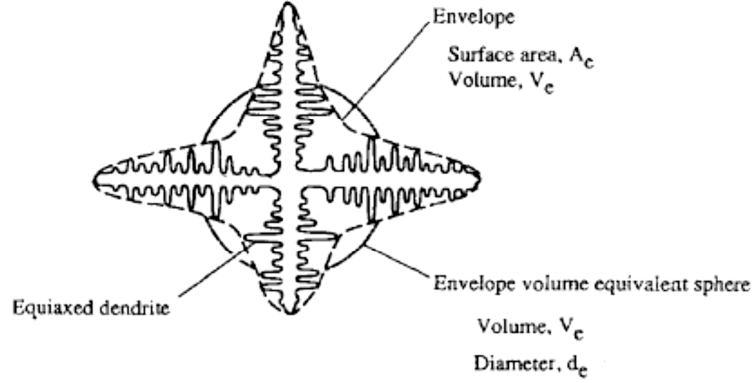
Fig. 3.8: Schematic of an equiaxed dendrite envelope [67]
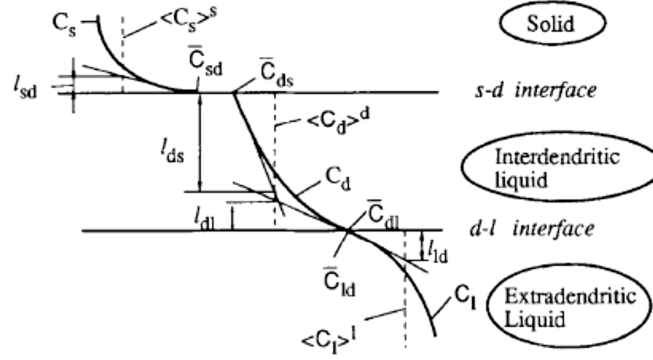
Fig. 3.9: Schematic illustration of the interfacial concentration and species diffusion lengths [67]

The physical meaning of Equation 3.8 is that the species flux rejected into the interdendritic liquid due to phase change (left-hand side (LHS)) is either diffused/convected into the solid and extradendritic liquid through interphase exchanges within the control volume (the first and second term on the right-hand side (RHS)), and is stored in the interdendritic region (third term on the RHS), or is advected and diffused out of the control volume (fourth and fifth terms on the RHS). Equation 3.8 actually describes the microscopic grain growth across the envelope interface, and the phase change rate Γs links the microscopic equation and the macroscopic equations together (for the full set of equations, see [71]).

Note that Wang and Beckermann considered the flow partitioning between the intedendritic and extradendritic region, as originally proposed in [74]. As schematically shown in Fig. 3.10, the liquid may flow either through the inter- or the extradendritic region, and the velocity of the total liquid v_f, interdendritic velocity v_d and extradendritic velocity v_l can differ from each other. The relationship between them is described in Equation 3.11.

$$f_f \rho_f v_f = f_d \rho_d v_d + f_l \rho_l v_l$$
<div align="right">Equation 3.11</div>

where subscript f denotes the total liquid, consisting of the inter- and extradendritic liquids, s denotes solid phase and d denotes interdendritic liquid phase.

For uniform flow distribution, $v_f = v_d = v_l$.
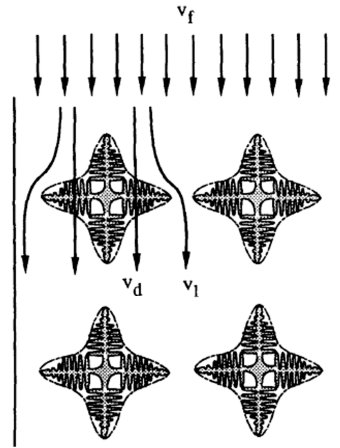
Fig. 3.10: Schematic of the portioning of the liquid flow through the inter- and extradendritic regions in equiaxed solidification [74]

Wang and Beckermann added the transport term resulted from flow portioning effect into the species and momentum conservation equations, and therefore exchange of solute and momentum between the interdendritic and extradendritic are accounted, and macrosegregation induced by sedimentation of the equiaxed dendrites as well as the flow of the extradendritic liquid can be better predicted. They have applied the model to a NH_4CI-70 wt.-% H_2O solution and good agreement have been found between the observed and predicted flow pattern and the crystal settling rates [73].

Wang and Bckermann utilized this two-phase model to predict the columnar-to-equiaxed transition (CET) in castings of A1-Cu and Sn-Pb alloys [75]. After that, Schneider and Beckermann presented an early multi-component two-phase model and applied it into a low alloy steel ingot [63]. In this model the interfacial concentration of liquid and solid are not calculated according to the level rule or Scheil equation, and instead, they are calculated by taking account of different levels of the solid-state diffusion (back diffusion). This model was later applied for the prediction of freckle formation in directional solidification of Ni-based super-alloys [76, 77]. Besides Schneider and Beckermann's model, other multicomponent models have also been proposed [78, 79], but these models were not widely used. Principally the models in the late 90's are able to predict the A segregation, but due to the limitation of computer source and the coarse grid, the prediction A segregates was out of the scope of the research work at that time..

Following the two-phase models of Beckermann et al., many studies in the 21 century have focused on the generation, growth and movement of equiaxed grains in convective melt, and the prediction of V-

segregation and A-segregation [51]. Development of the volume averaged models after 2000 included the extension of the two-phase models into three-phase models and three-dimension [80,81], morphology evolution of the equiaxed grains [82, 83], consideration of the shrinkage induced flow in order to predict the V-segregation [84], refinement of the mesh size for the prediction of the A-segregation [85, 86, 87], etc.

The three phase model develop by Wu and Ludwig [88] deals with the mixed columnar-equiaxed solidification and three phases in terms of the stationary columnar solid, equiaxed solid and liquid are considered. The columnar to equiaxed transition were predicted by using the hard-blocking mechanism, and the grain sedimentation was calculated by assuming the free equiaxed dendrites as globular grains. In 2009 Wu and Ludwig presented a modified volume-averaged equiaxed solidification model which accounts for the globular-to-dendritic transition of the equiaxed grains and the behavior of the extra- and interdendritic liquid in a grain envelope. The shape of the dendritic grain is simplified by an ''equivalent sphere'' similar as the envelope suggested by Combeau and Beckermann [82, 71]. The equiaxed grain starts to grow with globular (spherical) morphology, and a Zener-type diffusion field for steady-state growth of a sphere [69] was applied in order to calculate the grain growth velocity v_{glob}; as soon as the globular-to-dendritic transition occurs, the Lipton–Glicksman–Kurz tip growth kinetics [88, 89] was applied to estimate the evolution of the grain envelope v_{env}. The interdendritic melt and the solid dendrites were regarded as one hydrodynamic phase sharing the same velocity, and the other hydrodynamic phase is the extradendritic melt. The velocities of the two hydrodynamic phases are solved with a two-phase Eulerian approach, and transport of the mass and solute species of each thermodynamic phase region are considered individually. In this two-phase model, no columnar dendritic growth is taken into account.

In 2012, Li, Wu and Ludwig [85] developed a modified mixed three-phase model for a binary Fe-C alloy with 0.45 wt.-% carbon and compared the macrosegregation predicted from this model and a two-phase model to an industrial 2.45-t steel ingot. With the fine mesh size from 0.25mm to 2mm, some streak-like patches of positive segregation were predicted near the mould wall and even in the centre region. Since these streak-like patches are somehow looks like the so called A-segregation [90], they call thestreak-like segregation as quasi-A-segregation.

In the same year Li and Wu [86, 87] applied a two-phase columnar model to a Sn-10 wt.% Pb alloy which solidifies in a 3-D cavity and similar channel segregation as the quasi-A-segregation were again simulated, as shown in Fig. 3.11. Li and Wu have utilized the Rayleigh number which is often used in directional solidification of super alloys as a qualitative indicator for characterizing the origin of segregation channels in ingot solidification.
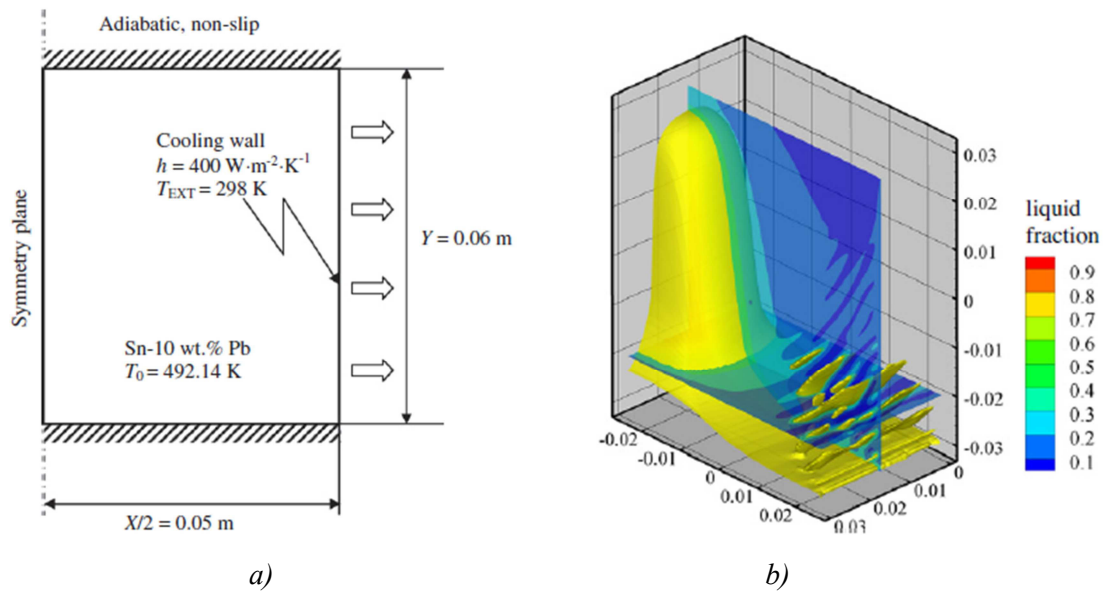
Fig. 3.11: a) Geometry and boundary condition of the calculation domain, b) fraction of liquid in a vertical center plane and a horizontal plane with 0.01m from bottom at 400 s [87]

Likewise, Combeau et al. developed another multiphase and multi-scale model based on Beckermann's volume averaged model [82, 83]. The model tackles the morphology evolution of the equiaxed grains and their motion, and also accounts for the flow of the interdendritic liquid in the region in which the grains are packed and motion of the grains is blocked. Three cases with fixed solid, free-floating dendritic grains and free-floating globular grains (Fig. 3.12) were simulated and compared with solidification of an industrial 3.3 t steel ingot. The comparison revealed that the most significant discrepancies lies in the globular case and therefore indicated the importance of a proper modelling of the grain morphology when considering the motion of free-floating grains in steel ingots. Combeau et al. have also predicted the fish-bone shape A-segregation at the top of the ingot with averaged grid size of approximately 7x12 mm (width x height), and with coarser grids A-segregates cannot be predicted, as shown in Fig. 3.12 a).

Other researchers in the past decade have also examined the numerical model and have modified the numerical simulation methods or solution schemes and the incorporation of mechanical stresses into simulations [91-96]. Today, the multiphase volume-average model has become the most promising model in the field of solidification simulation [80]. However, due to lack of information with regard to input parameters such as the nuclei density in the melt, nucleation undercooling and auxillary models for instance the solute redistribution mechanism at the solid/liquid interface, and the local heat transfer coefficient with consideration of gap formation during solidification and the sensitivity of this model on these parameters, prediction on macrosegragation remains is still limited. Meanwhile, the computational requirement of the complex macro-models is very high, especially for heavy ingots. In order to resolve the channel segregates, mesh sizes need to be smaller than the channel width and is usually of the order of a few millimeters or less to make sure that results are mesh independent [63,

97-99]. Nowadays the computational capability cannot enable the coupling of microscopic and macroscopic solidification phenomena precisely in very fine meshing, and this often lead to reduction of the mesh size or system geometry or introduction of significant simplifications [51]. To overcome these problems, considerable works still needs to be done to complement the input parameters and to improve the auxillary models, to refine the numerical solution schemes or to apply new computational techniques such as parallel computing.

a)   b)   c)
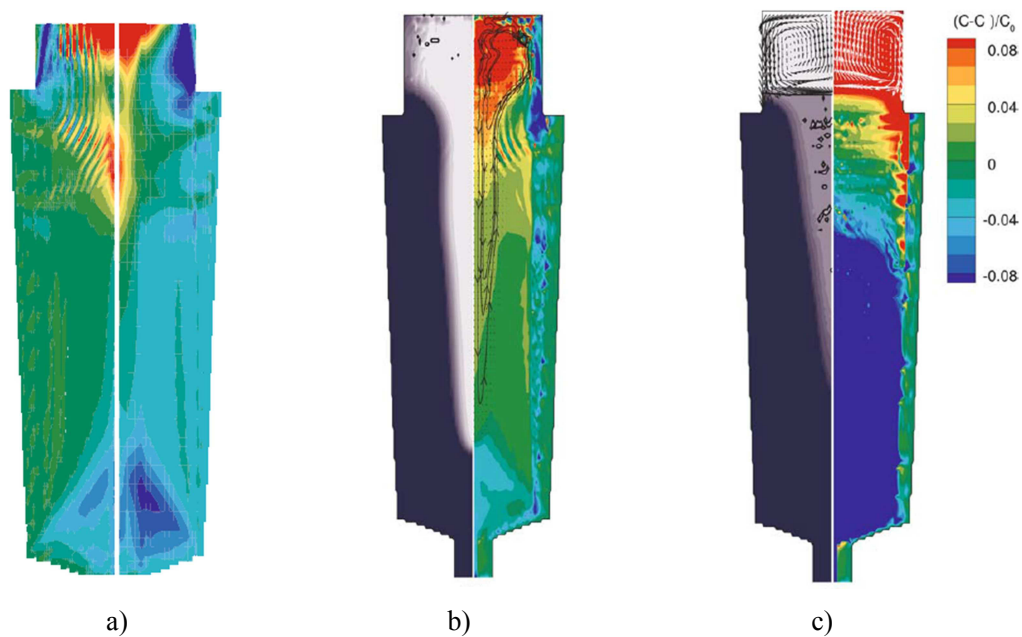
Fig. 3.12: a) effect of the grid size on the predicted carbon macrosegregation for the fixed-solid case, left: fine grid; right: coarse grid. b) simulation results for the case with free-floating dendritic grains, c) simulation results for the case with free-floating globular grains [82]

3.2.2   Commercial softwares

There are a few commercial software packages, such as MAGMASOFT, ProCast, TherCast which are able to calculate the mould filling and solidification path in ingot casting. By calculation of the temperature field, concentration field and velocity field, they can predict the hot spot, macrosegregation, porosities as well as inclusion distribution.

MAGMA 5 is a 3-D casting simulation software based on the finite difference method that is developed by MAGMA Gießereitechnologie GmbH since 1980's. The application of MAGMA5 in not limited in steel ingot casting, but also in the field of sand casting and investment casting for non-ferrous alloys. This software consists of a base module and a set of extension modules such as that MAGMASteel and MAGMAstress to cover most of the characteristics of casting. The major aspects that MAGMA 5 is capable are:

1) Pouring from ladles with calculation of the ladle characteristics
2) Mould filling simulation to calculate temperature, velocity and pressure distribution

3) Prediction of mould erosion during filling

4) Tracking of the development of re-oxidation and sand inclusions

5) Calculation of melt convection during solidification and corresponding casting macrosegregation

6) Quantification of centerline and macroscopic shrinkage

7) Prediction of sand burn-on and penetration

8) Crack prediction, stress and distortion of the casting.

ProCAST [100, 101] is a commercial finite element software package for casting simulation. The code is developed by ESI Group. It is composed of three major function modules in terms of pre-processor that is geometry editor and mesh generator, solver, and post-processer. The solver consists several modules such as thermal, radiation, fluid flow, stress, microstructure, macrosegregation, grain structure (CAFE) and optimization module. Furthermore, a material database is included in the software packages, either. With these modules, ProCAST allows modelling of ingot casting in following aspects:

1) Mould filling simulation with free surface evolution

2) Heat transfer and solidification modelling in the whole casting process

3) Flow filed including convection and turbulence

4) Macrosegregation

5) Coupled thermal-stress computation, air gap formation

6) Porosity and crack prediction

7) Microstructure and grain structure modelling

THERCAST [102] is another software package for the three-dimensional simulation of casting processes. Similar like ProCAST, it is also based on finite element method to describe the thermo-mechanical phenomena associated with the various phases of mould filling, solidification and cooling in and out of the moulds. The code was developed by CEMEF and TRANSVALOR. The capabilities THERCAST include:

1) Filling simulation to consider metal free surface, initialise the velocity and temperature field

2) Calculation of deformations and stresses in the castings and possible deformations in moulds.

3) Thermal computation, solidification modelling and grain structure prediction

4) Fluid mechanics computation, including convection

5) Macrosegregation calculation

6) Defects prediction, such as shrinkage, porosity, hot cracks and A-segregation lines.

The referred three software packages are the major commercial software packages for ingot casting today. The major limitation of these software packages is that in all these three models the solidification degree is directed calculated from temperature, in other words, the distribution of

fraction of solid versus temperature for the corresponding steel /alloy grades must be given as input before starting the calculation. This means that the local change of fs due to solid motion/sedimentation or solutally driven remelting will disturb the whole solidification system, therefore solidification phenomena such as sedimentation of grains or A-segregation formation cannot be included in the system. If the interfacial phase transformation rate is calculated instead of the empirical fs-T data, the problem of sedimentation and solutally driven remelting and so on can be handled.

3.2.3   Freckles criteria

Channel type segregations have been found in various kinds of alloys and castings [103-106]. In the field of directional solidification the channel type segregations are named as freckles, whereas in ingot casting they have another name: "A-segregation". Generally this channel type segregations are pencil-like chains of equiaxed grains and eutectic constituents which are highly enriched in solute and these line defects are usually distributed in a specific way in the section of a casting [39, 7]. Many researchers have studied the mechanism of channel type segregation formation experimentally and numerically with focus on channel nucleation, channel instability as well as channel prediction on different structural scales [108-111]. Today it is commonly believed that the freckles/A-segregates are induced by the thermal/solutal convective flow of the solute enriched melt.

Different criteria of freckles formation have been proposed since 1970's. Mehrabian and Flemings [50] have suggested an analytical criterion to examine whether the channels are under the condition of "stable flow", "intermediate flow" or "unstable flow".

$$\frac{\vec{v} \cdot G}{\dot{T}} < -1$$ Equation 3.12

where $\vec{v}$ is the flow velocity, G is the thermal gradient, $\dot{T}$ is the cooling rate. As referred in the former chapter and indicated in Equation 3.6, if $\frac{\vec{v} \cdot G}{\dot{T}} > 0$, the channels are under "stable flow" condition; if $\frac{\vec{v} \cdot G}{\dot{T}} < -1$, the channels are under "unstable flow" condition and channels are tend to form; if $-1 < \frac{\vec{v} \cdot G}{\dot{T}} < 0$, the channels are under "intermediate flow" condition. Fleming's criterion has a very concise physical meaning, but it is not easy to use because of the implicit form involved [107]. Besides that, the acceleration due to thermalsolutal buoyancy force or gravity force and the deceleration of drag due to dendritic morphology are not taken into account.

Copley suggested a criterion based on the unidirectional solidification experiments with $30NH_4Cl-H_2O$ aqueous solution [109]. It is concluded that freckles are caused by upward flowing liquid jets in the mushy zone. If the cooling rate ($\dot{T}$, equal to $G \times R$) is higher than a critical value, there is no freckles. For a given alloy, the formation of freckles is favored by decreasing the growth rate and thermal gradient.

$$G \times R \leq Crit. \hspace{4cm} \text{Equation 3.13}$$

Pollock and Murphy believed that in directional solidification freckle initiation is strongly related with the primary dendrite arm spacing [112]. Since the primary dendrite arm spacing is dependent on $G^{-1/2} \times R^{-1/4}$ according to the classic theory from Kurz and Fisher [88], the freckle formation is related with the product of $G^{-1/2}$ and $R^{-1/4}$.

$$G^{-1/2} \times R^{-1/4} \leq Crit. \hspace{3cm} \text{Equation 3.14}$$

Similarly, Suzuki and Miyamato have proposed another A-segregate criterion which is also based on the temperature gradient G and the growth velocity R [103]. They have reproduced the A-segregates under several cooling conditions by means of horizontal unidirectional solidification of a 0.7 wt.-% [C] steel. The cooling and solidification were investigated and the critical condition for the formation of A-segregation of this steel grade has been found:

$$\dot{T}^{2.1} \times G^{-1.1} \leq 8.75 \hspace{3cm} \text{Equation 3.15}$$

$$\text{or} \hspace{2cm} G \times R^{-2.1} \leq 8.75 \hspace{3cm} \text{Equation 3.16}$$

where $\dot{T}$ is the cooling rate (°C/min) and R is the solidification rate (mm/min) and G is the thermal gradient (°C/mm). If the product of $G \times R^{-2.1}$ is larger than 8.75, A-segregates are formed. Yamada et al. [114, 115] found that the critical value of $G \times R^{-2.1}$ depends strongly on the steel composition.

These referred four criteria are all thermal criteria depending on the cooling rate and isotherm velocity or temperature gradient. These G-R criteria have their strength in determination of the processing range of alloys, and have been widely applied due to their simplicity. However, these thermal criteria consider only the competition between isotherm velocity and growth velocity, and the solutally driven remelting is not taken into account. Besides, it does not always give the right judement, especially when the cast geometry deviates from simple cylinders or there are changes in the cross-sectional [116].

Considering the competition of driving force of convective flow and the drag force inside the mushy zone, Worster [117, 118] and later Beckermann et al. [119] introduced a "mushy zone" Rayleigh number in unidirectional solidification defined as:

$$Ra = \frac{gKh}{av} \cdot \left(\frac{\Delta\rho}{\rho_0}\right) \hspace{3cm} \text{Equation 3.17}$$

where g is the acceleration due to gravity, K is the average permeability over the depth, a is the thermal diffusivity, v is the kinetic viscosity of the liquid, $\Delta\rho$ is the density variation, ρ_0 is the density of the dendrite tip position, h is the characteristic length, and in the case of unidirectional solidification, h is the depth in the mushy zone measured from the dendrite tips; in the case of solidification in ingots, h is the distance from the liquidus isotherm to the inside of mushy zone.

The Rayleigh number can be treated as the ratio between the driving force of thermal/solutal buoyancy force and the drag force. If the driving force is large enough to overcome the drag force, instable convective flow will set on and thereby freckels will tend to form. The critical value of Rayleigh number was found to be around 33 for Pb-Sn [111,120-125] alloys and 0.25 for Ni-based super-alloys from both numerical simulations and experiments [119].

Various modelling of freckles formation have been conducted in the field of directional solidification [126, 127], and the Raleigh number based freckle criterion has been widely applied, verified and improved over the last few decades [12-13]. However, in the field of steel ingot casting, few works have been reported with regard to the A-segregation modelling and prediction. Most of the simulation works in ingot casting and commercial software packages such as MAGMA5 have utilized the thermal criteria suggested by Copley [109], Pollock and Murphy [112] or Suzuki and Miyamoto [113]. A few researchers have utilized the Rayleigh number based criterion in prediction of A-segregates [85, 86], however, due to the complexity of local heat transfer and growth in a solidifying ingot, whether this criterion can be applied for the prediction of A-segregation in ingot casting is not clear yet and demands further study.

3.3   Methods of measuring macrosegregation

As standard processes for qualitative characterization of macrosegregation in steel ingots, macroechting and sulphur print (Baumann method) proves useful insight into ingot features with regard to grain structure and morphology, segregation distribution intensity (to a certain extent) [128-130]. The macroechting method provides insight into the macrostrucutre including dendrite morphology as well as porosities, and sulphur prints indicate where sulphur are enriched and sulphides are located in the steel ingots and thereby implies important features of the macrosturcutre such as A- and V-segregation and CET, etc. Besides the two chemical methods that are applied after solidification, radioactive isotopes have also been utilized to track the convective flow and to imply the flow patterns in different stage of solidification [131, 132, 32].

Quantitative characterization requires normally great cost of production and analysis, especially for heavy ingots. In 1960's and 1970's, quantitative analysis of heavy ingots have been widely conducted for ingots up to 100 and 300 t [27]. At that time the wet chemical analysis techniques were commonly used and are still used today [68, 133].

Nowadays new methods such as Pulse Discrimination Analyser by Optical Emission Spectrometry (PDA-OES), energy-dispersive X-ray spectroscopy (EDX) and electron-probe micro-analyser (EPMA) have been developed for the quantitative characterization of the segregation in steel in different scales. PDA-OES measures the steel composition in macroscopic scale, and due to the convenient and fast

measurement, it is now a promising technique for future fast segregation assessment not only for cleanliness but also for macro-segregation [134-137]. EDX and EPMA are used to measure the local composition in microscopic level and then map the macrosegregation pattern by area scanning [138]. However, these two methods are usually applied for relative small sample area (a few millimetres), and for large ingots, the quantitative chemical analysis is very costly. By scale-up EPMA process which is able to analyse macro sections, Miyamura et al. have quantified the macosegregation in large samples with slab dimension up to 30 x 10 cm, so that the individual A-segregates can be analysed with great details [139].

Other alternative techniques include X-ray fluorescence spectroscopy (XRF) and **Q**uantitative **E**valuation of **M**inerals by **SCAN**ning electron microscopy (QEMSCAN). X-ray fluorescence spectroscopy is a promising method which uses the emission of characteristic fluorescent X-rays from a material that has been excited by bombarding with high-energy X-rays or gamma rays [140]. In 1970 Mehrabian and Flemings have firstly used X-ray fluorescence composition analysis to quantify the macrosegregation pattern of an Al-Cu alloy ingot by of ingot sections [48]. In 1981 Ridder et al. have applied the same technique to measure the composition profiles across a Sn-Pb ingot [53]. Today this technique is commonly applied in geological core logging, and can be quantitative and sensitive if properly calibrated [141]. QEMSCAN creates phase assemblage maps of a specimen surface and provides information such as elemental composition, particle and mineral grain size and shape, particle classes, porosity, etc. At the moment QEMSCAN are applied in the quantitative mineral characterisation of rocks, weathering products and most man-made materials [142], and it can also be used to quantify the inclusion distribution and macrosegregation and in ingots if the accuracy of chemical composition analysis is further improved.

Although the measurement of macrosegregation is very costly, it provides casting and solidification data for the validation of the numerical models. It is believed that if the accurate segregation measurements are appropriately combined with qualitative macrostructure characterizations, they will deliver more information and work as a strong tool for the validation of future models.

3.4   Water modelling using NH$_4$Cl solution

Since 1960's, many studies on solidification by using transparent analog have been reported. The NH^{4}Cl-70% H$_2$O solution possesses the advantage of good visibility and easy handlability at room temperature [143-146]. In 1966 Hunt [1] has examined the CET with NH$_4$Cl solution regarding the origin of the equiaxed dendrite nucleation as a pioneering work. From 1996 to 1998, a few studies have been performed with focus on microscopic solidification phenomena such as grain/dendrite growth [147] and growth of single equiaxed grains [148]. In 2003 Beckermann [149] has used a few thermocouples to measure the temperature field and to track the solidification front in order to validate

the simulation work. After 2005, some researchers have used the <u>L</u>aser <u>I</u>nduced <u>F</u>luorescence (LIF) and <u>P</u>article <u>I</u>mage <u>V</u>elocimetry (PIV) technique to quantify the temperature and concentration fields of the solution and the velocity field [150-151]. Today, water modelling using NH_4Cl-70%H_2O system has become a strong tool for investigation of solidification in connection with quantitative measurement and numerical modelling of solidification.

The present study aims to simulate the solidification process with focus on several solidification phenomena with regard to columnar growth and sedimentation of the equiaxed grains as well as fluid flow by using NH_4Cl solution. The saturated NH_4Cl solution was subject to different cooling and heating conditions and referred solidification phenomena have been quantitatively investigated and compared with ingot casting process with aim to transfer the knowledge of solidification to the real ingot casting process.

4 Modelling

The aim of the modelling is to gain deeper understanding of solidification in heavy ingots and continuous cast strands in connection with complex macroscopic solidification phenomena. The objective of this chapter is to introduce three different methods that are used in the present study to model the solidification process, in terms of hot modelling, cold modelling and mathematical modelling.

Compared to the cold and mathematical modelling, hot modelling has its advantage of reliable result. The boundary conditions and casting parameters as well as the steel composition are more close to the real industrial heavy ingot casting; and moreover, through hot models it is possible to obtain abundant results in terms of as-cast structure, macrosegregation and temperature evolution. The disadvantage of hot modelling is that the expense regarding cost and time is too high, and some of the solidification phenomena are not visible, such as the sedimentation of grains which can be observed through the cold modelling.

Cold modelling using the NH_4Cl-70% H_2O system has its benefits of good feasibility of conduction of experiments and good visibility of several solidification phenomena. In the present study, macroscopic solidification phenomena were observed and documented with a video camera, and in the past, with the help of amplifying lens and equipped camera, microscopic solidification phenomena such as growth of dendrite tips were observed and tracked. The limitation is that cold modelling can simulate the solidification only to a certain extent, since the crystallization of NH_4Cl is very similar to solidification with regard to columnar growth and movement of free equiaxed crystals. Several phenomena such as top cavity and solidification shrinkage induced segregation (V-segregates) are not possible to be reproduced by cold modelling. Furthermore, the heat transfer conditions and the growth rate of dendrites (solidification constant) in the cold modelling are not in the same level as in real ingots, therefore it is necessary to be aware of such differences while applying the results of cold modelling to the study of ingot solidification.

The mathematical modelling is a powerful tool to simulate the ingot casting process. It has the benefits of relative low cost in comparison with hot modelling especially for ingot trials with extreme large shape and mass. Furthermore, it is simple to obtain quantitative results such as the temperature field and concentration field, and by post-processing it is possible to visualize the mould filling and solidification in an easy way. The limitation is that the mathematical modelling is based on numerous of mathematical models, both macroscopic and microscopic, such as solute redistribution in the

liquid/solid interface, nucleation, columnar growth, equiaxed growth, interfacial drag during relative movement between liquid and solid phases, etc., the assumption and boundary conditions of the basic mathematical models determines the applicability and accuracy of the modelling. Meanwhile, as mathematical modelling is strongly depend on the computational science in terms of discretization method and numerical solution algorithm, the applicability of these methods to the mathematical model has large influence of the reliability and accuracy of the modelling results.

Based on the benefits and limitation of the different modelling methods, the present study attempts to take advantages of the three modelling methods in order to obtain information of solidification in large ingot from different aspects. By analyzing the results delivered from different models the author looks for the reasonable explanation or mechanisms of few phenomena in large ingot solidification which are still unclear and tries to give suggestion for the improvement of as-cast ingot quality in terms of structure and macrosegregation as well as cleanliness.

4.1   Hot models

Ingot casting experiments have been performed in the present work in attempt to obtain direct solidification information such as cooling curves, as-cast structure and macrosegregation. Unlike normal ingot casting trials, a special isolating mould made of isolation materials and refractory bricks has been constructed, and 500 kg molten steel solidifies inside the mould slowly. Since solidification in small ingots with laboratory scale cannot represent that in heavy ingots, the casting trials using the isolating mould simulate the slow solidification behavior in industrial scale large ingots, and that is how the term "hot model" comes from. To compare the solidification in large and small ingots, a series of ingot casting experiments with cast iron mould for ingots with weight of 100 kg have also been conducted, and the solidification characteristics such as cooling curves, as-cast structure and macrosegregation pattern have been quantified as well.

4.2   Cold models

Cold models refer to water modelling using NH_4Cl solution, and "cold" is compare to the temperature of ingot casting trials. A thin square-shaped mould has been built up with glass plates (front and back) and aluminum plates (left and right side). NH_4Cl solution is heated up to 70-80 °C, and solid NH_4Cl are added into the solution till saturation. After that the hot NH_4Cl solution is poured into the mould which is cooled from sides. Due to strong undercooling, NH_4Cl crystals start to precipitate and grow in the form of grains or dendrites, and this crystallization behavior is very similar to solidification in ingots with regard to columnar dendritic growth, sedimentation of free crystals, breakdown of dendrite tips and so on. With the help of the cold models, the dynamic process of some solidification phenomena can be simulate or visualized, offering the possibility to gain insight into solidification in

steel ingots.

4.3   Numerical models

Numerical simulation provides a strong tool of modelling ingot solidification process and prediction of macrosegregation and as-cast structure. A two-phase numerical model has been developed based on the volume-averaged theory of C. Beckermann [19] and the former work of A. Ludwig [48] as well as H. Combeau [93]. The numerical model has been applied for the 100 kg and 500 kg ingots from the hot models, without and with consideration of the movement of solid grains, respectively. The solidification model has been validated by comparison of the macrosegregation patterns between the simulated and measured results. Meanwhile, a one dimensional model for channel formation has been developed to test whether the potential channels in the CET region will be opened further by remelting or be closed by solidification under different cooling conditions and with various initial melt velocities. Furthermore, the Rayleigh number based criterion for channel formation prediction, which is commonly utilized in the field of unidirectional solidification, has also been tested and evaluated on the application in prediction of A-segregation in ingot casting.

5 Hot models

In this chapter two types of ingot casting trials and the successive analysis in order to investigate macrosegregation in ingots quantitatively and to obtain data and validation quantities for the present macrosegegation model are reported. Section 5.1 describes the experimental setup, casting procedure and casting variants for fast solidification in small ingots with the weight of 100 kg and 500 kg, and in Section 5.2 the measured results in terms of temperature profiles during casting and solidification, macrostructure, degree of macrosegregation of the as-cast ingots.

5.1   Experiments

A series of casting experiments with ingot weight of 100 kg have been carried out with a square shaped mould for rising casting with a negative cone. For all the experiments temperature measurement of the ingot and the mould as well as in the runner system have been performed, casting parameters with regard to superheat, hot top conditions as well as the usage of carbonyl iron powder have been varied and the solidification structure in terms of dendrite arm spacing, macrosegregation and CET position have been investigated.

The steel grade used in the present study is a high carbon low alloyed steel (Table 5.1). In order to obtain the target composition, online measurement has been carried out during melting. For each casting trial, one Minco sample was taken from the melt in the open furnace, and the composition of the sample was fast analyzed with the help of the Pulse Discrimination Analyzer (PDA). Based on the measured composition, certain amount of alloying elements was added into the melt after calculation. Sulfur powder is also added aiming to reach the [S] content between 0.01 wt.% and 0.02 wt.% for the subsequence macrostructure characterization using sulfur print. After solidification the as-cast ingots have been analyzed with regard to macrostructure, microstructure, macrosegregation of alloying elements and inclusion distribution.

Element	Fe	C	Al	Si	P	S	Mn
Percent / wt.%	rest	0.6	< 0.04	< 0.3	< 0.02	0.01 < [S]< 0.02	< 0.1

Table 5.1: Chemical composition of the medium carbon steel C60, Al killed

Besides the 100 kg ingot casting experiments with the cast iron mould, a special mould made of refractory and isolation materials have been constructed for ingot casting experiments with the weight of 500 kg, in order to simulate the slow solidification behavior of industrial scale large ingots. The casting type is bottom teeming, and the ingot has a negative cone for easier stripping. Temperature of

the ingot and in the mould wall has been measured during the whole casting and solidification process. The as-cast structures of the ingots have been revealed by sulfur prints, macro-etching and optical light microscopy (LOM), and the macrosegregation have been quantified with the help of the spark spectrometer. The 500 kg ingot casting experiments were mainly carried out by F. Zhai [152] in the frame of the present project.

5.1.1   Ingots with weight of 100 kg

5.1.1.1   Mould

The mould used for the 100 kg ingots is a permanent mould made of cast iron. As shown in Fig. 5.1, it has a dimension of 140 x 140 x 650 with a taper of 9.1 % / m where the taper is defined as $\frac{\Delta D}{D \cdot H} \cdot 100\%$ (see also Equation 5.1, page 51). The mould thickness is 60 mm. The top of the mould is integrated with exothermal hot-top plates with a thickness of 20 mm, and combined with the exothermal anti-cavity powder which is added on top of the melt after mould filling, the top of the ingot is kept warm and retain as the last solidified part of the ingot.
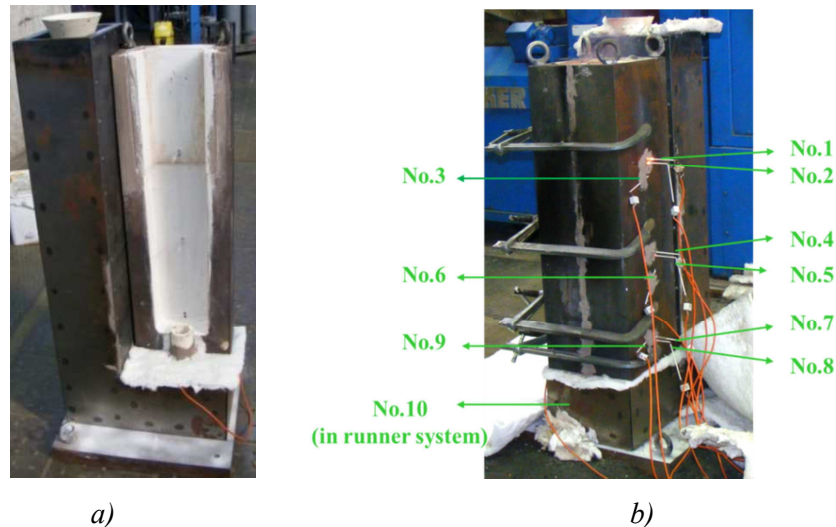

a)   b)

Fig. 5.1: a) Cast iron mould for the 100 kg ingots, b) mould instrumented with thermocouples

5.1.1.2   Temperature measurement

For each casting trial, ten thermocouples were used to measure the temperature of the ingot and the mould wall as well as in the runner system at different locations during pouring and solidification. Thermocouples No.1, 4 and 7 measured the temperature at the center of the ingot at top, middle and bottom height, whereas No. 2, 5, 8 measured the ingot temperature near the mould wall, and No. 3, 6, 9 measured the temperature at the mould outer surface, as in Fig. 5.1 b) shown. The temperature in the runner system near the entrance of the ingot was measured by thermocouple No. 10.

The thermocouples used in the present study are Pt-Rh (S) type with pure Pt at the cathode and Pt-10% Rh at the anode. The temperature range of the measurement of these thermocouples is from -30 °C to 1750 °C. All the thermocouples were protected by quartz glass tubes, as shown in Fig. 5.2. It needs to be mentioned that thermocouple No.1, which is the thermocouple at the top in Fig. 5.1 measures actually the ingot temperature at the hot-top area and if this thermocouple is in contact with the exothermal anti-cavity powder, the measure value can over the liquidus temperature of the melt.

Fig. 5.2: Thermal couples in the casting mould, top view

5.1.1.3   Experimental procedure and casting parameters

For each trial, the mould was pre-dried with flame right before pouring. If the composition and temperature of the steel melt were reached, the steel melt was firstly tapped into the ladle, as shown in Fig. 5.3 a), and then the ladle was transported to the top of the mould, Fig. 5.3 b) After that the steel melt was cast into the mould, (Fig.5.3 c)), and anti-cavity powder was added into the mould directly after the end of pouring (Fig. 5.3 d)).

| a) | b) |
| c) | d) |
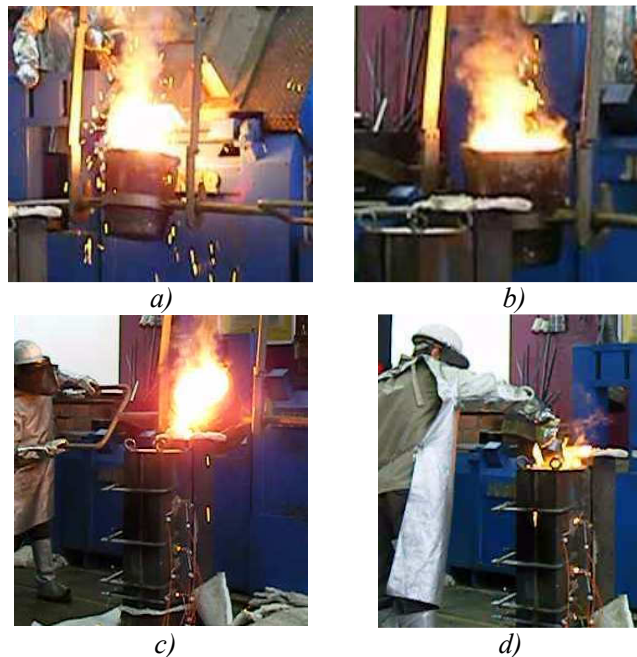
Fig. 5.3: Casting procedure of the 100 kg ingot, a) tapping, b) ladle transportation, c) mould filling, d) adding anti-cavity powder

In order to investigate the influence of casting parameters on the solidification structure and

macrosegregation, seven casting trials with different casting parameters in terms of casting superheat, pouring rate, hot top condition and addition of inoculants have been conducted, as shown in Table 5.2.

n°	Tapping temperature / °C	Casting Superheat / K	Pouring rate	Hot top	Inoculation or alloying	Thermocouple integrated
A 1	1662	12	2.5 kg / s	with	no	yes
A 2	1680	30	2.5 kg / s	without	no	yes
A 3	1676	26	2.5 kg / s	with	no	yes
A 4	1685	35	2.5 kg / s	with	no	yes
A5	1691	41	1.4 kg / s	with	no	yes
A6	1664	14	2.5 kg / s	with	140 g CIP	no
A7	1664	14	2.5 kg / s	with	50 g Al	no

Table 5.2: Casting trials of the 100 kg ingots with various casting parameters

The casting superheat was calculated as the temperature difference the initial melt temperature which was measured in the runner system at the beginning of pouring by thermocouple No. 10 and the liquidus temperature. Hot top plate has been used for all the trials except for A2. The pouring rate of A5 is lower than others, where the pouring time were ca. 40 s for the other five trials and 70 s for trial A5. Trial A6 was cast with inoculants, which is 140 g carbonyl iron powder (CIP), corresponding to 0.16 % of the cast weight, wrapped with thin aluminum foil into cored wire and was hanged in the mould before casting. This carbonyl iron powder contains 99.6 wt.% iron and the average particle size is ca. 50 μm. Trail A7 was cast with addition of 50 g aluminum granulate in the mould right before casting in order to investigate the distribution of inclusions in the ingot. Temperature measurements were performed for all the trials with integrated 10 thermocouples except for Trail A6 and A7.

During mould pouring and solidification, temperature of the ingot and the mould was measured and documented, and after complete solidification, ingots were cut up (Fig. 5.4 b)). The top of the ingot was cut with the length around 30 mm, which is dependent on the cavity depth, and the bottom of the ingot was also cut for around 30 mm, as shown in Fig. 5.4 a). The macrostructure of the as-cast ingots were revealed using sulfur print and macro-etching, and macrosegregation in transverse and longitudinal direction of the ingots have been measured by using PDA-OES, and the corresponding results will be presented and discussed in Section 5.2.1.
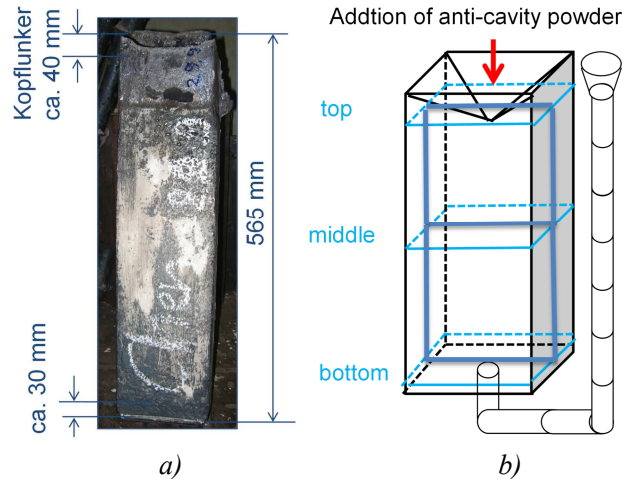
*Fig.5.4: a) As-cast ingot, b) sampling of the ingot*

5.1.2   Ingots with weight of 500 kg

As referred in Chapter 3, the quality problem of as-cast ingots in terms of macrosegregation arises significantly as ingot weight increases and remains unsolved in industrial heavy ingot production. The present work aims to study the solidification phenomena of heavy ingots, and slow solidification experiments with an isolating mould have been conducted to simulate solidification in large ingots. A series of casting experiments with ingot weight of 500 kg have been carried out with a square shaped mould for downhill casting. For all the experiments, temperature of the ingot at different locations have been measured to indicated the local solidification time, and after ingot solidification, macrostructure in terms of A-segregation and CET position have been analyzed, and macrosegregation have been also quantified with the help of PDA-OES.

5.1.2.1   Mould

The mould for the 500 kg ingot casting trials was specially designed and built up to withstand the ferrostatic pressure of the steel melt of around 4 bar above 1400 °C for several hours. Three types of refractory materials with increasing thermal conductivity (0.19-1.85W/mK) and decreasing strength from (80-0.3MPa) from inner to outer wall have been used to construct the mould, as shown in <u>Fig. 5.5</u>. The total thickness of the refractory materials of the mould is 300 mm and the 3 layers of these refractory materials are cemented to each other and integrated in a square-shaped steel box with its width and height of ca. 1m.
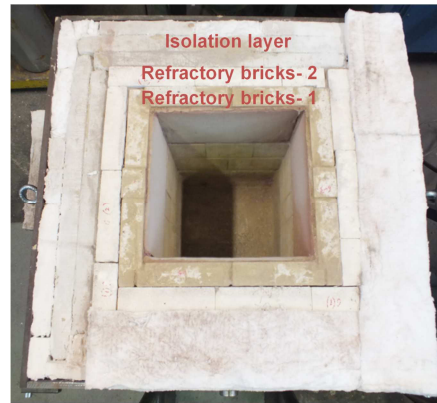
Fig. 5.5: Top view of the isolation mould for the 500 kg ingot

The inner dimension of the mould is 360 x 360 x 595 mm with a taper of 0.02 % /m. The top region of the mould is integrated with exothermic hot top plates in order to hold the melt temperature. The bottom of the mould was also isolated with three refractory layers, as shown in <u>Fig. 5.6</u>, and in order to support the melt and the first two layers at the bottom, a steel grid plate was used. On top of the mould is the cover which is also isolated with isolation plates, as shown in Fig. 5.6 and in <u>Fig. 5.7</u>. The assembly of all setups in this experiment is illustrated in Fig. 5.6. A tundish is assembled on top of the mould with a ceramic casting tube inserted through the mould cover into the mould. The steel melt will flow from the tundish through the casting tube into the mould and solidify in it.
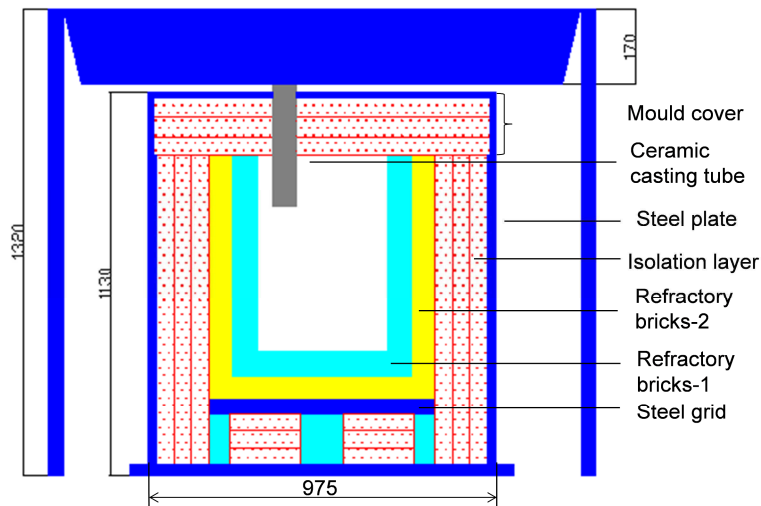

Fig. 5.6: Schematic illustration of the mould and the tundish for the 500 kg ingot (side view)

5.1.2.2 Temperature measurement

For all the three casting experiment, thermocouples made of platinum and rhodium (type S) wires were used to measure the melt temperature at different location of the ingot. These thermocouples were inserted from top into the melt, and they measured the ingot temperature in the geometric symmetry plane with the different distance to ingot center. Fig. 5.7 shows the illustration of the

location of the thermocouples for trial B2 schematically.

The two thick blue lines indicate the two thermocouples used in trial B2, and the measuring points are at ingot height of 350 mm. One thermocouple is close to the center with the horizontal distance of 25 mm, and the other is with a distance of 100 mm.

Besides the temperature measurement in the ingot, temperature of the mould wall was also measured at different depths with 7 thermocouples (Type K). Four thermocouples were inserted into the mould wall with the distance of 140 mm at mould front, back, left and right, and the other three elements were inserted at the one side of the mould with the distance to ingot surface of 76 mm, 140 mm, 190 mm and 240 mm. All the type K thermocouples measured the mould temperature at the ingot height of 295 mm. These thermocouples are also illustrated in Fig. 5.7, which are indicated by the red dots.
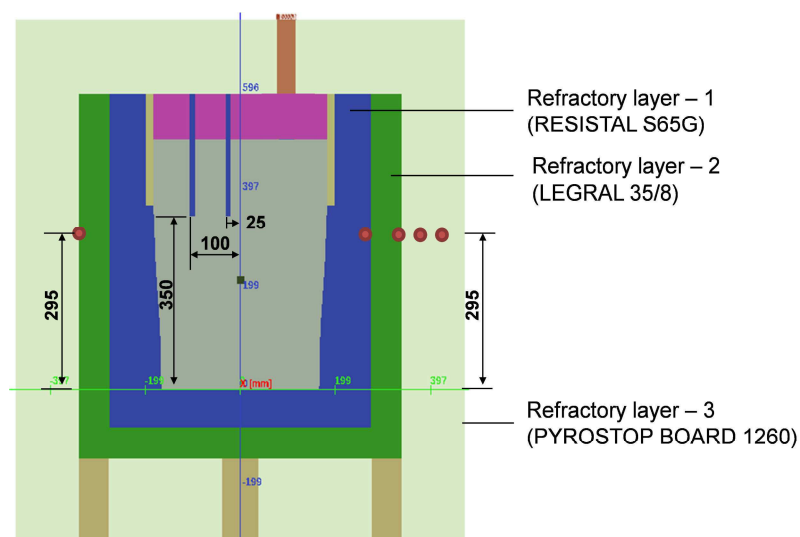
Fig. 5.7: Thermocouples in the ingot and in mould walls, view cut in ingot center plane, B2

The type-S thermocouples were integrated into the mould cover, as Fig 5.8 and Fig. 5.9 a) show. These thermocouples were protected by quartz glass tubes and then inserted into refractory tubes in trial B1 and into Cermotherm-tubes (ceramic metal, 60% Mo - 40% ZrO_2) in trial B2. Since the refractory protection tube broke das soon as the melt was poured into the mould due to thermo-shock, the temperature measurement for trial B1 was not successfully. In trial B2 the Cermotherm-tubes were used for better protection, and the temperature measurement were continuously performed from pouring till the end of solidification.
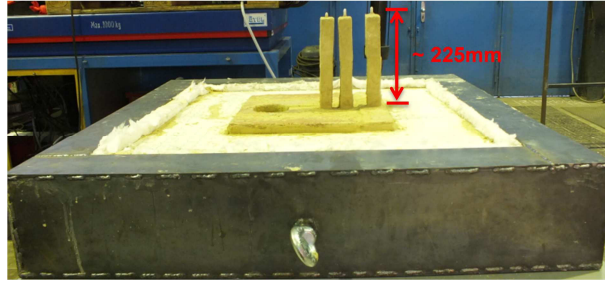
Fig. 5.8: Mould cover instrumented with thermocouples (Type S) and refractor protection tubes, B1

The type-K thermocouples used in present study are the sheathed thermocouples. They were inserted to the mould wall also from top, as Fig. 5.9 b) shows. For trial B1 every 30 minutes after pouring the temperature of the mould wall were measured till the value is below 400 ~ 500 °C, and for trial B2 the thermocouples were connected to the measuring facility and the computer so that the temperature measurement were conducted continuously from pouring till solidification ends.

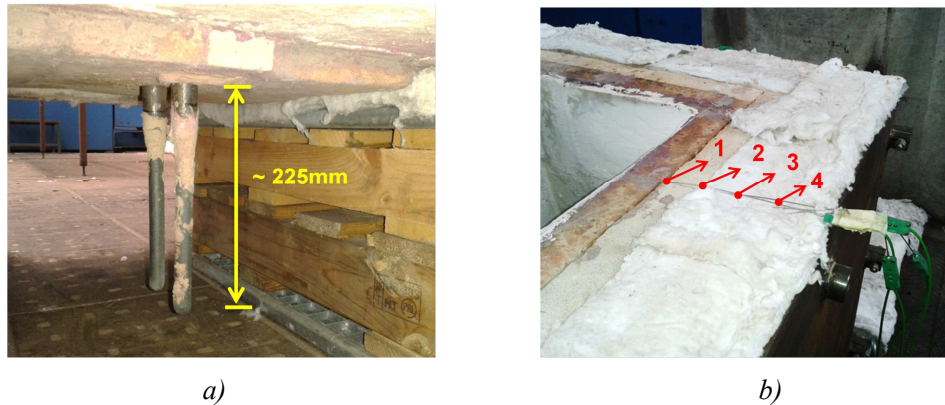| a) | b) |

Fig. 5.9: (a) Thermocouples (Type S) protected by Cermotherm-tubes, (b) thermocouples (Type K) used to measure the mould temperatures at different depths, B2

5.1.2.3   Experimental procedure and casting parameters

Before casting, the mould was dried with flame and preheated till up to 150 °C, meanwhile the tundish was also dried with flame, then the mould, mould cover and the tundish were assembled together. In order to protect the mould from the impact of the falling molten steel, three steel sheets were placed on the bottom of the mould, and 150 g aluminium pieces were added as alloying element to degas during solidification. A thin layer of aluminum silicate ($Al_2O_3 \cdot 2SiO_2 \cdot 2H_2O$) was coated onto the inner surface of the mould to ease stripping of the ingot later.

When the temperature and composition of the steel melt were reached, the molten steel was tapped from the open induction furnace into the tundish, as shown in Fig. 5.10, and the melt flows from right towards left, and through the ceramic casting tube the steel melt flows into the mould. Meanwhile the temperature measurement of the melt started right before mould pouring. The casting process last for

around 2 minutes, and directly after pouring, ca. 2 kg rice bowl ashes were added through the casting tubes in to the mould to protect the melt from heat loss at the top of the ingot.

Fig. 5.10: Casting of the 500 kg ingot at IEHK, direct tapping and use of a runner

Three casting experiments have been done with hot top conditions, as shown in Table 5.3.The location of temperature measurement inside the ingot and in the mould wall have been also varied to obtain the characteristic temperature data for validation of the numerical model.

n°	Superheat / K	Pouring rate	Hot top condition
B 1	127	4.04 kg/s	Hot top plate, without rice husk ash
B 2	124	4.08 kg/s	Hot top plate, with rice husk ash
B 3*	126	4.07kg/s	Hot top plate, with rice husk ash

Table 5.3: Casting trials of the 500 kg ingots

*: Trial failed due to steel melt leakage

After the casting trial, the ingots were delivered to a steel plant for cutting and sampling. The as-cast ingot and the sampling plan are illustrated in Fig. 5.11. Ingot B1 and B2 has the negative taper of 0.02 %/m, where the ingot tapers in the present study is calculated as:

$$Taper = \frac{D_{top} - D_{bottom}}{\overline{D} \cdot H} \cdot 100\%$$ Equation 5.1

where D_{top} is the length at top surface, m

D_{bottom} is the length at bottom surface, m

$\overline{D}$ is the average length, m

H is the height, m
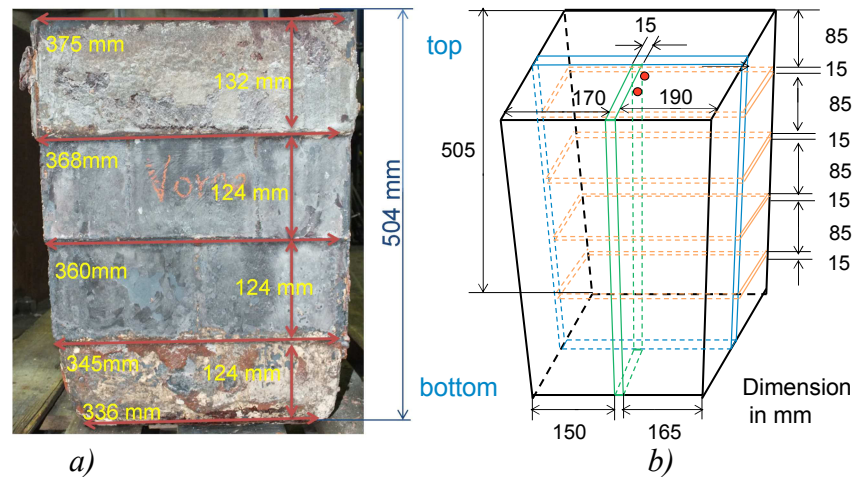
a)   *b)*

Fig. 5.11: a) As-cast 500 kg ingot, b) Sampling plan of the 500 kg ingot (B2)

The macrostructure of the ingot in terms of A- and V- Segregation and CET position were characterized by sulfur print and hot acid etching at IEHK; microstructure with regard to primary and secondary dendrite arm spacing, and macrosegregation in longitudinal direction and in transverse direction at different height of the ingot were quantified with the help of the spectrometer.

5.2 Results

The as-cast ingots with casting weight of 100 kg and 500 kg have been analyzed with regard to as-cast structure, macrosegregation as well as cleanliness, and the corresponding results and the temperature measurement are presented in this section. The 100 kg ingots were cut up in-house at IEHK, and further treatment such as machining and grinding were also conducted in-house. The 500 kg ingots were cut and machined at Dillinger Hütter resp. casting design. For sulfur printing the samples are ground with surface roughness between 6.3 μm and 12.5 μm. The as-cast structure have been revealed by sulfur print and macro-etching as well as micro-etching, the macosegregation of the ingots have been quantified with the help of spectrometer, and the cleanliness of the ingots have been characterized light optical microscopy (LOM).

5.2.1 Fast solidification ingots (100 kg)

The solidification of ingots with weight of 100 kg represents the fast solidification behavior of casts with relatively small cross-section, e.g. billet casting and small rounds casting in continuous casting process. This type of solidification process is completed within several minutes, and the solidification behavior is almost solely influenced by the heat extraction, therefore solidification structure is relatively simple in comparison with those of large ingots. The following sections present the results of temperature measurement during solidification of the 100 kg ingots, the as-cast structure, macrosegregation and inclusion distribution.

5.2.1.1   Temperature measurements

As mentioned in Section 5.1.1, the temperature of the ingot with regard to ingot center and ingot surface were measured from bottom to top of the ingot during the whole casting process from mould filling till solidification ends, and the temperature at the mould outer surface were measured with regard to ingot top, middle and bottom. The temperature at each time point were measured and documented, and the temperature curves were carefully analyzed and the first derivation of the curves were also calculated to obtain the liquidus temperature, solidus temperature and the cooling rate. Fig. 5.12-5.14 give the temperature curves at ingot top, middle and bottom with regard to ingot center, ingot surface and mould outer surface, respectively.
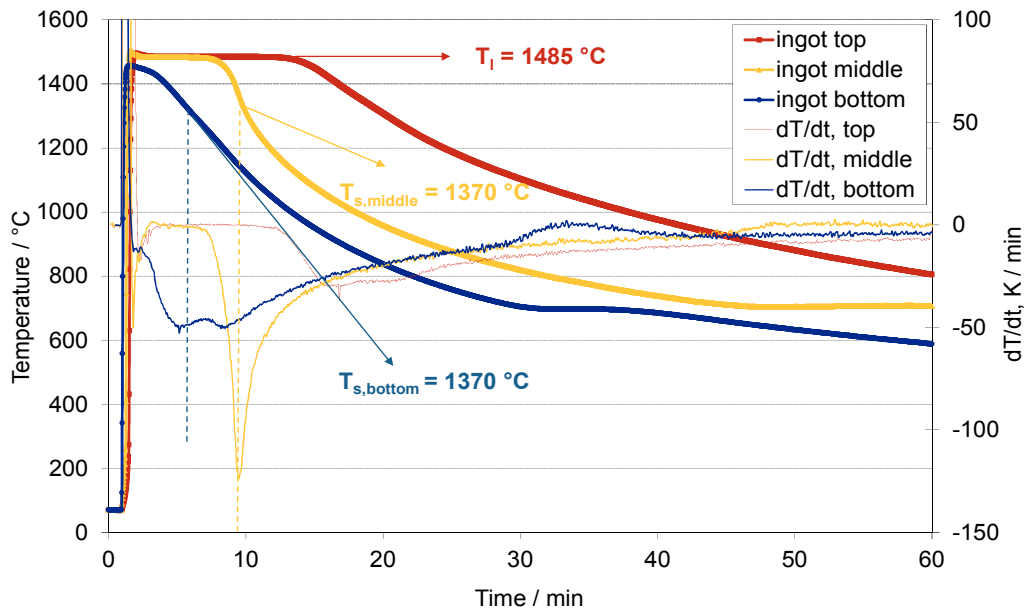

Fig 5.12: Temperature curves in ingot center, at top, middle of bottom, Trial A3 (no $T_{s,top}$ due to influence of exothermal anti-cavity powder)

The solidus temperature can be obtained by looking at the minimum value of the first derivation of the temperature curves, i.e. the dT/dt curves. When the local solidification ends, no latent heat can be generated any longer, and it leads to the turning point on the dT/dt curve, here is the minimum of the dT/dt curve, corresponding to the solidus temperature. For the temperature curves at ingot middle and bottom, the solidus temperature was found to be 1361 °C and 1370 °C, respectively. The difference lies probably in the system measurement error such as the delay of the temperature measurement due to usage of quartz-glass protection tube and the scattering of the temperature curve which made it difficult to find the minimum point, e.g. the dT/dt curve at ingot bottom, as shown in Fig. 5.12. The ingot temperature at ingot top is strongly influenced by the anti-cavity powder and the melt solidifies much more slowly than at ingot bottom and middle, and therefore the solidus temperature, i.e. the turning point of the cooling curve is very difficult to be found.
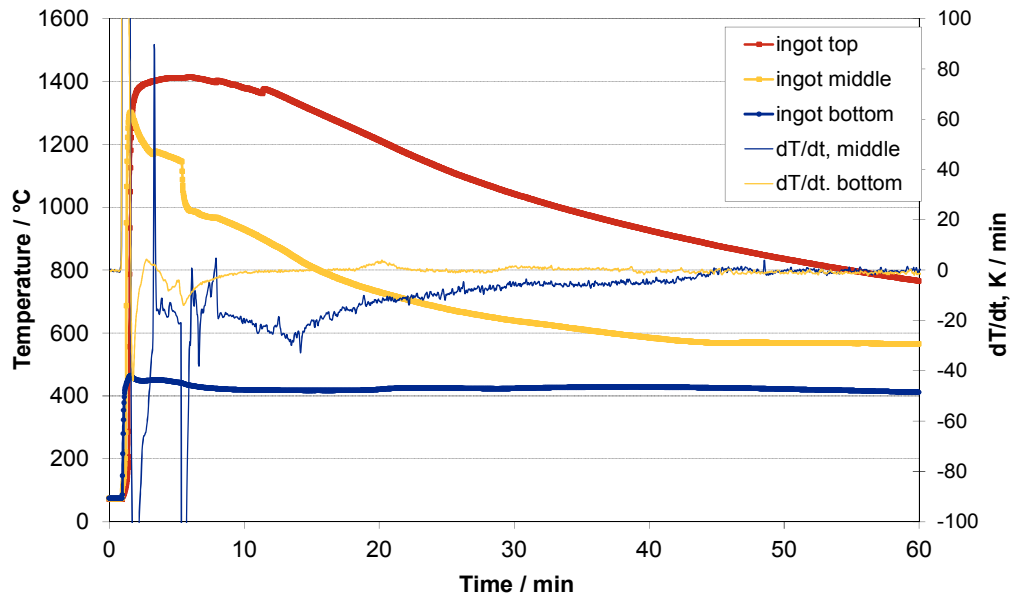
Fig 5.13: Temperature curves at ingot surface, at top, middle of bottom, Trial A3
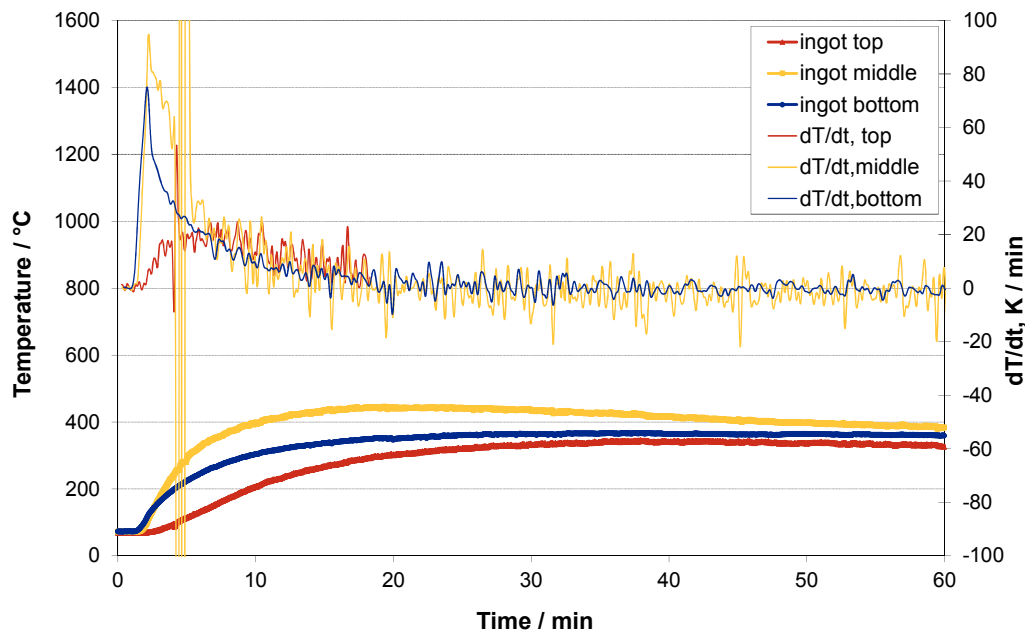

Fig 5.14: Temperature curves at mould outer surface, at top, middle of bottom, Trial A3

The liquidus temperature can be obtained from the stage at the beginning of the curve from Fig. 5.12. Since the temperatures were measured locally at different locations of the ingot, the time for the melt to cool down to the liquidus temperature is also different. The bottom of the ingot solidifies immediately after pouring, and the melt at the middle height of the ingot starts to solidify ca. 7 minutes after pouring due to superheat and latent heat which is generated from other part of the ingot. Due to the usage of exothermic anti-cavity powder after pouring, the top of the ingot starts to solidify latest, which is around 12 minutes after pouring.

From Fig. 5.12 it can be seen that the total solidification time for the whole ingot is around 15 minutes, and if no anti-cavity powder is used, the solidification time can be shorter. The cooling rate of the ingot varies dramatically during the whole solidification. The maximum cooling rate happens at ingot middle when solidification ends, the maximum cooling rate is -120 °C/min, which is 2 K/s. The cooling rate at ingot bottom calculated from the measured temperature curve is around -50 °C/min, which is 0.83K/s, and it could be larger than this value since scattering happens and the minimum point of the dT/dt curve could be lower. At ingot top the cooling rate is around -30 °C/min, which is 0.5 K/s.

The temperature curves at the ingot surface in Fig. 5.13 show that directly after pouring the temperature of the mould inner surface rises fast up to 1400 C and start to cool down. There is a turning point occurring at the ingot middle height at around 5 minutes after pouring that the temperature decreases in a sudden. If it is not the measurement error of the thermal element, then it could be related to the formation of air gap between the ingot surface and the mould inner surface. Combined with Fig. 5.12, it can be seen that around 5 minutes after pouring, the bottom part of the ingot is completely solidified, and the outer part of the ingot is also solidified with a certain shell thickness. Due to the solidification shrinkage, the air gap is very likely to happen at this moment and lead to a sudden decrease of mould inner surface temperature as indicated from the temperature curve.

The temperature of the mould outer surface (shown in Fig. 5.14) increases during the whole casting process till up to 540 °C, and due to the isolation of the hot top plate at the top, the temperature at the top of the mould increases the most slowly. From Fig. 5.13 and 5.14 it can be seen that the mould at the middle height of the ingot has the most inhomogeneous temperature field and therefore has the highest thermal stress. The inner surface of the mould at ingot middle is up to 1400 °C directly after pouring, whereas the outer surface is not yet heated up at this moment, and the temperature is around 70 °C, which is the initial temperature of the mould right before casting. From this it can be surmised that cracks are more likely to occur at the middle height of the mould.

The temperature curves at the beginning of casting are given in Fig. 5.15, and it can be seen that there is a hump in each cooling curve before the temperature stays at the liquidus temperature (T_l) value. This hump is related to the local superheat ΔT, which is difference between T_{max} and T_l (Fig.5.16) In reality, due to the temperature measurement delay, the cooling curve often show a smoother contour. In order to gain the ΔT value, two tangent lines from both sides of the hump are used and the cross point gives the value of local superheat ΔT, as shown in Fig. 5.16.
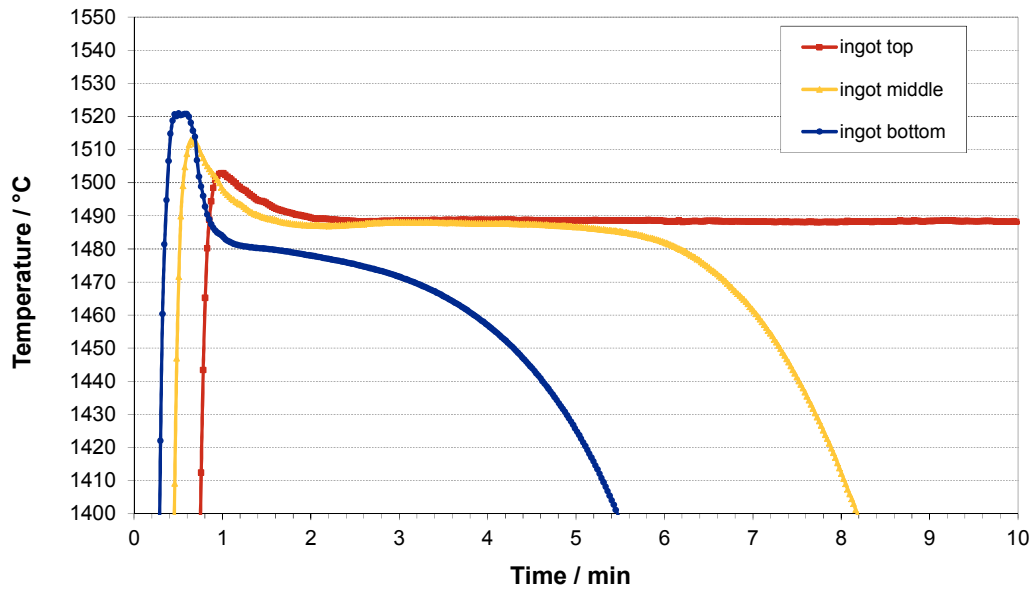
Fig. 5.15: Cooling curves at the maximum temperature region of ingot center for Trial A1

The local superheat value are obtained from cooling curves at ingot top and middle for all the 5 casting trials, and since most of the curves at ingot bottom don't show a clear hump, it is not possible to measure the local superheat at ingot bottom. The measured results for the 5 trials are summarized in <u>Fig. 5.17</u> and it seems that the local superheat ΔT strongly depends on the casting superheat and on the location of the ingots.
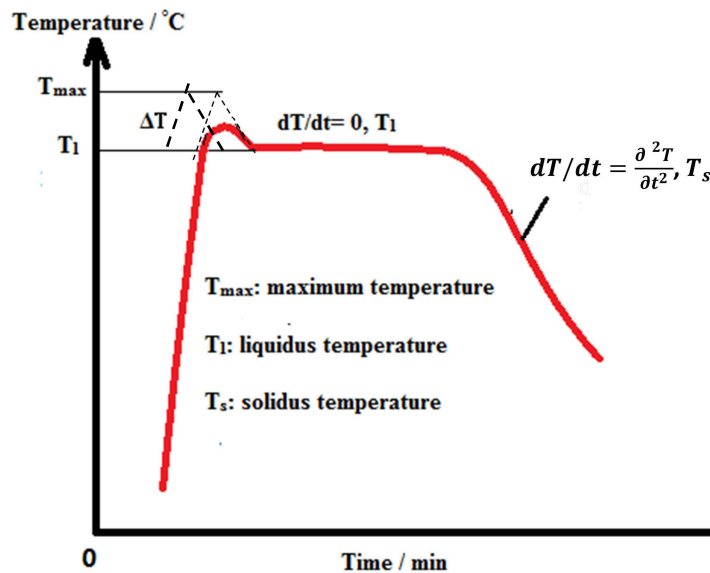

Fig. 5.16: Cooling curve during solidification process in present study

Generally the local superheat ΔT increases as the casting superheat temperature rises, and the local superheat at ingot top is lower than that at ingot middle, which might be due to the fact that during the uphill casting the melt loses certain heat when it reaches ingot top, and therefore the local superheat of the melt at ingot top is lower than that at ingot middle height. Similarly, if the melt is slowly poured into the mould, the superheat of the melt will be lost and decreased due to the long pouring time, as
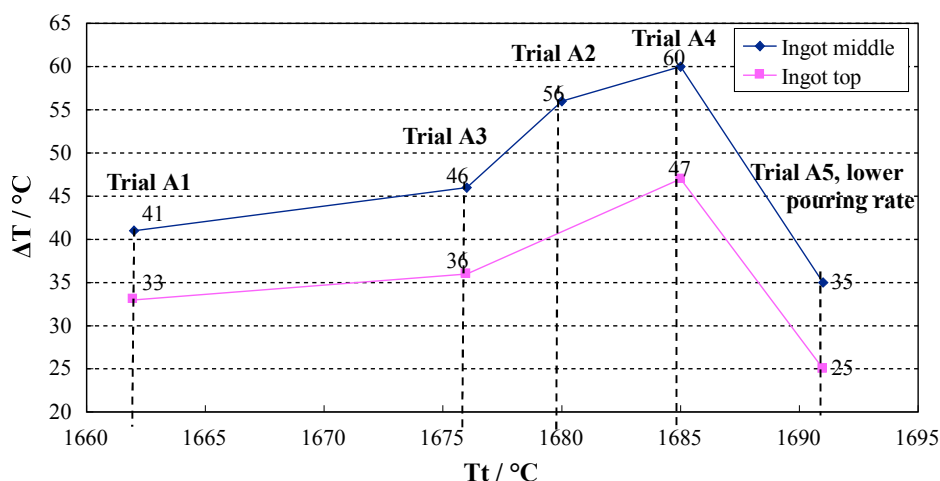
shown in Fig. 5.17.

Fig. 5.17: Difference of superheat temperature ΔT and the tapping temperature Tt in the furnace, Trial A1~A5

5.2.1.2 Macrostructure and macrosegregation

The macrostructure of the as-cast ingots for all the 5 trials are revealed firstly by sulfur prints, and then the macrosegregation of the alloying elements such as carbon, manganese, silicon, chromium, sulfur and phosphorus are quantified with the help of the Pulse Discrimination Analyzer along the transverse direction and the longitude direction.

Fig. 5.18 gives the sulfur prints along the center line of the ingots cast in trial A1, A2 and A3. The dimension of the as-cast ingots is ca. 540 mm x 140 mm x140 mm with a negative taper of 2.5%/m, and the head and foot of the ingot were cut down with the length of around 20-30 mm each, in order to exclude slag at ingot top and casting tubes at ingot bottom. Therefore sulfur prints of A1 and A3 do not represent the top cavity of the ingots, and since ingot A2 was cast without hot-top condition, therefore the top cavity is particularly deep, and the top cavity is completely displayed in the sulfur print.

Thin straight lines are used to mark the position of each columnar dendrites tip which can be recognized in the sulfur print, and the thick solid curve indicates the columnar-to-equiaxed (CET) position, as shown in Fig. 5.18. In ingot top region due to the usage of hot-top plates and anti-cavity powder, columnar dendrites are shorter. The relation between casting superheat and the averaged CET-position (except for the top region) are summarized for each ingot, as given in Fig. 5.19. For higher casting superheat, the columnar zone is wider. With the casting superheat around 95 K the columnar zone width is 44 mm, whereas with the casting superheat of 50 K the columnar zone is 33 mm wide, i.e. the width of columnar zone increases 0.25 mm for each Kelvin of the casting superheat increase. Fig. 5.19 also indicates that a lower casting speed has no critical influence on the CET-position.
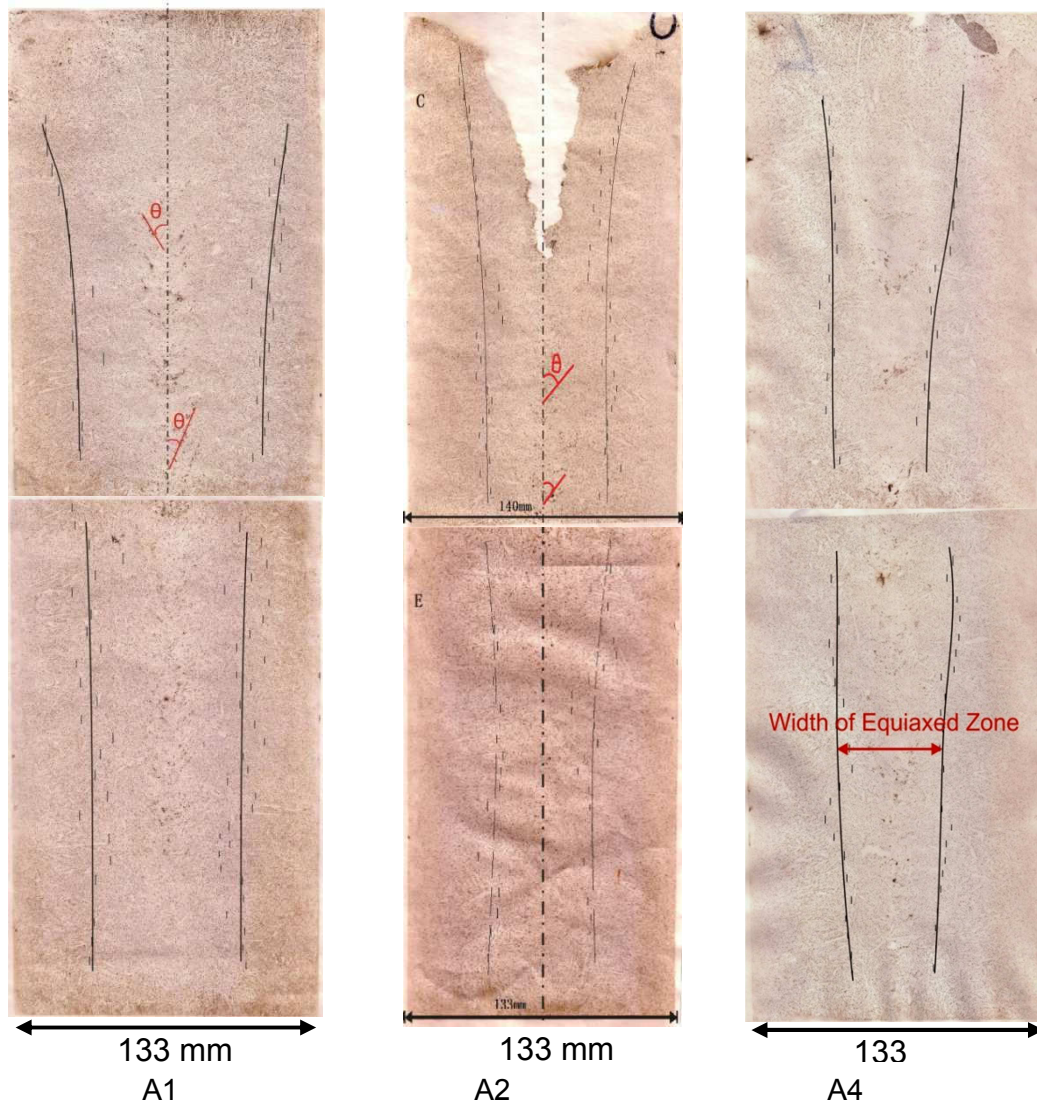
Fig. 5.18: Sulfur prints of the longitudinal cross-section of ingots A1, A2, A4
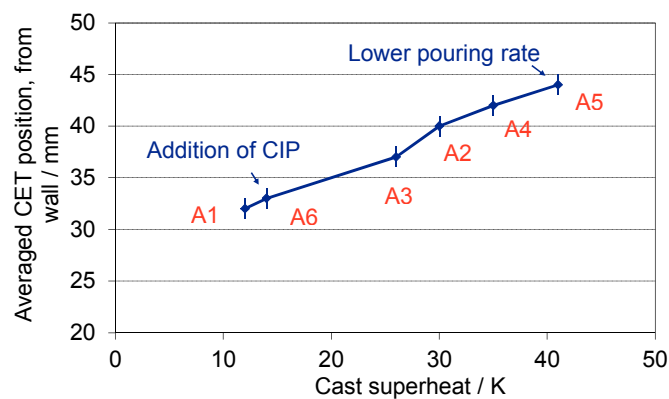

Fig. 5.19: CET-position of the ingots, A1, A2, A3, A4, A5, A6

The transverse cross-section of the as-cast ingots has also been revealed by sulfur printing. Fig. 5.20 shows the sulfur print of the middle plate of ingot A1. There is a center segregation circle with a diameter of 20 to 30 mm, where the dark points occur mostly. These dark points correspond to the V-

lines in sulfur prints along the longitudinal direction and the diameter of these V-spots is approximately between 0.5 to 1 mm.
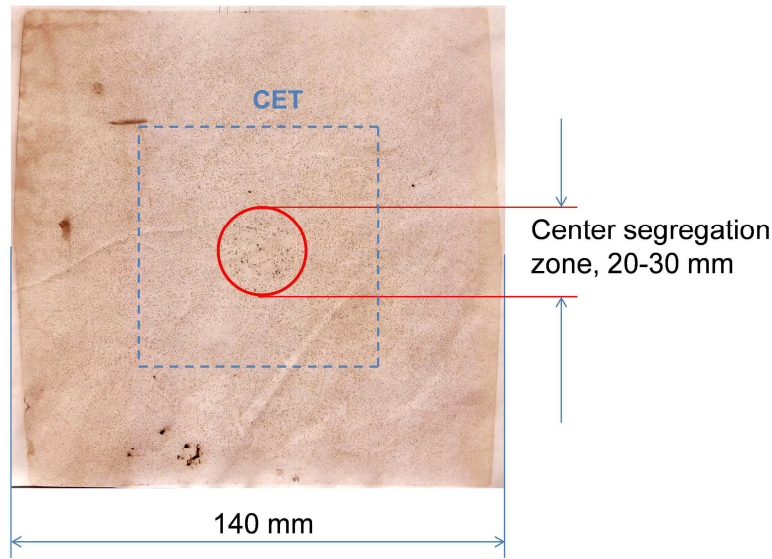

Fig. 5.20: Sulfur prints of the transverse cross-section of ingot A1

The macrosegregation of alloying elements have been measured with the help of Pulse Discrimination Analyser by Optical Emission Spectrometry (PDA-OES) technique. Sparks are generated between the sample and the electrode under Argon protection, whereby the atoms are vaporized, brought to higher energy stage and create emission spectrums. The emission spectrum is unique specific to each element and by measuring the emission intensity it is possible to count the amount of atoms of each element and finally calculate the total content of each element in the sample. As shown in Fig. 5.21, along the transverse direction, 10 measure spots have been chosen with at least 3 measurements on each spot, and along the longitudinal direction 38-40 spots were measured in a similar way. The averaged composition $\bar{C}$ for the whole ingot was determined as an average of composition of 6 measure spots in the columnar zone in the middle plate. The diameter of the measurement spot is around 6 mm.
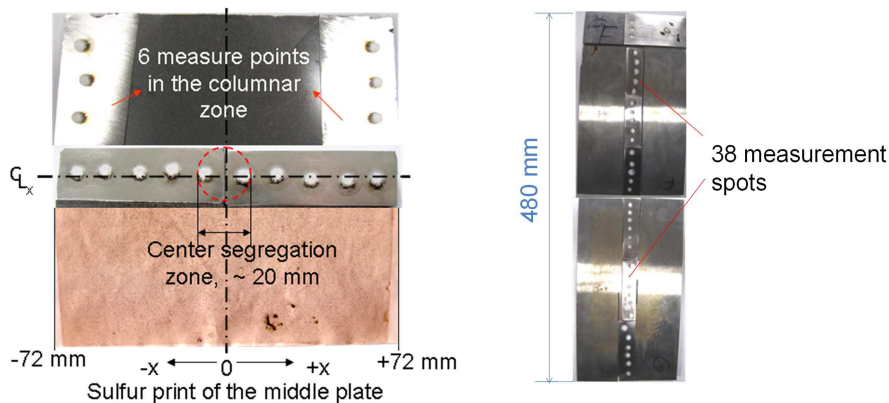
a) Along transverse direction　　　　　　*b) Along longitudinal direction*

Fig. 5.21: Illustration of the measured points for segregation characterization

In order to characterize the segregation intensity along the X-axis and Y-axis, a segregation index is defined for alloying elements:

$$\text{Segregation index of the alloying element} = \frac{c_i - \bar{c}}{\bar{c}}$$ Equation 5.2

where c_i is the concentration of one element at the individual measure point,

$\bar{C}$ is the averaged concentration of the element in the whole ingot.

The segregation index of carbon along the centerline of ingots A1, A2, A5 and A6 are shown in Fig. 5.20. Trial A1 and A5 were cast with the superheat between 12 K and14 K, whereas A2 and A5 were cast with a higher superheat, and A5 was cast with addition of 140 g Carbonyl Iron Powder (CIP) which contains 99.6 wt.% iron.
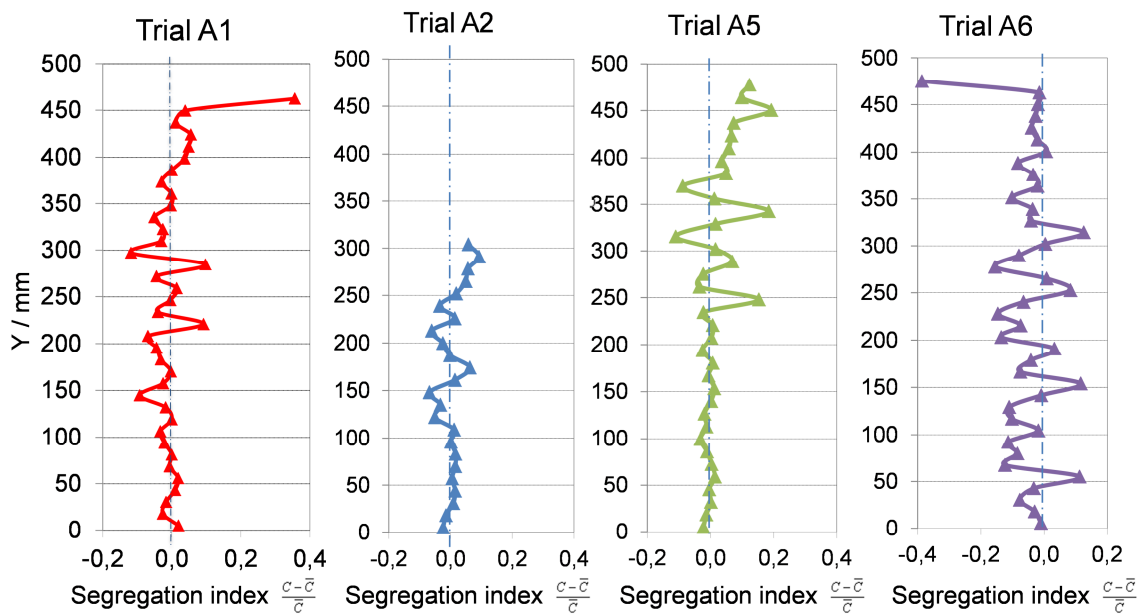

Fig. 5.22: Segregation index of carbon along the centerline of the metallurgical ingot center (A1:ΔT = 12 K, A2:ΔT = 30 K, without hot-top, A5:ΔT = 41 K, A6:ΔT = 14 K, with 140 g CIP)

Generally from Fig. 5.22 it can be seen that except A6, all the other three ingots have positive segregation of carbon at the upper portion of the ingot. Among these, ingot A5 has the highest tendency to segregate, and it might be due to the highest casting superheat that leads to a fast growth of columnar dendrites which drives the solute-enriched liquid into the center of ingot. The top part of A2 below the cavity is so porous that cannot be measured with the spectrometer, segregation of this part is unknown. However, according to the segregation curve it can be surmised that the segregation tendency of A2 is similarly as strong as A5, as both have a high segregation casting superheat.

Ingot A6 with the addition of CIP shows a relative low segregation tendency of carbon, and it seems that the CIP as nearly pure iron dilute the enriched alloying element along the center line of the ingot and hence suppress the central segregation. However, the scatter of the segregation curve of A6

implies that the V-segregation still exist in ingot center. The macrosegregation profiles of other alloying elements such as sulfur, phosphorus and silicon show the similar tendency as in Fig. 5.22.

The segregation profile of the alloying elements along the transverse direction at ingot top, middle and bottom are shown in Fig. 5.23. For all the six elements, considerable macrosegregation are found in the top plate. The segregation index for carbon at ingot top is up to 0.27, while at bottom negative segregation appears with an index of -0.08. Silicon has the similar tendency as carbon, with the maximum segregation index of 0.3. The segregation index for manganese and chromium is relatively low in the top plate, with the maximum value of 0.2 and 0.1, respectively. Compared to carbon, silicon, manganese and chromium, the segregation profiles of sulfur and phosphorus indicate higher tendency of segregation with maximum segregation intensity of 1.1 for sulfur and 0.9 for phosphorus.
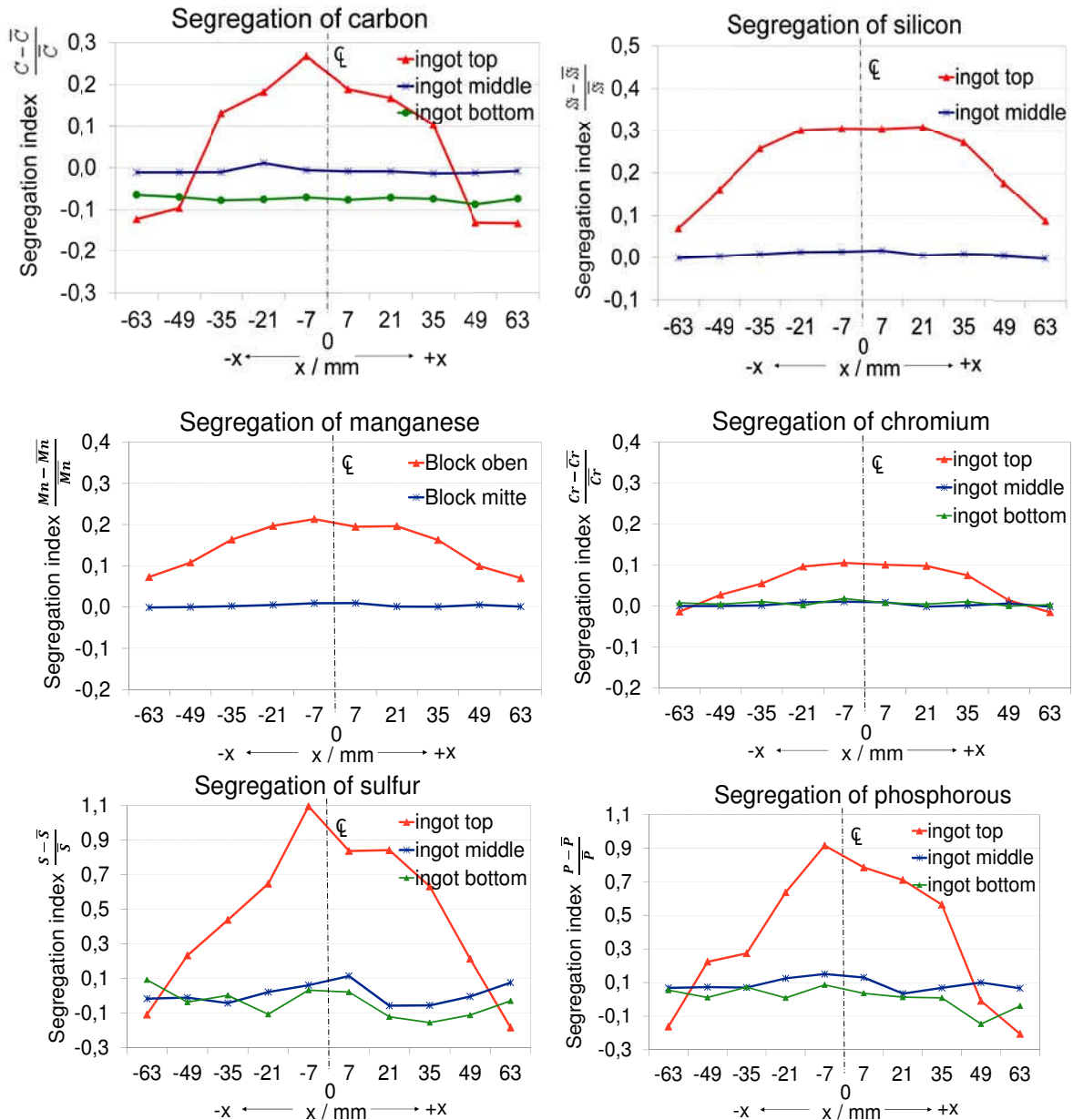

Fig. 5.23: Segregation profiles in transverse direction at ingot top, middle and bottom, A1

From the sulfur prints in Fig. 5.18 V-lines are clearly found to appear periodically, and for the trail with higher casting superheat (Trial A4), "mini-ingots" which is like a series of small ingots consisting of negative segregation at mini-ingot base and positive segregation at mini-ingot top occurs. It has been found that the averaged distance between the V-lines is different in each ingot, and the inclined angles of V-lines to gravity are also different. Since the V-segregation is caused by the columnar bridges that prevent the shrinkage cavity, the advancing rate of columnar dendrites may have a strong effect on the V-segregate formation. Therefore the relationship between the characteristics of V-lines and the casting superheat have been investigated and summarized in Fig. 5.24.

For trial A1 and A6 with lower casting superheat between 12 K and 14 K, the center equiaxed zone is relative broad with the width of around 70-75 mm, and the V-lines angels are between 25° and 28°, and the averaged periodic spacing is between 15 and 18 mm. For trail A4 and A5 with higher casting superheat of ca. 30 K, the width of the center equiaxed zone is reduced to around 55 mm, and the V-lines are relatively flat, with the inclined angels between 30° and 32°, and the averaged periodic spacing is also larger, which is between 20 and 25 mm. The fact that inclined angel of V-lines tends to become larger with larger superheat in the present study is in consistence with the research work reported by H. Tomono et.al. In his work he has studied the relationship between the inclined angles of V-lines and the width of the central equiaxed zone, and he found that the V-angles are smaller if the width of the central equiaxed zone increases [153].

a)   *b)*

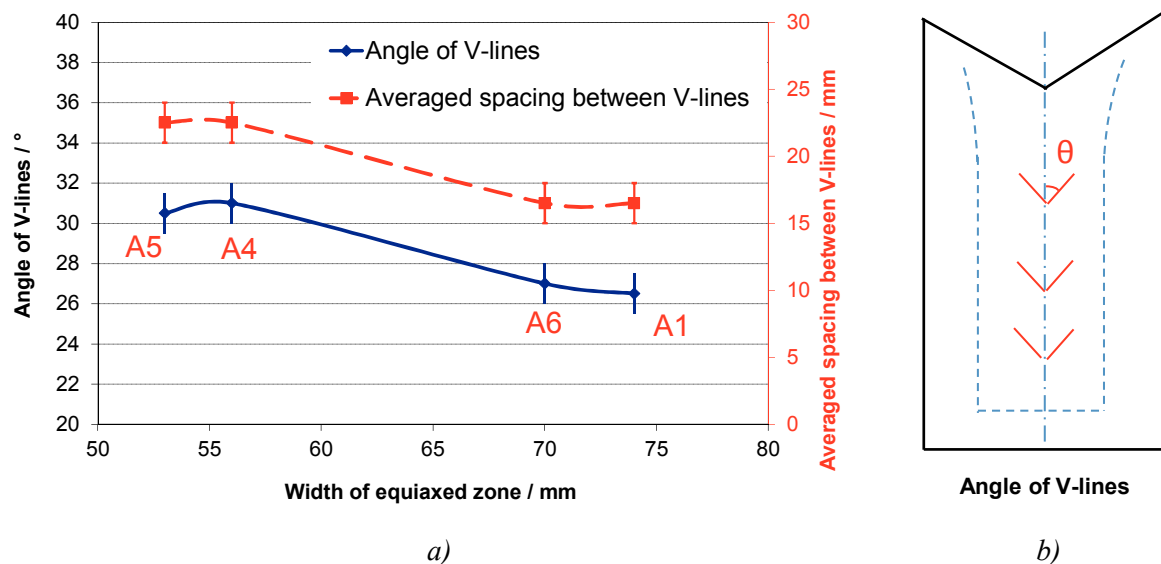*Fig. 5.24: a) Angles of V-lines and averaged spacing between V-lines vs. width of equiaxed zone, b) sketch of V-line angle*

The correlation between the V-line angle and the width of equiaxed zone can be explained by the interaction or friction force between the equixed grains which sink down on to the columnar dendritic bridge in ingot center and the columnar front. These equiaxed grains accumulate along the

solidification front and appears to form a funnel shaped contour of V-segregation. When the enriched liquid between the packed equiaxed grains is sucked and flow downwards due to negative pressure caused by shrinkage, a V-shaped segregation is formed. If the equiaxed zone is narrow, the friction force or the adhesion of equiaxed grains to the columnar front is strong enough to support the funnel shaped sedimentation layer, then the V-lines are shallower. Other way around, if the equiaxed zone is wide and the cohesive shear strength is not strong enough, the grains will move downwards and make the V-lines steeper.

5.2.1.3   Inclusion distribution, cleanliness

Since large inclusions have strong impact on mechanical properties of as-cast products, the distribution of large inclusions in ingots has been investigated with regard to the average number of large inclusions with diameter over 15 mm in the metallographic photos with magnification of 100x.

In each metallographic photo the diameter of every particle were measured and analyzed by the program Soft Imaging System Analysis 5.0, and the number of particles with the diameter over 15 µm were documented. For every sample at least three metallographic photos are taken for inclusion diameter measurement, and the numbers of large inclusions (> 15 µm) from the metallographic photos were averaged for each sample. The relationship between the inclusion distribution and the casting superheat, steel composition and macrosegregation have been studied and presented in this section.

The influence of the casting superheat on the inclusion distribution has been investigated by comparing the distribution of large inclusion particles (> 15 µm) between trial A1 and A2. Fig. 5.25 shows the number of large inclusions along the longitudinal direction of ingot A1 and A2.
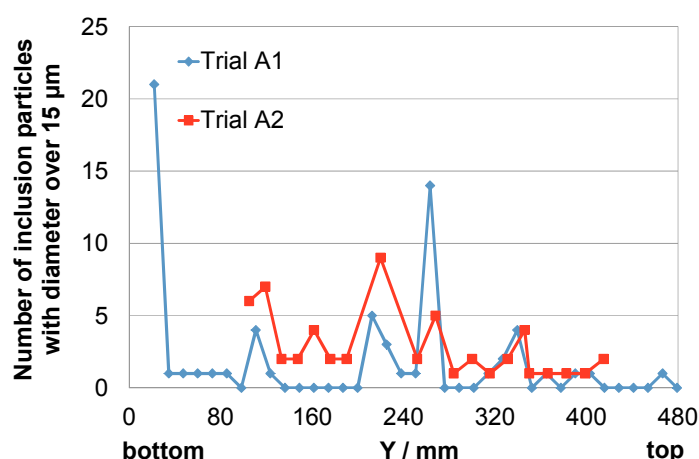
Fig. 5.25: Inclusion distribution in longitudinal direction (bottom to top) of ingot A1 and A2

Trial A2 was conducted with the casting superheat of 30 K whereas A2 was cast with the superheat of 12 K. From Fig. 5.25 it can be seen that in the upper portion of the ingot there are more large

inclusion particles in ingot A2 than in A1. Although at ingot top of A1 the absolute number is over 20, which might be due to the entrapment of the Al-yielding anti-cavity powder, the particle number in the rest part of A1 is lower. Since higher casting superheat allows a longer solidification time, which provides time for inclusions to growth and agglomerate and escape to the upper part of the ingot driven by the ascending flow. Meanwhile, high casting superheat leads to fast growth columnar dendrites, which will push the solute enriched melt into ingot center and cause stronger macrosegregation there. The inclusions could precipitate due to oversaturation of the alloying elements during solidification and the subsequent cooling.

In order to investigate relation between the macrosegregation and the steel composition, it is necessary to know the origin of the inclusion particles, therefore EDX analysis have been applied to investigate the chemical components of the inclusion. Several large inclusions with diameter over 15μm have been chosen in different positions of the ingots for the EDX analysis. Fig. 5.26 illustrate the analysis result of a few particles, where a) shows that the grey irregular shape particle with the diameter over ca. 20 mm is of MnS, the Al_2O_3 particles at its surrounding shows a spherical shape and a smaller size. Fig. 5.26 b) shows that different type of inclusion particles can agglomerate with each other and form larger particles.
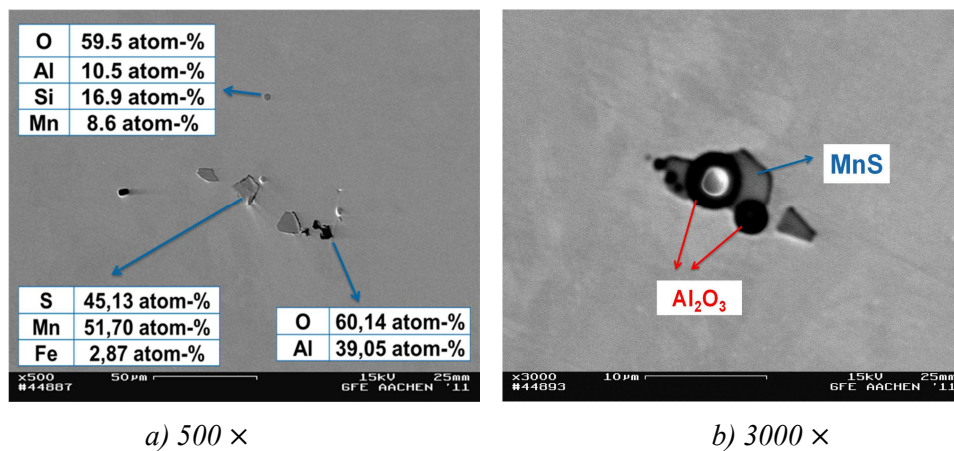

a) 500 ×   *b) 3000 ×*

Fig. 5.26 EDX analysis of typical inclusion compositions

By analyzing the inclusion composition at different position of the ingots using EDX, it has been found that the large inclusion particles (> 15 μm) are composed of mainly two types: manganese sulfide and aluminum oxide. EDX results show that the inclusions contain also Cr and Fe, but MnS and Al_2O_3 are dominating in most of the inclusions that were analyzed in present study.

Since manganese sulfide might form due to sulfur enrichment and aluminum oxide might be form during pouring, in order to clarify the origin of the inclusion particles, the relationship between macrosegregation and inclusion distribution has also been investigated. Fig. 5.27 and Fig. 5.28 show the segregation index of Al and Mn, S in combination with the number of large inclusion particles in

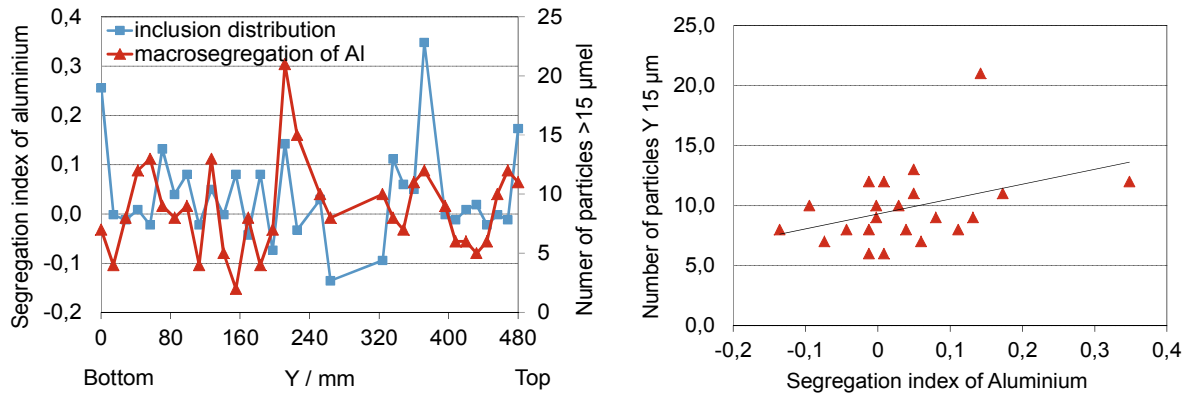longitudinal direction of ingot A7, respectively.

Fig. 5.27: a) inclusion distribution and macrosegregation of Al in longitudinal direction from ingot bottom to top, A7, b) relation between particle numbers (>15 μm) and segregation index of aluminium, based on a)
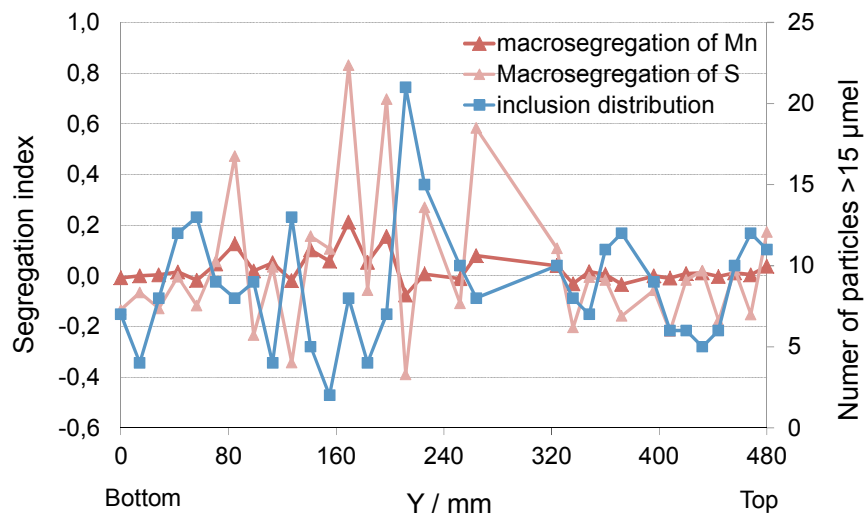
Fig. 5.28: Inclusion distribution and macrosegregation of Mn, S in longitudinal direction, A7

It seems that the macrosegregation profiles of aluminum in Fig.5.27 a) and 5.28 match the distribution of large inclusions quite well, whereas the relation between the segregation of Mn and S with the inclusion distribution is also clear that large inclusion mainly appears at the position where S and Mn are more enriched. For example, the peak of inclusion distribution at ingot height of 120 mm matches quite well to the peak of Al distribution in the same position, and the peak of inclusion distribution at height of 320 mm fits with the peak of Mn and S distribution quite well. Fig. 5.27 b) indicates the same tendency that a higher segregation index of aluminium corresponds to a high number of large inclusions with diameter over 15 μm.

From Fig. 5.27 and 5.28 it can be seen that in the ingot top region the inclusions are mainly aluminum oxides. This might be due to two aspects: on one hand the aluminum oxides float up to ingot top and

accumulate there, on the other hand the usage of Al-yielding anti-cavity powder could bring Al_2O_3 particles into the steel ingot. The facts that the oscillation peaks of element segregation and inclusion number always overlap to each other and these peaks appear periodically imply that at the large inclusions appears frequently at the V-segregates where the alloying elements are also segregated.

The inclusion distribution along the transverse direction of the ingot has also been studied with LOM. As Fig. 5.29 shows, the average number of inclusions (> 15 µm) at ingot top is larger than that at ingot bottom and middle, this correspond to the inclusion distribution in the longitudinal direction.
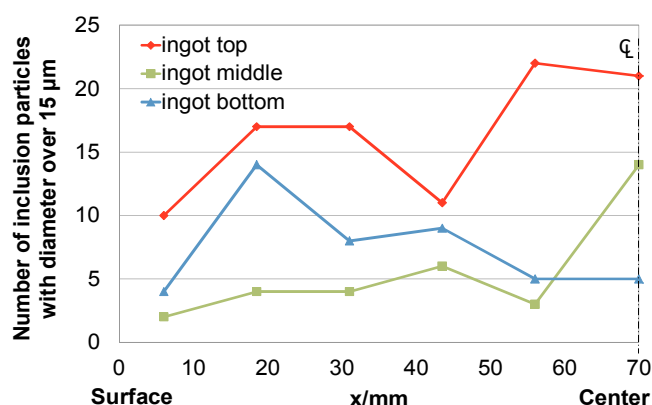
Fig. 5.29: Inclusions distribution in transverse direction in ingot A1at top, middle and bottom

The ingot center has more large inclusions especially at ingot top and middle, and at bottom there are fewer large inclusions. This might be due to the fact that samples in ingot top center and middle center are at the V-segregates and the sample at bottom center was taken from the bottom columnar zone where no V-lines appear. However, at ca. 20 mm from ingot surface more inclusions are found at bottom than in ingot middle. This could be due to the fact that during uphill casting, exogenous inclusions as oxidation products are brought into the ingot and move towards the solidification front, captured by the columnar dendrites, and stay there till the end of solidification.

Fig. 5.30: Segregation profiles in transverse direction at ingot top, middle and bottom, V1

The inclusion number at the top is also higher than at bottom and middle at ingot surface, and the

tendency is similar in columnar zone which is ca. 40-50 mm from the surface. It seems that the ingot top area is densely distri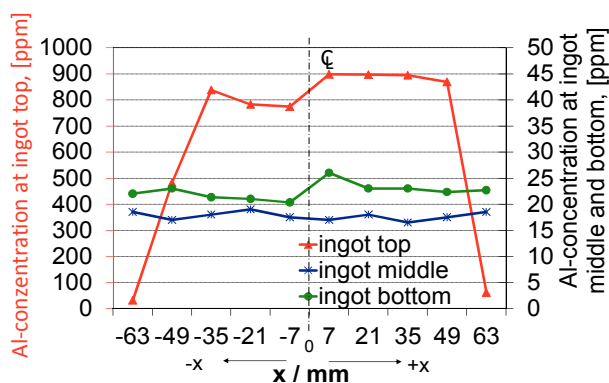buted with large inclusions from surface to ingot center. Combined with the concentration profiles of aluminum as shown in Fig. 5.30, it can be found that the aluminum concentration is particular high at top, with the value between 800 and 900 ppm, whereas at ingot bottom and middle the Al-concentration is around 15-25 ppm. This is closely related to the addition of anti-cavity powder on the top of the ingot after pouring end.

5.2.2   Slow solidification ingots (500 kg)

The slow solidification of ingots with weight of 500 kg in the isolating mould represents the solidification behavior of casts with extremely large cross-section, e.g. industrial-scale large ingots with the weight of several tons. The solidification time can be over several hours, and many complex solidification phenomena could happen, for instance remelting and sedimentation of equiaxed grains, and therefore the solidification structure is inhomogeneous. Some casting defects which cannot be found in small cast could appear in the large casts, such as A-segregates. The following sections present the results of temperature measurement during solidification of the 500 kg ingots and the as-cast macro-/microstructure as well as macrosegregation of alloying elements.

5.2.2.1   Temperature measurement

As referred in Section 5.1.2, the temperature measurements in the ingot were successful in trial B2, and this section represents all the temperature curves of the ingot and mould wall that were measured from trial B2. Fig. 5.31 shows the temperature curves measured at the two locations illustrated by in Fig. 5.7, which is at ingot height of 350 mm, with the distance of 25 mm and 100 mm to ingot center, respectively.
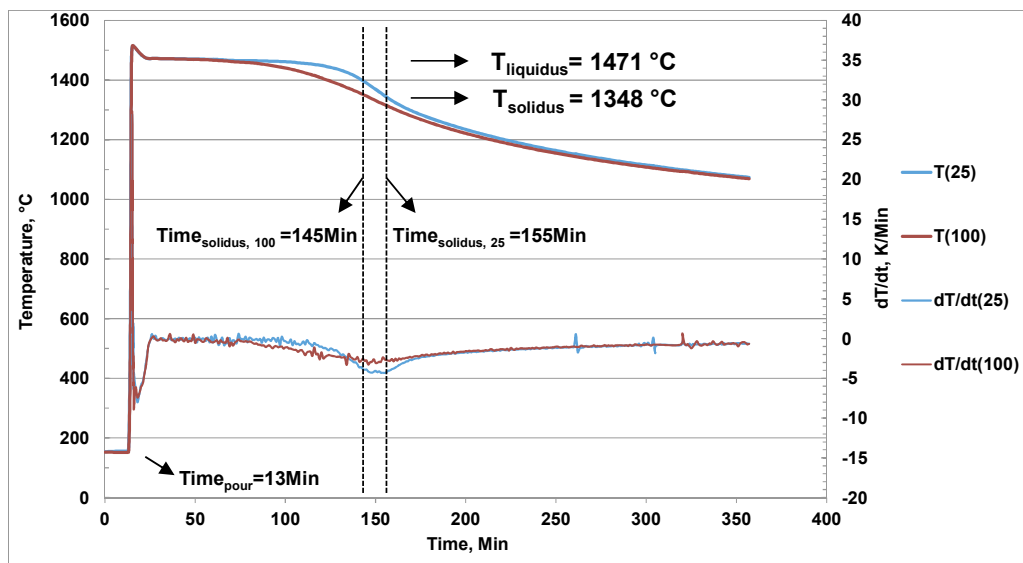

Fig.5.31: Cooling curves measured at 25mm and 100mm from ingot center at ingot height of 350mm, Trial B2

The liquidus temperature was read directly from the temperature curve as 1471 °C. To analyze cooling curves, the first derivation of the curve as the cooling rate has been calculated and sketched in the figure. The lowest point of the temperature gradient corresponds to the end of solidification, where the solidus temperature is obtained as 1348 °C. For the thermocouple at 25 mm from the center, at 155 min solidification completes, and for the thermocouple at 100 mm from the center, solidification finishes at 145 min. As pouring starts at 13 min of the curves, the complete solidification time is 142 min with the horizontal distance of 25 mm from the center and 132 min with the horizontal distance of 100 mm from the center, respectively.

As the last solidified region can be determined from the macrosegregation pattern of alloying elements where with the most severe segregation occurs, which will be referred later, it was found that the latest solidified spot, the so-called "hot spot" for ingot B2 is at the height of 370 mm and at 20 mm from the centerline which is close to the casting tube. This hot spot is marked in Fig. 5.32. The thermocouple with the distance of 25 mm (Position 1) to ingot center is actually 49mm away from the hot spot, and the other thermocouple (Position 2) is 124 mm away. Therefore, the total solidification time of the 500 kg ingot is over 142 mm. The distance between Position 1 and Position 2 is 75 mm, and the difference in solidification time is ca. 10 min, it can be estimated that the total solidification time of the whole ingot is roughly 150 min. As the reported solidification time of a 3t steel ingot in a square cast iron mould was 100-110 min [154], and the solidification time of a 6 t hexahedron ingot in a cast iron mould was 260 min [155], it can be deduced that solidification time of the 500 kg slow solidified ingot in present study corresponds to the solidification time of industrial scale ingot with the weight between 3t and 6 t.

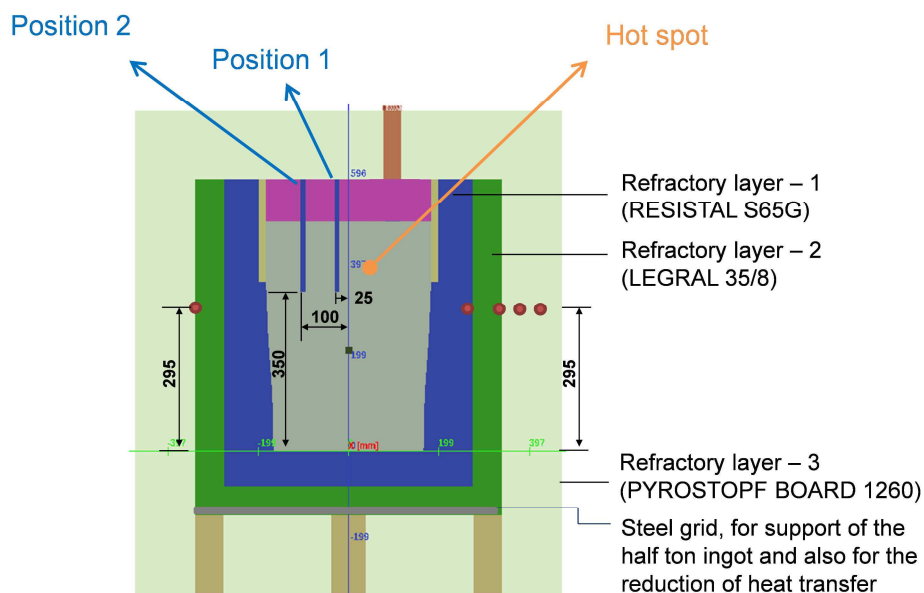*Fig. 5.32: Location of thermocouples and hot spot of the ingot, view cut in ingot center plane, B2*

Fig. 5.33 shows temperature curves measured in the mould wall with a distance of 140 mm to ingot surface at left, right, front and back sides. The temperature profiles of the mould wall are very similar to each other, indicating that the cooling rates from the four walls are also very similar. This implies that the metallurgical

center of the ingot might be very near to the geometric center, and helps us to find the metallurgical center for sample taking later. At 150 min after pouring when the solidification completes, the temperature at 140 mm to ingot surface has reached up to ca. 600 °C, and at 300 min after pouring, the mould temperature rose up to ca. 800 °C. This indicates that the thick mould wall which is made of refractory bricks and isolation materials is a great heat sink to cool the melt down. As soon as the melt is poured into the mould, columnar dendrite will grow from ingot outer surface towards center quite fast due to the large thermal gradient. This cannot be changed by preheat the mould inner surface up to 200-300 °C or add more isolation materials of the mould, since mould will absorb considerable heat in the beginning of solidification. Therefore for our isolating mould with the cast weight of 500 kg, the solidification time of 150 minutes cannot be further prolonged.
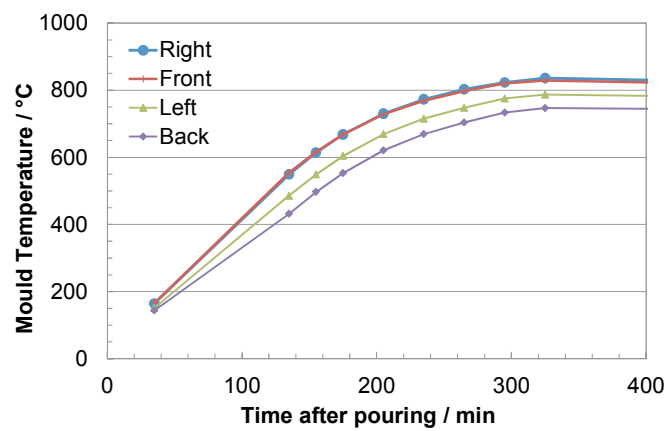

Fig. 5.33: Temperature curves measured in the mould wall at right, left, front and back side at distance of 140 mm to the surface of ingot B2 (the T-curve at right side overlaps with the T-curve at front)

Fig. 5.34 shows the mould temperature at different distance to the ingot surface at one side, with regard to 76 mm, 140 mm, 190 mm and 240 mm. At the distance of 76 mm ingot surface, the temperature of the refractory bricks has risen up to ca. 800 C till the end of solidification at 150 minutes. Since the measuring point is not in direct contact with the ingot surface, it is no possible to see when the air gap form between the ingot and the mould surface from Fig. 5.34. A potential measurement in future to detect the air gap formation could be to drill a small hole in the refractory brick and insert the thermocouple (type S) into the brick where the head of the thermocouple is exactly at the mould inner surface, as it was measured for the 100 kg ingot casting trials. If there is a turning point that can be found in the measured temperature curve during solidification, air gap appears very likely that the thermocouple loses direct contact with the ingot. However, the thermocouple should not be under protection of thick glass tubes, otherwise due to measurement delay the air gap cannot be detected.

Based on the measured temperature profiles of the mould wall, the temperature distribution from outer surface to the inner surface of the mould has been shown in Fig. 5.35 a). The thermal gradient is calculated by assuming $\frac{\partial T}{\partial x} \approx \frac{\Delta T}{\Delta x}$ at the measuring point. The maximum thermal gradient is calculated to be 7.54 K/mm at 90 minutes after pouring. The heat flux $\dot{q}$ is calculated as $\dot{q} = \lambda \cdot \frac{\Delta T}{\Delta x}$ with the simplification that the

thermal conductivity of refractory materials are independent on temperature. The heat fluxes have been calculated at different distance to mould outer surface, as shown in Fig. 5.35 b). The maximal heat flux happens with the value of ca. 13 kW/mK between 60 min and 120 min after pouring at the distance of 240 mm from mould outer surface, which is the nearest measuring point to the ingot. The farther from the ingot, the lower the heat flux during solidification is, and the value is lower than 2 kW/mK with the distance from 76 mm to 190 mm to the mould outer surface. After around 20 hours the heat flux calculated at different locations become to be unanimous where the heat transfer in the ingot and the mould is in steady state. As it was assumed that the thermal gradient near the calculation point is linear, the real thermal gradient can be larger than calculated, especially in the initial and middle stage of solidification.
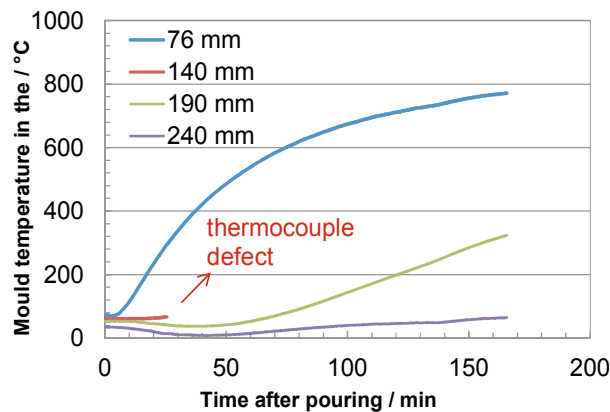
Fig.5.34: Temperature curves measured in the mould wall at different distance to ingot surface during solidification of ingot B2 (from outer to inner: 76 mm, 140 mm, 190 mm, 240 mm)
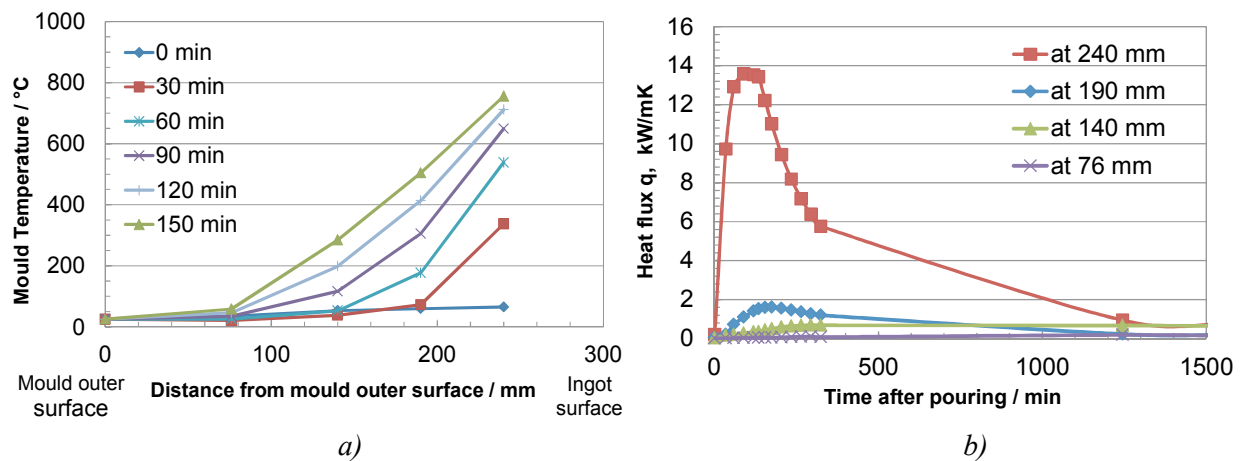
Fig.5.35: a) Temperature distribution of the mould wall from outer to inner surface at different time during solidification of ingot B2, b) heat flux calculated from temperature curves measured in the mould refractory, Trial B2

5.2.2.2 Macro- and microstructure

After the 500 kg ingot was completely solidified and cooled down for 2-3 days in the mould, the ingot

was stripped out from the top of the mould. The as-cast ingot is shown in Fig. 5.11 a), and the ingot geometry is also given in the section 5.1.2. After cooling down to room temperature the ingots (B1 and B2) were delivered to Dillinger Hüttenwerk to cut up and to take samples according to the sampling plan given in Fig. 5.11 b). Sulfur printing was used to reveal the macrostructure of the as-cast ingots (see also page 37 and page 52).

Fig. 5.36 shows the sulfur prints in the longitudinal cross sections of ingot B1 which are perpendicular to each other, with the red dashed line indicating the CET positions. It can be seen from both sulfur prints that there is a huge top cavity appearing under the columnar dendrites which grow from ingot top downwards. Since ingot B1 was cast without the rice husk ash on top, the top of the ingot start to solidify in the beginning, and the cavity caused by shrinkage is enclosed inside the ingot.

a)   *b)*

Fig. 5.36: Sulfur prints of the longitudinal cross sections of ingot B1, plane in a) is orthogonal to plane in b), height in mm

Different from the sulfur prints of the 100 kg ingots, there are no V-lines found in the sulfur prints of the 500 kg ingot, and instead, A-lines appear mainly at a distance of 40 ~ 100 mm from ingot surface and at the ingot height of 120 ~ 400 mm. The inclined angles of the A-lines to gravity differs from 5° to 10°, and it seems that the inner region of the A-segregation zone with the distance of 65 ~ 100 mm from ingot center, the A-lines are more inclined, and in the outer region of the A-segregation zone with a distance of 40 ~ 65 mm to ingot center, the A-lines are more parallel to gravity. It has been measured from the sulfur prints that the minimum length of A-lines is 3 mm, whereas the maximum length is 80

mm. The width of A-lines is measured between 1 and 2 mm from Fig. 5.36. The inclined angles of columnar dendrites were also measured, which grow from the sides of the ingot towards the center, and the angle between the columnar dendrites to gravity direction are mainly in the range of 55° ~ 70°. Another interesting fact is that the outer A-segregation region overlaps somehow with the CET zone, which appears at ca. 50 ~ 70 mm from ingot surface, and this will be discussed later.

Due to the unusual location of the top cavity, the as-cast structure of ingot B1 doesn't represent the large industrial-scale ingots completely, and therefore for trial B2 in order to avoid the enclosed top cavity, rice husk ash was added to cover the ingot top directly after pouring ends. Fig. 5.37 shows the sulfur prints of ingot B2 in the longitudinal cross sections, and it can be clearly seen that the major cavity appears at ingot top with a V-shaped contour, as in large industrial large ingots.
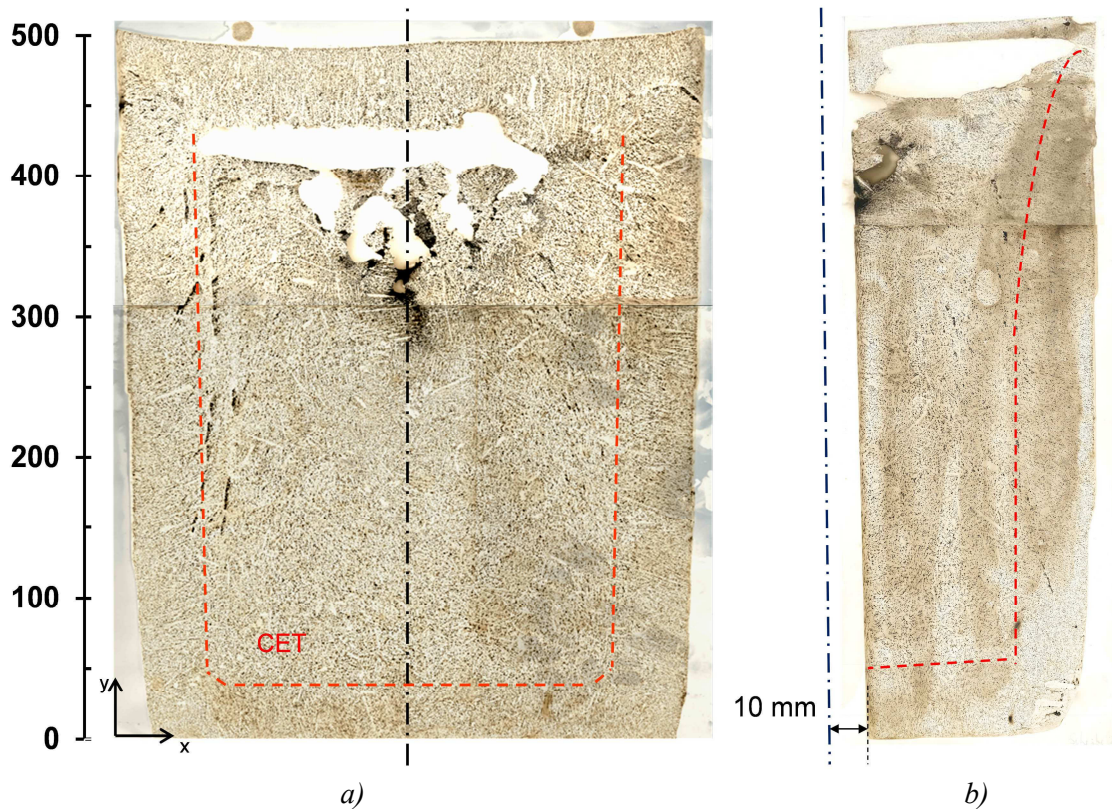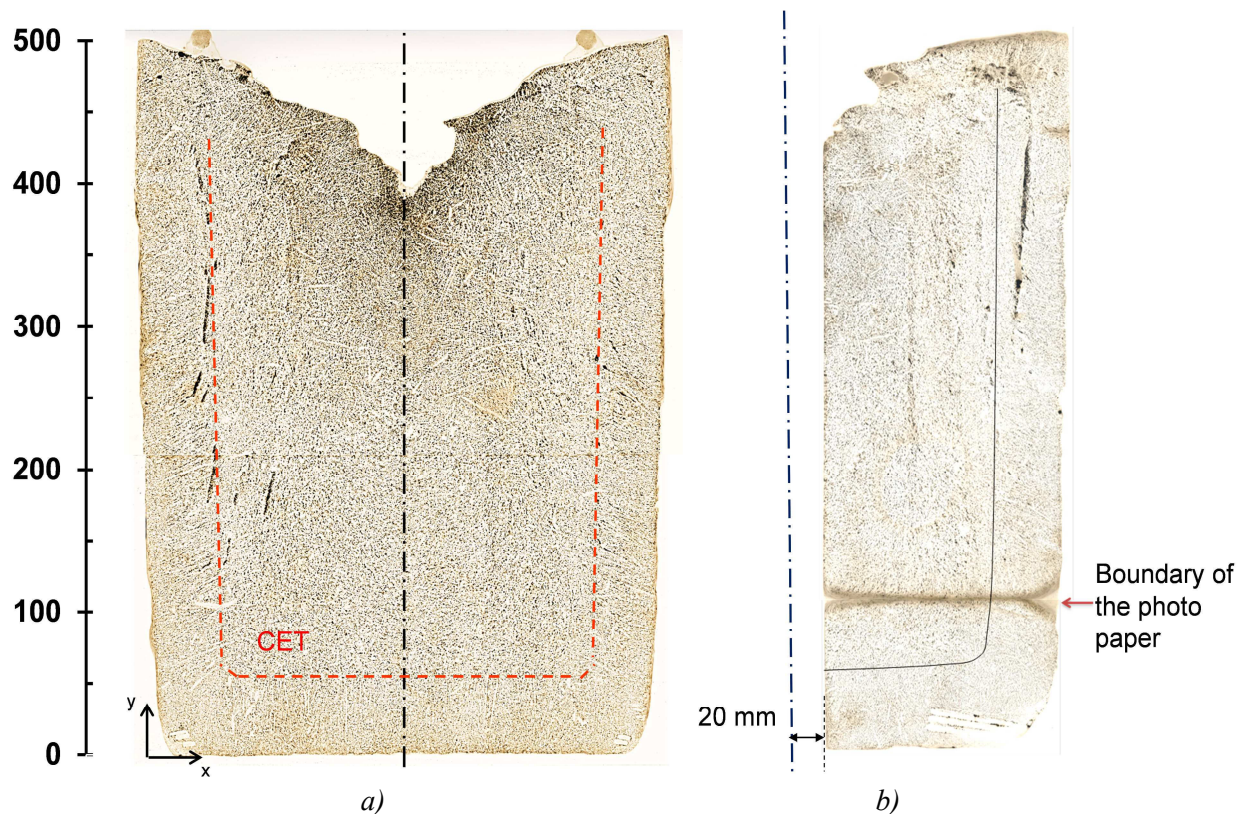

Fig. 5.37: Sulfur print of the longitudinal cross sections of ingot B2, plane in a) is orthogonal to plane in b), ingot H/D = 505 mm / 365 mm = 1.38, height in mm

The red dashed line indicates the CET-position, which is ca. 50 mm from ingot surface, and the CET zone covers with a width of around 20 mm. This is very similar to ingot B1, since the superheat temperature of the melt of B2 is very similar to B2, and for both trials the inner mould wall was preheated to ca. 150 °C before casting. The A-lines also appear at the similar position of the ingot B2 as in ingot B1, which is ca. 40 ~ 100 mm to ingot surface, starting somehow from the columnar front. The height range that the A-segregation zone covers is between 120 mm to 470 mm of the ingot

height, which is due to the fact that the position of the hot spot in B2 is higher than in B1 due to the better top isolation.

The sulfur prints in Fig. 5.37 indicated again that the A-segregation zone is composed of two regions: the inner region with the more inclined A-lines with the angle of $10° \sim 15°$ to gravity and the outer region with the more vertical A-lines with the angle of $5° \sim 10°$ to gravity especially in the upper part of the ingot. It seems that in the lower portion of the ingot the A-lines are equally inclined with the same inclined angle of ca. $10°$, and in the upper portion the inclined angle of the A-lines are more diverse, covering the range between $-5° \sim 15°$. The negative inclined angle is found at the left side of Fig. 5.37 around the ingot top region where there is a A-line pointing to the left top corner of the ingot, and it seems that this A-line has developed along the columnar dendritic front.

It is not easy to distinguish where initiates the A-lines from the columnar zone. Most of the time, a smooth curve which connects the segregation among columnar dendrites to the A-line can be seen, as illustrated in Fig. 5.38. Therefore it is not easy to determine the inclined angle of the A-lines as the inclined angle of single A-line actually does not remain a constant. During measurement of these A-lines, the major part of the A-lines was chosen to define the inclined angle.

a)   b)
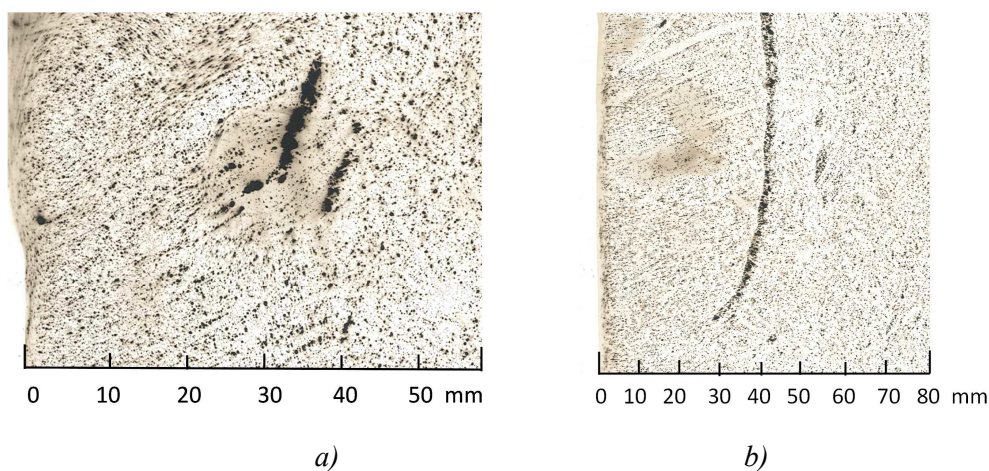
Fig. 5.38: A-lines that initiate from columnar zone in the sulfur print, B2

The macrostructure of the transverse cross section of the ingot has also been revealed by sulfur printing. The transverse plates of the ingots were taken according to the sampling plan in Fig. 5.11, and the sulfur print of the transverse plate 3, which is at 410 mm height of the ingot, is given in Fig. 5.39. It can be seen that the projections of the A-lines on the transverse cross-section are actually a couple of black points with a diameter of $1 \sim 2$ mm. The density of these A-dots in the A-segregation zone was measured, and the average distance between the neighboring points was found to be around 18 mm.

The sulfur print in Fig. 5.39 provides adequate information of the distribution of the A-segregates in

the ingot. The red dashed line indicated the CET-position, and the A-dots distributes mainly in a belt with a width of ca. 50 mm around the CET-position. Different from what has been observed from the sulfur print in longitudinal direction (Fig. 5.37), the A-dots are found much closer to the surface, and some of the A-dots appear actually in the columnar zone. Near the ingot center there are a few A-dots found, and the density is much lower than that near the ingot surface. Since plate 3 is at the ingot top region which is directly under the top cavity, the columnar zone is relatively narrower under the impact of the hot-top condition, the A-segregates which develops in correlation with the columnar front is also pushed outwards.
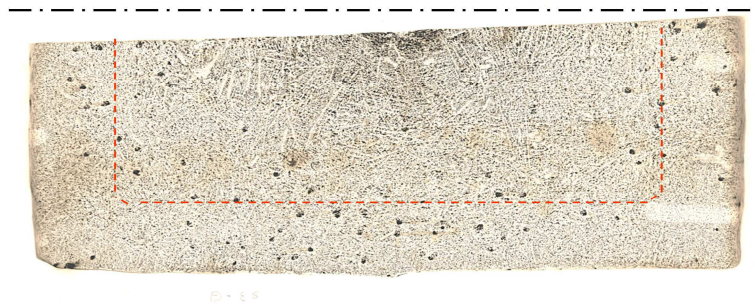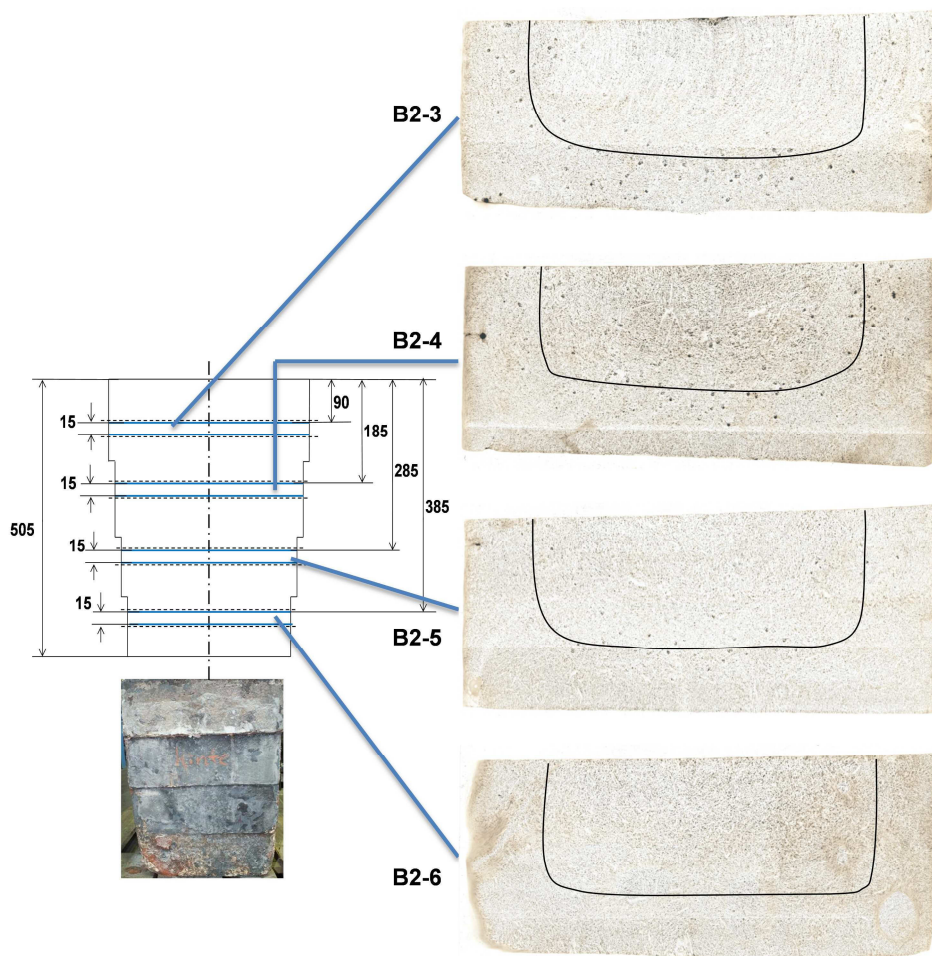

Fig. 5.39: Sulfur print for the transverse plate-3 (dashed line indicates the CET position)

Fig. 5.40: Positions of samples B2-3, A2-4, A2-5, A2-6 and their sulfur prints (solid line indicates the CET position)

The distributions of the A-dots in the transverse plates are very different from each other. Fig. 5.40 shows the sulfur prints of the transverse plate 3, 4, 5, 6, which are at the ingot height of 410 mm, 305 mm, 205 mm and 120 mm of ingot B2, respectively. A-dots can be found in plate 3, plate 4 and plate 5, and no A-dots are observed in plate 6, and this is in consistence with the A-lines distribution displayed in Fig. 5.37. From plate 5 to plate 3, i.e. from ingot bottom to top, the A-segregates move from inner part of the ingot towards the ingot surface, and the density of the A-segregates are higher in ingot top.

In order to quantity the distribution of A-dots along the longitudinal direction, the total amount of A-dots in the four sulfur prints (plate 3-6) of ingot B2 in Fig. 5.40 are counted. The results are shown in Fig. 5.41 a). As is can be observed from the sulfur prints, the total number of A-dots in the transverse plates increases from ingot bottom to top. For plate 6 which is at the height of 120 mm, there are no A-dots found, and for plate 5 at the ingot height of 220 mm, around 40 A-dots are found in the sulfur print. Plate 4 and plate 5, which are at the height of 305 mm and 410 mm of the ingot respectively, have much more A-dots than in the bottom half of the ingot. There are 88 A-dots found in plate 4 and 92 A-dots observed in plate 3. From this point of view, it can be concluded that in the A-segregation zone, the A-segregates are more densely distributed in the upper part of the ingot.
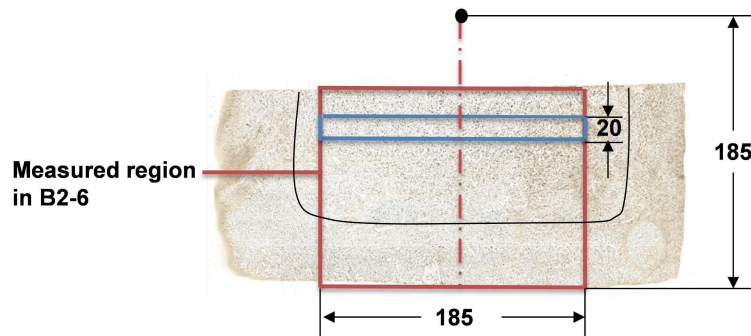
Fig. 5.41: The region in B2-6 used to count the amount of A-dots along the transverse directions at different ingot heights (solid line indicates the CET position)

To quantify the distribution of the A-segregates of the whole ingot, the distribution of A-dots along the transverse direction has been investigated for each sulfur print as well. As shown in Fig. 5.41, for each sulfur print of the transverse plate, a square shaped area has been chosen for measurement, which is illustrated by the red rectangular. Then this square was divided with several strips which have a width of 20 mm from ingot center to ingot surface, as illustrated by the red rectangular. In each strip the number of A-dots was measured, and the results show a discretized distribution of A-dots in the transverse direction from ingot center to surface at different height of the ingot, as given in Fig. 5.42 b).
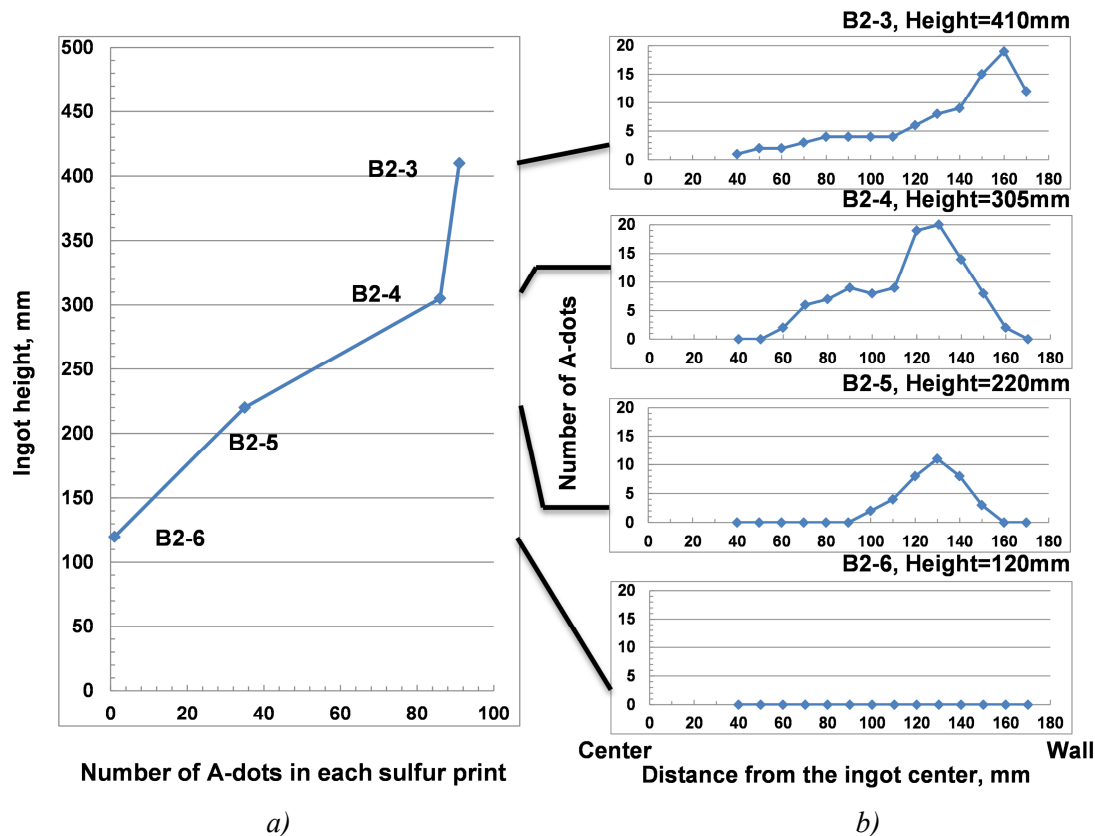
Fig. 5.42: Distribution of A-dots in the sulfur prints of B2, a) total number of A-dots from plate B2-3 to plate B2-6, b) distribution of the A-dots in the transverse direction in plate 3-6

It can be that except for plate 6, there is a peak in the distribution profile of each plate where maximum of A-dot number appears, and the location of the peak moves towards ingot surface as the height increases. For plate 5 at the ingot height of 220 mm, the peak appears at the radius of 130 mm, whereas for plate 3 at the height of 410 mm, most of the A-dots are found at the radius of 160 mm. Furthermore, the contours of the distribution profiles are not quite similar. For plate 6 the distribution profiles seems to obey an axial symmetrical distribution that has equally distributed A-dots at the both sides of the peak. The A-segregation zone in plate 6 is at the radius of 90 ~ 160 mm. For plate 4 it seems that the inner part of the ingot there are more A-dots found than in plate 6, and the A-segregation zone has been widened inwards to the radius of 60 mm. For plate 3 although the peak is moved outwards at the radius of 160 mm, the A-segregation zone is further widened into the center at the radius of 40 mm. For ingot B1 the distribution of the A-dots has been measured similarly, and the results are summarized in Fig. 11.1-3 in the appendices.

Based on the sulfur prints and the measurement results shown in Fig. 5.42, it can be concluded that the A-segregation zone in our 500 kg ingot is a like hollow cylinder with an irregular shape, as schematically illustrated in Fig. 5.43. This cylinder covers a range in ingot height from 120 mm to 470 mm, in ingot radius from 40 mm to 170 mm. The space enclosed by the inner surface of the cylinder is like a pyramid and the outer surface is stretched towards surface at ingot top. The shadow indicates the

density of the A-segregates inside the A-segregation zone. In ingot top region the A-segregates are mostly close to the surface, and in ingot middle height and bottom region the A-segregates mainly appear at the radius of 130 mm.

To obtain more detailed information of the solidification structure besides sulfur prints, the transverse plate was hot-etched and the macrostructure is shown in Fig. 5.44. From ingot surface to center, chill zone, columnar zone, CET zone and the equiaxed zone can be seen successively. As referred before, the columnar zone covers a width of around 50 mm, CET occur right before the columnar front with a range of ca. 20 mm. From the hot-etched dendritic structure, it can be clearly seen that the dendrites in the outer part of the equiaxed zone are coarser and these large dendrites are not quite compacted to each other, whereas in the inner part of the equiaxed zone, dendrites are much finer and more compact. The outer region of the equiaxed zone is named as "outer equiaxed zone", and the inner part as "inner equiaxed zone", since their dendritic characteristics are different.
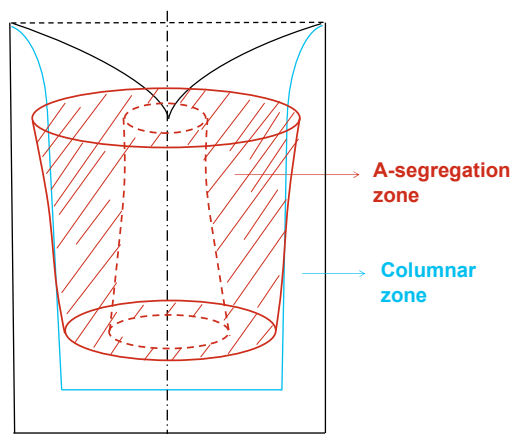
Fig. 5.43: Schematic illustration of the A-segregation zone in 3-dimension in the 500 kg ingot

By hot-etching it is able to see the A-dots from plate 5, as illustrated in Fig. 5.44. Since the alloying elements are more enriched at the A-segregates and hence more easily to be dissolved by etching. The A-dots in plate 5 appear mainly in the CET zone and in the outer equiaxed zone, as the dendritic structure are coarser less ordered, and the interspace between dendrites are larger, which result in a higher permeability for the melt flow.
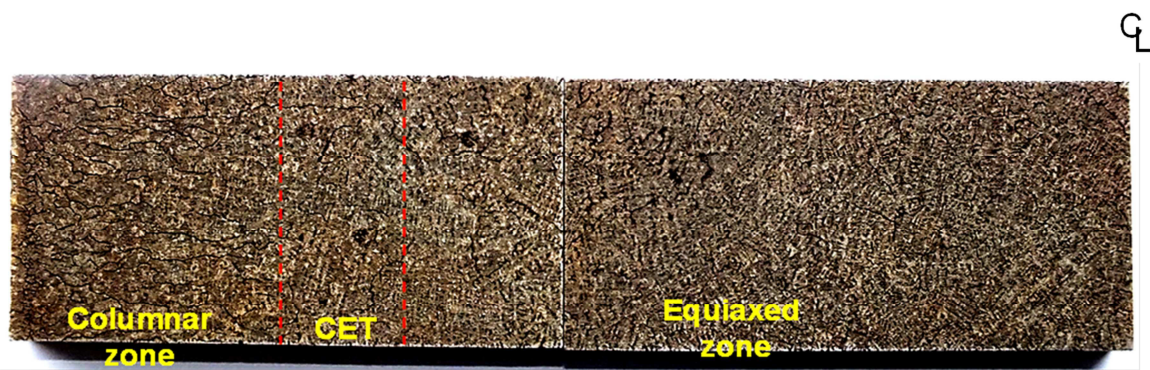
Fig. 5.44: Macro-etching of the transverse plate 5 at ingot height of 185 mm, B1

The dendrite structure can be further quantified by measuring the secondary dendrite arm spacing along the transverse direction by using light optical microscopy (LOM). For each sample, at least 10 values of the SDAS were measured and an average value was taken. Fig 5.45 shows the measured SDAS along the transverse direction at ingot height of 290 mm for B1, which is directly under the top cavity. Fig. 5.46 shows the SDAS distribution at ingot height of 120 mm for B2, which is at the bottom of the ingot.

a)   *b)*
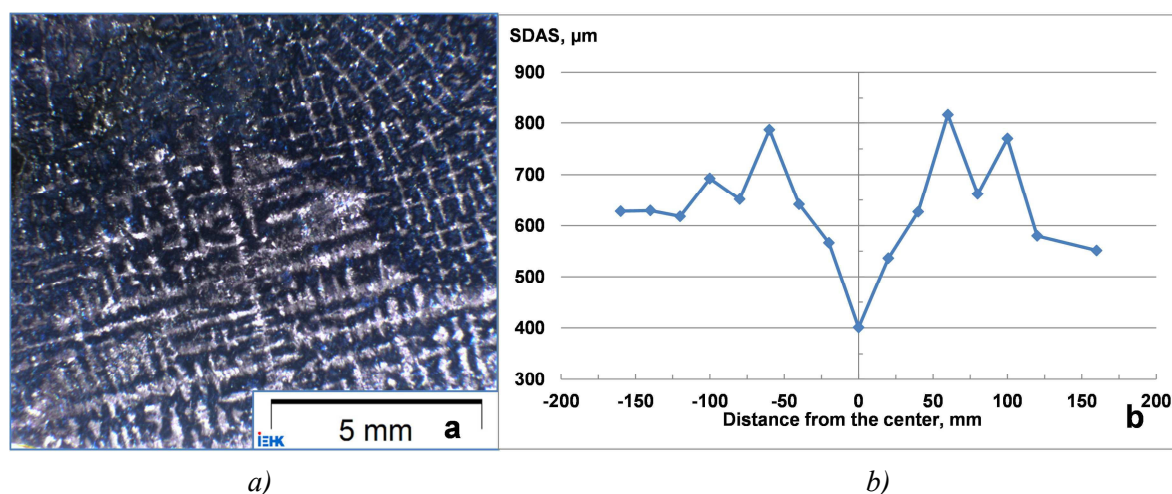
Fig. 5.45: a) Light microscopic photo for SDAS measurement, b) Distribution of SDAS along the transverse direction at the ingot height of 290 mm (direct under top cavity), B2
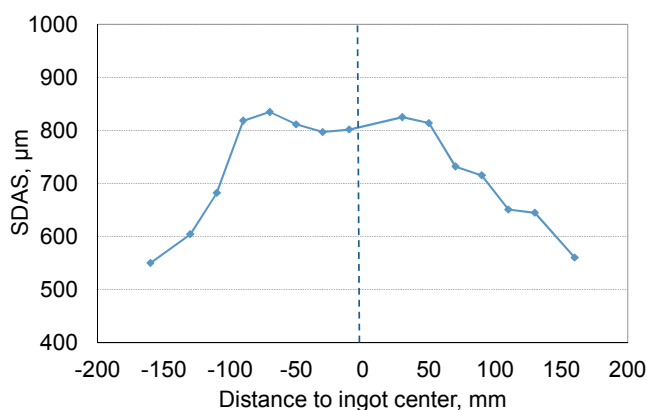
Fig. 5.46: Distribution of SDAS along the transverse direction at the ingot height of 120 mm, B1

It can be seen that the SDAS at the columnar zone are around 600 µm for samples coming from different ingot heights. In both the figures at the radius of 60 ~110 mm, SDAS distribution shows a higher value than in the center and in the columnar zone, and the maximum value appears at the radius of around 70 mm, which is ca. 820 µm at lower part and 800 µm at upper part of the ingot. The major difference between Fig. 5.45 and Fig. 5.46 lies in the SDAS value in ingot center. At the height of 290 mm the ingot center, which corresponds to the hot spot of B1, the dendritic structure is very fine with the SDAS value of only 400 µm, which is lower than the value in columnar zone of 600 µm. At the

ingot bottom with the height of 120 mm, the SDAS in ingot center is up to nearly 800 μm.

The local solidification time can be calculated from the empirical relationship between secondary dendrite arm spacing and the local solidification time according to Jacobi and Schwerdtfeger [156]:

$$\lambda_2 = A \cdot \theta_f{}^B \qquad\qquad \text{Equation 5.3}$$

$$\theta_f = (\frac{\lambda_2}{A})^{\frac{1}{B}} \qquad\qquad \text{Equation 5.4}$$

where λ_2 is the secondary dendrite arm spacing in μm, θ_f is the local soliditication time, $\theta_f = t(T_l) - t(T_s)$, A and B are constants, A = 15.8, B = 0.44, and these value have been already verified for the steel grad in the present study by the experimental measurement for the 100 kg ingots.

For the top center area (inner equiaxed zone) where the measured SDAS is ca. 400 μm, the calculated local solidification time is 26 min; for the columnar zone where SDAS is ca. 600 μm, the local solidification time is calculated to be 65 min; for the sedimentation zone of equiaxed grains and the outer equiaxed zone with the measured SDAS of ca. 800 μm, the calculated local solidification time is around 125 min.

The result that the hot spot area has the finest dendritic structure is very different from the imagination that the last solidified part should have the longest local solidification time due to the low thermal undercooling, and therefore has the coarsest dendritic structure. In fact, the driving force of dendritic growth in the hot spot area is dominated by the constitutional undercooling caused by the intensive macrosegregation there, which will be presented in the next section. Due to the strong constitutional undercooling the dendrites will grow fast, and therefore result in a low SDAS value. For the case in ingot bottom, the ingot center is actually in the sedimentation zone, which can be indicated by the macrosegregation pattern presented in the next section. In the sedimentation zone the alloying element is negatively segregated, which means that constitutional superheat occurs. This constitutional superheat further reduced the low thermal undercooling in ingot center, and under such low undercooling, i.e. driving force, the dendrites grow slowly and therefore it leads to a relatively high SDAS value in the sedimentation zone. It needs to mention that the dendrite size is also influenced by the grain density, and if large amount of nuclei/grains are introduced into the melt, e.g. by stirring or inoculation, the SDAS of the sedimentation zone can be reduced.

5.2.2.3 Macrosegregation

The macrosegregation of the alloy elements in the 500 kg ingots B1 and B2 have been investigated with regard to C, Mn, Si, Cr, S, P, Al with the help of the spectrometer PDA-OES at IEHK. Similar as in the 100 kg ingots, the averaged composition $\bar{C}$ for the whole ingot was determined as an average of composition of 6 measure spots in the columnar zone in the middle plate of each ingot.

Fig. 5.47 shows the position of the samples for the spectrometry analysis and the measuring point on the sample. The sample for investigation on the longitudinal direction was taken 20 mm from the geometric center line of the ingot, which is actually at the metallurgical center, and four samples at different ingot heights were taken in the transverse direction, respectively 120 mm, 220 mm, 370 mm and 410 mm, as illustrated in Fig. 5.47 a). Different from the spectrometry measurement for the 100 kg ingot, the interval between the measuring spots was minimized in order to make measurements side by side, in order to gain as much information of sample concentration as possible, especially along the longitudinal direction, as illustrated in Fig. 5.47 b).
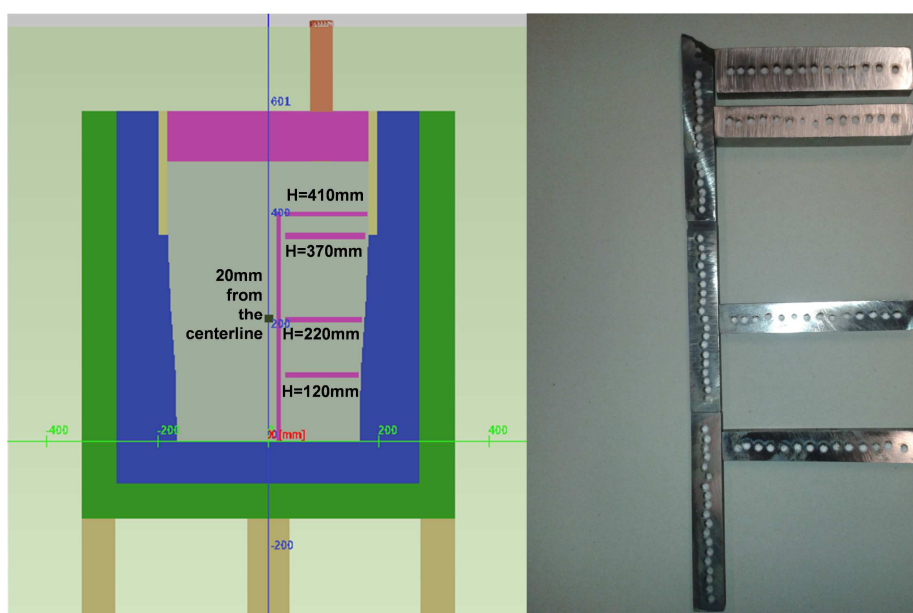
Fig. 5.47: Position of samples for spectrometry analysis, ingot B2

Fig. 5.48 and Fig. 5.49 show the segregation index of carbon and manganese along the longitudinal and transverse direction of ingot B2 as example. Negative segregation can be found in the lower half of the ingot with the negative segregation index of -0.05 for carbon and -0.2 for sulfur. This indicates that the height of the sedimentation cone of the equiaxed dendrites in ingot center is up to ca. 250 mm, and the negative segregation index of carbon in the transverse direction implies that the half width of the sedimentation cone is 120 ~ 130 mm from the height of 120 mm to 220 mm. Since the half ingot width is 180 mm, and columnar zone has a width of 50-70 mm, this means that the boundary of the sedimentation cone is exactly at the columnar front from the ingot height between 120 mm to 220 mm.

Positive segregation appear mainly in the upper portion of the ingot in ingot center with the radius up to 70 ~ 80 mm. Occasionally peaks of positive segregation are also found at the radius of 100 ~ 140 mm at the CET zone and the outer equiaxed zone, and this is due to the A-segregates.

Fig. 5.48: Carbon segregation index along the centerline and transverse direction, ingot B2

Fig. 5.49: Manganese segregation index along the centerline and transverse direction, ingot B2

Table 5.4 summarized the maximum and minimum segregation index of the seven alloying elements

for ingot B2. The positive segregation index of carbon is up to 0.38, corresponding to the carbon concentration of 0.74 % with the average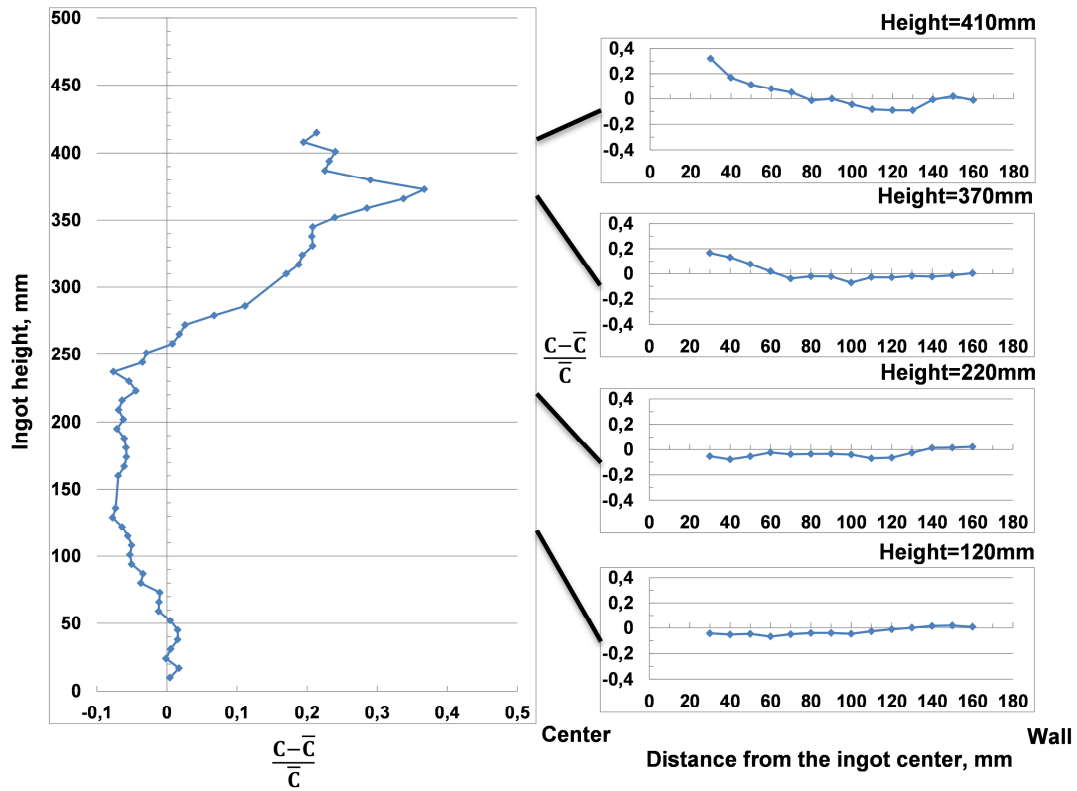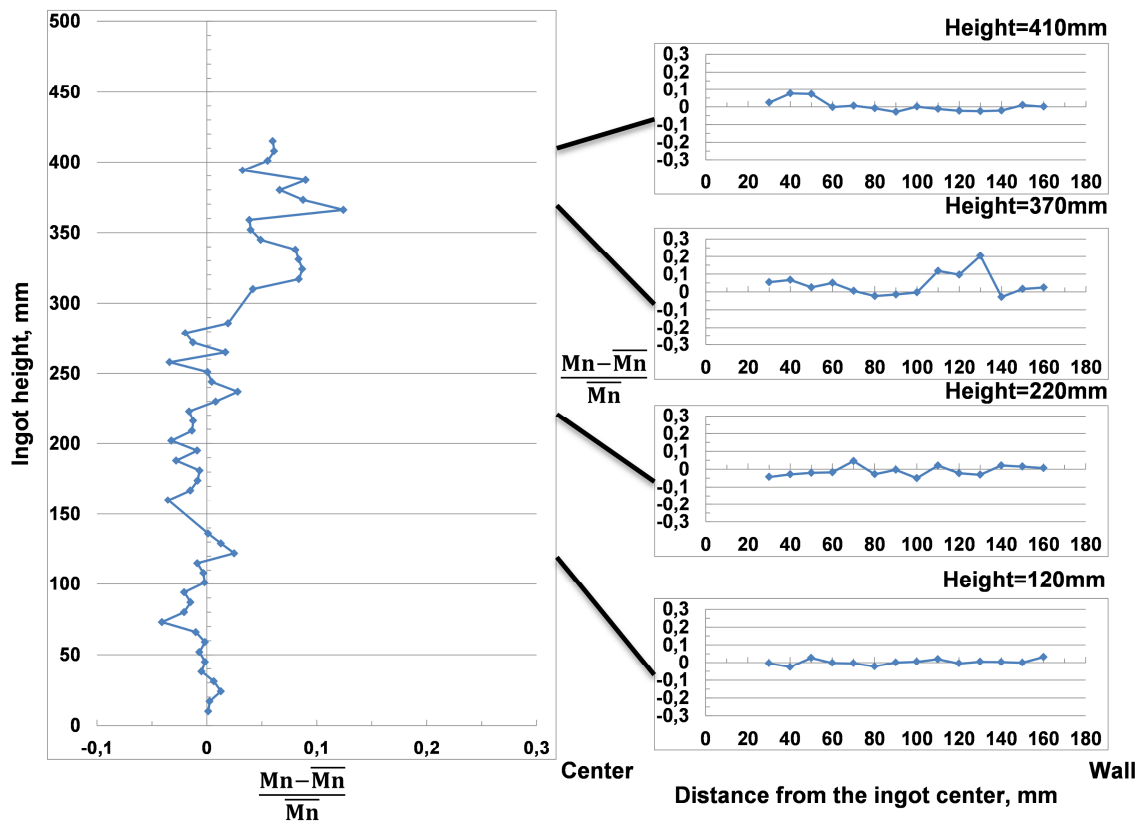d concentration of 0.538%. From the maximum segregation index it seem that phosphorous, sulfur and chromium are more likely to segregate, with the segregation index over 0.85, and silicon and manganese have a lower tendency of segregation, with the segregation index of around 0.12 and 0.13.

Element	C	Si	Mn	P	S	Cr	Al
Average composition, %	0.5380	0.4740	0.5220	0.0076	0.0193	0.175	0.03
Maximum segregation index	0.38	0.12	0.13	0.9	1.6	0.85	0.15
Minimum segregation index	-0.08	-0.04	-0.04	-0.25	-0.25	-0.04	-0.44

Table 5.4: Average concentration and segregation index of the alloying elements, B2

Being aware of the segregation characteristics of alloying elements, the steel composition can be adjusted to suppress some casting defects such as A-segregates that are induced by solutal buoyancy driven convection and by macrosegregation. For example, carbon and silicon are likely to segregate and their density is very low in comparison to steel, and in order to reduce the solutal buoyancy induced convective flow, their concentration should be decreased as low as possible, or more heavy alloying elements should be added. Chromium tends to segregate as well, but since their densities are slightly lower than steel, and the solutal convective flow will not be strongly accelerated. From this point of view, the dynamic process of remelting for A-segregation through the upwards convective flow should be suppressed. However, it should also be noticed that on the other hand, the enriched of alloying elements leads to the constitutional undercooling, and therefore provides kinetic driving force for remelting and for the formation of A-segregates.

Another interesting fact have been found that for both ingots B1 and B2, negative segregation of aluminum happens in ingot top especially in center, as shown in Fig. 5.50 and Fig. 5.51. Generally, aluminum is not segregated in the sedimentation zone of the equiaxed grains. There are a few peaks of the segregation index in this region, which could be due to the reason that single or agglomeration of aluminum oxides were caught by sinking equiaxed dendrites and brought down into the sedimentation zone, and our spectrometry measurements have detected one or more of these oxides in this area. In the hot spot region aluminum is strongly negatively segregated, with the segregation index lower than -0.4, which is adverse to other alloying elements, and is also different with the case in the 100 kg ingots.
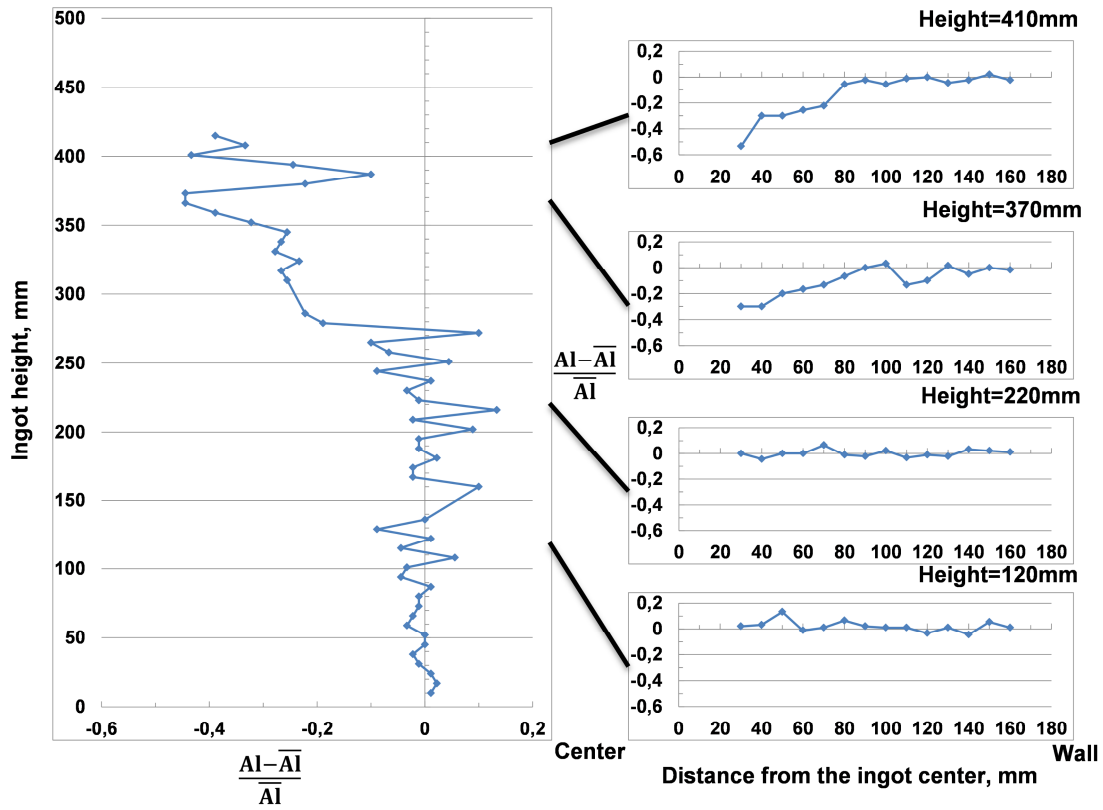
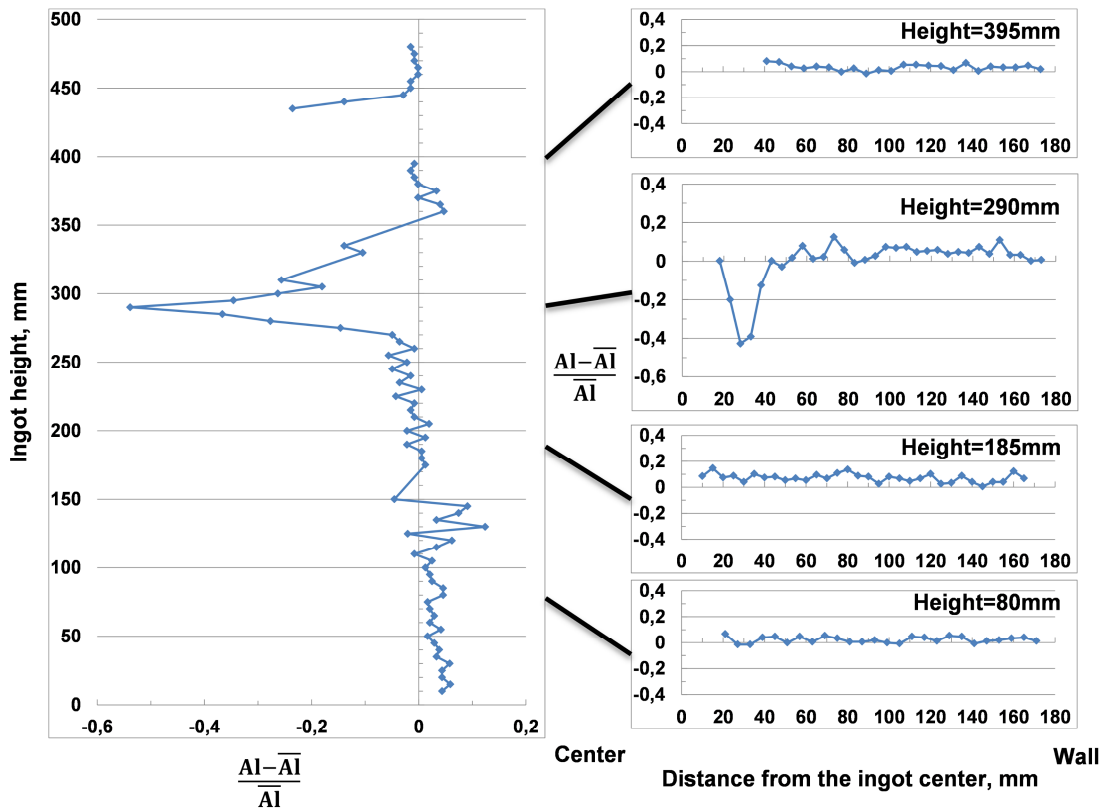Fig. 5.50: *Aluminum segregation index along the centerline and transverse directions of B2*

Fig. 5.51: *Aluminum segregation index along the centerline and transverse directions of B1*

The negative segregation index of aluminum can lie in the following factors. On one hand, as the

alloying elements are enriched in the upper part of the ingot, the iron content is lower in the upper part, and therefore the aluminium which dissolves in iron has a lower content as well. On the other hand, the dissolved aluminium in the steel can react with SiO_2 from the anti-cavity powder and form Al_2O_3 which appear as slag [157], as given in Equation 5.5. By such reaction, aluminium near the top of the ingot will be consumed and repelled out of the ingot and this leads to a lower aluminium content in the upper part of the ingot.

$$4\,[Al] + 3\,(SiO_2) <=> 2\,(Al_2O_3) + 3\,[Si] \qquad \text{Equation 5.5}$$
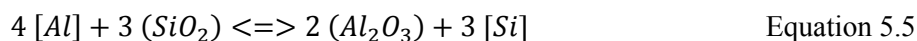
Other fact that could lead to this phenomenon is that during the downhill pouring and the convection during solidification, large amount of the aluminum has been oxidized, and the formed aluminum oxides were entrapped between the dendrite arms everywhere. The content of the alloyed aluminum in the melt was reduced and in ingot center where the melt solidifies last is free or with very low amount of the aluminum oxides. As our spectrometer measures the total amount of alloyed and oxidized aluminum, the Al-content in the hot spot is therefore lower than the averaged content.

The macrosegregation profiles of other alloying elements of ingot B2 are given in the appendices from Fig. 11.5-9. For ingot B1 the macrosegregation of the seven alloying elements were measured, and the results are summarized from Fig. 11.10-16 in the appendices.

The spectrometry analysis shows the positive segregation at the A-segregates, but since the spectrometer measures an area with diameter of 5 mm on the sample, the results of segregation is macroscopic. In order to quantify the segregation in the A-segregates in microscopic, Electron probe micro-analyzer (EPMA) have been used. The concentration field in the longitudinal cross section of an A-segregate and its surrounding was measured for alloying elements carbon, silicon, manganese and sulfur, as shown in Fig. 5.52.

The lightness indicates the intensities of characteristic X-rays of the alloying element, which corresponds to the concentration of the elements. The lighter the color is, the higher the concentration is. The concentration map of the four elements show a region with lighter color which is somehow inclined, and this region is the A-segregate. Compare to the surrounding, the concentration of silicon, manganese and carbon at the A-segregate are much higher. For element sulfur, at the A-segregate there are numerous light points on the concentration map, which indicates that large amount of sulfides are appearing at this region. If the locations of these light points for sulfur and for manganese are compared, it seems that the two overlap with each other, indicating that numerous MnS particles gather here. For element silicon the plenty of light points are also found in the concentration map, and their location seems to be different with manganese and sulfur, indicating that another kind of inclusion particles appear at the A-segregate.
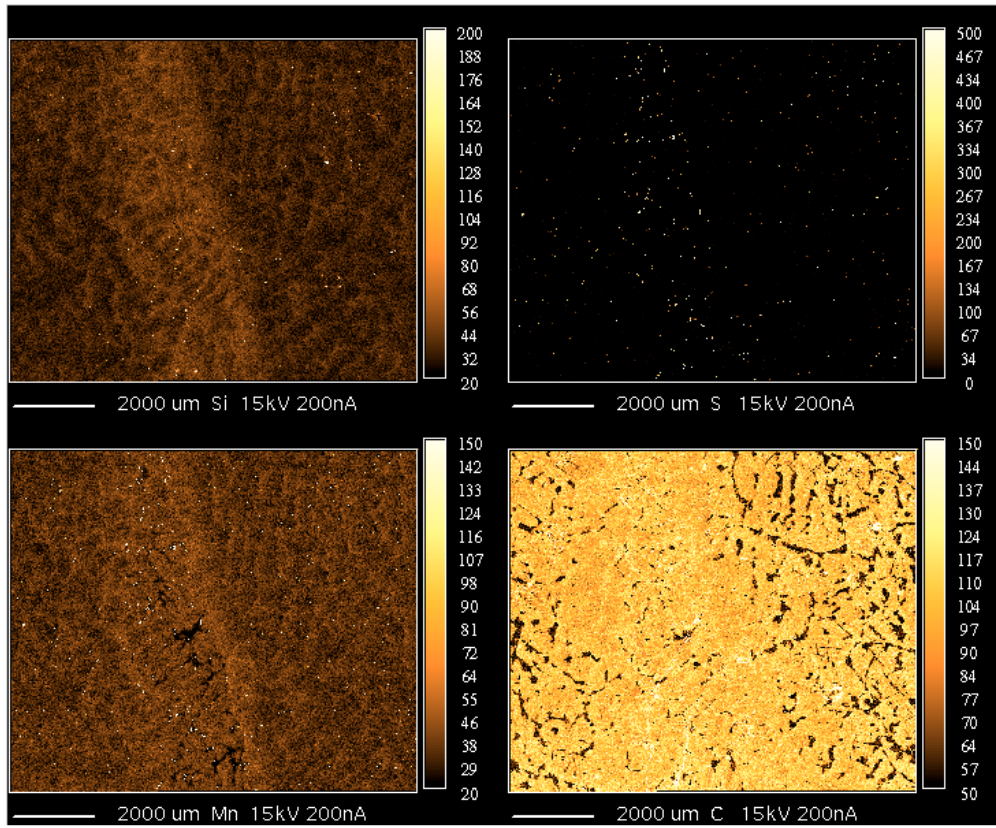
Fig. 5.52: Intensity diagrams of EPMA-measurements, in the longitudinal cross section of an A-segregate (Si, S, Mn, C)

Former researchers have described that the channel type segregations are pencil-like chains of equiaxed grains and eutectic constituents which are highly enriched in solute [49]. In our measured concentration map in Fig. 5.52, although it is not easy to distinguish the equiaxed grains, one can see that the structure at the A-segregate is finer than its vicinity, and the structure here is more porous.

It has also been found that concentration fields of element at the A-segregate are also not homogeneous. Alloying elements are mainly enriched at the boundaries of grains, and not all the grains at the A-segregate are high concentrated, and some of the grains have the same concentration as the surrounding. This can be further indicated by the concentration map in the transverse cross section of the A-segregates, as given in Fig. 5.53 a). It needs to mention that Fig. 5.52 a) actually shows the intensity of spectrums during EPMA measurement, and quantitative EPMA measurements which quantify the content of alloying element have been performed along a line with the length of 8000 μm, as illustrated in Fig. 5.53 a). The results are shown in Fig. 5.53 b) and c).
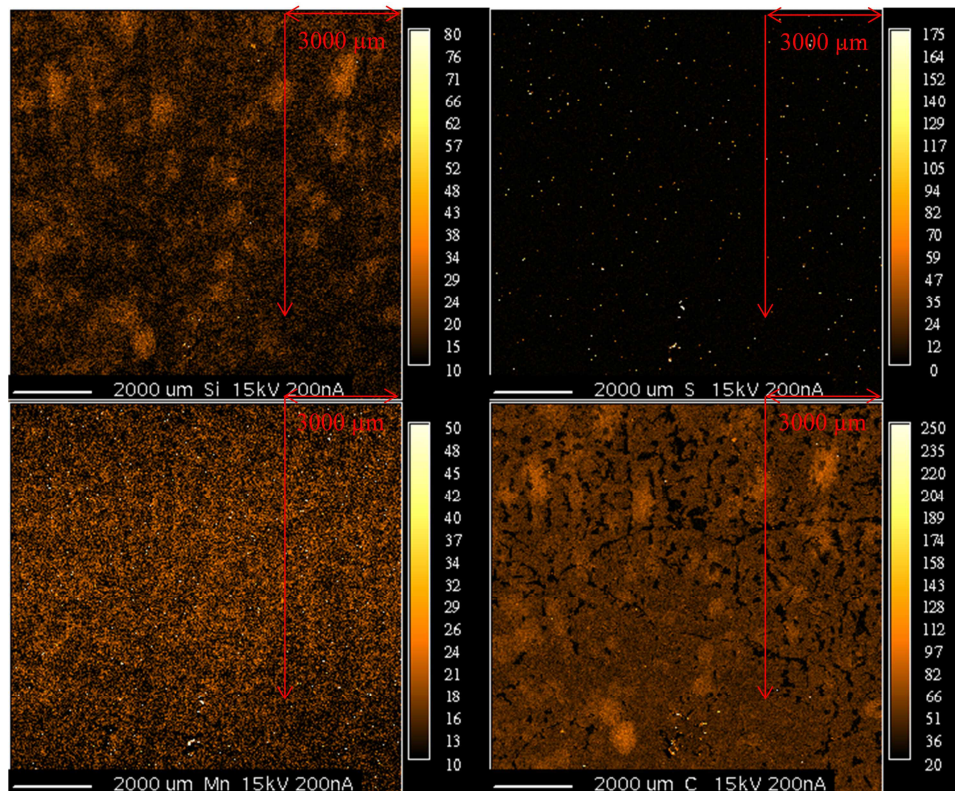
a)
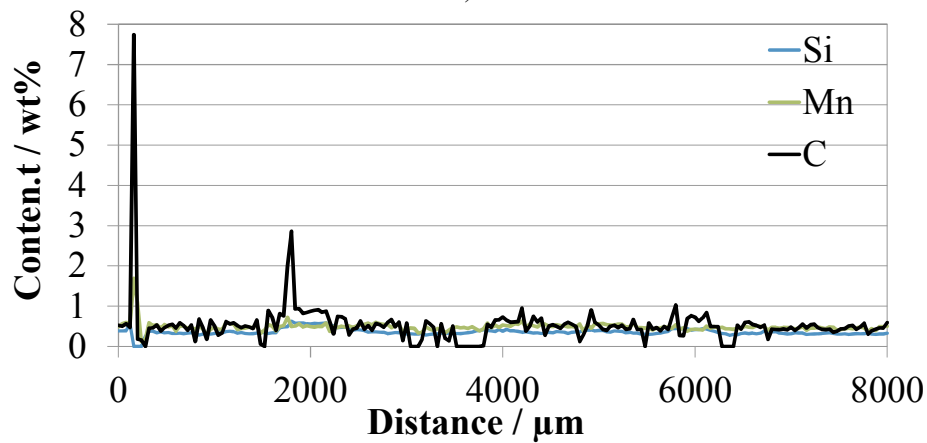
b)

c)

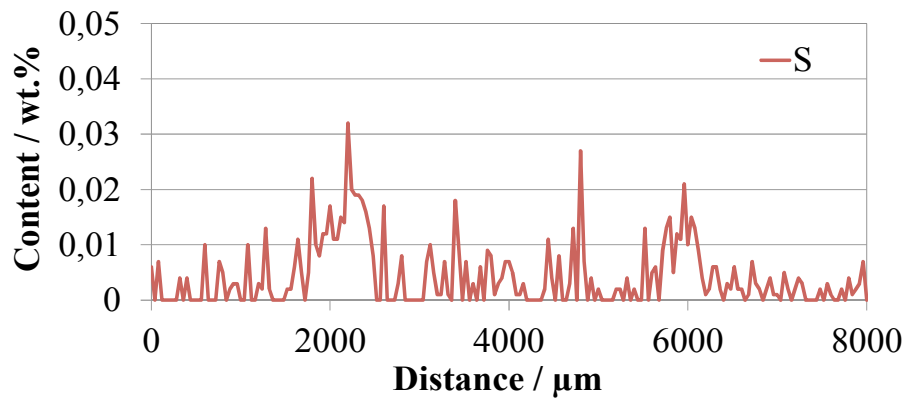*Fig. 5.53: a) Intensity diagrams of EPMA-measurements, in the transverse cross section of A-segregates (Si, S, Mn, C), b) and c) concentration of alloying element along the scanning line*

The maximum concentration and the corresponding segregation index are summarized in Table 5.5. The carbon content at the A-segregate is up to 1.1 wt.% whereas the average carbon concentration is 0.518 wt.%. The other three elements are also found to have highly content at the A-segregates, and the calculated value of $(C_m - \bar{C}) / \bar{C}$ is even higher than the macrosegregation index at the hot spot region.

Element	C	Si	Mn	S
Average concentration $\bar{C}$, %	0.518	0.378	0.538	0.0147
Maximum content C_m, %	1.06 *	0.629	0.718	0.032
$(C_m - \bar{C}) / \bar{C}$	2.04	1.67	1.34	2.17

Table 5.5: Average concentration and maximum content of the alloying elements, B1

*: The two peaks of carbon content 7.74% and 2.86% are ignored, as the both values are not representative for concentration of dissolved carbon in steel.

Different from the concentration map in longitudinal cross section that the A-segregate is observed by a wide light band with the width of ca. 2000 μm, in the transverse cross section several light spots with diameter of around 500 ~ 1000 μm were found. The assembly of two or three light spots forms the A-dot with the diameter of ca. 1.5 ~ 2 mm in the sulfur prints in ingot transverse direction. From the concentration map of carbon it can be seen that these light spots are actually composed of single dendrite arms or part of grain which are highly concentrated. This implies further that the grains at the A-segregates might not form at the same time. Some of the grains form at the early stage of solidification where the melt is not highly enriched, and some form at late stage of solidification and is surrounded by highly concentrated melt. The reason could be that the further growth of the earlier form grains are stopped by the highly concentrated melt flow inside the A-channel, and some of these grains are even remelted or partly remelted. After certain time, by further cooling the A-channel can be closed. Therefore the time window for the A-channel to close completely could be considerable long, and this will be discussed in the next section.

5.3   Discussion

After analyzing the 100 kg ingots and the 500 kg ingots in terms of macrostructure, microstructure, macrosegregation as well as the cooling curves during solidification, microsegregation, sufficient information of solidification structure was obtained which helps us chance to gain insight into the solidification process, and the comparison between the two types of ingot makes it easier for us to find and to understand the difference between solidification in large ingots and small ingots. In this section the different solidification regimes in ingot with small cross section and large cross section are discussed in Section 5.3.1 and 5.3.2, respectively, and furthermore based on analysis of the structure of our 500 kg ingot, the mechanisms of the A-segregates formation have been investigated, which is

presented in Section 5.3.3.

5.3.1   Solidification regimes in ingots with small cross section

If the sulfur prints are compared with the macrosegregation profiles in transverse and longitudinal direction at the same time, it can be found that the as-cast structure of the ingot is mainly composed of the outer columnar zone and the inner equiaxed zone. Marcosegregation happens mainly in the center segregation zone which is a cylinder with a diameter of 20 ~ 30 mm along the center line and in ingot top region directly after the top cavity. From the macrosegregation profiles in the transverse direction of the 100 kg ingot (Fig. 5.23) it can be seen that center segregation zone in ingot top has widen with the diameter up to 70 mm, which is probably due the narrow columnar zone caused by the hot-top condition, and in this wider area all the alloying elements are dramatically enriched. These solidification characteristics are summarized and illustrated schematically in Fig. 5.54.

In the center segregation zone, V-segregation occurs and the concentration along the center line vibrates strongly. Positive macrosegregation appears right at the V-segregates, whereas negative segregation is found at the V-segregation-free area in ingot center between the neighboring V-segregates. Generally the upper portion of the center segregation zone is mainly dominated by positive segregation, and the concentration at ingot bottom and ingot middle is very close to the ingot average concentration. This means that there is no sedimentation zone at the lower part of the ingot, since columnar dendrites grow so fast inwards that there is no time for the equiaxed dendrites to accumulate and form the sedimentation zone.
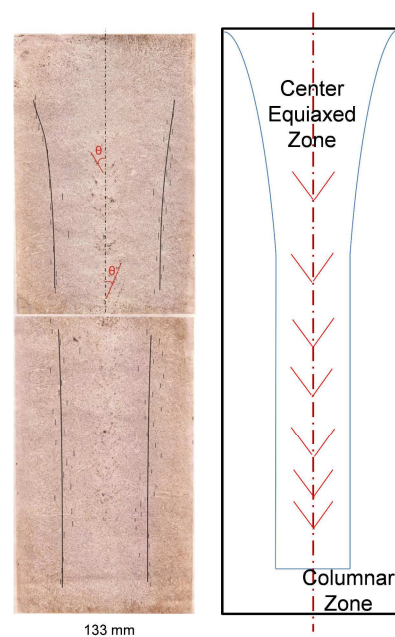

Fig. 5.54: Schematic illustration of the solidification structure of small ingots

The solidification in the small ingots can be divided into two regimes. The first regime is columnar dendritic growth with the growth direction perpendicular to the isotherms from the center towards ingot center. After certain time the columnar dendritic growth is blocked by the equiaxed grains. Some researchers suggested that as long as the fraction of equiaxed dendrites in front of the columnar dendrite tip is over 0.49%, the columnar dendrite is mechanically blocked by the volume of the equiaxed grains, and this is the so-called "hard blocking mechanism" [6]. Some researchers have reported another blocking mechanism namely "soft blocking", which means that due to the highly enriched bulk melt in front of the columnar front, the constitutional undercooling, which is the major driving force for the columnar dendrite to grow, is lost since the concentration difference between the local melt in front of the columnar dendrite tip and the bulk melt is no longer existing [7].

No matter which blocking mechanism works, as long as the columnar-to-equiaxed-transition starts, the second solidification regime begins, which is the equiaxed growth. In this stage, most of the equiaxed grains are fixed by the columnar dendritic bridges and are not able to move away from large distances, such as sinking down to ingot bottom or flushed by the convective melt flow. It can be imagined that at the bottom of the "mini-ingots" in ingot center, some equiaxed grains can sink down on top of the bridges, however, their moving distance are very limited by the long columnar dendrite arms. Similarly, the melt flow is highly influenced by the columnar dendritic bridges in ingot center, and therefore the scale of the thermal-solutal convection is much smaller than in large ingots, e.g. inside the "mini-ingots", and caused macrosegregation (V-lines, centerline in continuous casting) are also limited in the ingot center area around the columnar bridges.

In order to suppress the macrosegregation and the V-lines in the small ingots, the control of the columnar growth is crucial. Fast columnar growth will repeal more solutes into the melt which results in severe macrosegregation in ingot center and forms bridges which lead to the formation of V-lines and mini-ingots. By lowering the casting superheat, the macrosegregation along the ingot center line can be reduced, as indicated by the macrosegregation profiles in Fig. 5 22. There are other ways to suppress columnar growth in order to reduced center macrosegregation, such as mechanical or electromagnetic stirring and inoculation and so on.

Besides macrosegregation, cleanliness is one of the most important quality indices of ingots. For our 100 kg uphill cast ingots, inclusions are mainly found in ingot center at the V-segregates and at ingot top. Some of the inclusions at the V-segregates are formed during solidification and the subsequent cooling due to macrosegregation, since several peaks of the inclusion distribution profiles overlap with the peaks of the macrosegregation profiles of Mn, S and Al (Fig. 5.27 and Fig. 5.28). The inclusions in ingot top are mainly induced by the entrapment of Al-bearing anti-cavity powder. At ingot bottom near the surface number of large inclusions are also found to be higher than in ingot middle (Fig. 5.29),

which might be due to the introduction of exogenous inclusions brought by the melt flow from ladle and runner into the ingot. In order to enhance the cleanliness of small ingots, especially to reduce the amount of large inclusions, a low casting superheat is recommended, since the inclusion formation are closely related with macrosegregation of alloying elements.

5.3.2   Solidification regimes in ingots with large cross section

By combining the sulfur prints and the macrosegregation profiles as well as the SDAS measurements of the 500 kg ingots together, it is able to distinguish different zones of the as-cast structure and to quantify the location and the size of these zones.

For the case with hot top condition and anti-cavity powder, the columnar dendrites grow from sides and bottom, covering a columnar zone width of ca. 50 mm. The columnar zone near ingot top is narrowed by the hot top conditions and at ingot top no columnar dendrites can grow. At the lower portion of the ingot, sedimentation cone of the equiaxed grains are found, which is indicated by the negative segregation of carbon (Fig. 5.48). The height of the sedimentation zone is up to 250 mm in ingot center, and the half width of the sedimentation zone is 120 ~ 130 mm from the ingot height of 120 mm to 220 mm, which means that within this height range, the boundary of the sedimentation cone is at the columnar front. The SDAS-profile at the height of 120 mm along the transverse direction shows that two peaks are found at the half radius of 60 ~ 100 mm (Fig. 5.46), which indicates that the outer sedimentation cone is composed of larger grains than in inner cone.

The SDAS-profile along the transverse direction at the height of the hot spot (Fig. 5.45), shows that at ingot radius of 60 ~110 mm, dendrites have a largest SDAS value of 800 μm, and in hot spot region the SDAS value is the lowest, at about 400 μm, whereas in the columnar zone the SDAS is around 600 μm. As referred in Section 5.2.2.2, the equiaxed zone can be divided into "outer equiaxed zone" and "inner equiaxed zone" because the SDAS values are very different in these zones.

Based on the SDAS analysis, the location of the outer equiaxed zone and the inner equiaxed zone can be outlined. Combined with other solidification characteristics such as A-segregation zone and top cavity as well as columnar zone, Fig. 5.55 shows the as-cast structure of the large ingots in a schematic way.

The whole ingot consists of columnar zone, CET zone, outer and inner equiaxed zone in the upper portion and sedimentation cone of the equiaxed grains in the lower portion of the ingot. From outside to inside, the columnar zone, the outer equiaxed zone and the inner equiaxed zone covers one third of the radius respectively. The sedimentation zone is up to half height of the ingot, and the boundary of the sedimentation cone is at the columnar front. However, since the outer layer of the sedimentation

zone has a larger averaged SDAS value at the ingot height of 120 mm, it is possible to surmise that the outer equiaxed zone overlaps somehow with the sedimentation cone at the lower part of the ingot. In Fig. 5.55 the sedimentation zone is shown as a cone with a peak in the center. However, the contour of the sedimentation zone in the center plane can also be a cone with 2 peaks at or with flat top, which is depending on the nuclei density and the melt flow. The shape of the sedimentation cone will be further discussed in combination with the water-modelling experiments as well as the simulation results in Chapter 8. The A-lines mainly appear in the CET zone and the equiaxed zone, as the permeability for melt flow is the highest due to the relatively disordered dendritic structure and large SDAS value. The mechanism of the A-segregation will be discussed in the next section.
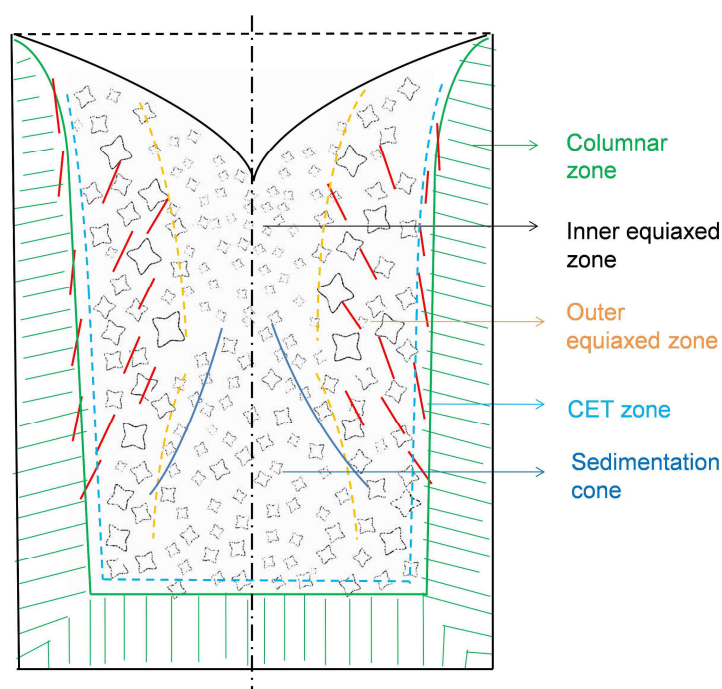
Fig. 5.55: Schematic illustration of the solidification structure of large ingots

As discussed in Section 5.2.2.2 already, the reason of the different SDAS lies in different driving force of dendritic growth. Fig. 5.56 illustrated the driving force of solidification from ingot surface to ingot center with regard to the thermal and constitutional undercooling schematically. Here the undercooling due to the surface energy which is related to the radius of the dendrite tip is not taken into account.

In the columnar zone the dendrite growth are mainly driven by the intensive heat transfer from the wall, i.e. thermal undercooling, and this thermal undercooling temperature decreases from ingot surface to center, as Fig. 5.56 a) shows. Meanwhile as solidification proceeds towards the center, the melt is enriched with more alloying elements, and the segregation in front of the dendrite tip is higher, which leads to a higher constitutional undercooling, especially in the center (Fig. 5.56 b)). In the hot spot area the dendrites growth are mainly driven by the constitutional undercooling caused by the macrosegregation there. The constitutional undercooling in hot spot is possibly even larger than the

thermal undercooling in columnar zone, and therefore the dendrites in hot spot area grow fast than the columnar dendrites, leading to a smallest SDAS value. Although the low SDAS in hot spot could be also influenced by the grain density, but the fact that SDAS is lower in hot spot than in sedimentation cone indicate the impact of large constitutional undercooling on grain size. In the outer equiaxed zone since the thermal undercooling is not as intensive as near the ingot surface, and the constitutional undercooling is also low due to low macrosegregation, the total undercooling is the lowest (Fig. 5.56 c)), therefore the grains grow so fast that the SDAS value is the largest in this zone. The undercooling in the sedimentation cone is similar to that in the outer equiaxed zone, but since the thermal undercooling in the center of the cone is even lower, and the nuclei density is relatively larger than in the equiaxed zone, the SDAS value in the center of the sedimentation cone is slightly lower than in the outer part.
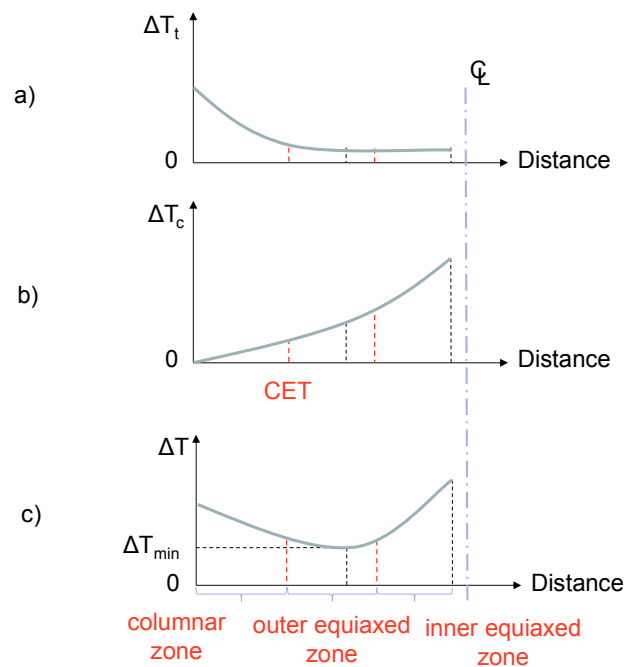
Fig. 5.56: Schematic illustration of the driving force ΔT along the transverse direction of large ingots

As a short summary, the solidification of large ingots has mainly three regimes: columnar dendrite growth controlled by the thermal undercooling (Regime I), outer equiaxed dendrite growth with lowest total undercooling (Regime II) and the inner equiaxed dendritic growth driven by the constitutional undercooling (Regime III). Solidification in the sedimentation zone of the equiaxed grains also belongs to Regime II.

Considering the ingot quality problems in terms of macrosegregation, it is essential to control the outer equiaxed zone so that the development of A-segregates can be limited, since most of the A-segregates are found in the outer equiaxed zone. One possibility is to increase the thermal undercooling during Regime II, for instance to cool down the mould with water spay after a certain solidification time, or to

fill the air gap between the mould surface and the inner surface with fluids with high thermal conductivity or gases which takes the heat of ingot surface away by convection. By increasing the cooling rate during the period of Regime II, the solidification time in this regime is decreased, SDAS will be decreased, and the space and time window of the A-segregates formation is also reduced. Another possibility is to decrease the segregation of alloying elements or to limit the buoyancy flow induced by macrosegregation. If the alloying elements that are very likely to segregate such as carbon, aluminum and chromium with elements are substituted with a lower segregation tendency such as manganese and titanium, or if heavier alloying elements like nickel are added to diminish the density difference between the segregated melt and the bulk melt, the convective flow that is driven by solutal buoyance force will be suppressed. The third possibility is to introduce numerous nuclei by mechanical/EMS stirring or by inoculation, so that the dendrite arm spacing of the equiaxed dendrites will be dramatically decreased due to the high grain density, and therefore the permeability for the melt flow in the outer equiaxed zone is much lower, and A-segregates will be suppressed with regard to length and width of the A-lines. This approach will lead to a shorter columnar zone due to the blocking of the columnar dendrites by the numerous equiaxed grains, and therefore the A-segregation zone is shifted to the outer part of the ingot. For ingots which are cast for hollow products with ingot inner part cut off, the location of the A-segregation zone must be paid special attention that the A-segregation zone should not be at the inner surface of the hollow products.

As for the quality problem with regard to macrosegregation especially the positive macrosegregation at ingot top, it is important to control the segregation index of alloying elements and to limit thermal-solutal convection. One measurement is to use stirring or inoculation to produce as many equiaxed grains as possible, to enlarge the sedimentation zone of the equiaxed grains. Although on one hand the sedimentation zone itself is a negative segregation zone which is low of alloying elements, the grain structure and mechanical properties are more homogenous than in the center segregation zone (the inner equiaxed zone). As a compromise to reduce the area of the center segregation zone, the sedimentation zone of equiaxed grains is enlarged. Another measurement is similar as the approach to suppress A-segregation, which is to use alloying elements which have low segregation tendency instead of elements which are very likely to segregation, and to balance the melt density by using heavy elements in order to decrease the solutal buoyancy that induces the convective flow in the whole ingot.

5.3.3   Mechanism of A-segregation formation

The discussion on mechanism of A-segregation formation addresses two key issues: when do the A-segregates form and where does the segregated melt come from?

Back to the fact that A-segregation zone can be divided into the inner region where the A-lines are

more inclined with the angle of 10° ~ 15° to gravity and the outer region where the A-lines are vertical to gravity with the angle of 5° ~ 10° especially in the upper part of the ingot, it is assumed that there are two types of A-segregates, i.e. two mechanisms of A-segregation at different location of the ingot.

The first type A-segregates are found in the outer A-segregation region at the CET zone, which is 20 mm in front of the columnar zone. Here the A-segregates form among the columnar dendrite tips and equiaxed grains which block the columnar growth. The segregated melt comes originally from the columnar zone between the columnar dendrite roots. A clear proof is in Fig. 5.38 that the half way crack is connected with the A-segregate as one line. Since the segregated melt is enriched with light alloying elements, the melt tends to flow upwards due to the solutal buoyancy force. In CET zone the grain structure is more disordered and loose than in the columnar zone, and therefore it is easier for the segregated melt to find its way to go up. It needs to mention that the A-segregates are not necessarily straight, especially in the initial stage. The segregated melt could flow through the potential channels among the dendrite arms and gather together. In this stage the flow direction of the segregated melt is more inclined, close to the angle of the half way cracks. The A-segregates in this stage are too thin to be found in the sulfur prints, or hard to be distinguished with the half way cracks. When the gathered melt flow is strong enough to remelt the dendrite arms by solute diffusion, the channel will be further widened and prolonged further, and the inner surface of the channel will be flushed smoother and the flow will be further accelerated. In this stage, the melt flow is less dependent on the dendrite structure and can flow more vertical upwards. Therefore the A-segregates in the outer A-segregation region are relatively thick and inclined with a smaller angle of 5° ~ 10° (see Fig. 5.36 and 5.37).

Among the columnar dendrites A-segregates can also develop, as long as the segregated melt can overcomes the flow resistance and gather together to open and widen the potential A-channels. Apparently in this case the possibility of A-segregates is lower than in CET zone. Only when the solidification time for the columnar zone is long enough and the melt is intensively segregation, A-segregates can be formed in the columnar zone. This can be indicated by the high amount of A-dots in columnar zone in the sulfur prints at ingot top at 410 mm high (Fig. 5.42). The ingot top is surrounded by isolation hot top plates and therefore the solidification time for the columnar dendrites is much longer than lower than the hot top plates.

The other type A-segregates are found in the inner part of the ingot which is at the outer equiaxed zone and with a more inclined angle of 10° ~ 15°. In the lower part of the ingot these A-segregates appear more close to the columnar zone, and in the upper part of the ingot they are more close to ingot center, which is far from the columnar front, and the inclined angles of these A-segregates are very similar no matter at lower part or upper part. Based on this, it is considered that these type of A-segregates do not origin from the half way cracks, and their formation are more related to the sedimentation cone of the

euiqaxed grains. The first mechanism of this type A-segregates happens when equiaxed dendrites sink down to the cone, and as the equiaxed dendrites accumulated, the pressure in the sedimentation cone is higher, and the initial interdendritic melt will be pushed out from the sedimentation zone. This causes the negative segregation in the sedimentation zone. The pushed segregated melt are gathered at the boundary of the sedimentation cone, and here there are enough interspace among the equiaxed dendrite is for the melt to flow through, to gather and to further open the potential channels. The second mechanism of this type of A-segregates happens when the sedimentation cone of equiaxed grains shrink, the induced solidification vacuum will suck the solute enriched melt to the gap between the sedimentation cone and its surrounding.

As the sedimentation cone grows upwards and inwards further, the boundary of the cone moves upwards and inwards, and so do the A-segregates. Therefore this type A-segregates are found from ingot bottom to top, in lower part at outer radius and in upper part at the inner radius of the ingot. Meanwhile, during sedimentation, the static pressure in the cone increases and thereby presses more segregated melt out of the sedimentation cone, which allows more A-segregates to form along the boundary between the sedimentation cone and the outer equiaxed grains. The A-segregates will form not only at the sedimentation cone boundary, but also over the sedimentation cone in the outer equiaxed zone. Since the melt tends to flow upwards, and the outer equiaxed zone has the largest SDAS, and hence a high permeability, therefore with the segregated melt coming from the sedimentation cone, A-segregates form also in the outer equiaxed zone at ingot top.

Since the A-segregates form along the boundary of the sedimentation cone, the flow direction of the segregated melt is strongly influenced by the shape of the sedimentation cone. The A-lines are found more inclined with the angle of 10° ~ 15°, close to the contour of the sedimentation cone.

6 Cold models

6.1 Experiments

The ammonium chloride (NH_4Cl) is a crystalline inorganic compound and soluble in water. Under standard ambient temperature and pressure (SATP) of 25°C and 1 bar the solubility of ammonium chloride lies at 392 g/l (Fig. 6.1). Cooling down the hot saturated solution will result in oversaturation of NH_4Cl solution, which leads to crystallization of the NH_4Cl solution as a phase transition from liquid to solid state. Since the crystallization of NH_4Cl solution is very similar to the solidification of metals with regard to columnar and equiaxed dendritic growth, columnar to equiaxed transition as well as sedimentation of grains, water-modelling using NH_4Cl solution can be used to simulate metal solidification. It offers not only the insight view of the complex solidification phenomena, but also provides data for the validation of numerical simulation of the solidification process.
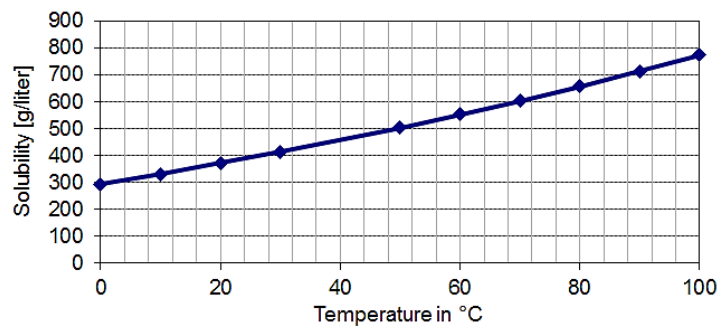
Fig. 6.1: Solubility diagram of ammonium chloride in water [157-159]

The water modelling experiments were mainly carried out by F. Firsbach [158] in the framework of the present study. Ammonium chloride aqueous solution with different NH_4Cl concentration (36%, 38%, 40%) was heated up to 60-80 ºC, at which the NH_4Cl are completely dissolved, depending on the solubility of NH_4Cl in water (Fig. 6.1). Then the solution was poured into the mould and cooled down there. During "solidification" in the mould, the temperature of the solution and the mould were measured, and the "solidification" process was documented by video camera and analyzed quantitatively further.

6.1.1 Experimental setup

A special square-shaped mould has been built up with glass plates (front and back) for a clear insight

and aluminum plates (left and right side) for better thermal conduction as well as a Plexiglas plate (bottom) for thermal isolation, as illustrated in Fig. 6.2. The inner dimension of the water model is 130 mm width (L) x 210 mm height x 18 mm depth. The water model can be cooled down or heated up from both sides at the aluminum plates.
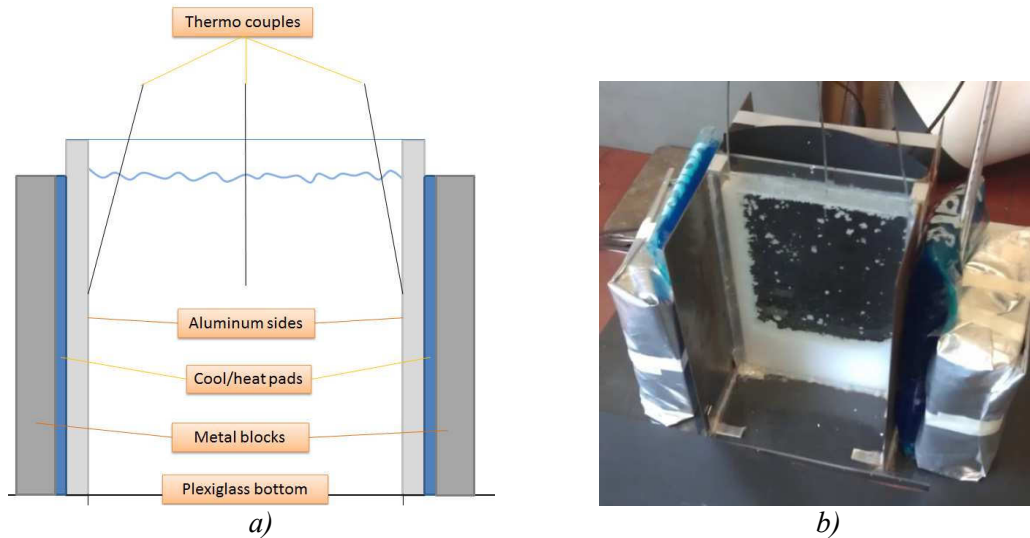

Fig. 6.2: a) Schematic illustration of the water model, b) square mould with thermocouples and cooling/heating pads integrated

As indicated in Fig. 6.2 b), the heating and cooling of the mould is realized by using cooling/heating pads on both sides. In order to ensure that the cooling pads are always in good contact with the aluminum plates, two steel blocks wrapped with isolation materials are used to support the cooling/heating pads. The inner surface of the aluminum plates has been carefully prepared by grinding with sand paper with the grit size R of 80, which corresponds to the surface roughness of around 190 μm.

To record the progress of "solidification" process of the NH_4Cl solution as a movie, an Canon XL2 video camera has been used. A high resolution was needed to increase accuracy of the dendrite measurement. The video data provide direct information for further quantification of the "solidification process" in terms of the growth rate of the columned dendrites, the sedimentation of the equiaxed grains and the sinking rate of the equiaxed grains as well as flow field of the solution. In order to enhance the contrast of the dendrites and the background, a sheet of black paper was placed behind and below the mould, as shown in Fig. 6.2 b).

In the present study this thin square mould has been utilized as a quasi-2D mould in order to gain insight into the crystallization process of the solution, and here it was important that crystallization happens only from both sides into the center and does not occur at the glass plates. The room temperature in the laboratory lies around 22°C to 25°C, which could leads to slight precipitation at the

glass sides, but since the cooling at the aluminum plates are so intensive that most of the dendrites and grains are formed at aluminum sides and growing towards mould center, and very few crystals are formed at the glass plates.
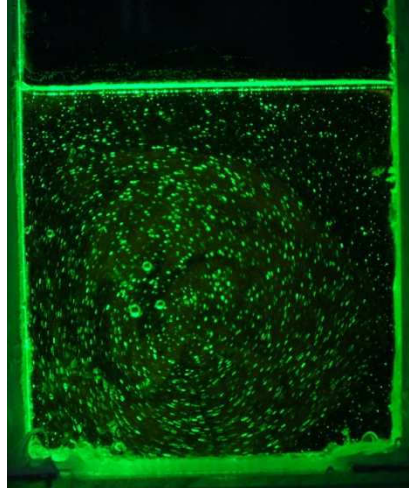

Fig. 6.3: Water-modelling using laser, fluid flow indicated by NH₄Cl particles and gas bubbles (view from side, illuminated by laser, exposure time 0.25 s)

Furthermore, water-modelling experiments combined with laser illumination have been conducted for a better contrast (shown in Fig. 6.3) and as a first attempt to quantify the flow field quantification by using e.g. particle image velocimetry (PIV) technique and concentration and temperature field analysis using laser induced fluorescence (LIF) method. Since the experimental investigation by using PIV and LIF is out of the scope of this study, the quantitative study of the flow and concentration field as well as temperature field are not performed furthermore. However, water-modelling combined with PIV and LIF techniques acts as a strong tool to investigate the solidification process in a quantitative way and can provide numerous data for the validation of numerical simulation.

6.1.2   Temperature measurement

The temperature of the NH₄Cl solution and the inner surface of the aluminum plates were measured with an YCT Date Logger Thermometer YC-747UD and type T thermocouples at each second during the experiments. The temperature range of type T is -25°C to 100°C and the accuracy is at about ± 1.0°C. As shown in Fig. 6.4, temperature measurements have been applied at three points: in the center of the mould to measure the solutions temperature and on both sides to measure the actual cooling or heating at the aluminum sides.
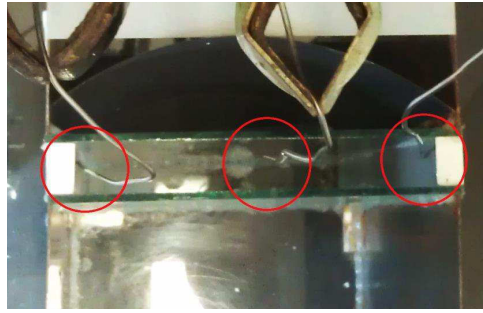
Fig. 6.4: Position of the thermocouples inside the mould (View from above)

The three measuring points are all at the middle height of the mould, as given in <u>Fig. 6.5</u>. Since the thermocouples could influence the precipitation process to a certain extent as they provide actually heterogeneous nucleation sites for NH_4Cl, comparison experiments were carried out with the same parameter and without thermocouples in order to evaluate the influence of the thermocouples, and it turned out that there is no crucial impact of these thermocouples on the crystallization process of the NH_4Cl solution.
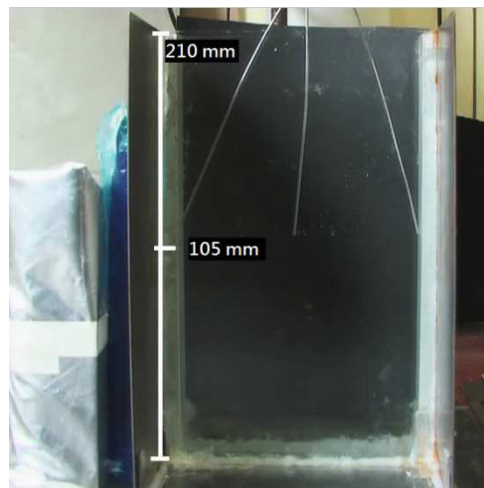
Fig. 6.5: Position of the thermocouples inside the mould (side view)

6.1.3   Parameter variation

Three series of experiments have been performed with various parameters in terms of the initial solution temperature before pouring, cooling and heating conditions as well as top isolation conditions, as summarized in <u>Table 6.1</u>. The concentration of the NH_4Cl stands for the initial concentration of the hot solution, and right before pouring the NH_4Cl solution was adjusted to be saturated, and the solution concentration varies upon the initial solution temperature. The initial temperatures of the solution and the aluminum plates have been measured by thermocouples.

Series No.	Experiment No.	NH4Cl concentration,	Initial temperature of solution	Initial temperature of left wall (inner)	Initial temperature of right wall (inner)	Top isolation
1	V5	36%	63.5°C	cold, 13.7°C	cold, 13.7°C	none
	V6	38%	69°C	cold, 14.2°C	cold, 15.1°C	none
	V7	40%	77°C	cold, 13.9°C	cold, 13.7°C	none
2	V8	36%	58.5°C	cold, 13.8°C	hot, 42.5°C	none
	V9	36%	61.5°C	cold, 15.1°C	hot, 31.3°C	none
	V10	36%	62.2°C	cold, 17.5°C	hot, 47.1°C	none
3	V14	36%	63°C	cold, 15°C	cold, 15°C	isolated

Table 6.1: Experiment parameters of the solidification simulation using NH₄Cl solution

The experiments in series No.1 were carried with both sides cooling to analyze the influence of superheat on "solidification", and in series No.2 experiments were carried out with one side cooling and one side heating in order to simulate the "solidification" of a half ingot. In series No.3 the experiments was conducted with top isolation in order to verify whether cooling from top will bring more nuclei into the crystallization system and therefore changes the "solidification" behavior.

6.2   Columnar dendritic growth

During "solidification" in square mould, it can be clearly observed that columnar dendrites grow from the cooled aluminum sides towards the center, as shown in Fig. 6.6. The width of the columnar dendrites at the middle height of the mould was measured at different time after pouring and the growth rate of the columnar dendrites are then calculated.

The measured width of the columnar zone at different time was then fitted to the square root law, which is usually used in casting processes, as given in Equation 6.1,

$$D = k \sqrt{t}$$
<div align="right">Equation 6.1</div>

where D indicates the width of the solidification shell and t indicates the solidification time.
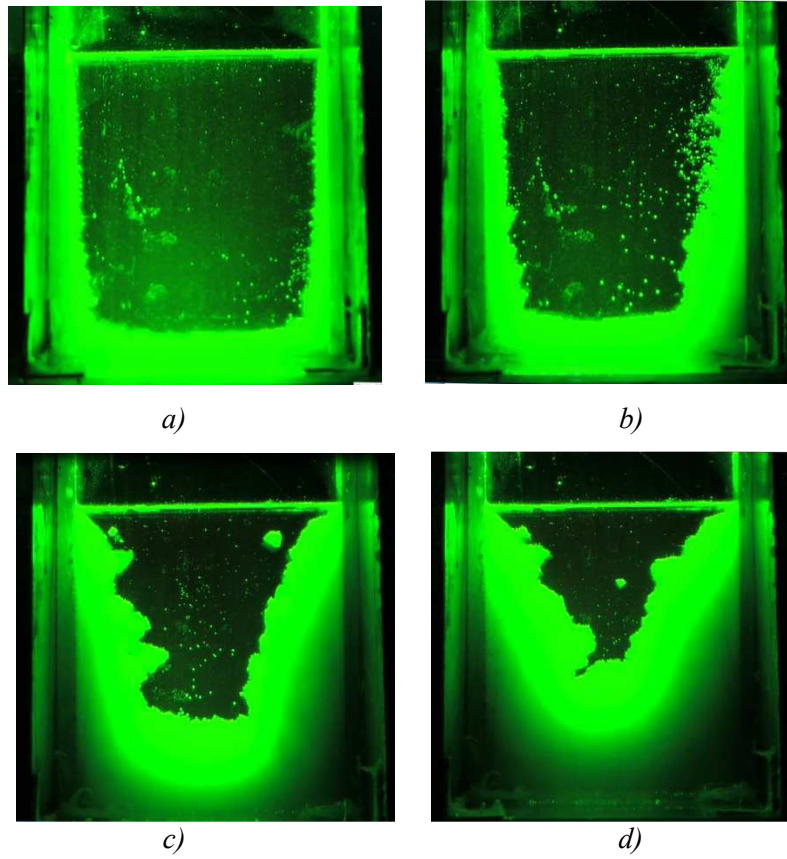
Fig. 6.6: "Solidification" at different time after pouring (laser illuminated), a) 10min, b) 15min, c) 25min, d) 40min

In the present study the solidification constant k is used to describe the growth rate of the columnar dendrites. Fig. 6.7 shows the profile of width of columnar dendrite zone along time in V5 as an example. The width of the columnar zone has been measured at different time after pouring, and the measured curves have been fitted according to the square root law, and the solidification constant was calculated from the fitted curve. The break of the thickness measurement at around 600 s at left side is due to the difficulty of distinguishing the columnar dendrite front from the sedimentation layer of the equiaxed dendrites, in other words, CET happened there and the growth of columnar dendrites was actually stopped. The "solidification rate" at the left side was calculated to be 5.1 mm/min$^{0.5}$, and at the right side is 2.0 mm/min$^{0.5}$. In continuous casting process the value of the solidification constant is over 20 mm/min$^{0.5}$.

It is considered that the growth rate of columnar dendrites in terms of the solidification constant is related with the temperature gradient. Therefore the temperature at mould sides and in mould center were measured and calculated the temperature gradient with simplification of linear thermal gradients as:

$$G_{\text{left}} = \frac{T_{center} - T_{left}}{\frac{1}{2}L}$$ Equation 6.2

$$G_{\text{right}} = \frac{T_{center} - T_{right}}{\frac{1}{2}L}$$

Equation 6.3

where G_{left} is the temperature gradient in the left half of the mould

G_{right} is the temperature gradient in the right half of the mould

T_{center} is the temperature at the center of the mould (solution's temperature)

T_{left} is the temperature at the mould's left side

T_{right} is the temperature at the mould's left side

L is the mould's width
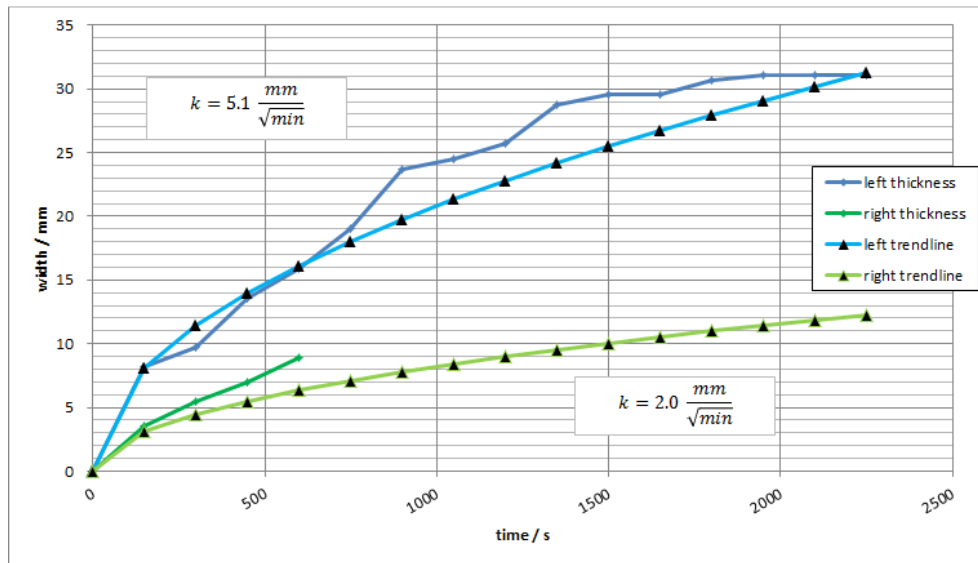
Fig. 6.7: Width of columnar dendrite zone for case with both sides cooling (V5)

Fig. 6.8 shows the calculated linear thermal gradients G at left and right half of the mould and the measured temperature curve at left and right of the mould and in mould centre. Apparently, the temperature gradient at left side is nearly two times large as the one at right side at the beginning stage of solidification, and the columnar growth is encouraged by fast heat extraction with large temperature gradient.
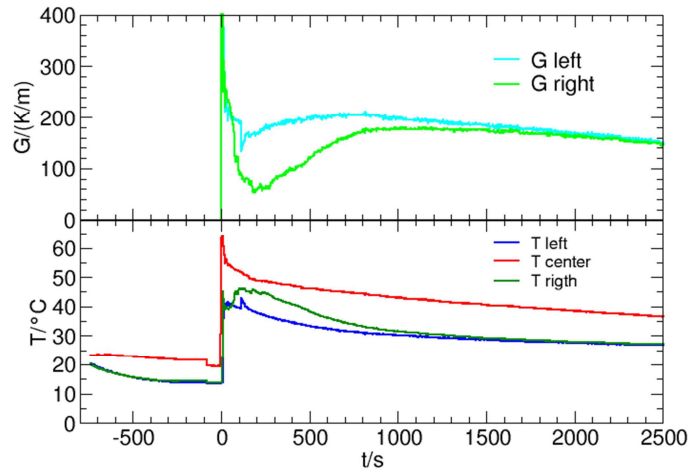
Fig. 6.8: Thermal gradient and temperature curves at left and right sides of the mould during solidification (V5)

For the case with cooling on the left side and heating on the right side, the growth of the columnar dendrites has also been quantified upon time. As illustrated in <u>Fig. 6.9</u>, columnar dendrites grow only from the cold left side with a solidification constant of 5.51 mm/min$^{0.5}$, whereas nearly no dendrites are found on the hot right side from beginning to end of solidification.

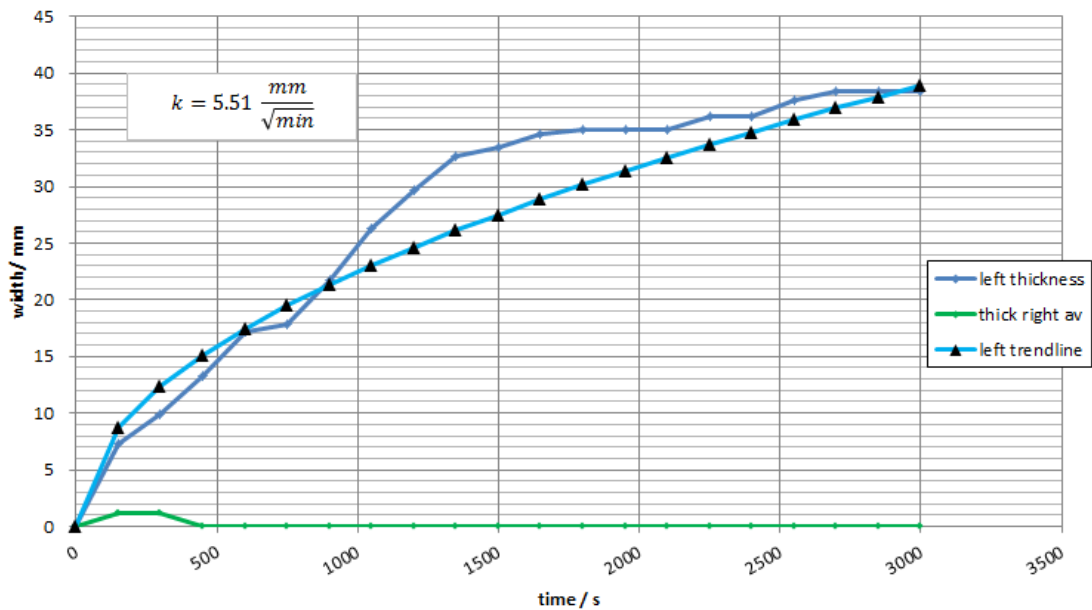*Fig. 6.9: Width of columnar dendrite zone for case with one side heating and one side cooling (V9)*
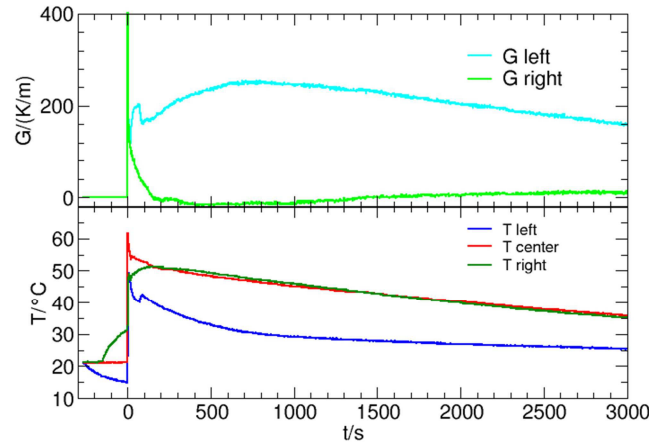
Fig. 6.10: Thermal gradients and temperature curves at left and right sides of the mould during solidification (V9)

The temperature gradient of this case is given in Fig. 6.10, where at the left side the temperature gradient is over 0.2 K/mm, and at the left side keeps at around zero. Due to a slightly higher temperature gradient in experiment V9 than in V5, the solidification constant in V9 is slightly larger than in V5, either.

The correlation between the solidification constant k and the temperature gradient G has been summarized in Fig. 6.11 based on the results from V5 to V10. A linear dependency of k on temperature gradient G has been found.

$$k = a \cdot G + b \hspace{3cm} \text{Equation 6.4}$$

where a, b are constants, and $a = 0.01 \ \frac{mm \cdot m}{\sqrt{min} \cdot K} = 1.29 \cdot 10^{-6} \ \frac{m^2}{\sqrt{s} \cdot K}$. The constant b varies with the initial solution temperature, and with the initial temperature of 60 °C, the value of b is 3.665 mm/min$^{0.5}$, whereas with initial temperature of 70-80 °C, the value is 0.203 mm/min$^{0.5}$. This can be explained by the fact that in the very early stage of solidification, the real temperature gradient near the cold wall is larger than the calculated linear gradient. The higher the initial temperature is, the larger the deviation between the local and calculated temperature gradient is.
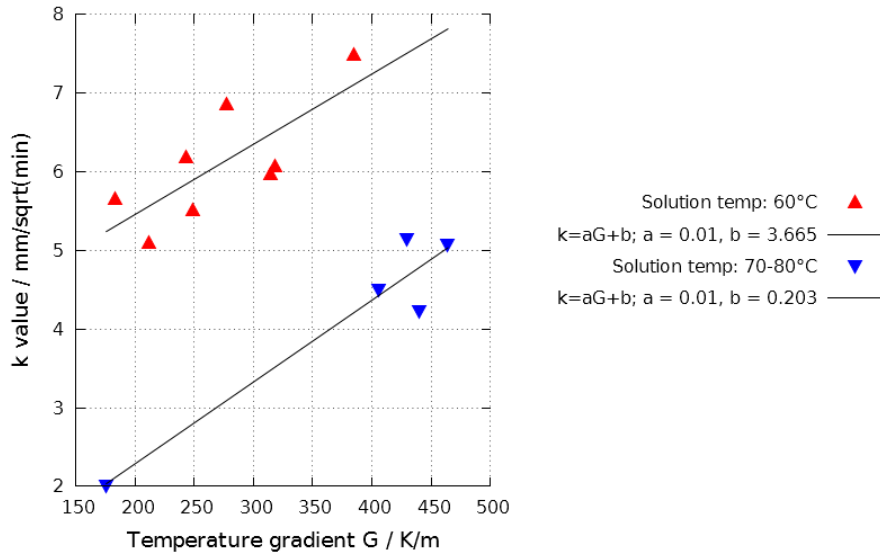
Fig. 6.11: Solidification constant k in relation to temperature gradient of different experiments

6.3   Sedimentation of equiaxed dendrites

It has been observed that during cooling, equiaxed grains are formed and sink down and accumulated at the bottom of the mould. In different stage of the "solidification" process, sedimentation of the equiaxed grains happens at different position in the mould, and the sinking path is not always straight downwards, instead, it is influenced by the liquid flow. The equiaxed grains can be dragged upwards firstly and then sink downwards due to the density difference between the liquid and solid phase. Meanwhile, the grains continue to grow while sinking, and the larger the grains grow, the easier they sink down. In order to investigate the sinking phenomenon, a few grains were traced by video which were sinking, and by recording their positions at different time during sinking, the sinking velocity of the individual equiaxed grains can be then calculated. Fig. 6.12 and Fig. 6.13 show the illustration of measured grain position and the velocity profiles of seven grains at different time of cooling, respectively.

As illustrated in Fig. 6.12, the distance between the individual grain and the water level were measured at different time while sinking, since most of the grains are formed in the vicinity of the water level due to the low temperature there, the initial position is considered to be at the water level. Fig. 6.13 shows the positions of seven grains versus their sinking time at different time after pouring.
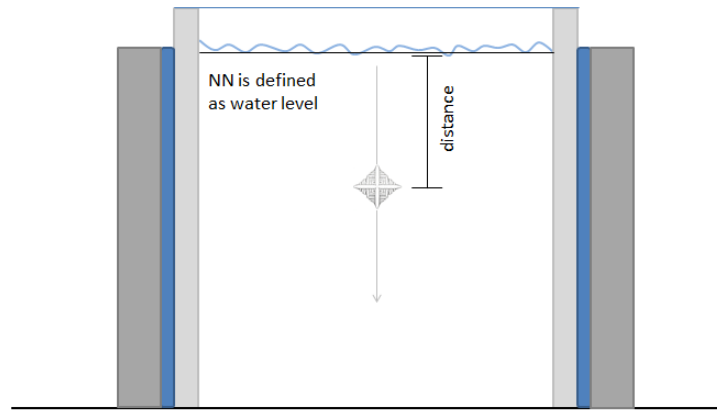
Fig. 6.12: Measurement of dendrite position to NN (water level)
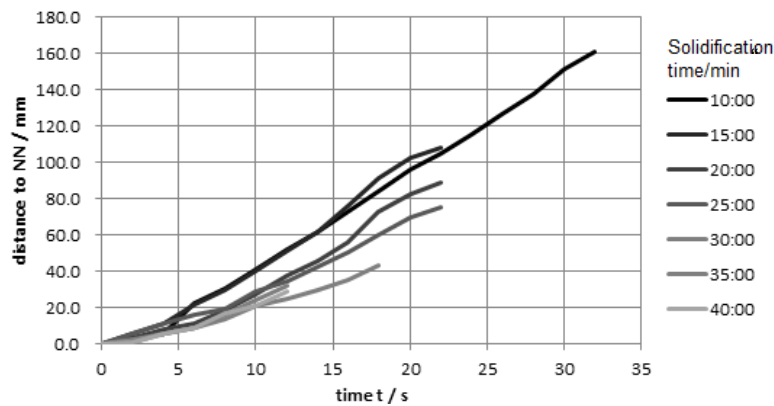
Fig.6.13: Sinking distance of grains vs. time (V9)

It can be found that the sinking velocity slightly increases while sinking, and this is consistent with the results reported by Appolaire [148]. At early stages, the equiaxed dendrite particles are rather small and they sink slowly due to their size. With advanced cooling of the solution, these grains can grow further due to enough undercooling and are denser in comparison with small grains, therefore the density difference is larger and the acceleration downwards is stronger, and the sinking velocity is up to 5 mm/s. At the late stage of the "solidification" (30-40 minutes after pouring) it has been observed that the grains tend to sink more slowly, where the sinking velocity is reduced to 2-3 mm/s. This is due to the influence of the local turbulence at the bottom area of the mould. The short curves for the grains at late stage are due to the fact that height of the sedimentation layer rises as time increases, and the space for the equiaxed grains to sink is thereby limited.

Fig. 6.14 shows the height of the sedimentation layer and the height growth rate versus time for experiment V6 with both sides cooling. The height at the left side, right side and middle position of the mould were measured at different time after pouring.
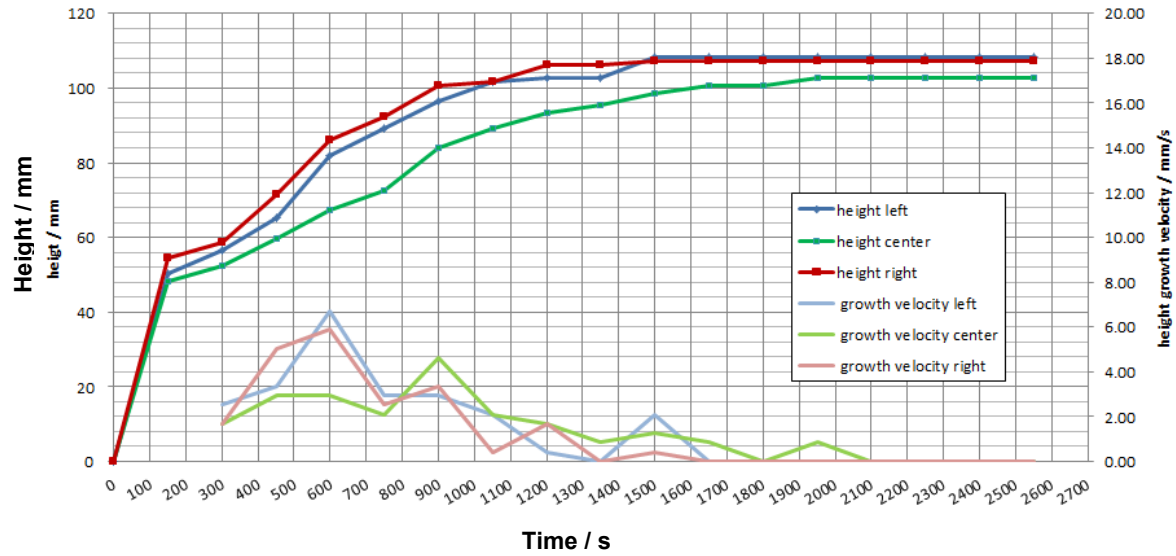
Fig.6.14: Height of the sedimentation layer vs. the growth rate of the sedimentation layer over time (V6)

In the beginning of "solidification", the height of the sedimentation layer increases with a relative fast rate up to 6 mm/s, and it approaches 0 mm/s as "solidification" further proceeds. It can also be found from Fig. 6.14 that the sedimentation layer at both sides are higher than in the middle all over the time, and this can be explained by the higher grain density at the side than in the middle. In the vicinity of the cool mould wall, strong undercooling results in the nucleation of numerous grains, and meanwhile the columnar dendrites which growth from the mould wall are flushes out by the strong natural convection along the cool wall. Both the homogenously and inhomogenously formed grains sink down to the foot of the mould wall and the turbulence flow at the mould corner intensify the grain accumulation. In the middle of the mould, fewer grains nucleate due to the smaller undercooling, and the ascending flow in mould centre caused by natural convection also reduces the sinking velocity, as referred before.

Since the growth rate of the sedimentation layer is greatly influenced by the grain density, it is supposed that the growth of the sedimentation layer might be related with the undercooling temperature which has impact on the nucleation rate. To confirm this hypothesis, the growth rate of the sedimentation layer dH/dt and the temperature difference dT between the local temperature and the initial temperature at which the solution is saturated at both sides and middle of the mould have been measured and calculated, and results are shown in Fig. 6.15.
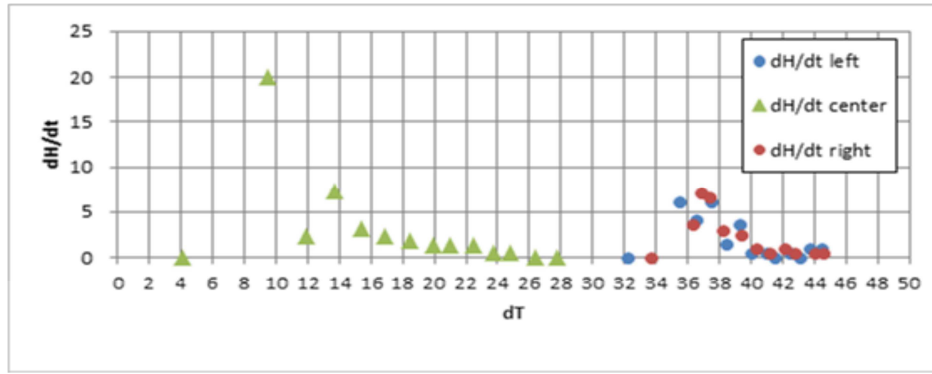
Fig. 6.15: Growth rate of the sedimentation layer over temperature difference for both sides cooling (V7)

$$\dot{N} = \frac{d(\Delta T)}{dt} \cdot \frac{n_{max}}{\sqrt{2\pi} \cdot \Delta T_\sigma} \cdot e^{-\frac{1}{2} \left(\frac{\Delta T - \Delta T_N}{\Delta T_\sigma} \right)^2} \qquad\qquad \text{Equation 6.5 [159]}$$

where $\dot{N}$ is the nucleation rate,

   n_{max} is the maximum grain density,

   ΔT is the undercooling temperature,

   ΔT_N is the undercooling temperature at which the distribution has a maximum,

   ΔT_σ is the Gaussian distribution width.
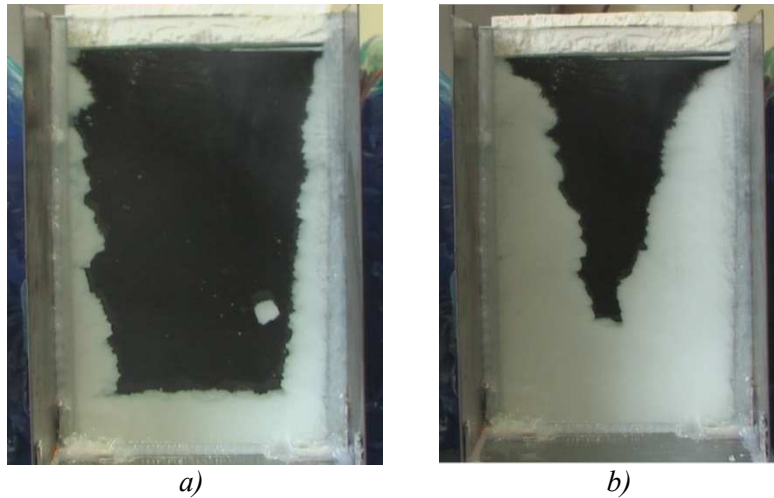
Fig. 6.16: Solidification with isolation a) at middle stage after 31 min, b) at final stage after 61 min (V14)

It has been found that a certain peak of the growth rate of sedimentation layer dH/dt at both sides occurs with dT around 36-40 °C, and the distribution of dH/dt along dT seems to obey a Gaussian distribution. This is in consistence with the heterogeneous nucleation theory suggested by Rappaz [159] that nucleation rate of equiaxed grains depends on the undercooling of the melt, as described in Equation 6.5. In the middle of the mould it seems from Fig. 6.14 that the growth of the sedimentation layer is also controlled by the heterogeneous nucleation since it also obeys a Gaussian distribution, and this might be attributed to the fact the most of the equiaxed grains in the middle are formed near the

water level as it is cooler there. If the top of the mould is isolated with isolation materials, as in experiment V14, less equiaxed grains are formed and the growth rate of the sedimentation layer in the middle of the mould is greatly reduced. The contours of the solidification front in terms of columnar dendrite tip and the sedimentation layer for this experiment are shown in Fig. 6.16 at different time points.

6.4   Fluid flow

Fluid flow is one of the most complex phenomena during solidification and it plays an important role on the quality of final as-cast products. Through conventional methods it is not possible to gain insight into the solidification ingots, and by water modelling, the fluid flow can be represented by the motion of the small particles and is thereby observed and documented. Two types of cooling conditions have been studied, with regards to both sides cooling, and one side cooling and one side heating, and the flow patterns are described schematically with major characteristics, as illustrated in Fig. 6.17 and Fig. 6.18.
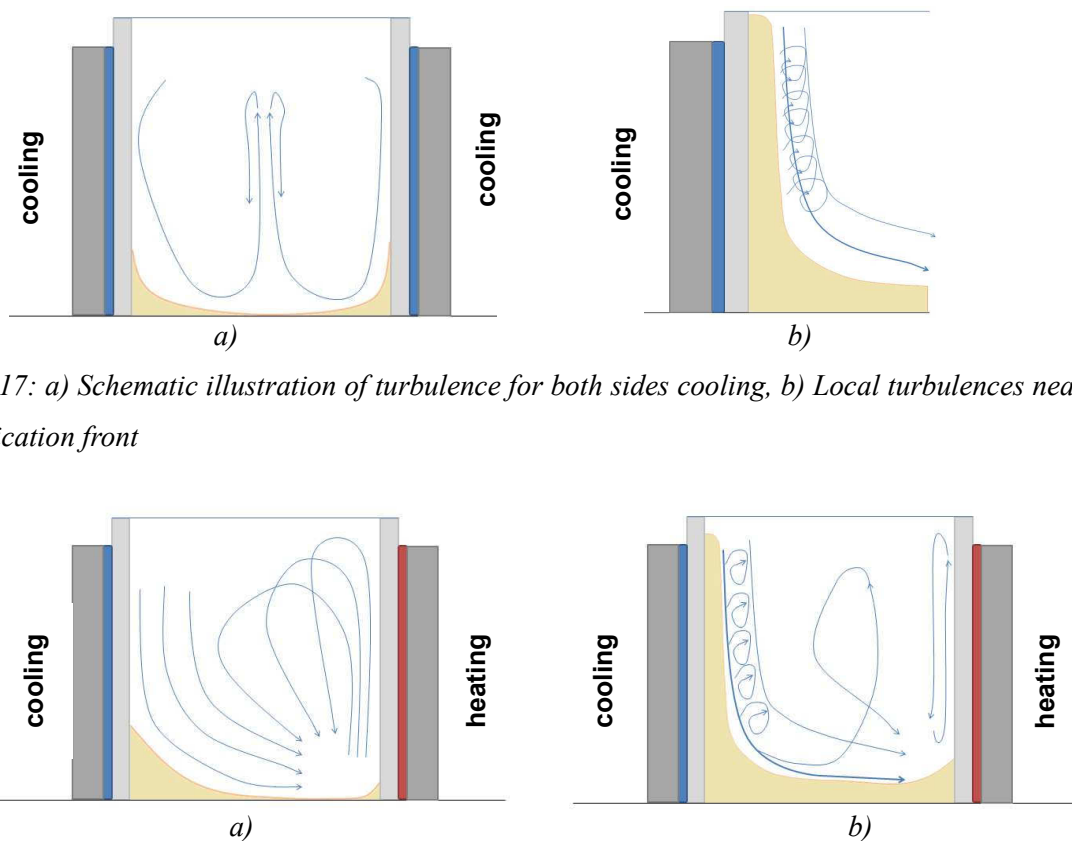
Fig. 6.17: a) Schematic illustration of turbulence for both sides cooling, b) Local turbulences near the solidification front

Fig. 6.18: a) Schematic illustration of turbulence for one side cooling and one side heating in early stage of solidification, b) Local turbulences near the solidification front

For the case of both sides cooling, the flow pattern is nearly axially symmetric, mainly descending at sides and ascending in the centre, as shown in Fig. 6.17 a), and due to the interfacial drag force, the

motion of the small equiaxed grains shares the similar pattern. In detail, they fall down close to the columnar front and move slightly upwards in the centre of the mould. However, large grains tend to fall down due to their density difference, especially near the cold walls. Close to the columnar dendrite front a local turbulence pattern has been observed, as shown in Fig. 6.17 b). While primarily the grains tends to fall down, a local clockwise spiral turbulence which start from the columnar front with an angle of 20°-40° from gravity brings the grains firstly upwards, and then this local turbulences join the main descending flow stream in front of the solidification front and bring equiaxed grains to the bottom.

For the case with one side cooling and one side heating, the flow pattern seems to be the half of the one for both sides cooling. At early stages the main stream flows downwards near the cool wall and upwards near the hot wall. After a while, a clockwise flow cycle is generated near the hot wall, as shown in Fig. 6.18 b). Meanwhile the simply downwards stream near the cold surface is replaced by the complex local turbulence in front of the columnar dendrite front. Both the flow patterns in Fig. 6.17 and Fig. 6.18 have the local spiral turbulence near the solidification front in common, which occurs only in the middle and later stage of solidification. It can be surmised that the formation of the local turbulence near the solidification front is actually related with the columnar dendritic structure, since in the beginning the cold surface is plain and smooth, and after a certain period of time dendrite tips extend into the solution and the columnar front is then composed of numerous dendrite tips which appears periodically, and this might lead to the spiral turbulence.

6.5   Channels

In the water modelling experiments channels have been observed at the cool side of the mould. Depending on the location, the observed channels are divided into two types.

The first types of channels locate at the transition zone between the columnar dendrite tips and the sedimentation bed of free crystals. Fig. 6.19 shows the evolution of this type of channel for a case with cooling on the left side and heating on the right side. The channel initiate at the time point when the columnar dendrite tips are blocked by the sedimentation bed. In this transition area, the dendrites are loosely compacted, and no grains can sink down to this area to close the channel up. Instead, the channel prolongates along with the sedimentation bed and finally forms a long and wide channel in the CET zone.

a)   *b)*   *c)*
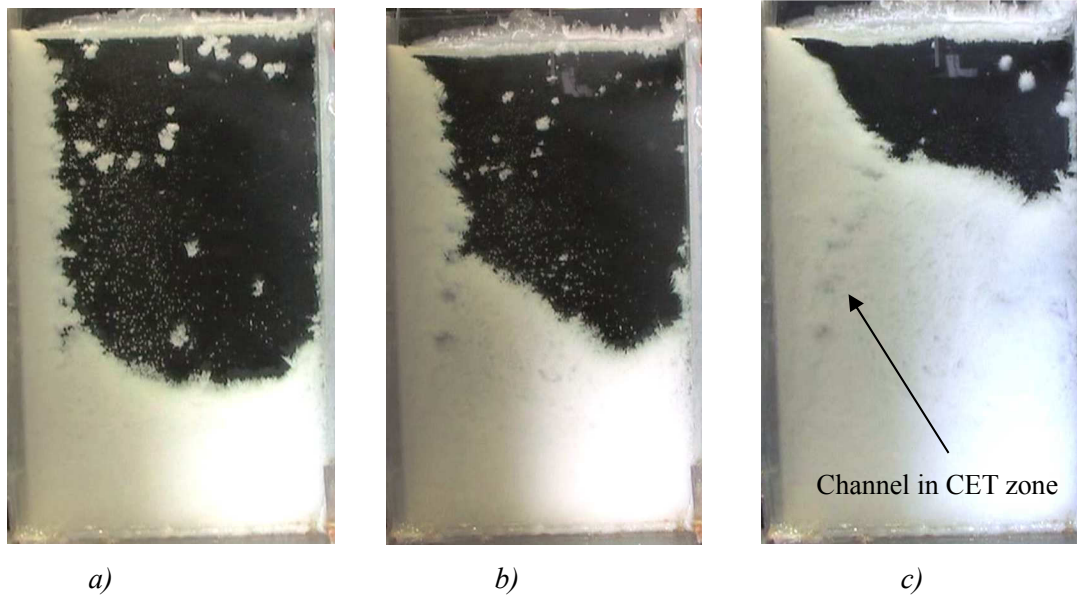
Fig. 6.19: a) Schematic illustration of turbulence for one side cooling and one side heating in early stage of solidification, b) Local turbulences near the solidification front

a)   *b)*
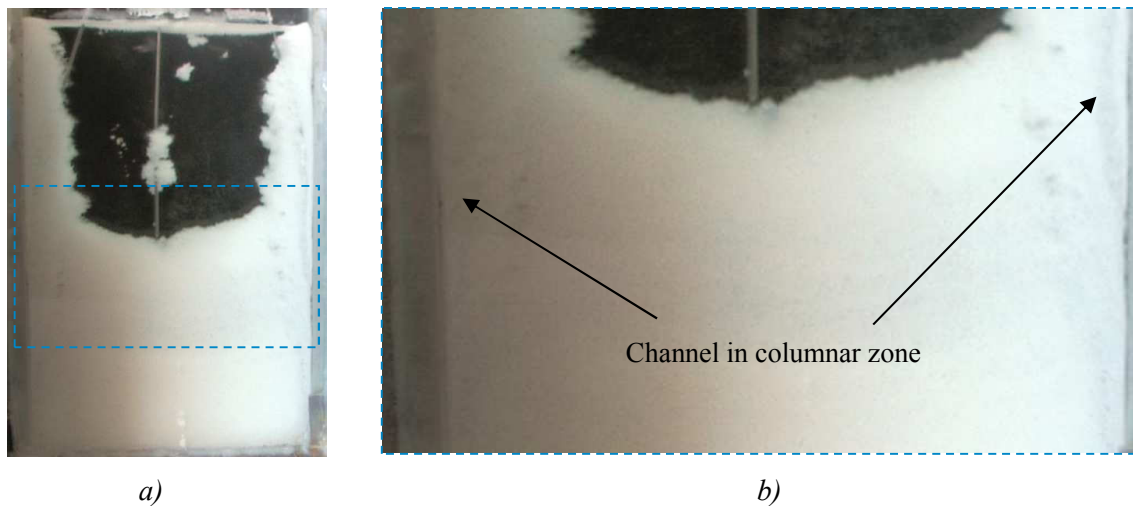
Fig. 6.20: a) Schematic illustration of turbulence for one side cooling and one side heating in early stage of solidification, b) Local turbulences near the solidification front

The second type of channels is much thinner, and they locate in the columnar zone which is more close to the mould wall. <u>Fig. 6.20</u> shows this type of channel in a case with both sides cooling. The black arrows indicate the channels are, and parallel to these channels, the first type of channel can be observed in the CET zone in the same figure. The initiation of the second type of channel is hard to distinguish, and as solidification proceeds, these channels are more clearly to be seen. Different from the first type of channels that only a single thick channel appear in the CET zone, more than one of the second type channels can be found at the same columnar zone. Based on the appearing time and location of the channels, it is speculated that the second type of channels are formed in correlation with remelting in the columnar zone.

6.6   Discussion

It needs to admit that the crystallization of NH_4Cl solution is not identical to metal solidification. Due to the solubility of NH_4Cl in water, not all the NH_4Cl can be crystallized from the solution, therefore the "solidification" of the NH_4Cl solution can never be completed as the solidification of metal. The inner equiaxed zone due to constitutional undercooling cannot be observed. Furthermore, ascribed to the weakness of the NH_4Cl-dendrites, bridging of the columnar dendrites cannot be observed before the dendrite breaks down. Meanwhile, the flushing of the liquid flow could break more dendrites and thereby brings more free crystals in the NH_4Cl water modelling than in the reality. All these bring difficulty in applying the results of cold models. Nevertheless, thanks to the great similarity between NH_4Cl-crystallization and metal solidification in terms of dendritic growth, fluid flow and sedimentation of free crystals as well as channel formation, the cold models provide us the possibility of direct observation of some complex macroscopic phenomena in heavy ingots and continuous cast strands. Furthermore, if the results of cold modelling with regard to temperature field and concentration field are quantified with the help of modern technology such as Particle Image Velocimetry (PIV) and Laser Induced Fluorescence (LIF), as A. Ludwig and co-workers [160, 161] did, the cold models could provide valuable data for the validation of numerical models.

7 Mathematic models

This section is dedicated to the description of a 2-D solidification model, its derivative model (A-segregation model) and its algorithms. The hypotheses for the macrosegregation model and the governing equations for quantities conservation in a representative volume element as well as equations that describe the interfacial solidification phenomena such as nucleation and growth are presented in Section 7.1. In Section 7.2, two different calculation domains and the mesh grids as well as the boundary conditions that are adopted from the geometries and casting conditions of the experimental ingots with weight of 100 kg and 500 kg are described, respectively. The solution algorithm and discretization methods as well as the computation organization for resolution of the governing equations are explicated in Section 7.3. The calculated results of the solidification model for the two types of ingots (100 kg and 500 kg) are presented in Section 7.4 and compared with the experimental results. In Section 7.5, the submodel for A-segregation calculation is explicated and the results of this sbumodel are presented. In Section 7.6 all the simulation results are discussed in detail.

7.1   Macrosegregation model

A volume averaged multiphase solidification model which deals with globular solidification has been developed for a binary Fe-C alloy system. This model is based on the macrosegregation model of Beckermann [67] and the work of A. Ludwig and M.Wu [48, 69] as well as Miha and Combeau [93, 94]. By using the volume averaging method, the solid and liquid phases in a representative elementary volume (REV) are treated separately and the field properties are averaged. In this model, the thermal and solutal buoyancy effect to the fluid flow are considered, the settling of the solid grains is taken into account, and the interfacial drag force in the liquid zone and in the mushy zone for the liquid and solid phases are both accounted. The assumptions of the model and a summary of the governing equations are given below.

7.1.1   Hypotheses

The model treats purely the solidification process in an ingot, and the mould filling process is not included. Therefore in this model the mould is initially full with steel melt that is considered to be stagnant and no solidification has taken place previously, as can be expected with the highly isolated mould. The modelling of fluid flow, heat transfer and solute redistribution as well as interfacial phase transformation in this solidification system is based on the following assumption:

1)   The fluid flow is considered to be laminar, Newtonian, and the dynamic viscosity of the melt is

assumed to be constant.

2) It is assumed that the solidifying system are composed of two phases: liquid phase and equiaxed/globular solid phase. The dendritic grains are simiplified as spherical particles, and the nucleation and growth of the grains are described by the diameter of the spherical particles.

3) The density of the melt and the solid phases are simplified that $\rho_l = \rho_s = \rho$, except for the buoyancy term in the momentum equations, so that the solidification shrinkage and the resulting flow are not considered. For the buoyancy term in equation, Boussinesq assumption is applied:

$$\rho_{lb} = \rho_{ref}[1 - \beta_T(T - T_{ref}) - \beta_C(C - C_{ref})] \tag{7.1}$$

$$\rho_{sb} = \frac{\rho_{ref}}{1 - \beta_{sl}} \tag{7.2}$$

where ρ_{lb} and ρ_{sb} are the liquid and solid densities in the buoyancy terms, β_T and β_T are the thermal and solutal expansion coefficients of the liquid phase, respectively, and β_{sl} is the thermal expansion due to solidification. In the present study, T_{ref} and C_{ref} are calculated as the average value of the temperature and concentration of the liquid phase in the whole calculation domain, respectively.

4) In mushy zone the solid phase is fixed and the interfacial drag force acting on the liquid in the mushy zone is calculated according to Darcy's law, with the permeability calculated by using the Kozeny-Carman equation [162]:

$$K = \frac{f_l^3}{(1 - f_l)^2} \cdot \frac{d^3}{180} \tag{7.3}$$

where f_l is the fraction of liquid, and d is the volume-averaged diameter of the grains. In the liquid zone the interfacial drag of free grains on steel melt is neglected, and the interfacial drag of the liquid phase on the free grains is accounted, so that the free grains can be flushed and move along with the convective flow.

5) The temperature of liquid and solid phases should be nearly the same in each volume element that $T_l = T_s = T$, therefore the heat transfer coefficient between the liquid and solid phases should be approaching to infinite. In the present study heat transfer coefficient is set to be 10^8 W/m^{2}K.

6) It is assumed that solidification or remelting at the solid/liquid interface is driven by constitutional undercooling or superheating, and the thermal undercooling and superheating are neglected since they are much smaller.

7) The interfacial phase transformation rate is determined by diffusion and solute redistribution that

is subjected to thermal equilibrium conditions. In other words, the interfacial concentration of liquid and solid are calculated according to phase diagram that

$$C_s^* = kC_l^* \tag{7.4}$$

where C_s and C_l are the interfacial concentrations for the solid and liquid, respectively, and the superscript * indicates the interfacial value. The average concentration of liquid and solid phase in the REV are calculated in a macroscopic level considering solute convection, diffusion between the neighbor REVs and solute exchange between liquid phase and solid phase due to phase transformation within the individual REV.

7.1.2 Conservation equations

Mass conservation

Considering that the total mass volume within a REV is $V_l + V_s = 1$ (see assumption 3 in section 7.1.1), the mass balance gives:

$$f_l + f_s = 1 \tag{7.6}$$

where f_l and f_l are volume fraction of liquid and solid phases, respectively. With the assumptions referred in Section 7.1.1, the mass conservation equations for liquid and solid phases are given separately:

$$\frac{\partial}{\partial t}(f_l \rho_l) + \nabla \cdot (f_l \rho_l \cdot \overrightarrow{u_l}) = M_{sl} \tag{7.7}$$

$$\frac{\partial}{\partial t}(f_s \rho_s) + \nabla \cdot (f_s \rho_s \cdot \overrightarrow{u_s}) = M_{ls} \tag{7.8}$$

Where $\overrightarrow{u_l}$ and $\overrightarrow{u_s}$ are the velocity of liquid and solid phases, respectively; M_{ls} is the mass transfer rate from liquid to solid, and M_{sl} ($= -M_{ls}$) is from solid to liquid. The unit of M_{ls} is kg/m³/s. A positive M_{ls} value indicates solidification, and other way around, a negative M_{ls} value implies that remelting takes place.

Enthalpy conservation

The enthalpy conservation equations for each phase are given:

$$\frac{\partial}{\partial t}(f_l \rho_l \cdot h_l) + \nabla \cdot (f_l \rho_l \cdot \overrightarrow{u_l} \cdot h_l) = \nabla \cdot (f_l \lambda_l \cdot \nabla \cdot T_l) + Q_{sl} \tag{7.9}$$

$$\frac{\partial}{\partial t}(f_s \rho_s \cdot h_s) + \nabla \cdot (f_s \rho_s \cdot \overrightarrow{u_s} \cdot h_s) = \nabla \cdot (f_s \lambda_s \cdot \nabla \cdot T_s) + Q_{ls} \tag{7.10}$$

where Q_{ls} and Q_{sl} ($Q_{ls} = -Q_{sl}$) are the energy exchange terms between the liquid and solid phase due to phase transformation. The unit of Q_{ls} and Q_{sl} is J/ m³/s. The terms λ_l and λ_s are the thermal conductivities of the liquid and solid phase. h_l and h_s are the enthalpy of the liquid and solid phase, respectively. The unit of h_l and h_s is J/kg. The enthalpy of each phase is calculated as follows:

$$h_l = \int_{T_{ref}}^{T_l} c_{p(l)}\, dT + h_l^{ref} \tag{7.11}$$

$$h_s = \int_{T_{ref}}^{T_s} c_{p(s)}\, dT + h_s^{ref} \tag{7.12}$$

where $c_{p(l)}$ and $c_{p(s)}$ are the specific heat capacities of the liquid and solid phases, and h_l^{ref} and h_s^{ref} are the enthalpies at the reference temperature T_{ref}. In the present study, the reference temperature is 273 K, and h_l^{ref} and h_s^{ref} are calculated by using FactSage to be 3.765×10⁵ J/kg and 1.2×10^5 J/kg, respectively.

It needs to be noticed that the energy exchange at solidification and at remelting are different. During solidification the mass which transfer from liquid to solid is M_{ls}, and the heat $h_l \cdot M_{ls}$ in the liquid phase cannot completely transfer to the new solid phase, since the new solid phase can only accept $h_s \cdot M_{ls}$. Therefore the rest heat $M_{ls} \cdot (h_l - h_s)$, i.e. the latent heat, will be distributed as follows: $f_s \cdot M_{ls} \cdot (h_l - h_s)$ go to the solid phase and $f_l \cdot M_{ls} \cdot (h_l - h_s)$ go to the liquid phase [163]. However, this will cause another problem that since Q_{ls} is not always the same as Q_{sl}, the temperature of the liquid and solid in one representative volume element could be different, and this is against our assumption that $T_l = T_s = T$. The solution in the present study is to use extremely large heat exchange coefficient H^* (e.g. 10^8 Wm⁻²K⁻¹) between the solid and liquid phases. The remelting process is similar, only the liquid phase need to absorb the latent heat of $M_{ls} \cdot (h_l - h_s)$.

$$Q_{ls} = M_{ls} \cdot h_s + f_s \cdot M_{ls} \cdot (h_l - h_s) + H^* \cdot (T_l - T_s) \tag{7.13}$$

$$Q_{sl} = - M_{ls} \cdot h_l + f_l \cdot M_{ls} \cdot (h_l - h_s) + H^* \cdot (T_s - T_l) \tag{7.14}$$

Species conservation

The volume-averaged concentration of liquid phase c_l and the solid phase c_s are solved from the species concentration equations:

$$\frac{\partial}{\partial t} (f_l \rho_l \cdot c_l) + \nabla \cdot (f_l \rho_l \cdot \overrightarrow{u_l} \cdot c_l) = \nabla \cdot (f_l \rho_l D_l \cdot \nabla \cdot c_l) + C_{sl} \tag{7.15}$$

$$\frac{\partial}{\partial t} (f_l \rho_l \cdot c_s) + \nabla \cdot (f_s \rho_s \cdot \overrightarrow{u_s} \cdot c_s) = \nabla \cdot (f_s \rho_s D_s \cdot \nabla \cdot c_s) + C_{ls} \tag{7.16}$$

C_{ls} is the species exchange rate from liquid phase to solid phase and C_{sl} is the species exchange rate from solid phase to liquid phase ($C_{ls} = - C_{sl}$). C_{ls} and C_{sl} has the unit of kg/m³/s. The terms D_l and D_s are the diffusion coefficients of the solute in the liquid and solid phases.

$$C_{ls} = C_s^* \cdot M_{ls} = k \cdot C_l^* \cdot M_{ls} \quad \text{(solidification)} \tag{7.17}$$

$$C_{sl} = C_s \cdot M_{ls} \quad \quad \text{(remelting)} \tag{7.18}$$

During solidification, the solute mass which would transfe from the liquid to the solid per unit volume and time, is $C_l^* \cdot M_{ls}$. However, due to the existence of solute partitioning, the solid phase can only accept $k \cdot C_l^* \cdot M_{ls}$, referring $C_s^* = k \cdot C_l^*$. During melting, the solute mass transferred from the solid to the liquid is $C_s \cdot M_{ls}$ per unit volume and time, and this solute mass can be accepted completely in the

liquid phase.

Momentum conservation

With consideration of the interfacial drag in the mushy zone and the thermal/solutal buoyancy force, the momentum conservation equation for the liquid is formulated in the Navier-Stroke equation:

$$\frac{\partial}{\partial t}(f_l \rho_l \cdot \overrightarrow{u_l}) + \nabla \cdot (f_l \rho_l \cdot \overrightarrow{u_l} \otimes \overrightarrow{u_l}) = -f_l \nabla P + \nabla \cdot (f_l \mu_l \cdot \nabla \cdot \overrightarrow{u_l}) - \frac{f_l^2 \mu}{K} \cdot \overrightarrow{u_l} + f_l(\rho_{lb} - \rho_l) + \overrightarrow{U_{sl}}$$

(7.19)

where $\overrightarrow{u_l}$ is the liquid velocity in vector, $\overrightarrow{U_{sl}}$ and $\overrightarrow{U_{ls}}$ indicate the interfacial momentum transfer across the solid-liquid interface due to phase transformation.

$$\overrightarrow{U_{sl}} = u_l \cdot M_{sl} \quad \text{(for solidification)} \tag{7.20}$$

$$\overrightarrow{U_{sl}} = u_s \cdot M_{sl} \quad \text{(for remelting)} \tag{7.21}$$

Since the influence of momentum transfer due to phase change is small, $\overrightarrow{U_{sl}}$ and $\overrightarrow{U_{ls}}$ are negelected in the present study. The term $-\frac{f_l^2 \mu}{K} \cdot \overrightarrow{u_l}$ indicates the interfacial drag force for the porous flow regime according to the Darcy model. In the present study, if $f_s < 0.6$, this interfacial drag term does not exist; if $f_s \geq 0.6$, the flow is in the porous flow regime and the interfacial drag must be taken into account. The term $f_l(\rho_{lb} - \rho_l)$ refers to the thermal/solutal buoyancy force acting on the local liquid phase in a representative volume element.

The solid phase is considered to be stable in the porous flow regime, where $f_s \geq 0.6$. If $f_s < 0.6$, the solid phase can still move, which is driven by the melt flow and the gravity force. In order to simplify the momentum equation of the solid phase, an explicit equation for the velocity of the solid grains is used [93]:

$$\overrightarrow{u_s} = \overrightarrow{u_l} + \frac{4 \cdot d_e^2 \cdot f_l}{3 \cdot C_d \cdot \mu_l \cdot R_e} \cdot (-\nabla p + \rho_s^b \cdot \vec{g}) \tag{7.22}$$

Where d_e is the volume-averaged diameter of the globular grains, R_e is the Reynolds number. C_d indicates the interfacial drage between the liquid and solid phase, where

$$C_d = \frac{48 \cdot C_{ke} \cdot (1 - f_l)}{R_e} + C_{ie} \tag{7.23}$$

$$R_e = \frac{\rho \cdot f_l \cdot d_e}{\mu_l} \cdot (\overrightarrow{u_l} - \overrightarrow{u_s}) \tag{7.24}$$

$$C_{ke} = \begin{cases} \frac{25}{6} & f_l \leq 0.5 \\ \frac{1}{2} \cdot \left(\frac{f_l^3}{1-f_l}\right) \cdot \left(\frac{1+4.7 \cdot (1-f_l)}{1-1.83 \cdot (1-f_l)}\right) & f_l > 0.5 \end{cases} \tag{7.25}$$

$$C_{ie} = \begin{cases} \frac{7}{3} & f_l \leq 0.5 \\ \frac{24 \cdot (10^E - 1)}{R_e \cdot (1 - 0.9 \cdot (f_l - 0.25)^{\frac{1}{3}} \cdot (1-f_l)^{2/3})^3} & f_l > 0.5 \end{cases} \tag{7.26}$$

$$E = 0.261 \cdot R_e{}^{0.369} - 0.105 \cdot R_e{}^{0.431} - \frac{0.124}{1+(log_{10} \cdot R_e)^2} \tag{7.27}$$

7.1.3   Nucleation and growth

The nucleation is considered as heterogeneous nucleation based on M. Rappaz's theory that the heterogeneous nucleation rate of equiaxed grains obeys a Gaussian distribution of the melt undercooling [159]. As illustrated in Fig. 7.1, when the melt undercooling reaches ΔT_N, the nucleation rate is the maximum.
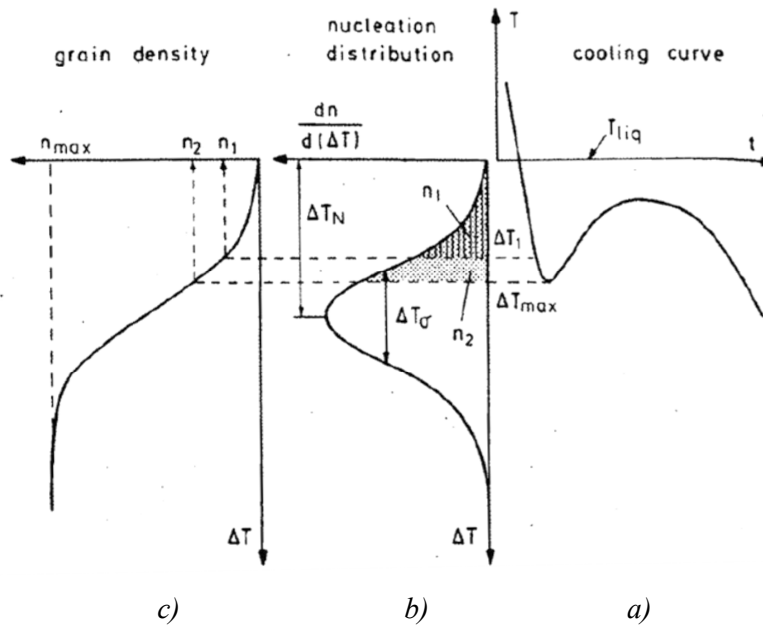

Fig. 7.1: Nucleation model used in the microscopic calculation of equiaxed solidification. At a given undercooling (a), ΔT_1, the density of nuclei, n_1, within the liquid is given by the integral (c) of the distribution [159]

The heterogeneous nucleation rate of equiaxed grains is given in Equation 7.28:

$$N = \frac{dn}{dt} = \frac{dn}{d(\Delta T)} \cdot \frac{d(\Delta T)}{dt} = \frac{d(\Delta T)}{dt} \cdot \frac{n_{max}}{\sqrt{2\pi}} \cdot e^{-\frac{1}{2}(\frac{\Delta T - \Delta T_N}{\Delta T_\sigma})^2} \tag{7.28}$$

where N is the nucleation rate, n is the distribution of nuclei, ΔT is the melt undercooling, n_{max} is the maximum nuclei distribution, ΔT_N is the mean nucleation undercooling, and ΔT_σ is the standard deviation of the Gaussian distribution of nucleation rate. The three parameters (ΔT_N, n_{max}, ΔT_σ) must be determined experimentally [159].

Since it is assumed that interfacial phase transformation is driven by constitutional undercooling or superheating, here the melt undercooling is calculated as the constitutional undercooling.

$$\Delta T = T_f + m \cdot C_l \tag{7.29}$$

where T_f is the melting point of the pure iron, m is the liquidus slope, and C_l is the volume-averaged liquid concentration.

Considering the grains transportation and nucleation, the conservation equation for nucleation is:

$$\frac{\partial n}{\partial t} + \nabla \cdot (\overrightarrow{u_s} \cdot n) = N \tag{7.30}$$

where n is the volume-averaged nuclei distribution.

In order to define the growth of the globular/equiaxed dendrites, grains are considered to be sphere shaped and the grain growth velocity is in the radius direction, which is according to the theory of Kurz and Fisher [88]. At the liquid/solid interface, thermodynamic equilibrium is assumed, the distribution of concentration and temperature of the liquid and solid phases at the interface are shown in Fig. 7.2.
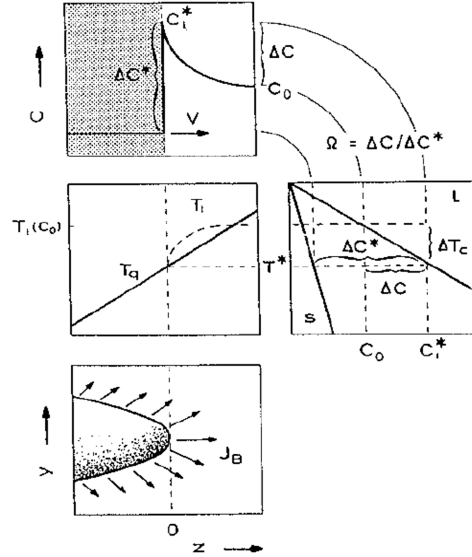
Fig. 7.2: Solute rejection at the tip of the dendrite [88]

The grain growth velocity v_e is given by:

$$v_e = \frac{D_l}{r_e} \cdot \frac{C_l^* - C_l}{C_l^* - C_s^*} = \frac{2 \cdot D_l}{d_e(1-k)} \cdot \left(1 - \frac{C_l}{C_l^*}\right) \tag{7.31}$$

where r_e is the volume-averaged radius of the equiaxed grains, C_l^* and C_s^* are the interfacial concentrations of the liquid and solid phases.

The volume-averaged mass transfer between liquid and solid phase M_{ls} and M_{sl} are defined by considering the total surface area of spherical grains and taking the impingement by an Avrami-factor $(1 - f_s)$ into account, given as:

$$M_{ls} = v_e \cdot (n \cdot 4\pi r_e^2) \cdot \rho_s \cdot (1 - f_s) \tag{7.32}$$

$$M_{sl} = -M_{ls} \tag{7.33}$$

7.2   **Mesh and boundary conditions**

The solidification model is adopted to two types of ingots in the present study, with weight of 100 kg and 500 kg. Since it is assumed that solidification behavior in the ingots is symmetrical along the centerline, half of the ingots have been calculated, i.e. the 2-D calculation domains represent a half ingot, as shown in Fig. 7.3. The geometry and boundary conditions of the calculation domains are given according to the casting experiments as presented in Chapter 5. The top of the ingots are considered to be isolated as anti-cavity powder was used in experiments to reduce the heat loss. The side and bottom of the ingots are considered to have the same heat transfer coefficient, since the width of the columnar zone from ingot side and at the bottom are comparable for both ingots. The taper of the ingots have been ignored in the calculation domains for simple computation. The geometry of the calculation domain for the 100 kg ingot is 70 mm × 560 mm (Fig. 7.3 a)), and for the 500 kg ingot is 180 × 500 mm (Fig. 7.3 b)). For the 100 kg ingot the mesh size is 5 mm × 7.5 mm, and for the 500 kg ingot the mesh size is 9 mm × 12 mm.
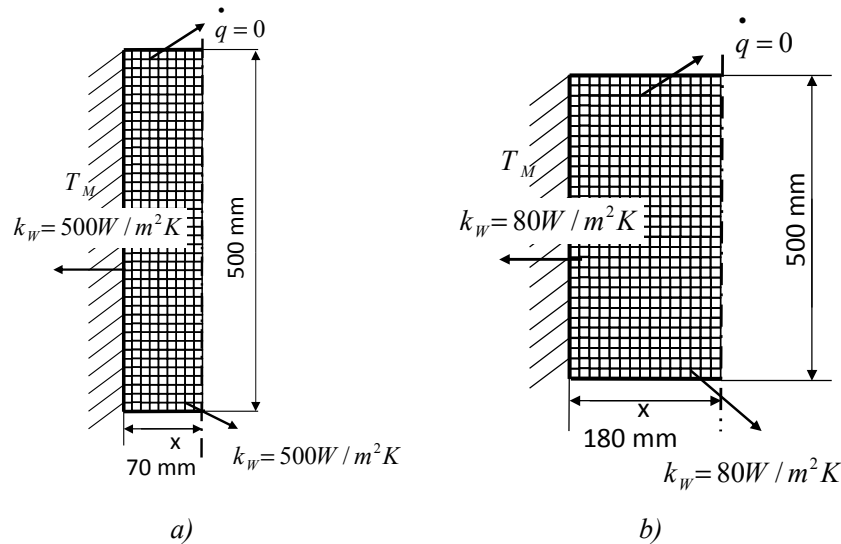

Fig. 7.3: Mesh of the ingots, a) 100 kg fast solidification ingot, b) 500 kg slow solidification ingot

The temperature of the mould inner surface for the simulation is set to be 300 °C for the 100 kg ingot and 500 °C for the 500 kg, which are simplified as a constant from the measured curves of the mould temperature. The heat transfer coefficient from ingot surface to mould is considered to be the same from side and from bottom. For the 100 kg ingot the heat transfer coefficient is 500 W/m^{2}K, and for the 500 kg ingot is 80 W/m^{2}K. The top of the both ingots are considered to be isolated, since hot-top and isolation powder were used in ingot top region to prevent top cavity in the casting experiments.

The steel grade in the numerical simulation in the present study is simplified to be a Fe-C binary alloy with 0.6 wt.% [C], and other parameter and properties used for simulation are summarized in Table 7.1.

Property	Variable	Value	Unit
Initial temperature	T_0	1490	°C
Initial average concentration	C_0	0.6	wt.-%
Liquid average density	ρ_0	6950	kg/m^3
Thermal expansion coefficient	β_T	$2 \cdot 10^{-3}$	K^{-1}
Solutal expansion coefficient of carbon	β_C	$1.1 \cdot 10^{-2}$	wt.-%$^{-1}$
Thermal conductivity of liquid steel	λ_l	33.94	W/(m·K)
Thermal conductivity of solid steel	λ_s	33.94	W/(m·K)
Diffusion coefficient of carbon in liquid	D_l	$2 \cdot 10^{-8}$	m^2/s
Diffusion coefficient of carbon in solid	D_s	$5.6 \cdot 10^{-10}$	m^2/s
Liquid slope of the Fe-C phase diagram	m_l	-80	K/wt.-%
Distribution coefficient of carbon	k	0.2894	1
Dynamic viscosity of liquid steel	μ	$6 \cdot 10^{-4}$	kg/(m·s)
Heat transfer coefficient between the solid and liquid steel in a REV	H^*	$1 \cdot 10^8$	Wm^{-2}K^{-1}

Table 7.1: Thermal physical properties of the binary Fe-C alloy [19,164, 165]

As the solidification of the 100 kg ingot is so fast with the actual complete solidification time of around 10 minutes, the columnar dendrites grow very fast, and nearly no equiaxed grains can settle down to the ingot bottom and form the sedimentation cone. Therefore in our solidification model for the 100 kg ingot, solid phase is considered to be stationary, and the momentum equation for only the liquid phase is solved. For the 500 kg ingot both liquid and solid velocities are calculated in the solidification model.

7.3   Solution algorithm

The governing equations given in Section 7.1 were firstly discretized using Finite Volume Method (FVM), and then solved numerically. The solutaion algorithm and in terms of equation discretization, boundary conditions and resolution strategy are given in this section in detail.

7.3.1   Equation discretization

As all the governing equations in the present study are for transient problems, the variables along the whole time step (dt) and along the whole representative volume element ($dx \cdot dy \cdot 1$) are integrated. The calculation domain in the present study is a 2-D domain, therefore integration have been made along both x and y direction during equation discretization. Nearly all the governing equations contain diffusive term (heat transfer, species transfer) and convective terms (flow). The diffusive terms are discretized using Central Difference Scheme and the convective terms are discretized using the first order upwind scheme.

In order to avoid problems during discretization that normal grid (collocated grid) fails to detect the wave velocity field, "staggered" grid are used in the present study. The staggered grid means that

scalar quantities (mass, enthalpy, concentration, nuclei density) are acting and calculated on the nodes, and vector quantities (velocity u and v) are calculated on the points that lie on the face of the control volumes [166], which is on the nodes of different grids. The collocated grid means that all the scalar and vector quantities are stored and calculated on the nodes of one grid.
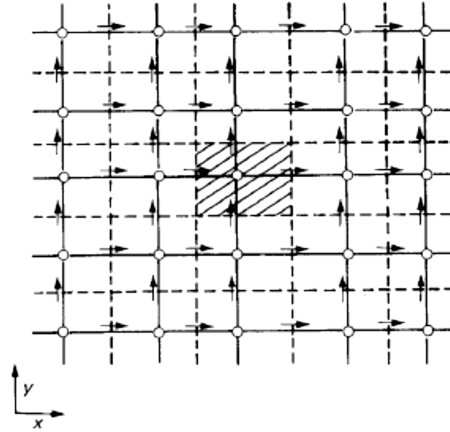

Fig. 7.4: Staggered location for velocity u and v. → *indicate u, and* ↑ *indicate v,* ○ *indicate other scalar quantities [166]*

Fig. 7.4 shows a two dimensional grid pattern. The shadowed area indicates the scalar control volume, and scalar quantities such as pressure, temperature, species concentration and so on are stored and calculated on the nodes of the scalar control volume (scalar node). The location for velocity u in x-direction and v in y-direction are placed on the face of the control volume.

For the two dimensional problem in the present study, three different grids are need, for scarlar quantities, for velocity u and for velocity v. Fig. 7.5 gives the illustration of the control volumes of the three staggered grids for a two dimensional discretization system. It can be seen that the u-control volume is half-step staggered from the scalar control volume in x-direction, whereas the v-control volume is half-step staggered from the scalar control volume in y-direction.

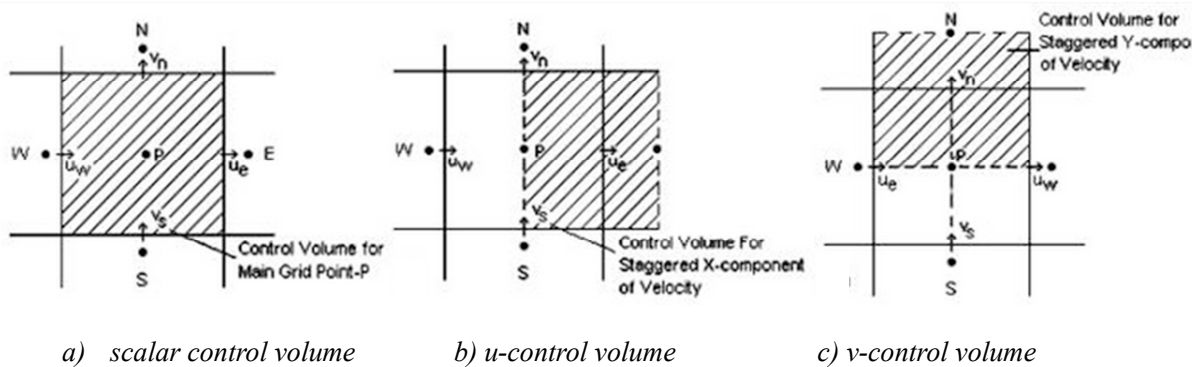a)   scalar control volume   b) u-control volume   c) v-control volume

Fig. 7.5: Control volume for scalar quantities, u and v [168]

7.3.2   Boundaries

Considering the drag and the heat transfer near the mould wall, special conditions have been included as the source term for the momentum equation and energy equation. For the drag force near mould wall, the shear stress τ_u which is acting on the flow in the x-direction by the wall is given [168] as:

$$\tau_u = \mu \cdot \frac{u_P}{\Delta y_p} \tag{7.34}$$

where τ_u is the shear stress acting in the x-direction

   μ is the viscosity of the fluid

   u_P is the fluid velocity u on the u-control node near the wall

   Δy_p is the distance between the u-control node and the wall

The shear force in the x-direction and in the y-direction can be written as follows:

$$F_u = -\tau_u \cdot A_{cell} = -\mu \cdot \frac{u_P}{\Delta y_p} \cdot A_{cell} \tag{7.35}$$

where $A_{cell,u}$ is the area of the u-control volume near the wall.

The source term of the drag force in the momentum equation for velocity u is given:

$$S_u = -\frac{\mu}{\Delta y_p} \cdot A_{cell,u} \tag{7.36}$$

Similarly, for the momentum equation of velocity v the source term of the drag force is:

$$S_v = -\frac{\mu}{\Delta x_p} \cdot A_{cell,v} \tag{7.37}$$

If the temperature of the inner surface of the mould wall is defined to be Tw, the heat flux that transfer from the wall surface to the u-control volume near the wall is calculated as:

$$q_u = -\frac{\mu}{\sigma} \cdot \frac{c_p \cdot (T_{p,u} - T_w)}{\Delta y_p} A_{cell,u} \tag{7.38}$$

where σ is the Prandtl number of the laminar flow,

   c_p is the specific heat capacity,

   $T_{p,u}$ is the temperature of the node of the u-control volume.

The source term of the heat transfer in x-direction in the energy equation is:

$$S_u = -\frac{\mu}{\sigma} \cdot \frac{c_p \cdot (T_{p,u} - T_w)}{\Delta y_p} A_{cell,u} \tag{7.39}$$

For the heat transfer in y-direction, the source term in the energy equation is:

$$S_v = -\frac{\mu}{\sigma} \cdot \frac{c_p \cdot (T_{p,v} - T_w)}{\Delta x_p} A_{cell,v} \tag{7.40}$$

7.3.3   Resolution strategy

After construction of the equation discretization0, the governing equations are numerically solved with

self-programmed code in Matlab. To ensure the mathematic stability of equation solution and to achieve higher accuracy, the fully implicit scheme has been used.

The solution procedure for the governing equations in this study is shown in <u>Fig. 7.6</u>. In every time step Δt, momentum equations and energy equations as well as species equations are calculated at each node. The momentum equations (Equation 7.19 and 7.22) are calculated firstly, and the interfacial phase transformation (Equation 7.32) are calculated secondly. Then the mass conservation equations (Equation 7.7 and 7.8) are solved. If at one node, the fraction of solid is smaller than 0.99, energy equations (Equation 7.9 and 7.10) and species equations (Equation 7.15 and 7.16) will be solved. If the fraction of solid is over 0.99, interfacial phase transformation is stopped at this node, and the source term due to phase transformation in the governing equations will be set to zero.
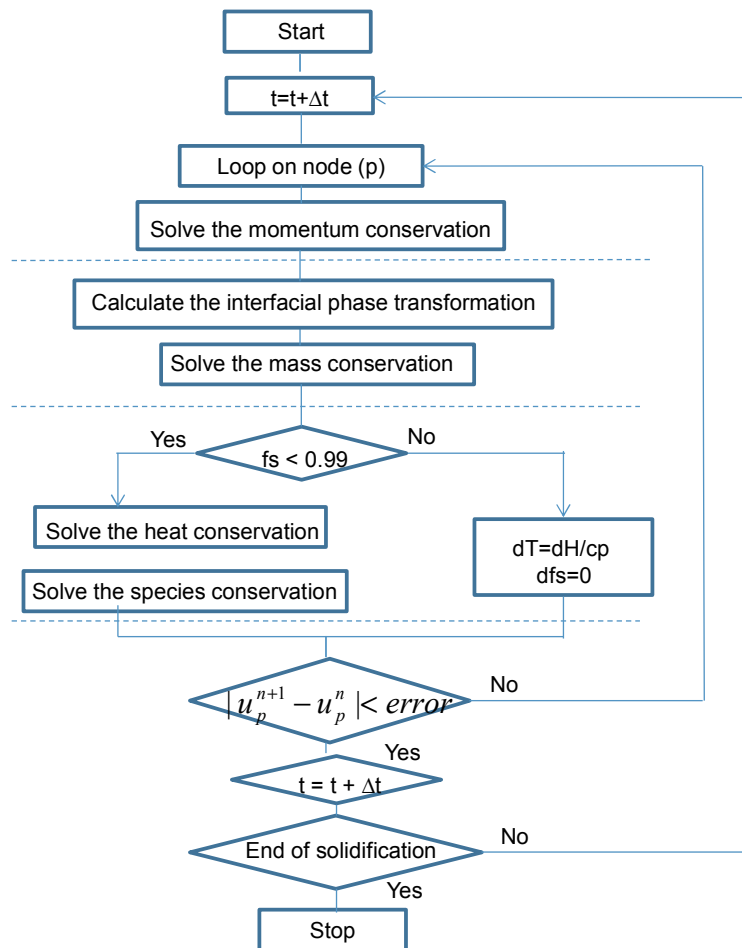
Fig. 7.6: Flow chart of the resolution procedure of the governing equations

After solving all the governing equations in sequence, residual errors are calculated for the momentum and energy conservation. If the calculated residual error is larger than the critical value, iterations are needed inside the loop. The critical residual error for the momentum equation is 10^{-4}, and for the energy equation is 10^{-6}. For each time step, around 20 ~ 40 iterations are necessary to decrease the

normalized residual of the enthalpy and velocity. Depending on the iteration times, the time step used in the present study varies from 0.001 s to 0.005 s.

For solving the algebraic equations (discretized differential equations), Gauss-Seidel point-by-point method has been chosen as the iterative method, which means that the variables are calculated by visiting each node in a certain order. In the present study, the nodes are swept in a line in x-direction from boundary to center, then scanned line by line in y-direction from bottom to top. By sweeping in this manner, the boundary conditions are transmitted at a rate of one grid interval per iteration. For the two-dimensional problem in the present study, at least two iteration loops are needed, for sweeping in x-direction and in y-direction, respectively. The iteration times mentioned previously, which is around 20~40, refers to the outer iteration loop.

For the resolution of the momentum equation (Equation 7.19), the continuity equation should also be obeyed. The continuity equation in a two-dimensional form is given as follows:

$$\frac{\partial \rho}{\partial t} + \frac{\partial (\rho u)}{\partial x} + \frac{\partial (\rho v)}{\partial y} = 0 \tag{7.41}$$

Since the variables u and v appear in both the momentum and continuity equations, the two equations are coupled in a complex way. Furthermore, the pressure P is found in both equations, however, no direct way of solving the pressure can be found.

Therefore, the SIMPLER algorithm has been used in the present study to link the pressure and the velocities. This algorithm starts with a guessed velocity filed, and then it calculates the coefficients of the momentum equation and the pressure P^* from the guessed velocity field. After that the calculated pressure P^* is used to calculate the non-correted velocity field u^* and v^*. Based on the non-corrected velocity field u^* and v^*, a pressure-correction P' is calculated. Finally the velocity field u and v are corrected by the pressure-correction term P'. After solving the momentum equations, the other discretized equations for temperature and speicies are solved. If convergenvy has not been achieved, the guessed velocity field will be substituted by the calculated velocity field from last iteration and the calculation will be repeated until convergency.

7.4   Results

In this section, the simulation results of the 2-D macrosegregation model which is applied for the 100 kg ingot and the 500 kg ingots are presented and compared to the experimental measurement in terms of carbon concentration in longitudinal and transverse direction of the ingots. Section 7.4.1 presents the calculated fields of temperature, fraction of solid, velocity of liquid and solid phases as well as the mixed concentration for the 100 kg ingot, and the calculated results for the 500 kg ingot are presented in section 7.4.2.

7.4.1   Solidification of the 100 kg ingot

It needs to be noticed that the boundary conditions and the simplification of the solidification model are not real for the small and fast solidification of the 100 kg ingot, but for the comparison between the solidification model with and without consideration of the sedimentation of the equiaxed grains, the simulation of the 100 kg ingot solidification has been conducted. Fig. 7.7-10 show the simulation results of the 100 kg ingot with regard to the temperature field, fraction of solid and liquid velocity field as well as the liquid concentration field at the solidification time of 20 s, 120 s, 280 s and 460 s.

Tl (1320~1490 °C)   fs (0~0.90), ul (~7 mm/s)   Cl (0.6~1.9 wt.%)
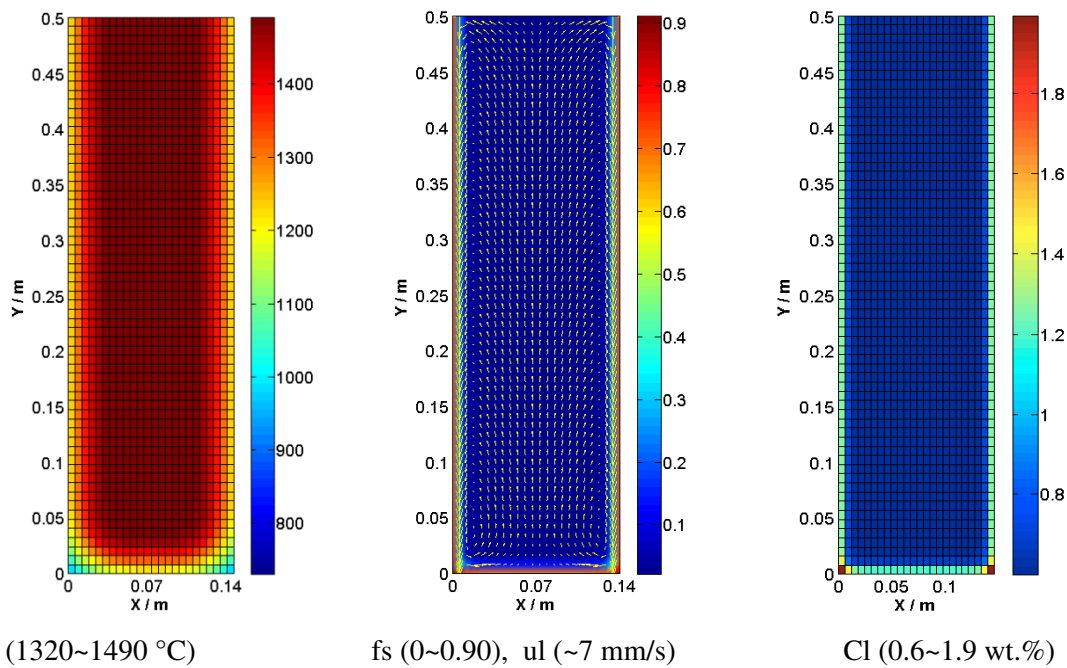
Fig. 7.7: Results of a simulation, 20s after cooling started

Tl (987~1490 °C)   fs (0~0.99), ul (~10.8 mm/s)   Cl (0.6~4.0 wt.%)
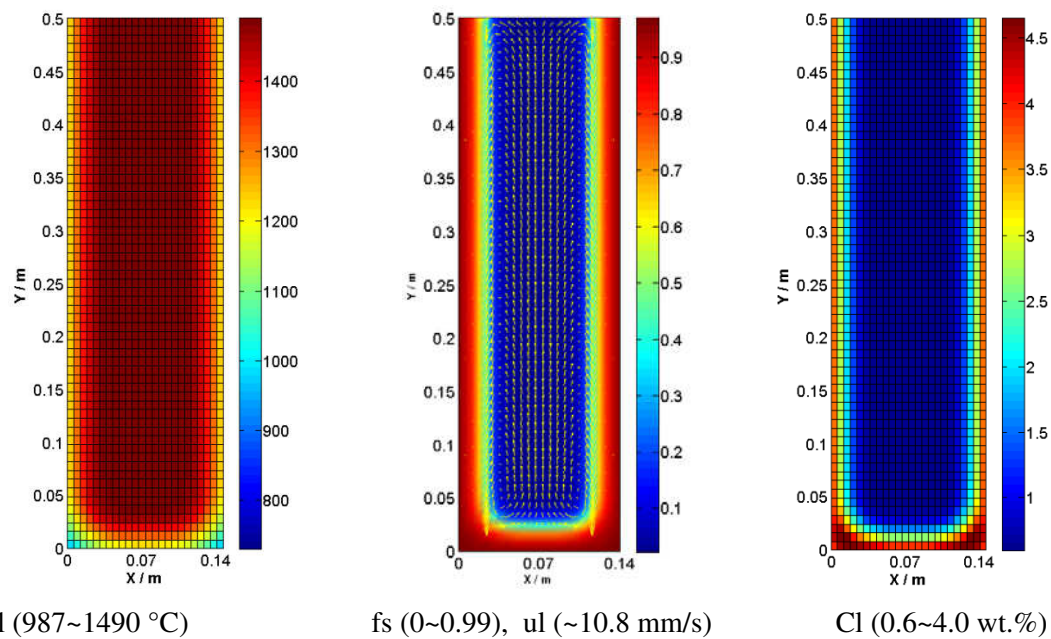
Fig. 7.8: Results of a simulation, 120s after cooling started

Tl (822~1486 °C)   fs (0~0.99), ul (~14 mm/s)   Cl (0.62~4.3 wt.%)
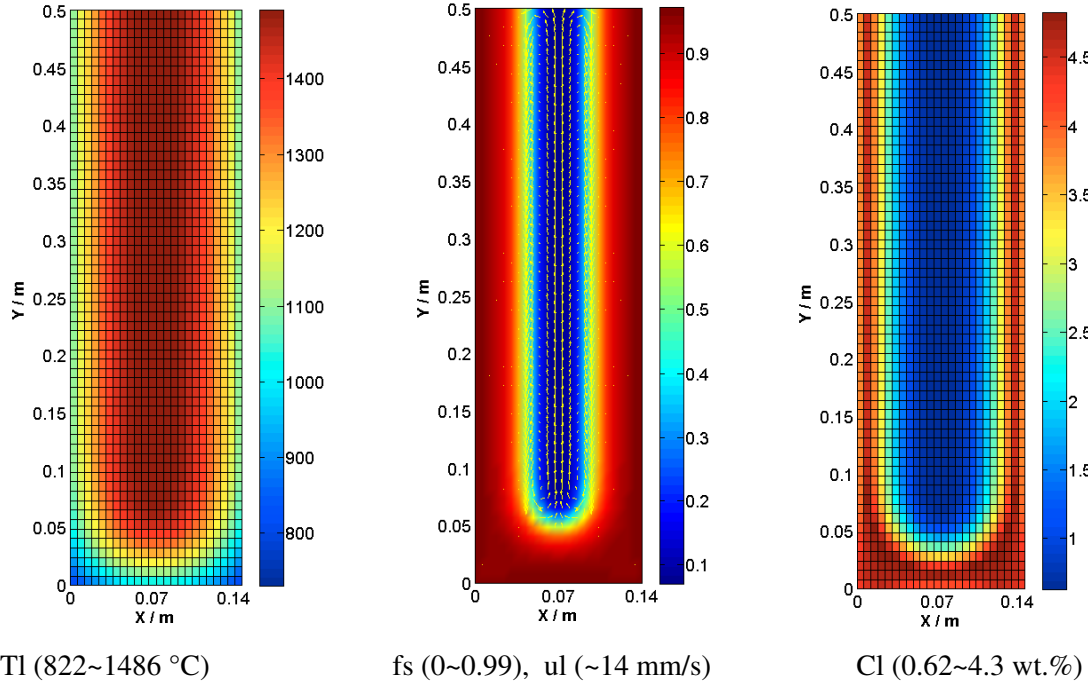
Fig. 7.9: Results of a simulation, 280s after cooling started

Tl (730~1486 °C)   fs (0.56~0.99), ul (~7.1 mm/s)   Cl (1.1~4.4 wt.%)
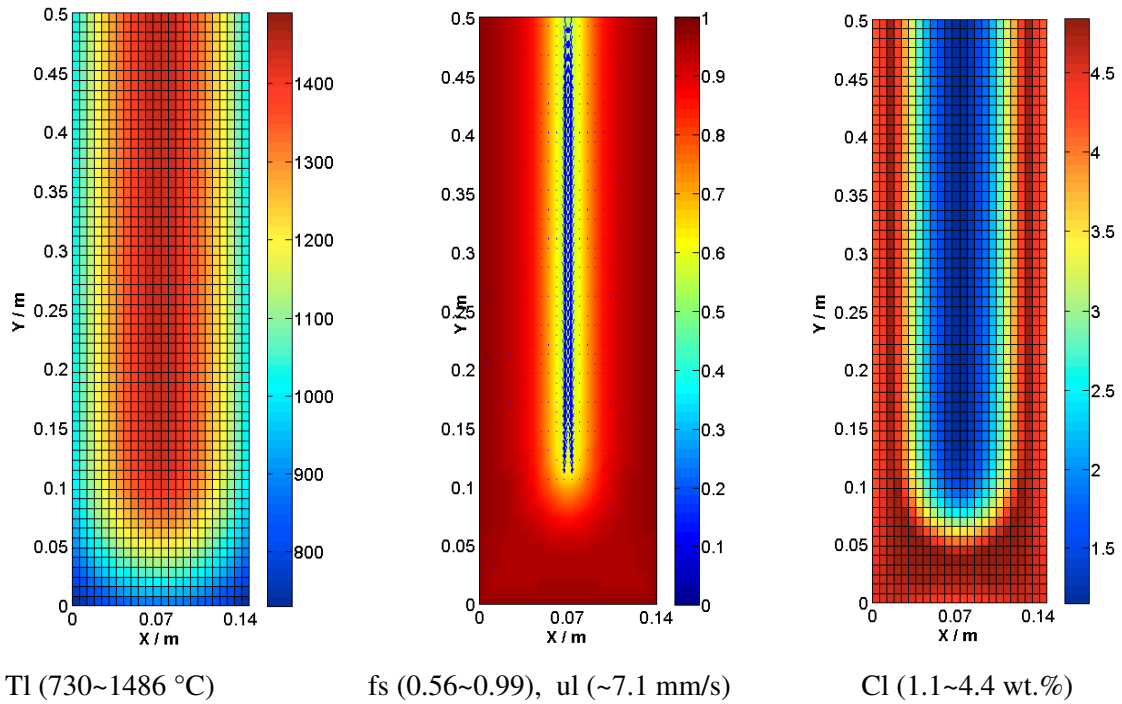
Fig. 7.10: Results of a simulation, 460s after cooling started

The isotherms from the temperature fields appears to be a "U"-shape which moves inwards as time increases. The field of fraction of solid and liquid concentration show the similar "U"-contour. As solidification proceeds, the solid/liquid front approaches to ingot center from side and from bottom. At 460 s, the rest liquid remains a slim strip along the ingot center line, which is very similar to the case in continuous casting.

The liquid velocity field appears a classic natural convection pattern that the cold melt near the mould surface moves downwards and the melt in the center moves upwards. The maximum liquid velocity appears at the solidification front and in ingot center, and the absolute value is up to 14 mm/s in the middle stage of solidification. Due to the interfacial drag, the liquid velocity is zero if the fraction of solid is over 0.6. The solid phase in the 100 kg ingot is set to be stationary, as referred in section 7.2. After solidification completes, the calculated carbon concentration field is illustrated in Fig. 7.11. The carbon concentration field shows a positive segregated long strip along the ingot center line with the carbon concentration of ca. 0.66% and a negative segregated area near the ingot surface at the bottom and at both sides with the carbon concentration of around 0.5 %. From ingot outside to inside the carbon concentration increases quite smoothly, and no sudden change of concentration is found. The reason might be due to the fact that the flow fluid in the 100 kg ingot obeys a smooth natural convection pattern. No solid phase is allowed to move and to disturb the liquid convection in the 100 kg ingot model.
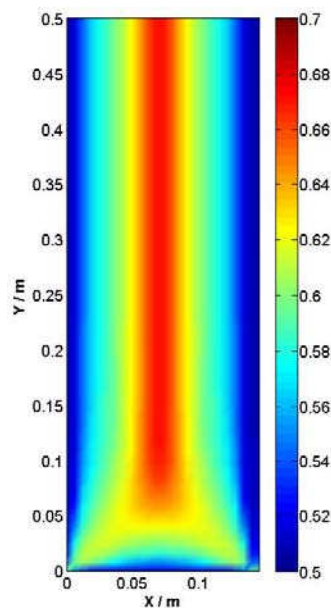
Fig. 7.11: Calculated carbon concentration field of the 100 kg ingot

As dendritic growth plays an important role in the solidification of the 100 kg ingot, and during solidification columnar dendritic structure interacts with the segregated melt in in micro- and macroscopic level, the present two-phase model is somehow limited for such cases. However, the simulation of the 100 kg ingot solidification was conducted with attempt to compare the solidification model with (500 kg ingot) and without (100 kg ingot) consideration of the sedimentation of the equiaxed crystals. This will be presented in Section 7.4.2 and the influence sedimentation of equiaxed crystals on the simulation results will also be discussed.

Fig. 7.12 shows the comparison of carbon concentration along the transverse direction at top and

bottom of the ingot between simulation and experiments results. Both results show higher carbon segregation index in the middle with the value above 0.2 and lower segregation index near ingot surface of around -0.1, whereas at ingot bottom slight negative segregation happens with the segregation index of carbon of nearly -0.1.
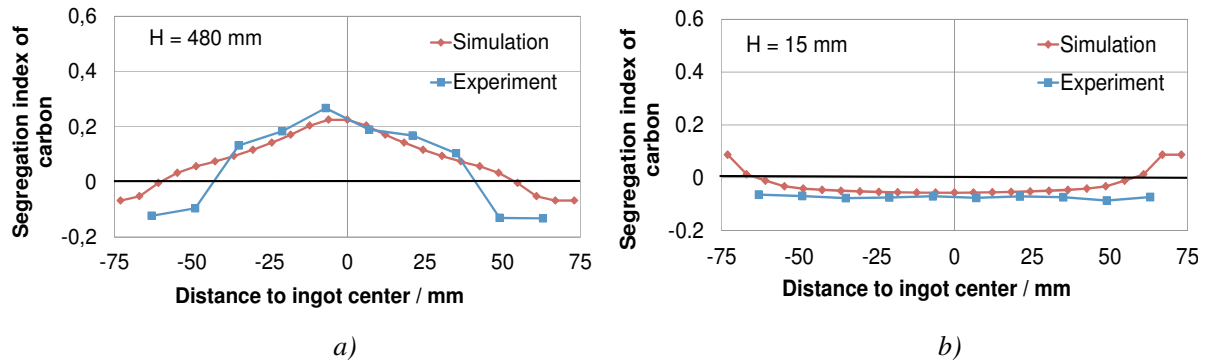

Fig. 7.12: Comparison of carbon concentration in the 100 kg ingot in transverse direction between experimental and simulation results, a) ingot top, at the height of 480 mm, b) ingot bottom, at the height of 15 mm

It seems that at ingot top and bottom the prediction fits the reality quite well, and from this point of view, the present two-phase solidification model for the 100 kg ingot works for the start-up and final state of ingot solidification, and for the progress of ingot solidification, future work still needs to be done to extend the two-phase solidification model to a three-phase model which includes both columnar and equiaxed dendritic structure, so that the prediction of ingot solidification will be more close to the reality.

7.4.2   Solidification of the 500 kg ingot

Fig. 7.13-16 give the simulation result for the 500 kg ingot with regard to temperature, fraction of solid, mixed concentration of the liquid and solid phases at solidification time of 12 min, 37.5 min, 75 min and 111 min. The calculated total solidification time is around 120 min. Different from the solidification model for the 100 kg ingot, the solidification model for the 500 kg ingot takes into account the movement of the equiaxed grains, i.e. the sedimentation of equiaxed dendrites. Owing to that, the solidification front at ingot bottom increases faster than at ingot side; the solidification front at ingot side is also not parallel to the mould surface, instead, the lower part of the solidified shell is thicker than the upper part, which is quite similar to the experimental observation in the water modelling experiments using NH_4Cl-solution presented in Chapter 6 (Fig. 6.6)

Tl (1132~1490 °C)   *fs (0.02~0.99), ul (~7.1 mm/s)*   *Cmix (1.1~4.4 wt.%)*
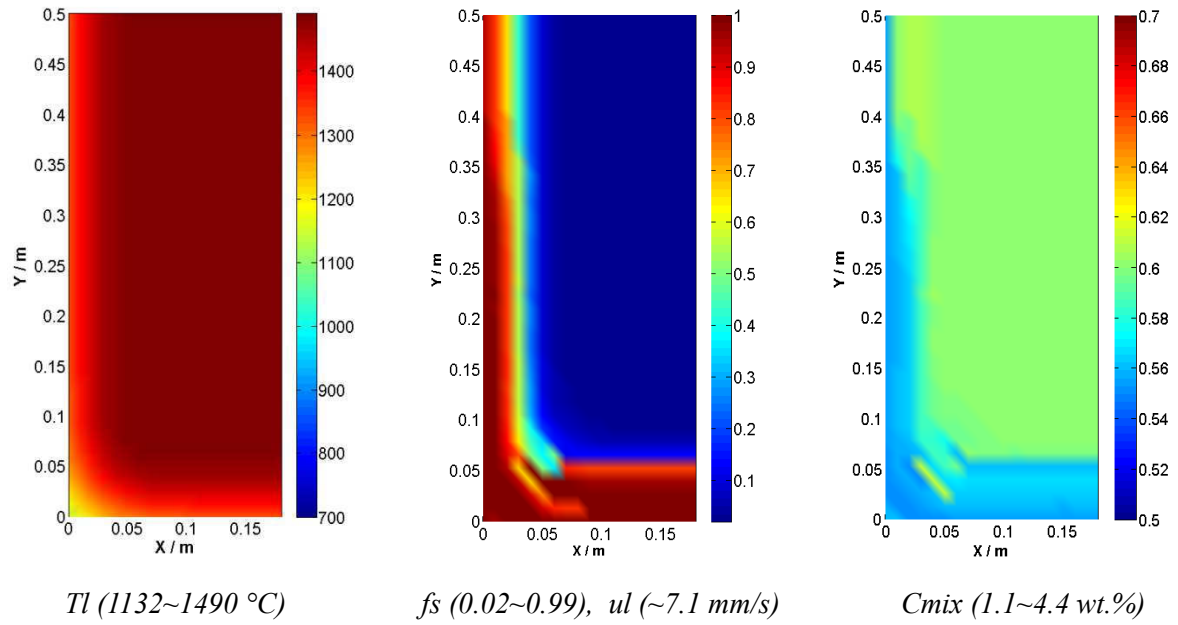
Fig. 7.13: Simulation results of the 500 kg ingot, 12 min after cooling started

Tl (730~1486 °C)   *fs (0.56~0.99), ul (~7.1 mm/s)*   *Cmix (1.1~4.4 wt.%)*
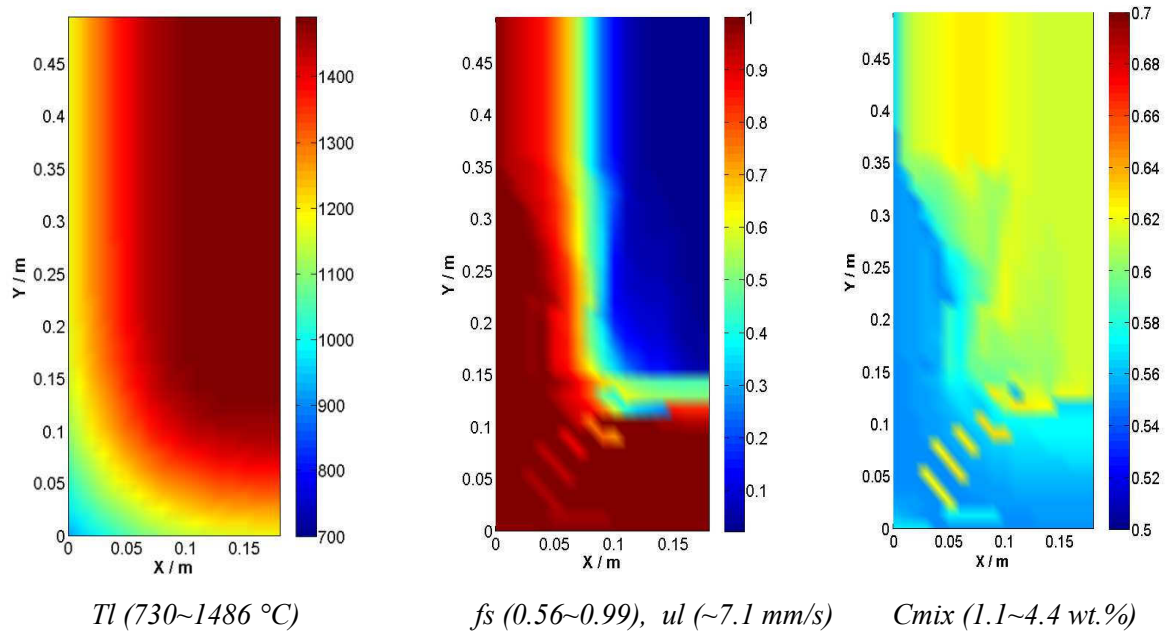
Fig. 7.14: Simulation results of the 500 kg ingot, 37.5 min after cooling started

Tl (730~1486 °C)   fs (0.56~0.99), ul (~7.1 mm/s)   Cmix (0.52~0.67 wt.%)
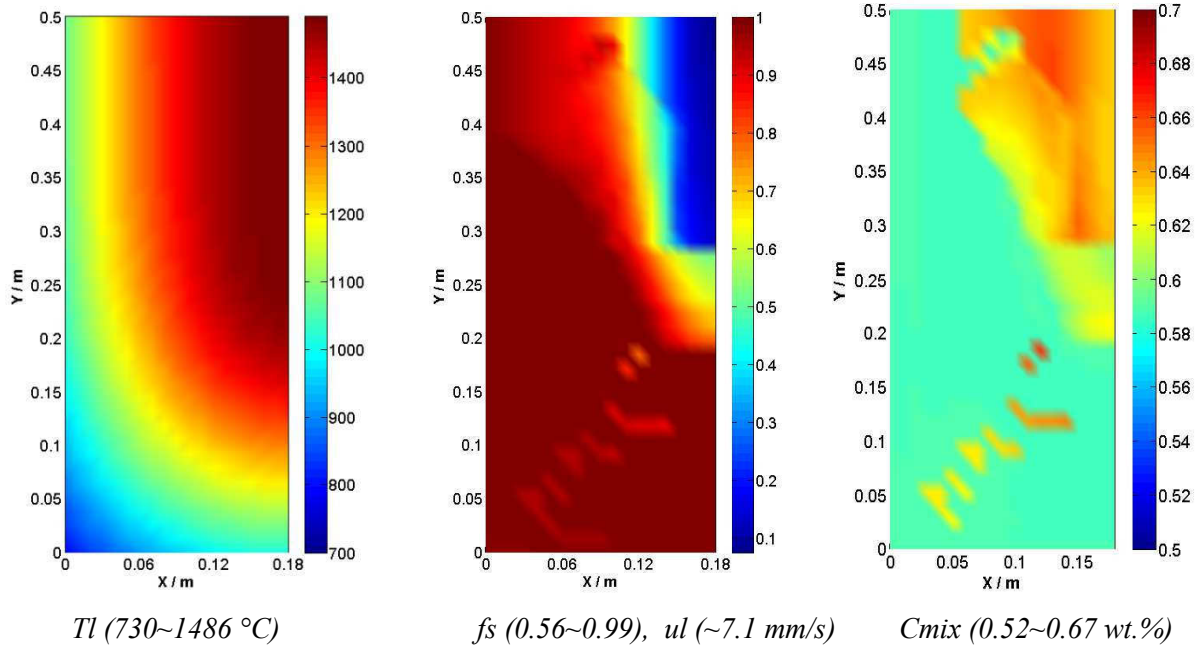
Fig. 7.15: Simulation results of the 500 kg ingot, 75 min after cooling started

Tl (730~1486 °C)   fs (0.56~0.99), ul (~7.1 mm/s)   Cmix (0.52~0.67 wt.%)
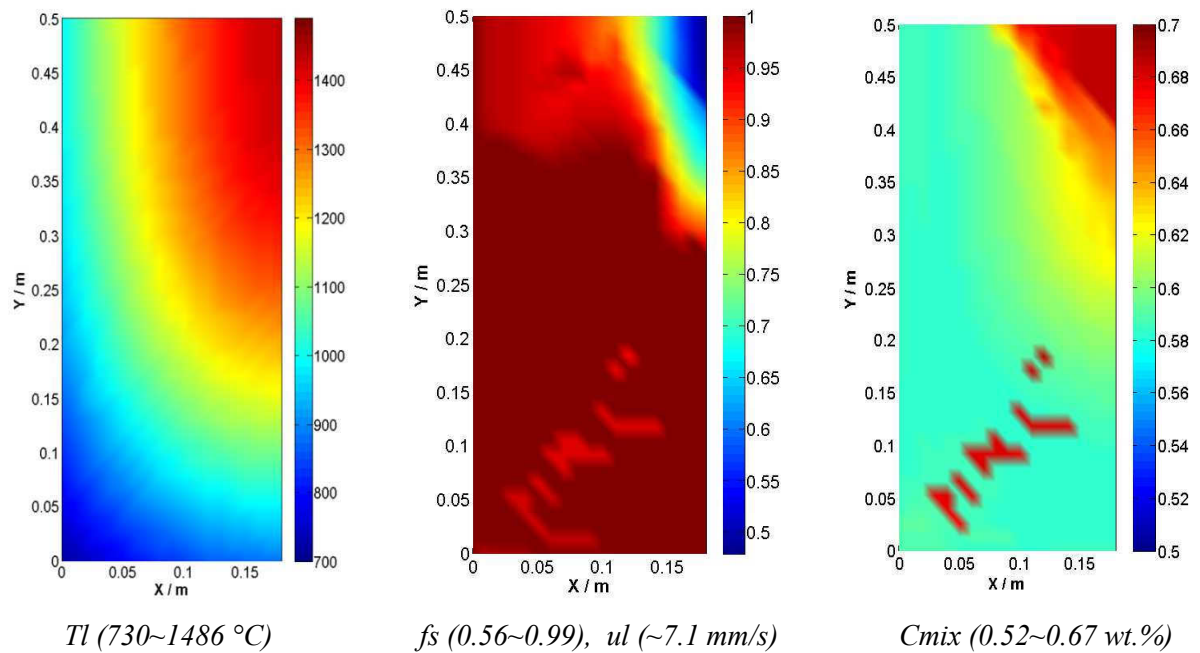
Fig. 7.16: Simulation results of the 500 kg ingot, 111 min after cooling started

As the solidification proceeds, solid grains are growing and settling, and the solidification front keeps moving inwards and upwards. At the solidification time of 111 minutes, the sedimentation cone of equiaxed grains reaches approximately half height of the ingot, and the last solidified part is at the ingot top region with the depth of around 200 mm. Although the hot-top condition is not included in the simulation, due to the consideration of sedimentation of grains, the simulated solidification front of the 500 kg ingot is much closer to the real case than of the 100 kg ingot.

From Fig. 7.13 to Fig. 7.16, the fields of fraction of solid and carbon concentration show a unhomogenous distribution at the bottom corner of the ingot. A series of channels are found in this area where the fraction of solid is lower and the mixed concentration is higher. It seems that enriched melt are stored in these channels are the channels are formed in the solidified shell, initiating from the bottom corner and to the inner part of the ingot, as the solidification front moves inwards.

The simulated flow velocity fields of the 500 kg ingot at different solidification time are given in Fig. 7.17. Similar to the flow field in the 100 kg ingot, natural convection pattern is observed where the maximum flow velocity appears near the solidification front, with the value of around 20 mm/s. This is larger than the maximum velocity in the 100 kg ingot, and the reason could be that the solidification time is longer and thus the acceleration time for the melt is also longer. Due to the wider geometry of the 500 kg ingot, the flow velocity in ingot center is more homogenous, ca. 6 mm/s, which is similar to the center velocity of the 100 kg ingot.

15 min   *50 min*   *100 min*
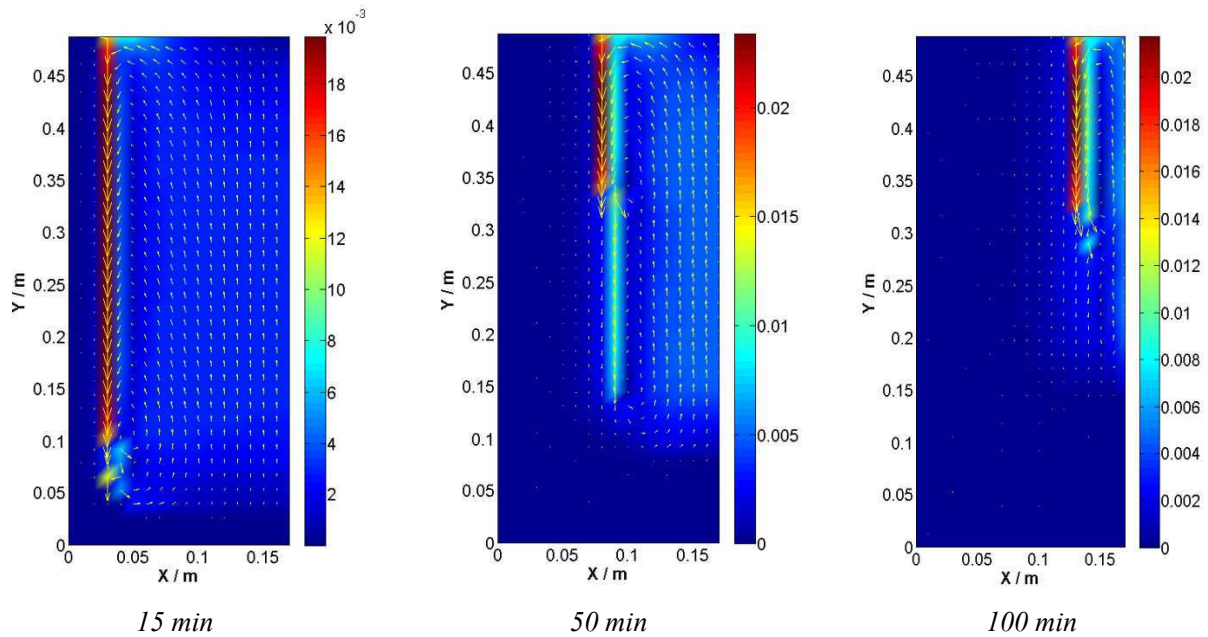
Fig. 7.17: Velocity field of liquid phase at different solidification time

Fig. 7.18 shows the velocity field of the equiaxed grains at different solidification time. As given in Section 7.1.2, if the fraction of solid is lower than 0.6, solid grains can be flushed by the melt, and this is the dominating factor of the solid velocity. Besides that, solid grains can sink down due to their density difference to the bulk liquid. Furthermore, the calculation of solid velocity must also obey the mass continuity equation, and these three factors are indicated in Equation 7.22.
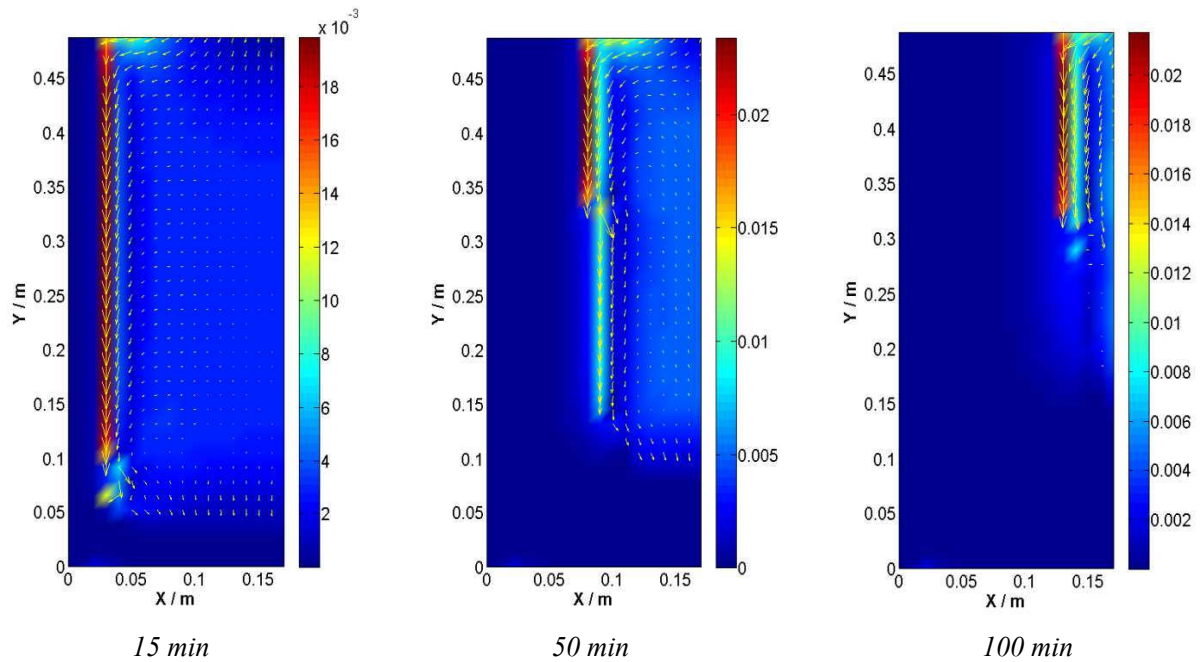
15 min	*50 min*	*100 min*

Fig. 7.18: Velocity of solid phase at different solidification

The velocity fields of the solid grains are quite similar to the flow velocity field, except at ingot top and bottom region where the flow velocity is small, the settling of the grains can be implied by the downwards arrows. Similar as the flow velocity, maximum solid velocity appears near solidification front, and in ingot center the solid velocity is near zero, which is owing to the offset of the upwards flow and the sinking velocity in ingot center. Therefore the predicted contour of the sedimentation layer is not a cone shape as expected, and instead, it appears to be a relative plain sedimentation bed.

Turbulence has been found at the solidification front where stage appears, and this can be seen clearly from the flow field of the solid phase (Fig. 7.18). Along the solidification front, the fluid flow will be disturbed by sudden change of geometry, therefore turbulences are caused. These stages are caused by the sedimentation of the equiaxed grains which settles firstly at the bottom corner and then accumulate in front of the solidification front. Due to the relative coarse mesh for the 500 kg ingot in the present study, stage change with smaller geometry cannot be calculated, and more turbulence along the solidification shall be simulated if a finer mesh is used. Similarly turbulence has also been found in the NH4Cl-water-modelling experiments that spiral turbulences occur at the solidification front after a certain solidification time. Columnar dendrite tips array periodically at solidification front and sudden geometry changes are caused periodically and lead to the spiral turbulence at the solidification front.

Fig. 7.19 gives the calculated carbon concentration field after solidification (a) and the measured carbon concentration profile along ingot center line (b). Fig. 7.20 shows the comparison between the simulation and experiment results of carbon concentration profile along ingot transverse direction at different ingot heights, e.g. 410 mm which is directly under the top cavity, 370 mm where maximum positive segregation is found by experiments, and 220 mm which is in the sedimentation zone.
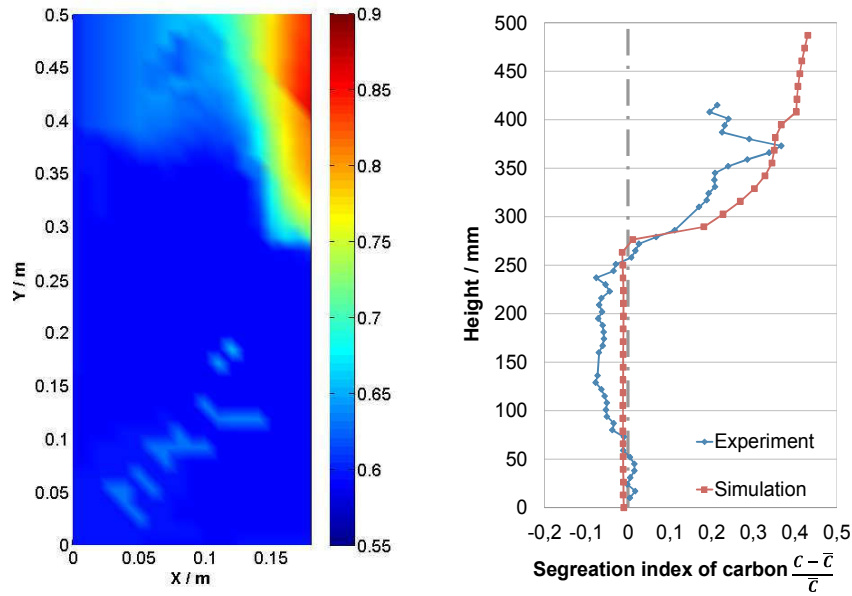
Fig. 7.19: Comparison of carbon concentration of the 500 kg ingot between experimental and simulation results, a) simulated carbon concentration field, b) measured carbon concentration profile along ingot center line
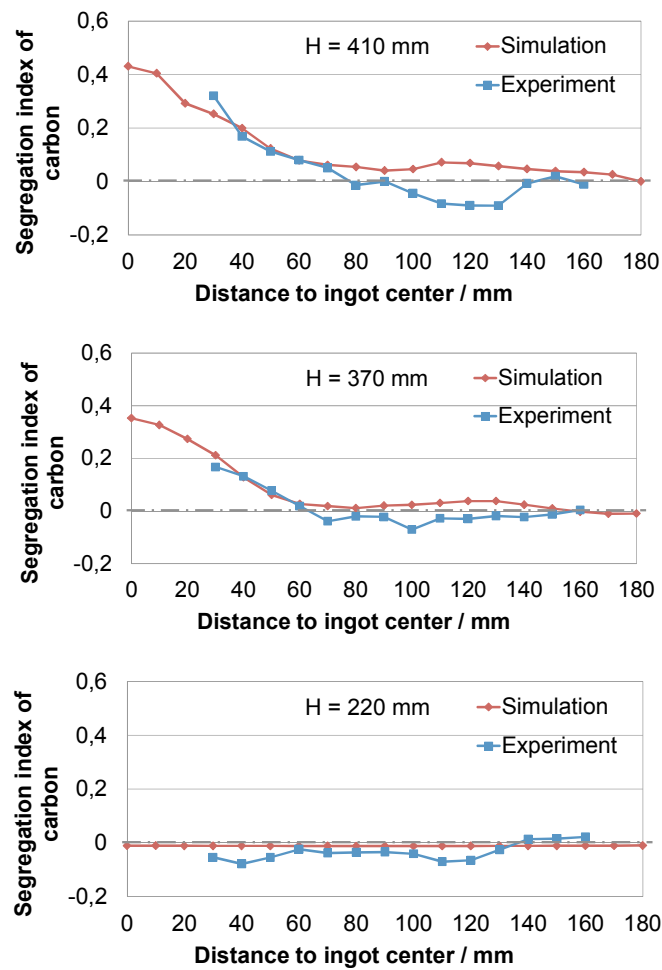

Fig. 7.20: Comparison of carbon concentration in the 500 kg ingot in transverse direction between experimental and simulation results

It seems that compared to the concentration results of the 100 kg ingot, the calculated carbon concentration profiles are more consistent to the experimental results. Both the positive and negative segregation are predicted to be at the right location of the ingot, and the value of segregation is also quite similar to the experiments, especially in the transverse direction. The positive segregation is somehow calculated to be higher in ingot center from ingot height 280 mm to 410mm than the experimental results. The reason could lie in the microsegregation model used in the present study that thermal equilibrium are considered at the growth front, i.e. the interfacial concentration of liquid and solid phases are calculated from the phase diagram. This means that at the end period of solidification where melt temperature approaches to the solidus temperature, the interfacial liquid concentration can reach 2.5%, and at the positive segregation area the high carbon concentration of the melt will reduce the local solidus temperature and therefore increase the interfacial melt concentration further. In order to quantify the microsegregation among dendrite arms, EPMA measurement has been performed for the 100 kg ingot and the 500 kg ingot, as referred in Chapter 5 (e.g. Fig. 5.52 and 5.53) and it turns out that the maximum value of the measured local carbon concentration is up to 1.1%, which is far lower than the calculated 2.5%. Therefore the overestimated microscopic solute redistribution will lead to overestimated macrosegregation. To modify the simulation model, a possible way is to include the influence of phase transformation rate, i.e. thermal dynamics, for example to use the metal-stable phase diagram under different cooling rates instead of the phase diagram under thermal equilibrium condition.

Above the ingot height of 410 mm cavity occurs, and no measurement can be done along the ingot center line above 410 mm. Since volume shrinkage is not included in the present model, porosity and top cavity cannot be predicted. To take consideration of the shrinkage, the gas phase should be added to the liquid-solid two phase system, so that not only porosity and top cavity will be calculated, but also the shrinkage-induced flow can be taken into account, i.e. the V-segregation can be simulated.

The concentration of the negative segregation zone seems to be unified and lower than the experiment results, as in Fig. 7.19 b) shows. In reality, in the sedimentation zone of equiaxed grains, the inter-dendritic enriched melt are pressed outside of the sedimentation zone due to the high pressure, and this results in a negative segregation zone. In the present model the dendrite morphology are not taken into account, and the equiaxed dendrite are simplified as globulitic grains, therefore no inter-dendritic is considered. The sedimentation zone is actually composed of numerous "hard balls" which keep growing. Therefore the value of the carbon concentration in the sedimentation zone seems to be somehow unified. In reality due to the static ferrostatic pressure the solute enriched interdendritic melt is pressed out and forms A-segregation, as in Section 5.3.3 discussed, and the rest sedimentation zone forms the negative segregation zone. In the solidification model this "squeeze" of the rest melt among the grains due to pressure is not taken into account, and as a result the simulated concentration in the sedimentation zone is slightly higher than measured value.

7.5   A-segregation submodel

Since the 2-D simulation model has a relative coarse mesh size (9 mm × 12 mm), and the measured A-channels have a width around 2 to 2.5 mm, the prediction of the A-segreagation is not possible in this model. If a finer mesh size for example 1mm or 2 mm is used, the computational expense will be dramatically increased. In order to investigate the mechanism of A-channel formation and the impact factors of A-segregation, a one dimensional submodel for A-segregation modelling has been developed based on the experimental measurements and simulation result of the 500 kg ingot.

It is known that during solidification, the microstructure in the CET area is somehow less ordered than the columnar zone and the center equiaxed zone. Therefore it is considered that there are a few potential channels in front of the columnar zone among the equiaxed grains, and through this potential channels the solute enriched melt can flow from the root of the columnar dendrites upwards and inwards. If the entering melt is hot or highly concentrated with solute, thermally driven remelting or solutally driven remelting can occur inside the potential channels. During solidification the channels are subjected to certain heat extraction, solidification can also take place. Whether the channels will be widened or closed is determined by the competition between remelting and solidification, which depends on the cooling rate, melt concentration as well as flow velocity as on.

In this submodel it is assumed that the calculation domain is one of this potential channels. It is parallel to gravity and has a length of 100 mm, which is the typical length of the A-lines measured in our 500 kg ingots. As illustrated in <u>Fig. 7.21</u> a), solute enriched melt can enter the channel from bottom with an entering velocity and flow through the channel upwards. The channel locates in front of the columnar front and is under certain heat extraction in the horizontal direction. A thermal gradient difference ΔGx has been defined to describe the heat flux. As illustrated in Fig, 21 b), G_1 is the thermal gradient at the left wall of the channel, and G_2 is the gradient at the right wall. ΔGx equals to G_1 minus G_2, and thus the heat flux $\dot{q}$ is

$$\dot{q} = \lambda \cdot (G_1 - G_2) = \lambda \cdot \Delta Gx \tag{7.42}$$

where λ is the averaged thermal conductivity of the liquid and solid phase in the channel. If ΔGx is large, the heat extraction rate is also large, and thus the cooling is fast; if ΔGx is small, cooling is slow.

The governing equations of the 1-D A-segregation submodel are almost the same to those of the 2-D model, except that the solid phase in the channel is considered not movable. The mass transformation rate M_{ls} indicates the phase transforamtion rate of remelting or solidification. If the value of M_{ls} is positive, solidification takes place, and if negative, remelting happens.
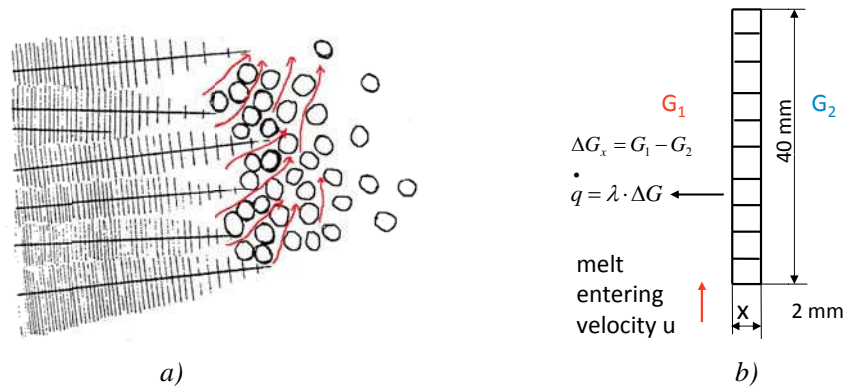
Fig. 7.21: a) Schematic illustration of the potential channel in the mushy zone, b) calculation domain of the 1-D A-segregation submodel

The boundary conditions of the A-submodel are calculated from the simulation results of the 2-D simulation of the 100 kg ingot and the 500 kg ingot. As shown in <u>Table 7.2</u>, four cases have been calculated. In all the cases channels are selected to locate in front of the columnar dendrites at around half height of the ingot and with the initial fraction of solid of ca. 0.4 to 0.6, for both the 100 kg and the 500 kg ingots.

For example case C1 is selected to be at 30 mm from the mould wall at the solidification time of 120 s of the 100 kg ingot, and the thermal gradients Gx is calculated from the simulated temperature field of the 100 kg ingot at 120 s, as shown in <u>Fig. 7.22</u>. The relative thermal gradient ΔGx is calculated from the thermal gradient profile and the ΔGx value at the distance of 30 mm to the mould wall is calculated by interporlation of the ΔGx curve. The averaged concentration of the liquid and solid phase as well as the radius of the equiaxed grains are also obtained from the 2-D simulation results at 120 s, and they are used as the initial conditions of the A-submodel calculation. For the case C2, C3 and C4, the parameters and initial conditions are selected in the same way.

	100 kg ingot		500 kg ingot	
Case No.	C1	C2	C3	C4
Initial fraction of solid	0.40	0.60	0.43	0.60
ΔGx [K/mm]	2.968	1.837	2.09	0.188
Tl [°C]	1462	1442	1460	1440
Cl [wt.%]	0.89	1.14	1.00	1.00
Cs [wt.%]	0.22	0.25	0.21	0.24
r_e [μm]	135	161	260	171
Distance to mould wall / mm	30	42	90	120
At solidification time [s]	120	240	2450	3600

Table 7.2: Parameters and initial conditions for the A-submodel simulation
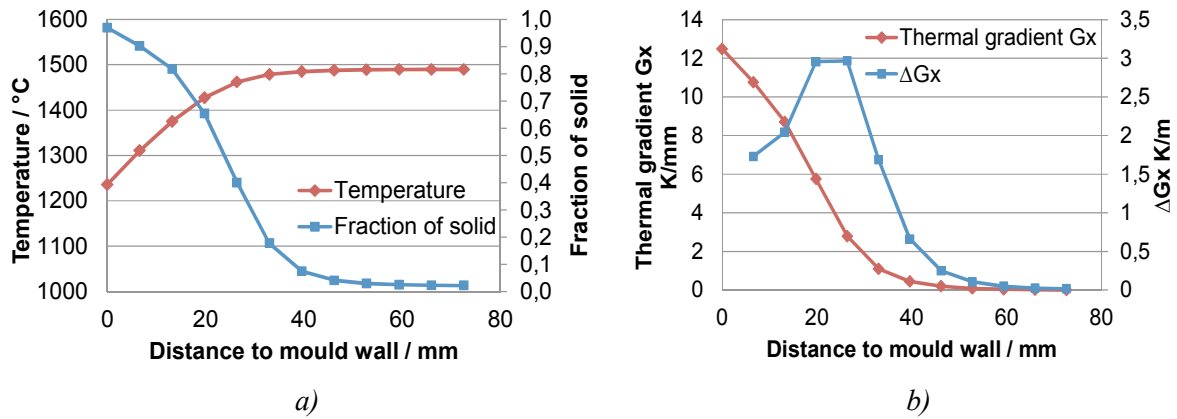
Fig. 7.22: Simulation results along the transverse direction of the 100 kg ingot, at 120 s, a) temperature and fraction of solid, b) thermal gradient G and gradient difference ΔGx

For the four cases C1-C4, highly enriched melt with carbon content of 1.5% are forced to flow into the channel from bottom to top with an entering velocity of 0.1 mm/s. As the heat extraction rate for the four cases are different, the potential channel can be closed up or widened, and the change of fraction of solid indicate whether remelting or solidification takes place. Fig. 7.23 gives the profile of fraction of solid along the channel at different time after the enriched melt flows into the channel for cases C1 and C2, which has a relative high thermal gradient difference ΔGx, i.e. relative high heat extraction rate $\dot{q}$ in the 100 kg ingot.

For case C1 with a high ΔGx of 2.968 K/mm, the initial fraction of solid in the channel is 0.4, shown in Fig. 7.23 a). After 15 s the fraction of solid along the whole channel increases over 0.55, and meanwhile the fraction of solid increases also along the channel. As time increases, this tendency is more clearly to be seen. At 75s after flow begins, the fraction of solid in the channel is over 0.8 at the channel entrance and around 0.85 at the end of the channel. Similar tendency can be found in C2 with a lower ΔGx of 1.837 K/mm. The initial fraction of solid of case C2 is 0.6, and after 100 s the solid fraction rises to 0.87 at channel entrance and 0.9 at t channel exit. Both cases indicate that solidification is dominating in the channel and the channel is closed ascribed to high cooling rate (high heat extraction rate).
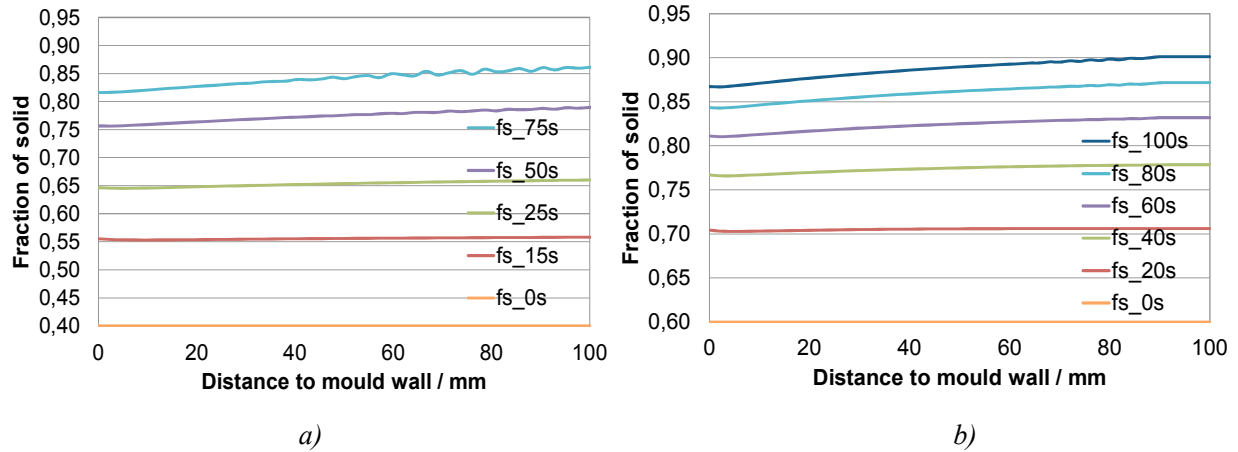
a)   *b)*

Fig. 7.23: Distribution of solid fraction along the channel in the 100 kg ingot,, a) case C1, fs=0.4, ΔGx=2.968 K/mm , b) case C2, fs=0.6, ΔGx=1.837 K/mm

Attributed to the change of solid fraction and thereby the change of drag force in the channel, the flow velocity of the melt varies upon time, which can be seen from Fig. 7.24. For both cases C1 and C2, the enriched melt entries the channel with an initial velocity of 0.1 mm/s. As time increases, the increased fraction of solid reduces the flow permeability, resulting in higher interfacial drag, thereby the melt velocity decreases gradually from 0.1 mm/s to 0.005 mm/s. It need to mention that the velocity acceleration due to solutal buoyancy force needs to be taken into account, nevertheless the magnitude of the drag force in the channel is much higher than the solutal buoyancy force, therefore melt velocity reduces as solid fraction increases.
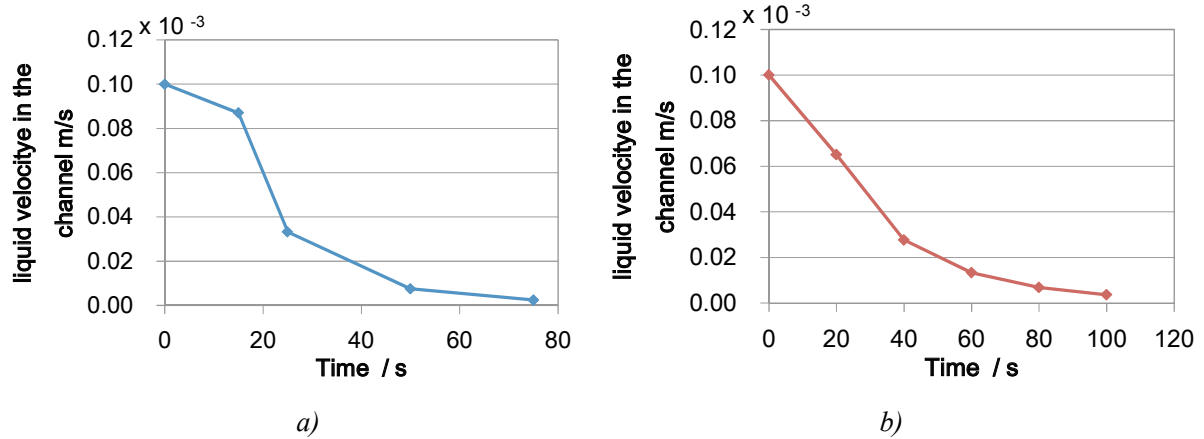

a)   *b)*

Fig. 7.24: Distribution of liquid velocity along the channel in the 100 kg ingot, a) case C1, fs=0.4, ΔGx=2.968 K/mm, b) case C2, fs=0.6, ΔGx=1.837 K/mm

As referred in former section that the melt flow should obey the mass continuity referred (Equation 7.41), and in the A-submode it is considered that the steel melt is not compressible, $\frac{\partial \rho}{\partial t} = 0$, and Equation 7.41 can be written as:

$$\frac{\partial(\rho u)}{\partial x} + \frac{\partial(\rho v)}{\partial y} = 0 \tag{7.42}$$

Since the A-submodel is a one-dimensional model, in another word, the velocity change along the channel should be zero, the calculated flow velocity is the same along the channel. If the A-submodel is extended to two dimensions, the flow velocity can also vary upon the location inside the channel.

Opposite to case C1 and C2 from the 100 kg ingot, the cases C3 and C4 from the 500 kg ingot with lower heat extraction rate indicate that remelting takes place and the channels are opened gradually. As in Fig. 7.25 illustrated, the initial fraction of solid for case C3 is 0.4, and after 50 s the solid fraction at channel entrance is reduced down to 0.26 where at channel exit is around 0.3. As the time increases to 150 s, solid at channel is further dissolved by carbon diffusion with solid fraction at entrance of 0.02 at the exit not more than 0.1. After 200 s the initial solid phase is completely dissolved and thereby the channel is fully opened.

Similar to case C3, remelting occurs also in case C4 where the initial fraction of solid if 0.6 and the thermal gradient difference ΔGx is 0.188 K/mm, slightly higher than that in C3. Different from case C3 that remelting happens homogenously along the channel where the change of solid fraction is nearly the same from the entrance to the exit of the channel, the channel in Case C4 is more opened at the entrance than at the exit. For example after 50 s the solid fraction at channel entrance is reduced to 0.3 whereas at the middle part and exit of the channel the solid fraction stays at around 0.58. After 100 s the entrance of the channel is completely opened whereas at exit the channel remains undissovled with the solid fraction of around 0.4. The local phase transformation rate is the competition result of solidification and remelting, which is influenced by the carbon concentration difference between the liquid and solid phases, the local super-/undercooling, the grain size and number of grains as well as the flow velocity.
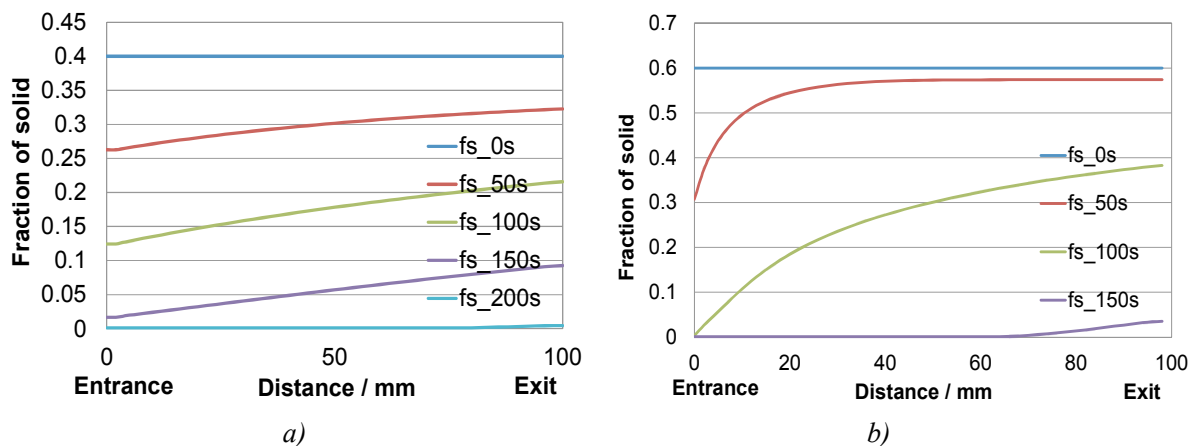
Fig. 7.25: Distribution of solid fraction along the channel in the 500 kg ingot, a) case C3, fs=0.4, ΔGx=0.209 K/mm, b) case C4, fs=0.6, ΔGx=0.188 K/mm

As illustrated in Fig. 7.26 the flow velocity inside the channel for case C3 and C4 increases dramatically as time increases. The initial entry velocity is 0.1 mm/s, the same as in C1 and C2. For

case C1, the melt velocity after 50 s rises to 4 mm/s, and after 150 s at which the solid fraction if not more than 0.1, the melt velocity increases up to 18 mm/s. Similarly is for case C4 that at 150 s the channel is fully opened and the melt velocity is 25 mm/s.
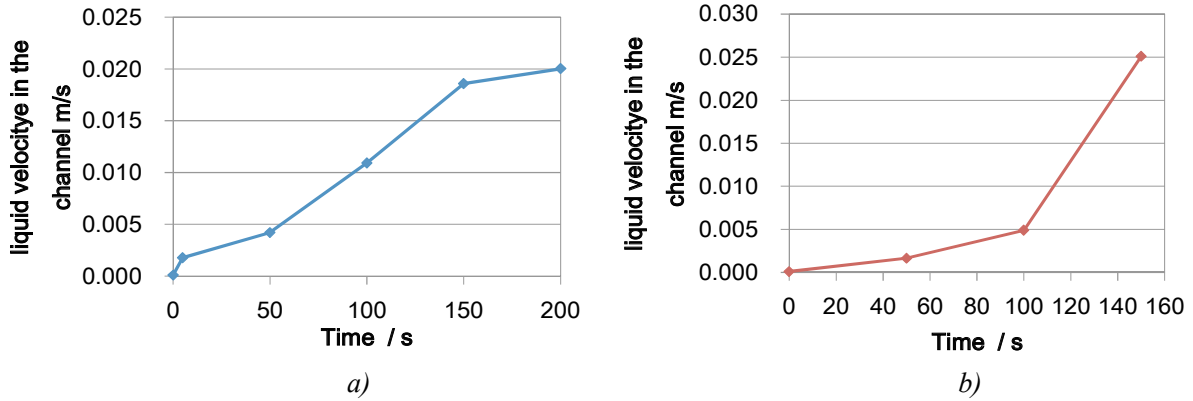

Fig. 7.26: Distribution of liquid velocity along the channel in the 500 kg ingot, a) case C3, fs=0.4, ΔGx=0.209 K/mm, b) case C4, fs=0.6, ΔGx=0.188 K/mm

As introduced in Chapter 3 (section 3.2.3), Rayleigh number based criterion is widely used to determine the instable development of freckles, especially in the field of directional solidification of superalloys. In ingot casting, the Rayleigh number in mushy zone has also been applied to describe the stability of channel formation [86, 119, 169, 170]. If the Rayleigh number is larger than the critical value, the thermal/solutal buoyance force overcomes the drag force, and instable convective flow will set on, solutal remelting takes place and freckles will be formed. The critical Rayleigh number which indicates the existence of freckles have been reported in a number of experimental studies with various critical values from 0.25 to more than 300 for different alloys with different cooling and growth conditions.

In the present simulation work, the Rayleigh number has been calculated according to Equation 3.17 (see page 36) for each case and Fig. 7.27 and Fig. 7.28 show the profiles of the Rayleigh number along the channel at different time for case C1 and C3, respectively. For case C1, the calculated phase transformation rate (mass from liquid to solid in one representative volume element) is between o and 10 kg /s/m^3, meaning that solidification is dominating. The corresponding Rayleigh number is lower than 0.03 and keeps decreasing as time increases (Fig. 7.27).

For case C3 where remelting dominates, the Rayleigh number is calculated to be much larger. At 5s the Rayleigh number is around 9, and at 50 s is ca. 27. After 100 s the Rayleigh number is over 80. At the entrance of the channel where solid phase is lower and the channel is more opened, the Rayleigh number is especially large, and as remelting proceeds, the Rayleigh number at the entrance approaches infinite.
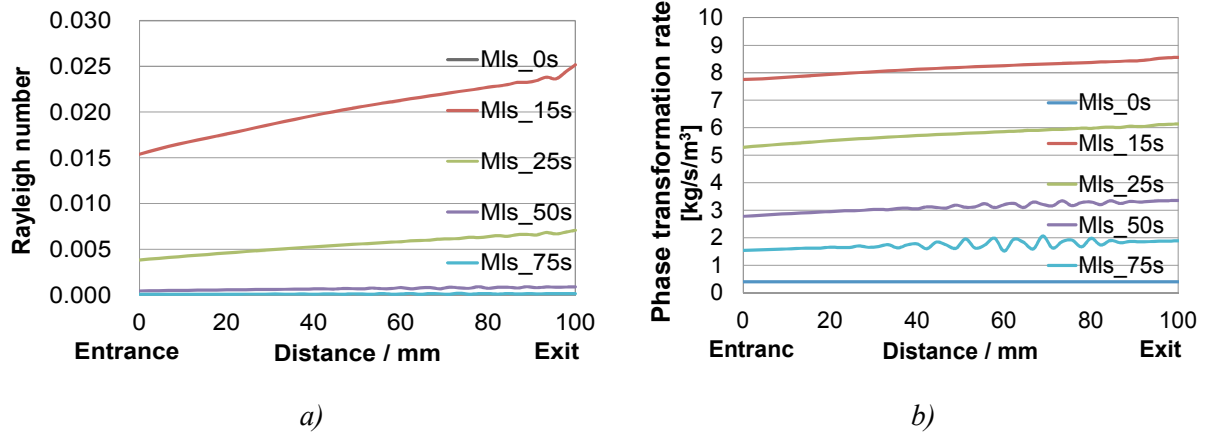
a)   *b)*

Fig. 7.27: Distribution of Rayleigh number and phase transformation rate along the channel, case C1

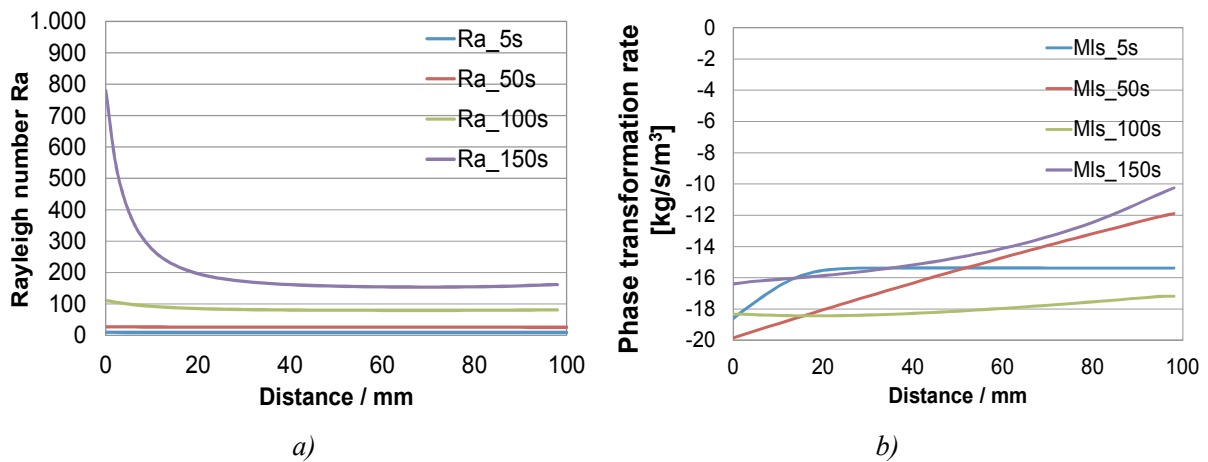*a)*   *b)*

Fig. 7.28: Distribution of Rayleigh number and phase transformation rate along the channel, case C3

Both figures clearly indicate the tendency that if solidification happens where the phase transformation rate Mls is positive, the Rayleigh number is small; and if remelting takes place where Mls is negative, the Rayleigh number is large. This is attributed to the fact that the Rayleigh number is proportional to the permeability (Equation 3.13), which is closely related to the fraction of solid and the grain morphology (Equation 7.3). Remelting leads to the decrease of solid fraction and therefore the increase of the permeability. As a result, the faster the remelting is, the higher the Rayleigh number is.

Since according to the Rayleigh number based criterion, the critical Rayleigh number is essential for the prediction of channel formation, through the simulation work it has been attempted to find the critical Rayleigh number as well as its correlation with solidification parameters. The detailed results of these simulation work are summarized and presented in another paper [171]. However, it was found that a critical value for the Rayleigh number is not possible to be distinguished. Due to the complexity of cooling and melt flow in ingot casting, an already opened channel can still be closed, since in ingot casting the cooling direction may not be parallel with the flow direction, and the channel could be opened only for short time with limited opened length and then closed again by strong cooling which is perpendicular to the flow in front of the open channel. This is obviously different from the case in

unidirectional solidification that once the instable melt is onset, the channel will be not closed again, as the melt flow is parallel to the cooling direction.

Therefore, although the local Rayleigh number was once infinitely large, instable remelting might still not happen. Therefore it is not reasonable to distinguish the instability channel formation in ingot solidification by using one critical value, instead, only the complete Ra-curve versus time can represent the development of channels. Nevertheless, the local Rayleigh number can still be used in ingot casting to imply the intensity of local remelting.

7.6   Discussion

In this chapter the solidification of the 100 kg and the 500 kg ingots have been simulated with a finite volume model without and with consideration of the setting of the equiaxed grains, respectively. The comparison of the simulation results and the experimental results regarding carbon concentration indicate that the two-phase volume-averaged model in this study is capable to simulate the solidification of the 100 kg and the 500 kg ingots. Especially with consideration of the movement of the equiaxed grains, the sedimentation cone and the macrosegregation which is attributed to the relative movement of solid and liquid phases is able to be predicted to a large extent.

7.6.1   Interfacial solidification model

For the 100 kg ingot, the comparison of the carbon centration profiles in x- and y-direction implies that the model successfully predicted carbon concentration along the x-direction, especially at the bottom and the top of the ingot. Nevertheless the positive macrosegregation along the ingot center is somehow "overestimated". The reason has been discussed in section 7.4.1 that the model considers the grains as solid hard spheres and the enriched melt can flow through the interspace between these spheres. In the reality, due to the complex dendritic morphology and the therefore induced resistance force through the dendrite arms, the enriched melt stays partly around the dendrites as interdendritic melt, and the rest melt which is outside of the dendrites is driven by the thermal/solutal buoyancy force. Sometimes the melt flow will be stopped or reduced by bridging of the columnar dendrites or even driven by the shrinkage and forms V-segregation in ingot center. By simplification of the dendrite morphology, the permeability of the mushy zone will be overestimated, and the effect of drag force is suppressed. Therefore the calculated melt flow is calculated to be faster, which leads to a faster re-distribution of the alloying elements. As a result, the predicted macrosegregation in ingot center will be higher than the reality. Similarly, for the 500 kg ingot, the positive macrosegregation at ingot top is higher than the measured results.

Besides dendrite morphology, the mathematic model of the phase transformation kinetics at the liquid /

solid interface has a considerable effect on the simulation result. As referred in Section 7.1.1, it is considered that the driving force of phase transformation is dominated by constitutional undercooling or superheating, i.e. the local concentration of the liquid and solid phase. During solidification, carbon diffuses from the solid grains to the surrounded melt and piles up at the solid/liquid interface. The accumulated carbon at the solid/liquid interface is further distributed by diffusion and convection in the liquid phase. In the present study, it is assumed that at the solid/liquid interface, the liquid and solid phases are locally in thermodynamic equilibrium and the interfacial liquid and solid concentration are obtained from the phase diagram. In reality, the interfacial concentrations are also influenced by the reaction kinetics, e.g. the diffusion rate in solid and liquid state as well as convection in liquid phase. Therefore at the beginning and middle stage of solidification, the equilibrium interfacial concentration is still applicable. As solidification proceeds, the concentration in the liquid and solid phases gets higher, and at the latest stage of solidification the difference between the equilibrium interfacial concentration and the real concentration is considerable large. This explains the fact that among dendrite arms the carbon concentration is measured to be 1.1% by EPMA whereas the calculated value is around 2.5% for the 500 kg ingot.

Furthermore, if the cooling rate is taken into account, fast cooling leads to the fact that species atom cannot complete distributed homogenously in liquid and solid phases, therefore at each temperature, the liquid and solid concentration are lower than those in equilibrium. This is the so-called metastable phase diagram. The faster the cooling is, the larger the deviation of the concentration between stable and metastable phase diagram is. As a suggestion for the subsequent work in future, utilization of the metastable phase diagrams with different cooling rate for the interfacial liquid and solid concentration would be a possible solution to minimize the deviation brought by the equilibrium interfacial concentrations to the numerical model.

7.6.2   Sedimentation of equiaxed grains

One of the targets of the present study is to simulate the sedimentation of the equiaxed grains in large ingots. The influence of momentum of liquid phase is considered here, the pressure due to mass continuity and the gravity/buoyancy force as well as the friction force on the equiaxed grains. The simulation results imply that the movement of the solid grains are mainly dominated by the convective flow, and only if the liquid velocity is low enough (e.g. lower than 5 mm/s), the effect of gravity force on the grains can be observed. In the present simulation the momentum exchange between liquid and solid phases due to phase transformation as well as the exchange of momentum and mass between the interdendritic liquid and the bulk liquid are ignored as they are enough small compared to the liquid momentum and gravity. It is undeniable that these factors could influence the sinking velocity as well as the grain morphology as equiaxed grains grow while sinking down or flushed up by the bulk flow. With consideration of momentum and mass exchange, the local concentration and temperature filed

will be simulated more exactly and the sedimentation behavior and as well as the concentration field inside the sedimentation zone will be more approaching to reality.

The shape of the sedimentation zone was commonly considered as cone-shaped, which was often observed from the as-cast macrostructure of large ingots. During the water-modelling experiments with NH_4Cl solution and numerical simulation, the author has found that although the final shape of the sedimentation zone is a single-peak cone, during solidification the sedimentation zone is not necessary to be cone-shaped. In the last paragraph it is discussed that the velocity of the solid grains are mainly determined by the flow velocity and the gravity force, and thereby the solid velocity can be upwards or downwards at different location of the ingot.

Since the liquid velocity is strongly depending on the cooling intensity, it can be surmised that if the cooling rate of the ingot is varied, the natural convection intensity will be changed, and the center flow velocity will also be changed. If the center upwards flow velocity is larger than the sinking velocity of the grains, the sedimentation cone will not appear in the center, and grains will be brought to the upper part of the ingot, settle down to the bottom corner, and form two peaks of sedimentation layer in a 2-D cross section, as indicated by the water-modelling experiments (Fig. 6.17 a). In a round ingot the contour of these peaks of the sedimentation zone appears to be a cycle in front of the columnar zone, and in the ingot with square-shaped cross section, the peaks form a square. As the columnar zone approaches to ingot center, the peaks of the sedimentation cone moves towards center as well, and finally the peaks merge together at the ingot center and form a single-peak sedimentation cone.

This is in consistence with the theory of Schwerdtfeger [172] that the peak of the sedimentation zone appears not at the ingot center since the density of free grains in ingot center is too low, and instead, it happens in front of the columnar dendrite tips where the fraction of solid is 0.2, as Fig. 7.29 illustrates. Only if the center upwards flow velocity is smaller than the settling velocity, the one-peak sedimentation cone could be formed since the beginning of solidification, as long as there are enough free crystals in the center of the ingot to sink down.
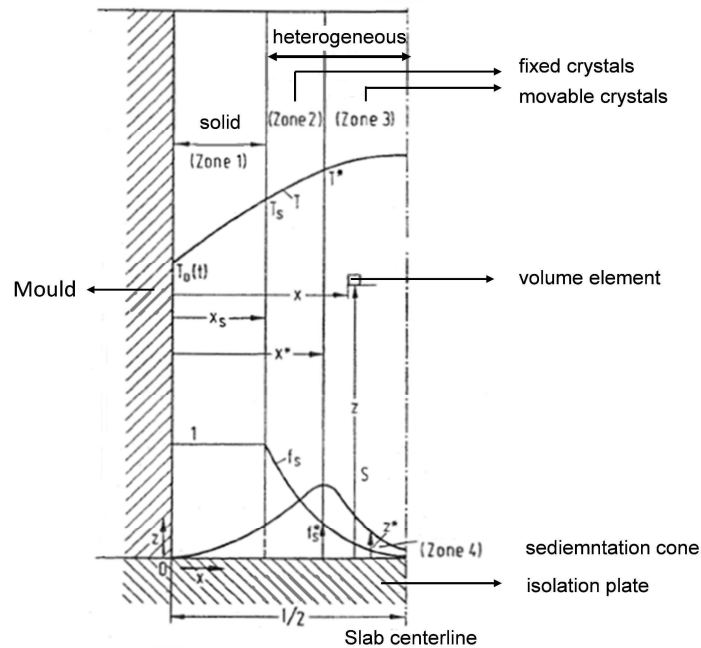
Fig. 7.29: Sedimentation model of Schwerdtfeger [172]

7.6.3   Simulation of A-segregation

The other target of the present study is to investigate the formation mechanism of A-segregation. The two dimensional simulation results show a few channel-like strips in the carbon concentration field at the left bottom corner (the cold corner) of the ingot. These types of channels have also been reported by former researchers like Li and Wu [85, 86, 87] and Combeau [83]. According to their opinions, these channels are very likely the A-channels. However, from the experimental observation from the sulfur print in Chapter 5 it was found that the A-lines appear at around the middle-radius part of the ingot, especially close to the CET region, and at ingot bottom no A-lines have been found. As discussed in Section 5.3.3, the A-segregations are formed either due to remelting by the highly concentrated melt from the columnar dendrite roots, or due to the squeeze effect of the solute enriched interdendritic melt out of the sedimentation zone by ferrostatic pressure. Because the present solidification model negelected the dendritic morphology and the pressure change inside the sedimentation cone, the type of A-segregation which is attributed to the squeeze of interdendritic melt cannot be simulated. If the simulated channles belong to the other type of A-segregation due to remelting, they are supposed to appear at the top and middle height of the ingot at round midde-radius instead of appearing inside the sedimentation zone. From the A-submodel it has been found that low cooling rate benefits remelting. The "channels" locate at the cold corner where the cooling rate is relative high. Furthermore, the A-segregation are measured from sulfur prints to be around 2~2.5 mm in width, and the mesh size of the solidification model for the 500 kg ingot is much larger than 2.5 mm. All these cannot support the idea that this type of "channels" are the so-called A-lines. The author suggests that these "channels" are attributed to the the waves or turbulence at the corner of the calculation domain, and they are

somehow multiplited numerically from corner to center. If the coupling between the momentum equation and the mass / species equations in the solidification model is modified, the effect of the waves/turbulence might not influence the concentration field any further.

The present study has attempt to find the A-segregation criteria by using a one dimensional submodel, and it seems that the simple Rayleigh number based criterion is not applicable for the prediction of the A-channel in ingot casting. To predict the channel formation inside the ingot, a comprehensive solidification model with strong coupling of the macro- and microscopic level, with as fine as enough mesh to represent the dendrite morphology, and with reasonable treatment of the thermal dynamics of interfacial phase transformation is demanded. Meanwhile, ascribed to the geometry of large ingots in which A-segregations appear, the required computational resource for such a model is out of the scope of the present work. By utilization of the up-to-date computational technology such as parallel simulation, the calculation could be speeded up. As a vision for future, to combine the microscopic simulation model such as Automaten Cell and Phase Field Method with the macro/micro coupled model like Volume Average method could be a final solution to many complex solidification phenomena such as A-segregation, V-segregation as well as inclusion entrapment and so on.

8 Synthesis and discussion

The production of heavy steel ingots and continuous cast strands demands adequate control of the quality of as-cast semi-products. Due to the complexity of solidification in these large continous cast strands and ingots, knowledge of some macroscopic phenomena such as sedimentation of crystals and A-segregation are lacking. The present work focused on the quality of as-cast heavy steel ingots with regard to macrosegregation, and investigated solidification phenomena such as growth and movement of dendrites, fluid flow driven by thermal/solutal buoyancy force, remelting and channel formation through hot modelling, cold modelling and numerical modelling.

The hot modelling provides direct information for the understanding of solidification in heavy ingots. The slow solidification test with 500 kg ingot in a isolating mould represent the solidification process in industrial scale ingots with the weight between 3 and 6 t. The appearance of A-segregation in the as-cast 500 ingots further supports the similarity of solidification in the isolated 500 kg ingots and in the industrial scale heavy ingots. The comparison between the 100 kg ingot and the 500 kg isolated ingots in terms of the as-cast structure, cooling curves as well as macrosegregation pattern indicates that the difference between the two cases is the driving force of solidification.

For the 100 kg ingot the as-cast structure is mainly divided into columnar zone and equiaxed zone, where the driving forces of solidification in the both zones are dominated by thermal undercooling. Due to fast cooling the columnar dendrites grow fast from mould wall towards ingot center and forms columnar zone, and at one moment the columnar dendrite tips are blocked by the equiaxed crystals. Attribute to the high cooling rate and high growth rate, the segregated species have little time to redistribute by diffusion and convection in a large scale in the ingot, hence the rest melt in the equiaxed is not highly enriched. Therefore the driving force of solidification in the equiaxed zone is not only constitutional undercooling, rather dominated by thermal undercooling.

For the 500 kg ingot, the as-cast structure can be divided into columnar zone, outer equiaxed zone, sedimentation zone and inner equiaxed zone, as illustrated in Fig. 5.55, and three solidification regimes have been found. For the columnar zone the dendritic growth are controlled by thermal undercooling, which is Regime I. In the outer equiaxed zone where the secondary dendrite arm spacing is highest (ca. 800 μm), solidification is controlled by lowest undercooling, and this undercooling is a summation of thermal undercooling and constitutional undercooling, which is Regime II. The solidification in the sedimentation zone belongs also to Regime II, as the secondary dendrite am spacing in this region is similarly high, which is also around 800 μm. In the inner

equiaxed zone the solidification is driven by a summation of thermal and constitutional undercooling where the constitutional undercooling is dominating, and this is Regime III. Solidification in this region is faster compared to the rest three zones, since the secondary dendrite arm spacing is lowest (ca. 400 µm) in this region, where in columnar zone is around 600 µm (Fig. 5.45-46).

Due to the low driving force of solidification in the outer equiaxed zone, the growth of dendrite in this zone is slow, and due to the large secondary dendrite arm spacing, the permeability of melt in this area is especially high. Both conditions benefit the formation of channel, and A-segregates are found in the outer equiaxed zone, mainly in front of the columnar dendrites or along the contour of the sedimentation cone between the columnar front and the equiaxed crystals.

Similarly, in the cold models, channels have also been observed between the columnar dendrites and the sedimentation zone. In the beginning the equiaxed crystals in the sedimentation zone block the growth of columnar dendrite tips, and in this columnar to equiaxed transition zone grains are loosely compact than in the columnar zone and the sedimentation zone. As the equiaxed grains further sediment, the sedimentation zone is higher, and the loosely compact area extends further along the contour of the sedimentation zone and forms a channel-like area with low solid fraction, as in Fig. 6.18 illustrated. In the transition area, more than one channels have been observed along the sedimentation cone. These channels did not disappear during the whole crystallization process, and instead, they are observed from the initiation of CET till the end of "solidification". In addition to these channels, a few channels have also been found in the columnar zone, with a smaller inclined angle to gravity. This type of channels are thinner than the first type, and the initiation of this type of channels is not clearly distinguished. As solidification proceeds, this type of channels become more visible till the end of solidification. From this point of view, this type of channels seem to have more correlation with remelting.

As the location of the two types of channels in the NH$_4$Cl water modelling is very similar to the A-segregates in the 500 kg ingot, it is speculated that the time window of these channels in the cold models might be also comparable to the A-segregates in the hot models. The A-segregates with a larger inclined angle along the contour of the sedimentation cone might be initiate as soon as sedimentation cone forms, and they develops further along with the sedimentation cone, and the other type of A-segregates with smaller inclined angle might form after certain time of columnar growth due to remelting. The longer the solidification time is, the longer the remelting time is, and the thicker the A-segregates are. In the present study, the A-segregates with smaller inclined angle in front of the columnar dendrites are measured to be thicker than those with larger inclined angle along the contour of the sedimentation cone, indicating that remelting takes place for a relative long time.

Besides the channels, the cold modelling simulates the sedimentation of the equiaxed crystals as in heavy ingots as well. The shape of the sedimentation zone is at the beginning a plain sedimentation bed, and then due to high undercooling near the mould wall, the distribution of free crystal are higher near the columnar front, and more crystals are sedimented at the foot of the columnar zone. Meanwhile, influenced by the natural convection, the center of the sedimentation zone appears a small peak in the middle stage of solidification. As solidification proceeds, the intensity of natural convection decreases, and the central peak disappear again at the end stage of solidification, and the sedimentation zone appears to be a shallow bowl-shape where lower in center and higher at sides. This is very unlike the sedimentation zone observed in the hot models. The reason could be that the NH4Cl-dendries are so weak that they are easily broken by the intensive convective flow and hence the growth of the columnar zone is dramatically reduced. Therefore the sedimentation zone is blocked by the columnar dendrites and it stays to be a plain shaped bed for a long time in the cold models.

The simulation of the 500 kg ingot also shows a relative plain sedimentation bed with more fraction of solid near mould sides and less fraction of solid in the center, as in Fig, 7.13-16 illustrated. The reason can be easily explained by the velocity field of solid grains shown in Fig. 7.18. As the velocity of free dendrites is mainly influenced by the liquid velocity and gravity, due to natural convection, the crystals in front of the columnar zone are brought by the flow downwards and sink down very fast, with a calculated velocity of up to 18 mm /s and a mean velocity of 4 mm/s in the region that is 30 mm to solidification front. In the cold models, the sinking velocity of single grain has been measured to be up to 6 mm /s. It is difficult to compare the sinking velocity of NH_4Cl crystals and steel crystals, since the density difference to the bulk liquid are different between the two, and the natural convection intensity of liquid phase is also different between the cold models and the hot models as the cooling conditions are different. What can be found is that the simulated sinking velocity in the 500 kg ingot deviate dramatically from mould wall to center, indicating a dominating impact of fluid flow on sinking, whereas in the cold models the grains seems to sink with a more homogenous velocity distribution, implying that the convective flow has minor influence on the crystal sinking compared to gravity force. Nevertheless, since in the present simulation the dendritic morphology is not considered, the dragging force of the fluid to the crystals could be underestimated. If the dendritic morhplogy is taken into account, the calculated velocity of solid could be smaller. Furthermore, the present model describes the liquid and globulitic grains, and hence the contour of the sedimentation zone is not recognizable. If the model is extended to a three phase model with liquid, equiaxed grains and columnar dendrites, the as-cast structure could be better predicted with regard to sedimentation zone and CET.

Another phenomenon that occurs both in the cold models and in the numerical simulation is the turbulence at the solidification. As describe in Section 6.4, local spiral turbulence is generated near the

columnar front a certain time of solidification in the cold model. This local spiral turbulence could impact the breakdown of dendrite tips and thus influence the nuclei density, or might have an effect on the interdendritic flow among the columnar dendrites and thereby influence the initiation of remelting and channel formation. In the early stage of solidification where the solidification front is plain and relatively smooth, no such spiral turbulence is observed. The author surmises that the formation of the local turbulence is in correlation with the periodically appearing columnar dendrite tips. In the simulated liquid velocity field, local turbulence has been found at the solidification front where sudden geometry change appears. This geometry change is caused by sedimentation of equiaxed grains and therefore is not periodic, therefore single turbulence is generated. Furthermore, due the coarse mesh size, the local turbulence cannot be simulated precisely. If a finer mesh is applied, and the periodically columnar dendritic structure is included in the model, the local spiral turbulence might be reproduced by numerical simulation.

As several phenomena of heavy ingot solidification are very similar to those in heavy strands and blooms in continuous casting with the diameter up to 900 mm, and several quality problems in terms of A-segregation and inhomogeneous as-cast structure as well as cleanliness are very similar in both casting techniques, it is considered that the investigation results in the present study could be transferred to continuous casting in a certain range. For example the A-segregation mechanism suggested in the present study can be applied for the A-segregate formation in heavy continuous cast blooms, and the Rayleigh number which indicates the local remelting and solidification behavior can also be used in the numerical simulation of solidification of the continuous cast strands. Nevertheless, people should be aware of certain differences such as: the sedimentation of grains in a bending type continuous cast strands is different from that in ingot casting and is influenced by both gravity force and the flow direction; the fluid flow in continuous cast strands is more complex due to electric magnetic stirring (EMS) in different stages. Unfortunately in the present study, samples from continuous cast heavy strands are not available due to the limitation of cost and time, however, further investigation in the field of heavy continuous cast strands and blooms should be carried out, A simple way would be to simulate the fluid flow and the sedimentation behavior of the equiaxed grains under the flow conditions in continuous cast strands or blooms by using the cold modelling with NH_4Cl-70% H_2O solution.

9 Conclusions

With focus on quality of as-cast heavy steel ingots and continuous cast strands, the present study investigated a few complex solidification phenomena which are characteristics in heavy ingots and continuous cast products by using three methods, namely ingot casting experiments (hot modelling), water-modelling experiments with NH_4Cl solution (cold modelling) and numerical modelling.

The hot modelling has simulated the slow solidification process in industrial scale heavy ingots by utilization of an isolating mould and revealed the typical as-cast structure of heavy ingots that comprises A-segregates and sedimentation cone. The cold models have revealed the dynamic solidification process in a two dimensional cross-section, which includes the columnar dendritic growth, sinking of free equiaxed grains, breakdown of columnar dendritic tips, evolution of the sedimentation bed and the convective flow pattern. The numerical models have utilized the measurements and observation from hot models and cold models as input data, and simulated two types of solidification process for ingots with small cross-section and large cross-section, respectively, providing new possibility of prediction of macrosegregation and as-cast structure in large ingots. The results of the three types of modelling have been analyzed, compared and discussed, and following conclusions have been drawn:

1. The total solidification time of the 500 kg isolated ingots is over 140 min, which represents the solidification time of ingots with the weight between 3 and 6 t. The maximum carbon macrosegregation index C/C_0 of 0.4 is also consistent with the macrosegregation of ingots with weight of 5-6.2 t.

2. The as-cast structure of the 500 kg ingots can be divided as columnar zone, outer equiaxed zone which includes the CET region, the sedimentation cone of equiaxed crystals and the inner equiaxed zone which locates above the sedimentation cone. The averaged secondary dendrite arm spacing is lowest in the inner equiaxed zone (ca. 400 μm) and highest in the outer equiaxed zone and the sedimentation cone (ca. 800 μm), and in the columnar zone is around 600 μm. The calculated local solidification time in inner equiaxed zone (hot spot) is 25.8 minutes, which is the shortest; and in the outer equiaxed zone as well as in the sedimentation cone of equiaxed grains the local solidification time is longer, which is around 124.6 minutes; in the columnar zone the local solidification time is 64.8 minutes. Based on this, three solidification regimes have been summarized for the solidification in different zones. Solidification in the columnar zone obeys Regime I where the driving force is mainly

thermal undercooling; solidification in the outer equiaxed zone and in the sedimentation zone obeys Regime II with a lowest driving force, which is a summation of thermal and constitutional undercooling; solidification in the inner equiaxed zone obeys Regime III where the driving force is dominated by the constitutional undercooling.

3. A-segregates have been observed in the sulfur prints of the as-cast 500 kg ingots. A-segregates appear in the hollow cylinder region in ingot height from 120 mm to 470 mm and in ingot radius from 40 mm to 170 mm, which lies in the outer equiaxed zone with relative long local solidification time and high flow permeability. The inclined angle of A-lines is $10° \sim 15°$ to gravity in the inner region and $5° \sim 10°$ in the outer region as well as in the upper part of the ingot. Based on this, three mechanisms of A-segregation formation have been suggested: the first type of A-segregates initiate among the columnar dendrites and broad through remelting by the solute enriched melt; the other type of A-segregates lie between the sedimentation cone and the columnar zone, they develop along with the sedimentation cone and the solute enriched melt comes from the melt that is pressed out from the sedimented crystals or sucked in by cone shrinkage.

4. The two-phase solidification model based on volume-average-method can simulate the solidification process for both ingots with small cross-section and large cross-section. The comparison of the macrosegregation index of carbon between the simulation results and experimental results shows that the calculated carbon concentration distribution fits the measured results quite well, although at ingot top from height of 280 mm to 410 mm the positive segregation is slightly overestimated be 0.45 rather than 0.4 in reality. The sedimentation of free equiaxed grains has been considered in the model, and the calculated height of sedimentation zone of 270 mm is in good consistence with the measured height of 250 mm.

5. The one dimensional model for A-channel formation has modeled the opening and closing of potential channels in solidifying ingots and has found that low cooling rates and high flow velocity benefit the opening of channels by remelting. Further study shows that due to the complexiy of cooling and melt flow in ingots, an already opened channel can still be closed, and therefore a critical Rayleigh number for distinguish of remeling and solidification is not possible to be found, in other words, the Rayleigh number based criterion for channel formation is not applicable for the A-segregation prediction in ingot casting. Instead, the local Rayleigh number indicates the intensity of local remelting or solidification at one moment, and only the complete Rayleigh number over time and space represent the development of channels.

6. The water-modelling experiments using NH_4Cl solution show a local spiral turbulence at the

columnar dendrite tips certain time after solidification starts, which has an effect on the breakdown of columnar dendrite tips and thereby the formation of nuclei for solidification.

10 References

[1] D. Senk, R. Wolff, Z. Chen, P. v. Schweinichen: Solidification Research – Key to Best Products and Processes, *METEC 2011*, Düsseldorf, Proc. Session 20, CD-ROM

[2] J. Eisenkolb, R. Fandrich, H. Jung, *Stahl und Eisen* 130 (2010), pp. 28-44.

[3] J.A. Dantzig, M. Rappaz, *Solidification*, EPFL Press, Switzerland, 2009, pp. 1-22.

[4] G. Gruenbaum, et al., *A Guide to solidification of the steels*, Jernkontoret, Stockholm, 1977, pp. 28

[5] M.C. Flemings, *Solidification Processing*, McGRAW-Hill, New York, 1974, pp. 134-172.

[6] J.D. Hunt, *Mater. Sci. Eng.* 65 (1984), pp. 75

[7] M.A. Martorano, C. Beckermann, *Metall. Mater. Trans.* A, 34 (2003), pp. 1657

[8] V.R. Voller, C. Beckermann, *Metall. Mater. Trans.* A, 30 (1999), pp. 2183-2189.

[9] M. Drouzy, C. Mascré, *Mem. Et. Sci. Rev. Metall.* 58 (1961), pp. 241–260.

[10] S.C. Flood, J.D. Hunt, *Metals Handbook* 9th edn. (Am. Soc. Mater. Int.), 15 (1988), pp 130–136.

[11] G.H. Gulliver, *J. Inst. Met.* 9 (1913), pp. 120-157.

[12] E. Scheil, *Z. Metallkd.,* 34 (1942), pp. 70-72.

[13] H.D. Brody, M.C. Flemings, *Trans. TMS-AIME*, 236 (1966), pp. 615-624.

[14] M. C. Flemings, *Segregation in castings and alloys*. *Proc. Elliott Symp.* (Iron & Steel Soc.), 1990, pp. 216–235.

[15] M.C. Flemings, *Metall. Mater. Trans. B,* 5 (1974), pp. 2121-2134

[16] C. Beckermann, *Encyclopedia of Materials: Science and Technology*, Elsevier Science, 2001, 4733-4739, ISBN: 0-08-0431526.

[17] M.C. Flemings, *Scand. J. Met.*, 5 (1976), pp. 1-15.

[18] H. Fredriksson*, Cand. Metall. Q.*, 30 (1991), pp. 235-244.

[19] J.P. Gu, C. Beckermann, *Metall. Mater. Trans. A,* 30 (1999), pp. 1357–1367.

[20] A. Olsson, R. West, H. Fredriksson, *Scand. J. Metall.*, 15 (1986), pp. 104-112.

[21] J. Campbell, *Castings*, Butterworth-Heinemann, Oxford, 1993, pp. 146.

[22] A. Ghosh, *Sadhana*, 26 (2001), Parts 1 & 2, pp. 5–24

[23] *Steel Statistical Yearbook*, Economics Committee, Brussel, 2012.

[24] J. Alex, Perspectives of Ingot Casting and Forging Industry in Europe and Worldwide, *ICRF 2012* (1st International Confernece on Ingot Casting, Rolling and Forging), Aachen.

[25] *Heavy Manufacturing of Power Plants*, World nuclear Association, 2013, http://www.world-nuclear.org/info/Nuclear-Fuel-Cycle/Power-Reactors/Heavy-Manufacturing-of-Power-Plants/

Heavy Manufacturing of Power Plants, World nuclear Association, 2013, http://www.world-nuclear.org/info/Nuclear-Fuel-Cycle/Power-Reactors/Heavy-Manufacturing-of-Power-Plants/

[26] Techforum ThyssenKrupp, Issue 1 (2011), pp 19.

[27] J. Delorme, M. Laubin, *Casting and solidification of steel*, 1 (1977), pp. 214-276

[28] P. Machovčák, A. Opler, Z. Carbol, A. Trefil, K. Merta, J. Zaoral, M. Tkadlečková, K. Michalek, *Archives of Materials Science and Engineering*, 58 (2012), pp. 22-27.

[29] D.R. Liu, X.H. Kang, B.G. Sang, D.Z. Li, *Acta Metall. Sin.*, 24 (2011), No.1, pp. 54-64.

[30] A. Kumar, M. Založnik, H. Combeau, Experimental and Numerical Studies on the Influence of Hot Top Conditions on Macrosegregation in an Industrial Steel Ingot, *ICRF 2012* (1st International Confernece on Ingot Casting, Rolling and Forging), Aachen.

[31] L. Hartmann, C. Ernst, J. S. Klung, Simulation of ingot casting processes at Deutsche Edelstahlwerke GmbH, Witten, Germany, *ICRF 2012* (1st International Confernece on Ingot Casting, Rolling and Forging), Aachen.

[32] H. Combeau, A. Kumar, M, Založnik, I. Poitrault, G. Lacagne, A. Gingell, T. Mazet, G. Lesoult, Macrosegregation Prediction in a 65 ton Steel Ingot, *ICRF 2012* (1st International Confernece on Ingot Casting, Rolling and Forging), Aachen.

[33] J.R. Blank, F.B. Pickering, *The solidification of Metals*, Iron and Steel Institute, London, 1968, pp. 370-376.

[34] G. Lesoult: *Mater. Sci. Eng. A*, 413-414 (2005), pp. 19-29.

[35] H.F. Bishop, F.A. Brandt, W.S. Pellini, *J. Metals. Trans.*, 4 (1952), pp. 44-54.

[36] G. Lepie, H. Rellermeyer, *Arch. Eisenhüttenw.*, 37 (1966), pp. 925-934.

[37] H. Rellermeyer, *Gießen und Erstarren*, Verlag Stahleisen, Düsserldorf ,1967.

[38] F. Oeters, *Z. Metallk.,* 63 (1972), pp. 301-306.

[39] E. Steinmetz, Stahl und Eisen, 98 (1978), pp. 614-619.

[40] J.Q. Wang, P.X. Fu, H.W. Liu, D.Z. Li, Y.Y. Li, *Materials and Design*, 35 (2012), pp. 446-456.

[41] Z.J. Ji, S.Q. Li, Y.L. Zhang, G.W. Tang, *Steel Research Int.*, 84 (2013), pp. 94-100.

[42] D.R. Liu, B.G. Sang, X.H. Kang, D.Z. Li, *International Journal of Cast Metals Research*, 23 (2010), pp. 354-363.

[43] X. Liang,Y.G. Li, B. Zhao, Y. Wang, *Advanced Materials Research*, 468-471 (2012), pp 1026-1030.

[44] M.C. Flemings, G.E. Nereo, *Trans. Metall. Soc. AIME*, 239 (1967), pp. 1449-1461.

[45] M.C. Flemings, R. Mehrabian, G.E. Nereo, *Trans. Metall. Soc. AIME,* 242 (1968), pp. 41-49.

[46] M.C. Flemings and G.E. Nereo, *Trans. Metall. Soc. AIME*, 242 (1968), pp. 50-55.

[47] I. Ohnaka, T. Fukusako, *Trans. Iron Steel Inst. Jpn.*, 21 (1981), pp. 485-494.

[48] A. Ludwig, M. Wu, *Metall.Mater. Trans.* A 33 (2002), pp. 3673-3683.

[49] R. Mehrabian, M. Keane, M.C. Flemings, *Metall. Trans.* B, 1 (1970), pp. 1209-1220.

[50] I. Ohnaka, *Trans. Iron Steel Inst. Jpn.*, 26 (1986), pp. 1045-1051.

[51] E.J. Pickering, Macrosegregation in Steel Ingots: The Applicability of Modelling and Characterisation Techniques, *ISIJ Int.* 653 (2013), pp. 935-949.

[52] T. Fujii, D.R. Poirier, M.C. Flemings, *Metall. Trans.* B, 10 (1979), pp. 331-339.

[53] S.D. Ridder, S. Kou, R. Mehrabian, *Metall. Trans.* B, 10 (1981), pp. 435-447.

[54] W. Liu, *Finite element modeling of macrosegregation and thermomechanical phenomena in solidification processes*, Doctoral thesis, Ecole des Mines de Paris, 2005.

[55] W. D. Bennon, F. P. Incropera, *Int. J. Heat Mass Transfer*, 30 (1987), pp. 2161-2170.

[56] V.R. Voller, C. Prakash, *Int. J. Heat Mass Transfer*, 30 (1987), pp. 1709-1719.

[57] W. D. Bennon, F. P. Incropera, *Metall. Trans. B*, 18(1987), pp. 611-616.

[58] V.R. Voller, A.D. Brent, C. Prakash, *Int. J. Heat Mass Transfer*, 32 (1989), pp. 1719-1713.

[59] P. Bousquet-Melou, B. Goyeau, M. Quintard, F. Fichot, D. Gobin: Int. J. *Heat Mass Transfer*, 45 (2002), pp. 3651-3665.

[60] M. Zaloznik, H. Combeau, *Comp. Mater. Sci.*, 48 (2010), pp. 1–10.

[61] J. Ni, C. Beckermann, *Metall. Trans. B*, 22 (1991), pp. 349-361.

[62] S. Ganesan, D.R. Poirier, *Metall. Trans. B*, 21 (1990), pp. 173-181.

[63] M.C. Schneider, C. Beckermann, *Metall. Trans. A*, 26 (1995), pp. 2373-2388.

[64] C. Beckermann, R. Viskanata, S. Ramadhyani, *Numerical Heat Transfer*, 10 (1986), pp. 557-570.

[65] C. Beckermann, R. Viskanta*, Int. J. Hear Mass Transfer*, 30 (1987), No. 1, pp. 1547-1551.

[66] C. Beckermann, R. Viskanta, Trans. ASME, 111 (1989), pp. 416-424.

[67] C.Y. Wang, C. Beckermann, *Metall Mater. Trans. A*, 24 (1993), pp. 2787-2802.

[68] H. Combeau, M. Zaloznik, S. Hans, P. E. Richy, *Metall. Mater. Trans. B*, 40 (2009), pp. 289-304.

[69] M. Wu, A. Ludwig, *Metall. Mater. Trans. A*, 37 (2006), pp. 1613-1631.

[70] Q. Du, D.Z. Li, Y.Y. Li, *Acta Metall.Sin.*, vol. 36 (2000), pp. 1197-1200.

[71] C.Y. Wang, C. Beckermann, *Metall.Mater. Trans. A*, 27 (1996), pp. 2754-2764.

[72] C.Y. Wang, C. Beckermann, *Metall.Mater. Trans. A*, 27 (1996), pp. 2765-2783.

[73] C.Y. Wang, C. Beckermann, *Metall.Mater. Trans. A*, 27 (1996), pp. 2784-2795.

[74] C.Y. Wang, S. Ahuja, C. Beckerman, H.C. de Groh III, *Metall. Mater. Trans. B*, 26 (1995), pp. 111-119.

[75] C.Y. Wang, C. Beckermann, *Metall.Mater. Trans. A*, 25 (1994), pp. 1081-1093.

[76] M.C Schneider, J.P. Gu, C. Beckermann, W.J. Böttinger, U.R. Kattner, *Metall. Mater. Trans. A.*, 28 (1997), pp. 1517-1531.

[77] C. Beckermann, J.P. Gu, W.J. Böttinger, *Metall.Mater. Trans. A,* 31 (2000), pp. 2545-2557.

[78] C.J. Vreeman, M.J.M. Krane, F.P. Incropera, Int. J. Heat Mass Transfer, 40 (1997), pp. 3827-3835.

[79] J.M. Krane, F.P. Incropera, *Int. J. Heat Mass Transfer*, 40 (1997), pp. 3828-3835.

[80] M. Wu, A. Ludwig, *Metall.Mater. Trans. A*, 38 (2007), pp. 1465-1475.

[81] A. Ludwig, M. Wu, *Mater. Sci. Eng. A*, 109 (2005), pp. 413–414.

[82] H. Combeau, M. Zaloznik, et al., *Metall. Mater. Trans. B*, 40 (2009), pp. 289-304.

[83] H. Combeau, A. Kumar, M. Zaloznik, *Transactions of the Indian Institute of Metals*, 62 (2009), pp. 285-290.

[84] K.D. Carlson, Z. Lin, R. Hardin, C. Beckermann, Modelling of Porosity Formation and Feeding

Flow in Steel Casting, *Proceedings of the 56th SFSA Technical and Operating Conference*, Paper No. 4.4, Steel Founders' Society of America, Chicago, IL, 2002.

[85] J. L., M. Wu, A. Ludwig, *Int. Conf. on MCWASP XIII* (13th Modeling of Casting, Welding and Adv. Solidification Processes), 2012, Schladming (Austria).

[86] J. Li, M. Wu, J. Hao, A. Ludwig, *Comp. Mater. Sci.*, 55 (2012), pp. 407–418.

[87] J. Li, M. Wu, J. Hao, A. Kharicha, A. Ludwig, *Comp. Mater. Sci.*, 55 (2012), pp. 419–429.

[88] W. Kurz, D.J. Fisher, *Fundamentals of solidification*, 4th edn., Zurich, Trans Tech Publications, 1998.

[89] J. Lipton, M.E. Glicksman, W. Kurz, *Mater. Sci. Eng.*, 65 (1984), pp. 57-63.

[90] J.J. Moore, N.A. Shah, *Inter. Metals Rev.*, vol.28 (1983), pp. 338-356.

[91] S. Gouttebroze, M. Bellet, H. Combeau, *C. R. Mecanique*, 335 (2007), pp. 269-279.

[92] V. R. Voller, A. Mouchmov, M. Cros, *Appl. Math. Model.,* 28 (2004), pp. 79-94

[93] M. Zaloznik, H. Combeau, *Comp. Mater. Sci.*, 48 (2010), pp. 1–10.

[94] M. Zaloznik, H. Combeau, *Comp. Mater. Sci.*, 48 (2010), pp. 11–21.

[95] D.R. Liu, D.Z. Li, B.G. Sang, *J. Mater. Sci. Technol.,* 25 (2009), pp. 561-567.

[96] Z. Chen, S. Arnsfeld, D. Senk, *Int. Conf. on MCWASP XIII* (13th Modeling of Casting, Welding and Adv. Solidification Processes), 2012, Schladming (Austria).

[97] S. D. Felicelli, D. R. Poirier, A. F. Giamei, J. C. Heinrich: *JOM*, 21 (1997), pp. 21-25.

[98] P. K. Sung, D. R. Poirier and S. D. Felicelli, *Int. J. Numer. Meth. Fluids*, 35 (2001), pp. 357-370.

[99] J. Guo, C. Beckermann, *Numer. Heat Transf.,* Part A, 44 (2003), pp. 559-576.

[100] https://www.esi-group.com/software-services/virtual-manufacturing/casting

[101] ProCAST user manual, 2013

[102] http://www.transvalor.com/en/cmspages/THERCAST.6.html

[103] R.J. McDonald, J.D. Hunt, *TMS-AIME*, 245 (1969), pp. 1993-1997.

[104] A.F. Giamei, B.H. Kear, *Metall. Trans.,* 1 (1970), pp. 2185-2192.

[105] K.O. Yu, J.A. Oti, W.S. Walston, *Int. Met. Rev.,* 45 (1993), No. 5, pp. 49-51.

[106] M.R. Brige, J. Beech, *Solidification Technology in the Foundry and Cast House*, The Metals Society, London, 1980.

[107] W.H. Yang, W. Chen, K.M. Chang, et al., *Metall.Mater. Trans. A.*, 32 (2000), pp. 397-406.

[108] A. Hultgren, *Scand. J. Metall.,* 2 (1973), pp. 217-227.

[109] S.M. Copley, A.F. Giamei, S.M. Johnson, M.F. Hornbecker, *Metall. Trans.,* 1 (1970), pp. 2193-2204.

[110] C. Frueh, D.R. Poirier, R.G. Erdmann, S.D. Felicelli, *Mater. Sci. Eng. A*, 345 (2003), pp. 72–80.

[111] L. Yuan, P.D. Lee, *Acta Mater.*, 60 (2012), pp. 4917-4926.

[112] T.M. Pollock, W.H. Murphy, *Metall. Mater. Trans. A*, 27 (1996), pp. 1081-1094.

[113] K. Suzuki, T. Miyamoto, *Tetsu-to-Hagane (J. Iron Steel Inst. Jpn.),* 63 (1977), pp. 53-62.

[114] H. Yamada, T. Sakurai, T. Takenouchi, *Tetsu-to-Hagane (J. Iron Steel Inst. Jpn.)*, 29 (1989), pp.

97-104.

[115] H. Yamada, T. Sakurai, T. Takenouchi, *Tetsu-to-Hagane (J. Iron Steel Inst. Jpn.)*, 29 (1989), pp. 105-112.

[116] A.L. Purvis, C.R. Hanslits, R.S. Diehm, *JOM*, 46 (1994), pp. 38-41.

[117] M.G. Worster, *J. Fluid Mech.*, 237 (1992), pp. 649-669.

[118] M.G. Worster, *Ann. Rev. Fluid Mech.*, 1(1997), pp. 91-122.

[119] C. Beckermann, J.P. Gu, W.J. Boettinger, *Metall.Mater. Trans. A.*, 31 (2000), pp. 2545-2565. Gandin-1997

[120] C.A. Gandin, M. Rappaz, *Acta Mater.,* 45 (1997), pp. 2187-2195.

[121] H. Dai, H. Dong, N. D'Souza, J.C. Gebelin, R.C. Reed, *Metall. Mater. Trans. A*, 42 (2011), pp. 3439-3446.

[122] H.B. Dong, P.D. Lee, *Acta Mater.*, 53 (2005), pp. 659-668.

[123] S.N. Tewari, R. Shah R, *Metall. Mater. Trans. A*, 27 (1996), pp. 1353-1362.

[124] J. Sarazin, A. Hellawell, *Metall. Mater. Trans. A*, 19 (1988), pp. 1861-1871.

[125] M. Bergman, D. Fearn, J. Bloxham, *Metall. Mater. Trans. A*, 30 (1999), pp. 1809-1815.

[126] D.G. Neilson, F.P. Incropera, *Int. J. Heat Mass Transfer*, 34 (1991), No. 7, pp. 1717-1732.

[127] H. Combeau, F. Roch, I. Poitrault, J.Ch. Chevrier, G. Lesoult, *Advanced Computational Methods in Heat Transfer,* Vol. 3: Phase Change and Combustion Simulation, Springer-Verlag, New York, 1990, pp. 79-90.

[128] G. F. Vander Voort: *Metallography: Principles and Practice*, ASM International, OH, 1984, pp. 752.

[129] ASTM-381-01, Standard Method of Macroetch Testing Steel Bars, Billets, Blooms, and Forgings, *Annual Book of ASTM Standards*, Vol. 03.01, 2000.

[130] ASTM-340-00, Standard Test Method for Macroetching Metals and Alloys, *Annual Book of ASTM Standards*, Vol. 03.01, 2000.

[131] A. Kohn, *Proc. Conf. "The Solidification of Metals"*, The Iron and Steel Institute, London, 1968, pp. 357-362.

[132] K.W. Andrews, C.R. Gomer, *Proc. Conf. "The Solidification of Metals"*, Iron and Steel Institute, London, 1968, pp. 363-369.

[133] R. Tanzer, W. Schutzenhofer, G. Reiter, H. P. Fauland, L. Konozsy, A. Ishmurzin, M. Wu and A. Ludwig, *Metall. Mater. Trans. B*, 40 (2009), pp. 305-311.

[134] R. Meilland, F. Ruby-Meyer, M. Hemmerlin, et al., *European Polymer Journal*, No. 21415 (2005), pp. 1-67.

[135] A.J. Brown, Ed. R. Tommellini, *Proc. of 6th Int. Conf. Progress in Analytical Chemistry in the Steel and Metals Industries*, Luxembourg, 1999, pp. 405-412.

[136] Z Chen, P.v. Schweinichen, D. Senk, A. Lob, Comparison of as-cast structure of ingots of different steel grades with regard to effects of casting parameters, *ICRF 2012* (1st International

Conference on Ingot Casting, Rolling and Forging), Aachen.

[137] P. v. Schweinichen, Z. Chen, D. Senk, Metall. Trans. A, 44 (2013), pp. 4445-4449.

[138] D. Senk, E. Erdem, S. Stratemeier, *Int. J. Cast. Metals Res.*, 22 (2009), No. 1-4., pp. 94-98.

[139] I. Taguchi, K. Miyamura, H. Soga, *Trans. Iron Steel Inst. Jpn.*, 24 (1984), pp. 883-890.

[140] B. Beckhoff, B. Kanngießer, N. Langhoff, R. Wedell, H. Wolff, *Handbook of Practical X-Ray Fluorescence Analysis*, Springer, 2006, ISBN 3-540-28603-9.

[141] I. Croudace, W. Rindby and A. Rothwell: *New Techniques in Sediment Core Analysis*, No. 267, Geological Society Special Publication, London, 2006.

[142] P. Gottlieb, G. Wilkie, D. Sutherland, E. Ho-Tun, S. Suthers, K. Perera, B. Jenkins, S. Spencer, A. Butcher, J. Rayner, *JOM*, 52 (2000), No. 4, pp. 24-25.

[143] K.A. Jackson, J.D. Hunt., D.R. Uhlmann, T. P. Seward, *Transactions of the metallurgical society of AIME*, 236 (1966.), pp. 149-158.

[144] A. Ohno, *The solidification of metals*, Iron and Steel Institute, London, 1968, pp. 349-355.

[145] W. Jie, Y. Zhou, *Metall. Trans. B*, 20 (1989), pp. 723-730.

[146] K. Kaneko, T. Koyaguchi, *Journal of Volcanology and Geothermal Research*, 96 (2000), pp.161-174.

[147] G. Hansen, S. Liu, S. LU, A. Hellawell, *Journal of Crystal Growth*, 234 (2002), pp. 731-739.

[148] B. Appolaire, V. Albert, H. Combeau, G. Lesoult, *Acta Materialia*, 46 (1998), pp. 5851-5862.

[149] C. Beckermann, C.Y. Wang, *Metall. Mater. Trans. A*, 27 (1996), pp. 2784-2795.

[150] M. S. Kharicha, S. ECK, L. Könözsy, A. Kharicha, A. Ludwig, *International Journal of Cast Metals Research*, 22 (2009), pp. 168-171.

[151] S. Eck; M.S. Kharicha, A. Ishmurzin, A. Ludwig, *Mater. Sci. Eng. A*, 413–414 (2005), pp. 79–84.

[152] F. Zhai, Study of slow solidification of a 500kg ingot in an isolated mold, Master thesis, Institut für Eisenhüttenkunde, RWTH Aachen, 2013.

[153] H. Tomono, Y. Hitomi, S. Ura, A. Teraguchi, K. Iwata, K. Yasumoto, *Trans. ISIJ*, 24 (1984), pp. 917-922.

[154] P. Lan, Y. Li, J. Zhang, R. Zhang, J. Wang, H. Zhang, *Extraction and Processing Division Congress*, 2012, pp. 71-78.

[155] A. Kermanpur, M. Eskandari , H. Purmohamad, M.A. Soltani, R. Shateri, *Materials and Design*, 31 (2010), pp. 1096-1104.

[156] H. Jacobi, K. Schwerdtfeger, Metall. Trans. A, 7(1976), pp. 811-820.

[157] D. Senk, Materials Science Forum, 638-642 (2010), pp. 3628-3633.

[158] F. Firsbach, Water-modeling of ingot solidification by using NH_4Cl solution, Bachelor thesis, Institut für Eisenhüttenkunde, RWTH Aachen, 2012.

[159] M. Rappaz, *Int. Mater. Rev.*, 34 (1989), pp. 93-123.

[160] S.M. Kharicha, S. Eck, L. Könözsy, A. Kharicha, A. Ludiwig, *Int. J. Cast Metals Res.,* 22

(2009), No.1-4, pp. 168-171.

[161] S. ECK, M.S. Kharicha, A. Ishmurzin, A. Ludwig, *Mater. Sci. Eng. A*, 413–414 (2005), pp. 79–84.

[162] M. Leva, et al., *Fluid flow through Packed and Fluidized systems*, U.S. Government Printing Office, 1951, pp. 22.

[163] T. Wang, S. Shan, X. Zhang, J. Jin, M. Wu, A. Ludwig, B. Pustal, A. Bührig-Polaczek, *Acta Metall. Sin.*, 42 (2006), pp. 584-590.

[164] A. Kagawa, S. Moriyama, and T. Okamoto, *J. Mat. Sci.*, 17 (1982), pp. 135–144.

[165] T. Massalski, H. Okamoto, P.R. Subramanian, *Binary Alloy Phase Diagrams*, 2nd Edition, Vol. 3, ASM International, Materials Park, OH, 1990.

[166] S.V. Pantaka, Numerical heat transfer and fluid flow, McGraw-Hill Book Comany, New York, 1980, pp. 119.

[167] S. Acharya, B.R. Baliga, K. Karki, J.Y. Murthy, C. Prakash and S.P. Vanka, J. Heat Transfer 129(2007), pp. 407-424.

[168] F.J. Wang, *Analysis of computational fluid dynamics: CFD software principles and application*, Xinhua publishing house, Beijing, 2004, pp. 69.

[169] J.C. RamirezAMIREZ, C. Beckermann, *Metall. Mater. Trans. A*, 34 (2003), pp. 1525-1536.

[170] M.I. Bergman, D.R. Fearn, J. Bloxham, M.C. Shannon, *Metall. Mater. Trans. A*, 28 (1997), pp. 59-866.

[171] Z. Chen, D. Senk, Investigation on the A-Segregation Channel Instable Development in Large Ingot Casting, *STEELSIM 2013* (5th International Conference on Modelling and Simulation of Metallurgical Processes in Steelmaking), Session 4, Ostrava.

[172] Y.Chuang, K.Schwerdtfeger, Arch. Eisenhüttenwesen, 44 (1973), pp.341-347.

Appendices

Element / wt.%	Fe	C	Al	Si	P	S	Mn
Ingot B1	rest	0.518	0.0484	0.369	0.0155	0.0136	0.521
Ingot B2	rest	0.538	0.030	0.474	0.0076	0.0193	0.523

Table A1: Average composition of the 500 kg ingot B1 and B2, measured from the columnar zone by PDA-OES at IEHK
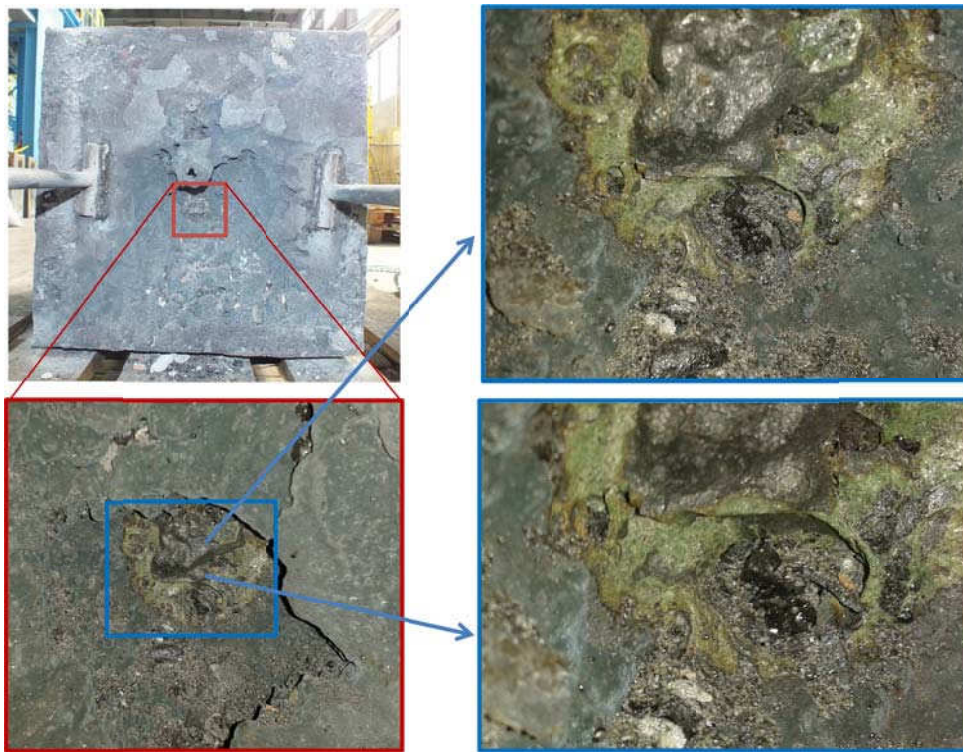
Fig. A1: Slag formation at the top cavity of the 500 ingot B2 (with the usage of the anti-cavity powder)
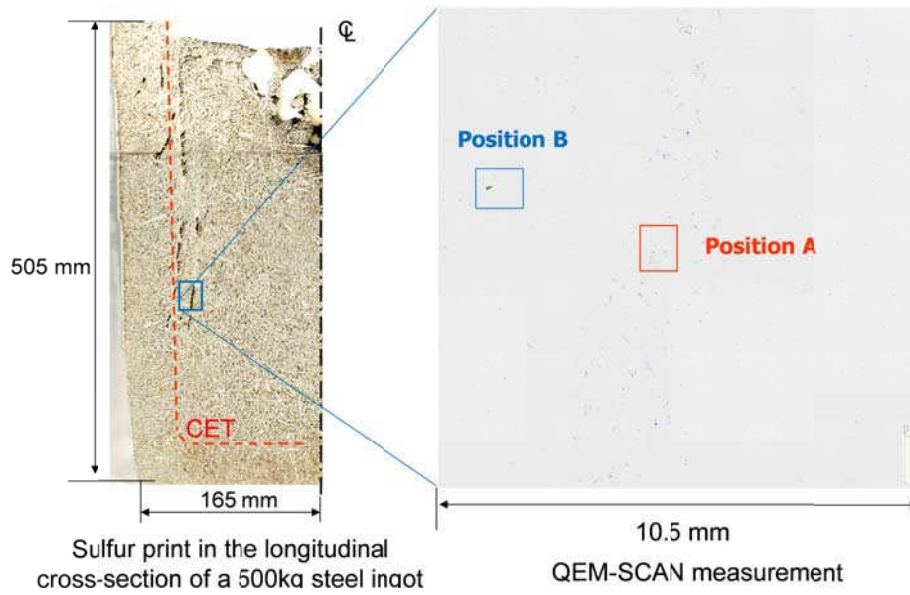
a)
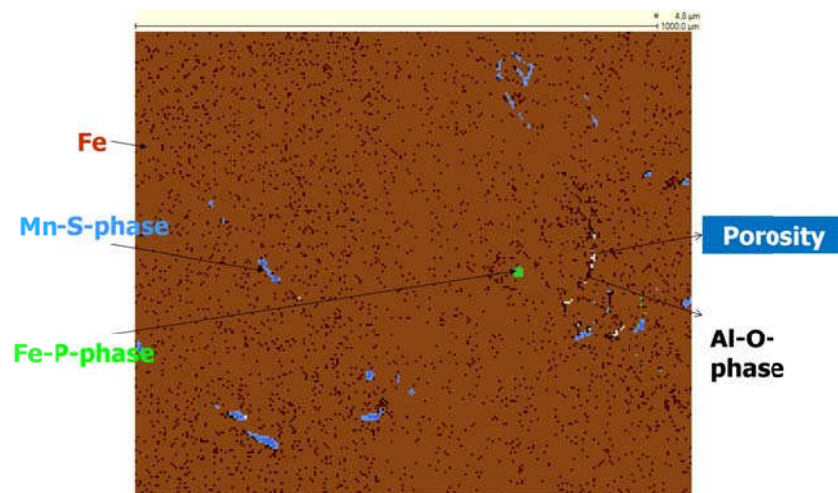
b)
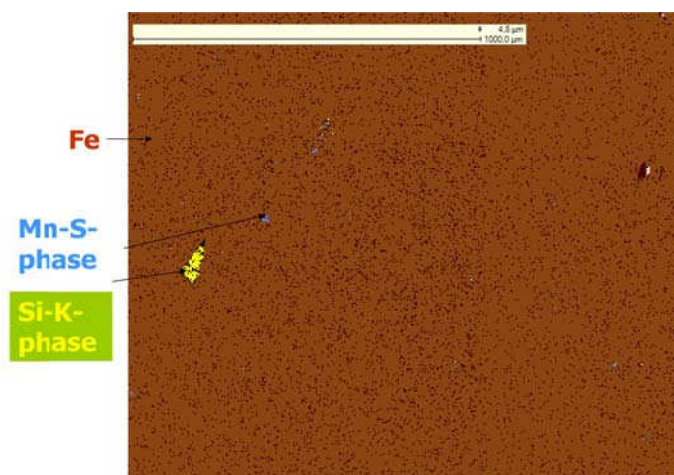
c)

Fig. A2: Phase assemblage maps of the A-segregates area measured by QEMSCAN, ingot B1, a) EDX of the A-segregate area and sampling, b) QEMSCAN results of position A, c) QEMSCAN results of position B
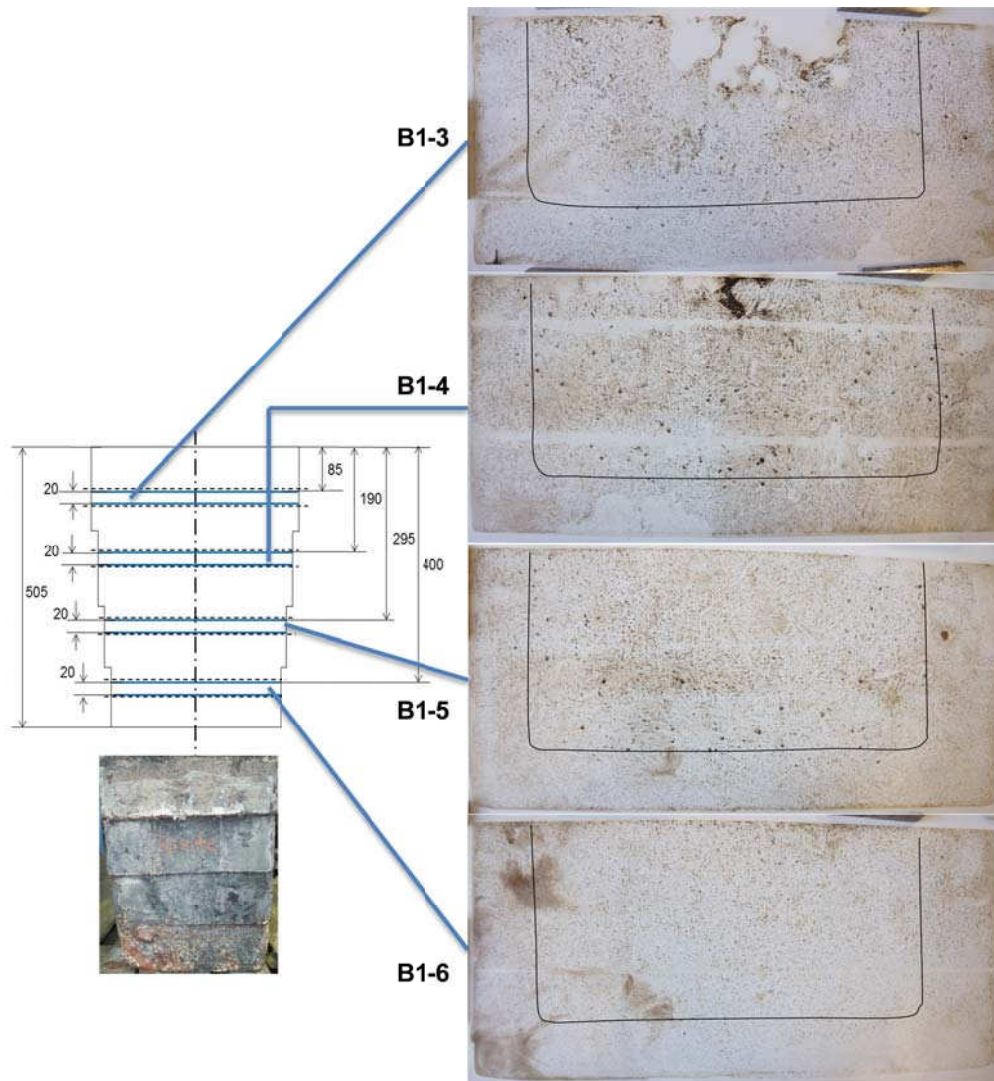
Fig. A3: Positions of samples B1-3, B1-4, B1-5, B1-6 and their sulfur prints (solid dark line indicates CET positions)
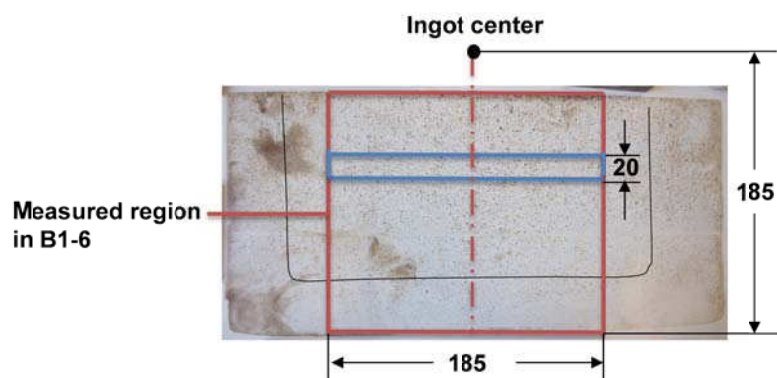
Fig. A4: The region in B1-6 used to count the amount of A-dots along the transverse direction (solid dark line indicates CET positions)
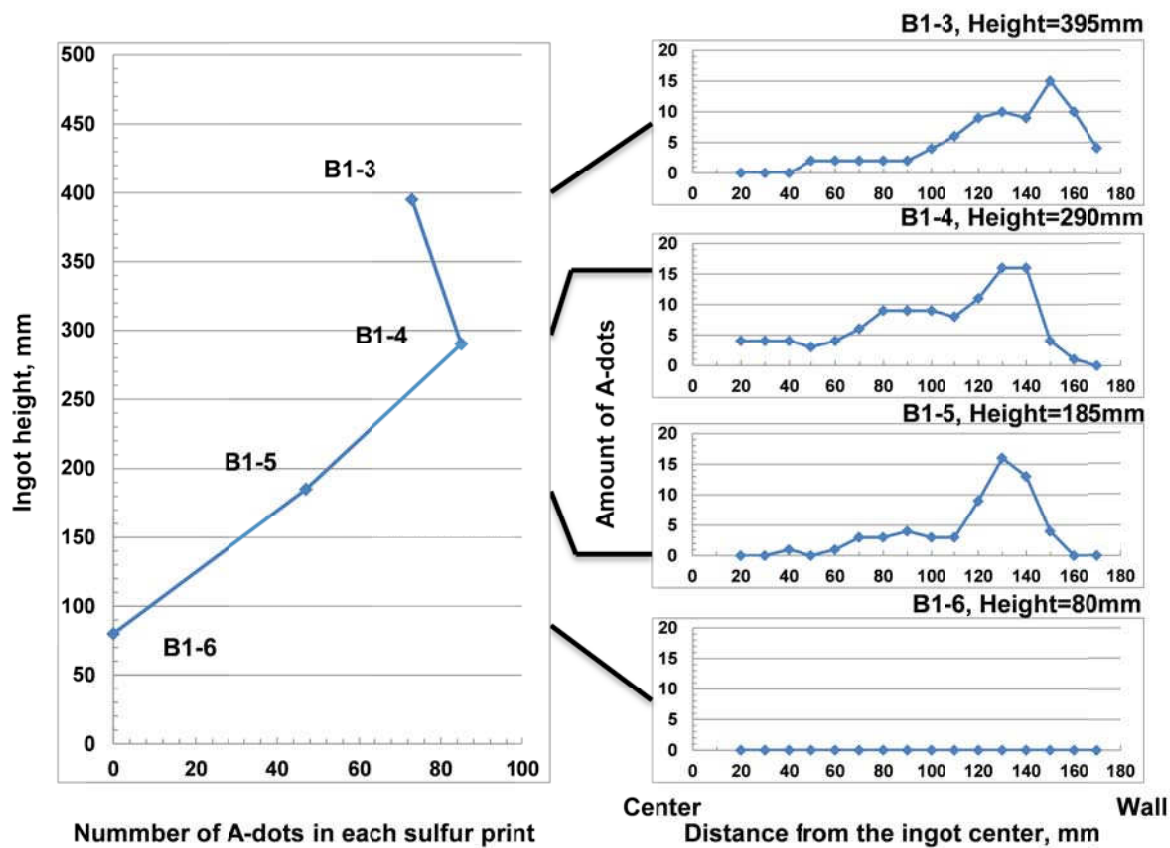
Fig. A5: Distribution of A-dots in the sulfur prints of B1 along the transverse directions at different ingot heights
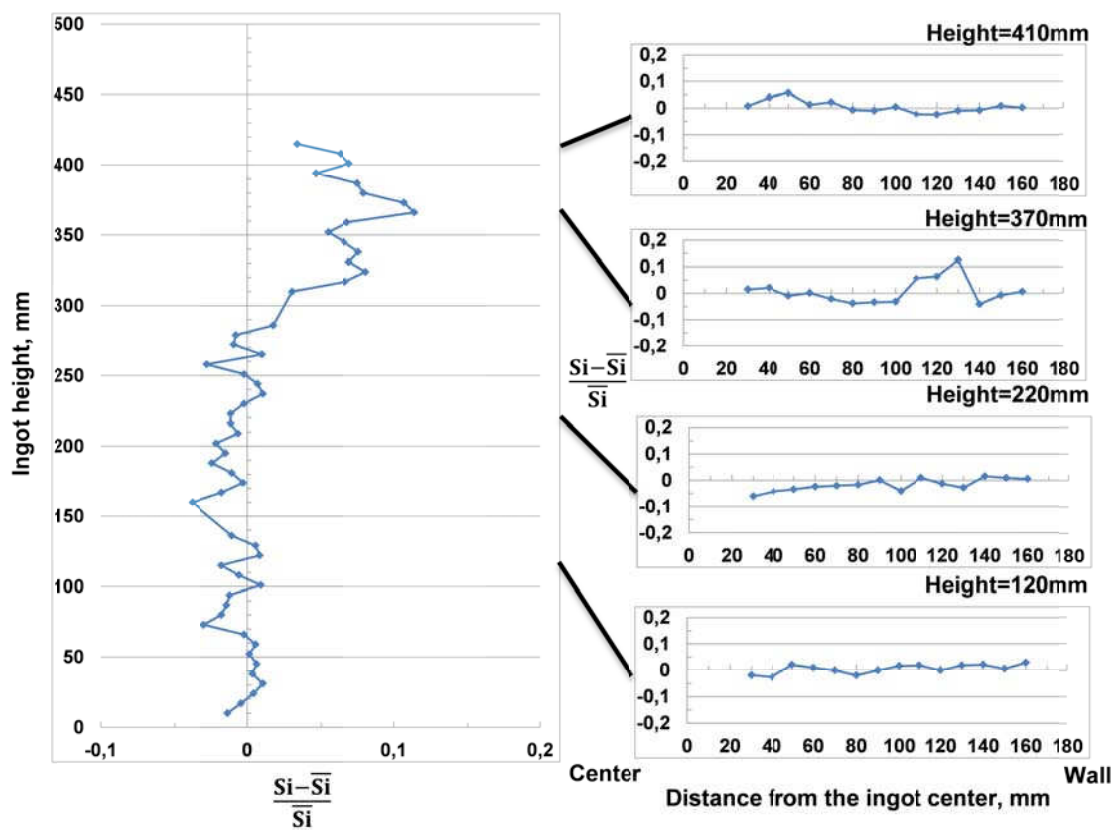
Fig. A6: Silicon segregation index along the centerline and transverse directions of B2
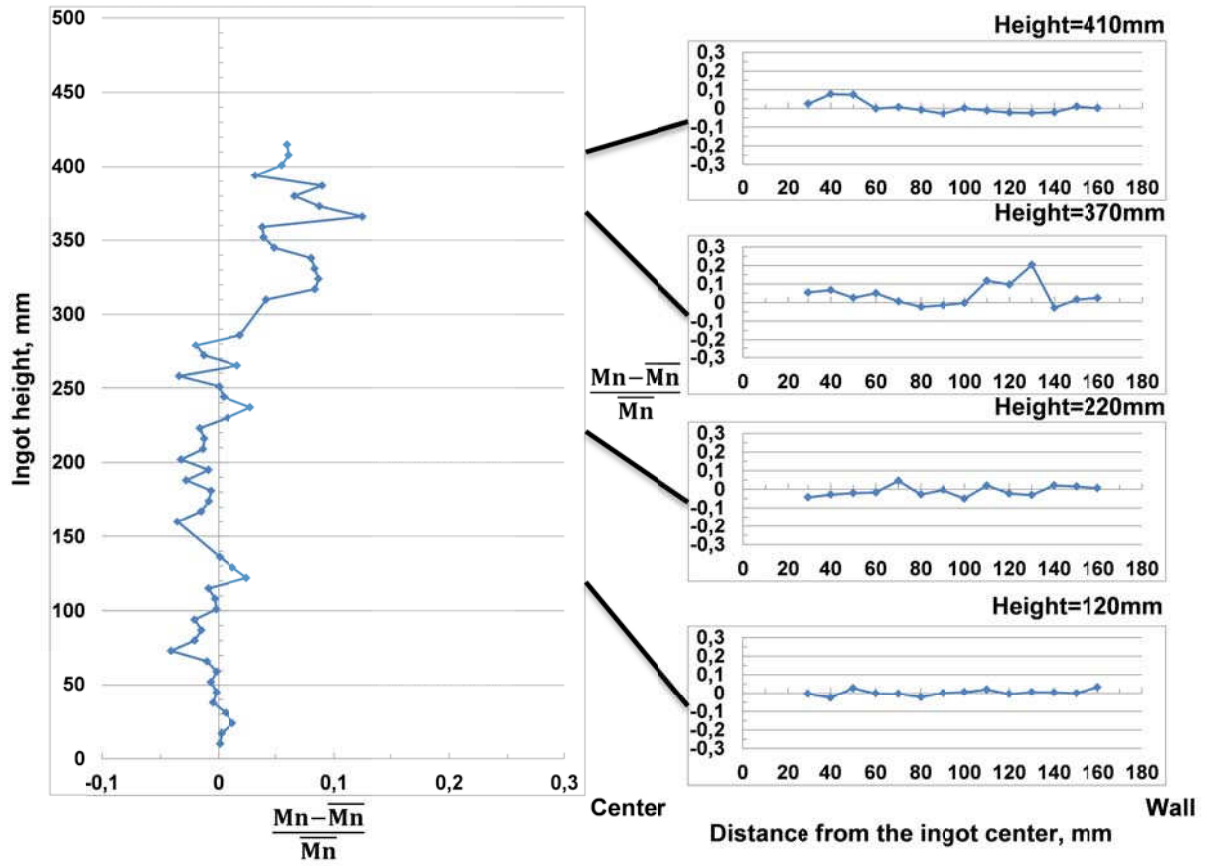
Fig. A7: Manganese segregation index along the centerline and transverse directions of B2
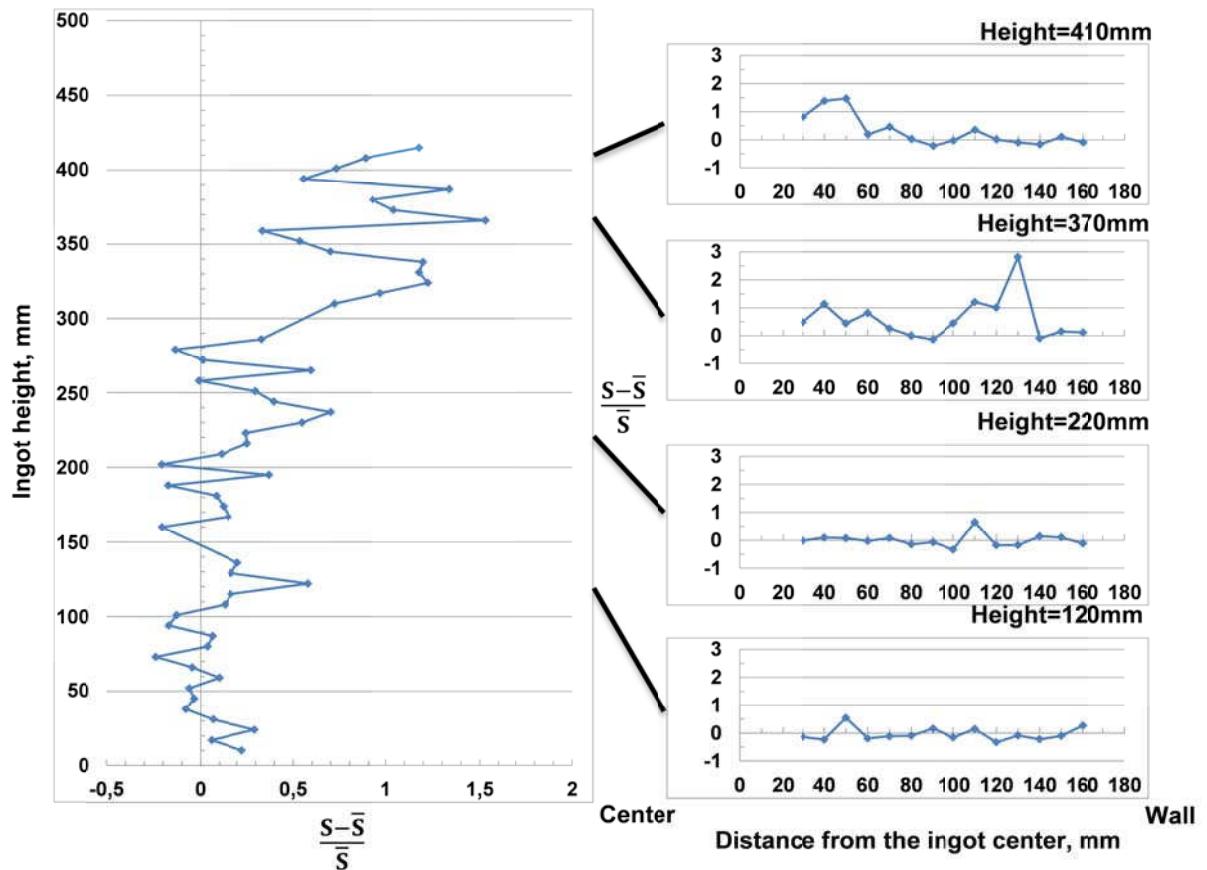
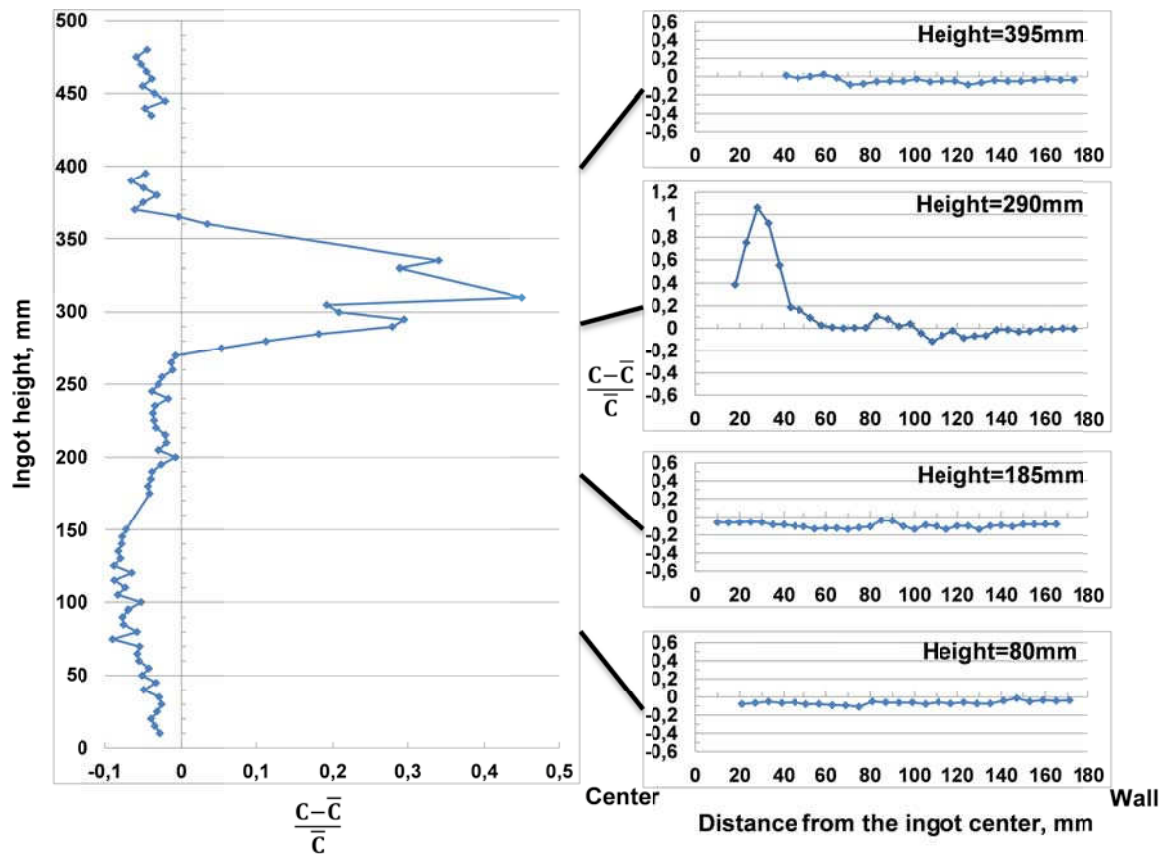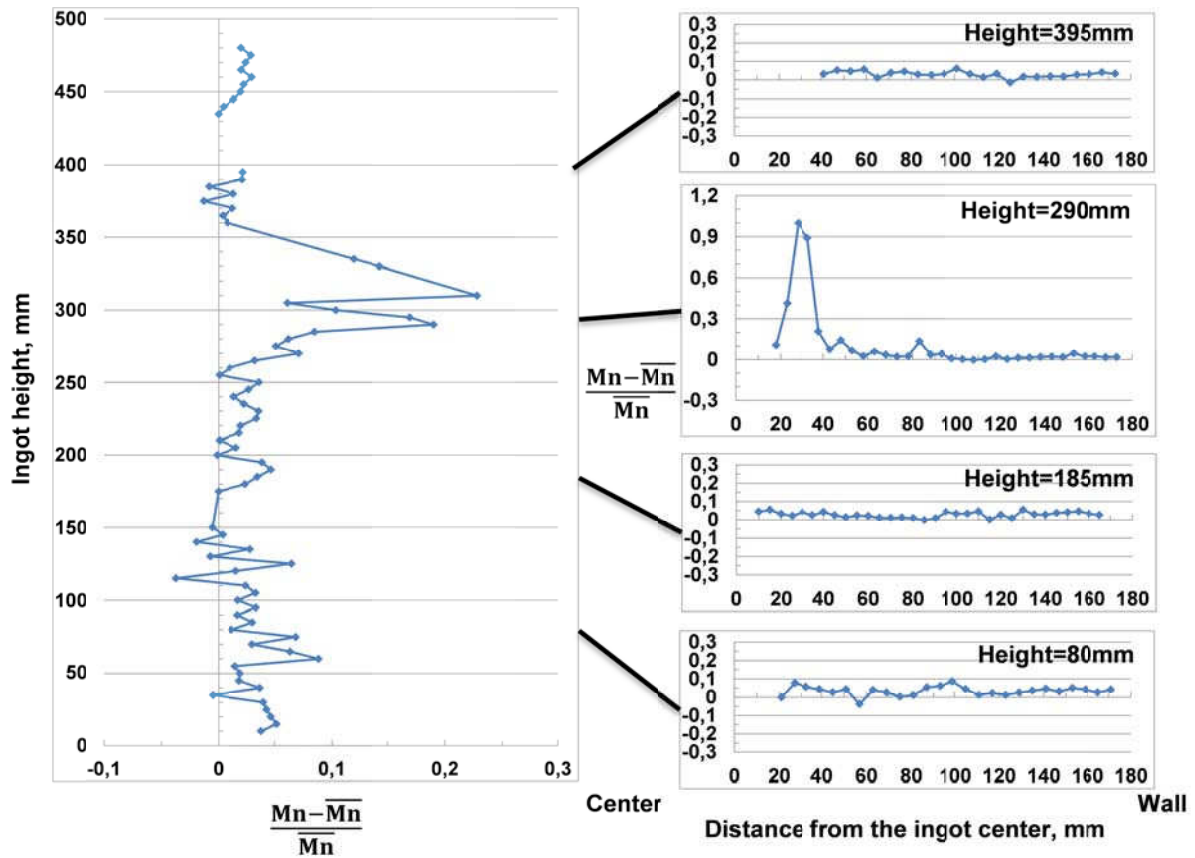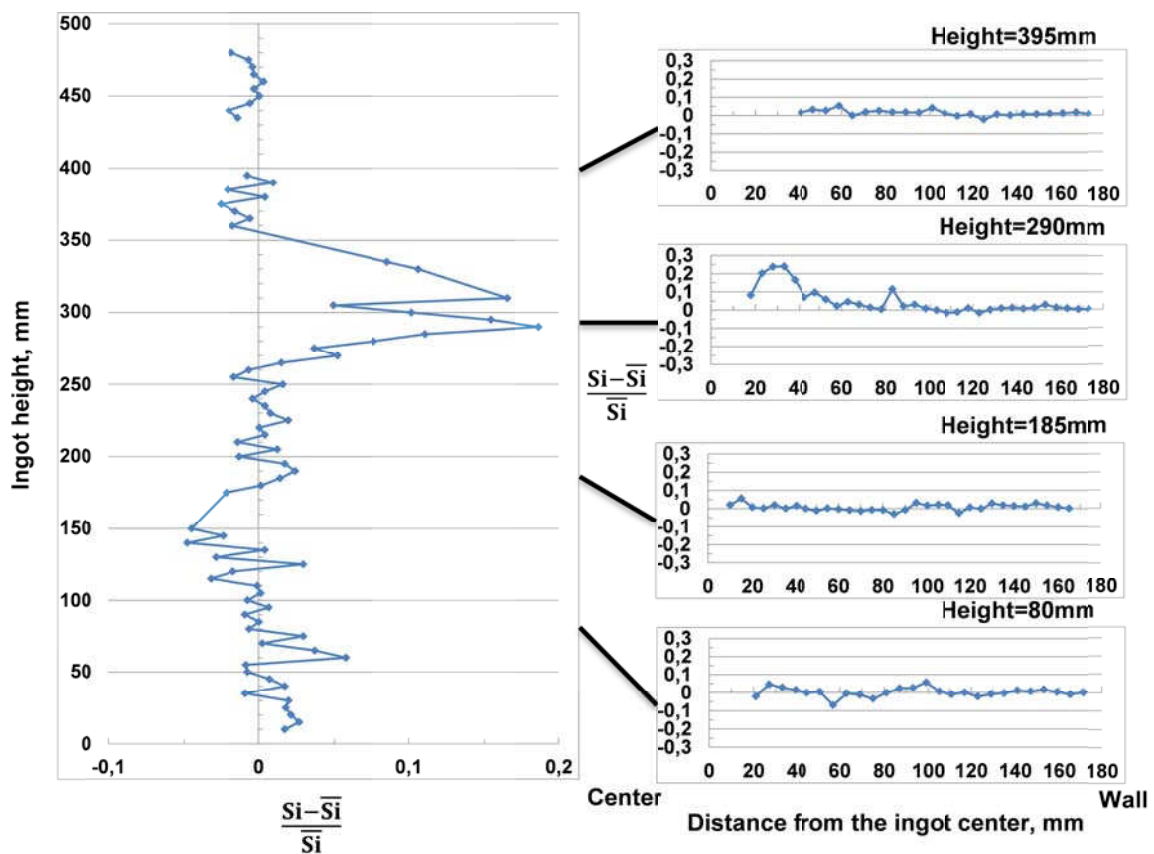Fig. A8: Sulfur segregation index along the centerline and transverse directions of B2
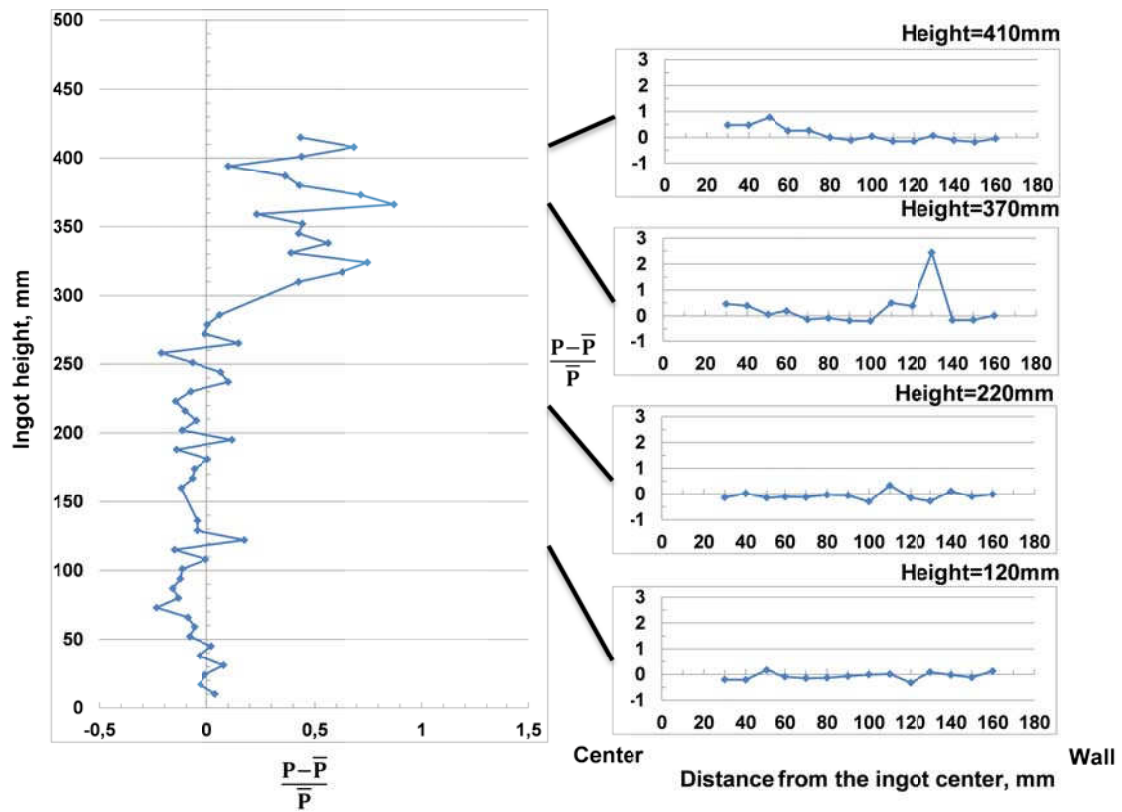
Fig. A9: Phosphorous segregation index along the centerline and transverse directions of B2
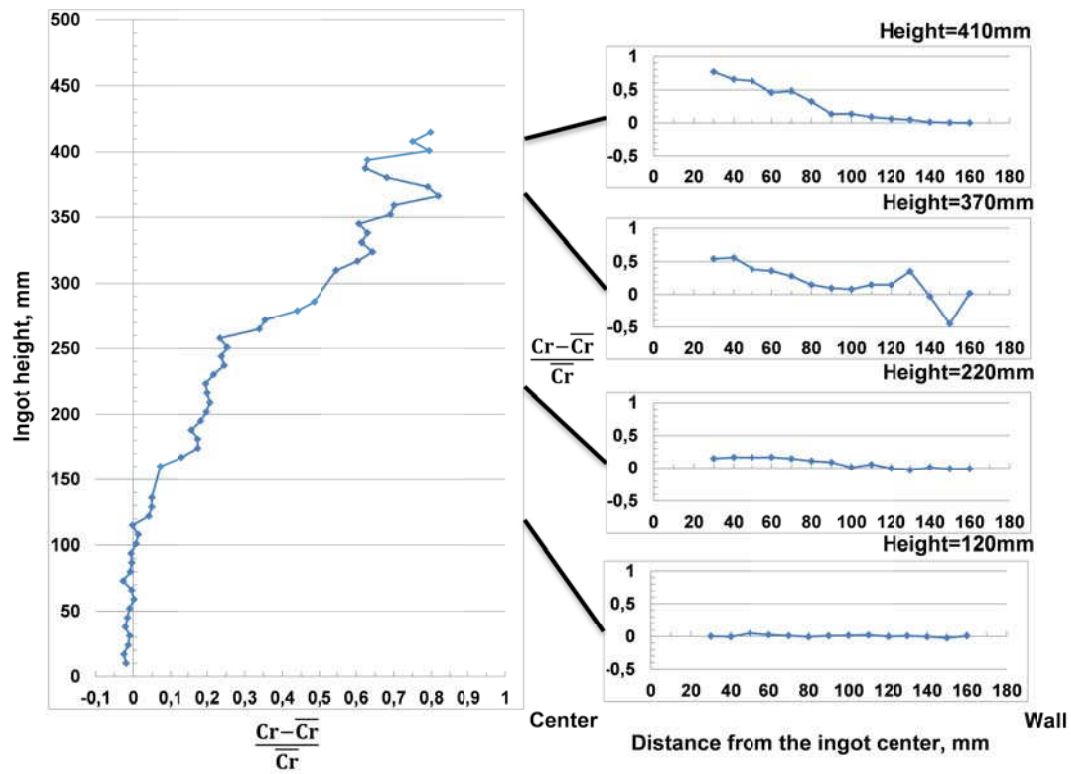
Fig. A10: Chromium segregation index along the centerline and transverse directions of B2
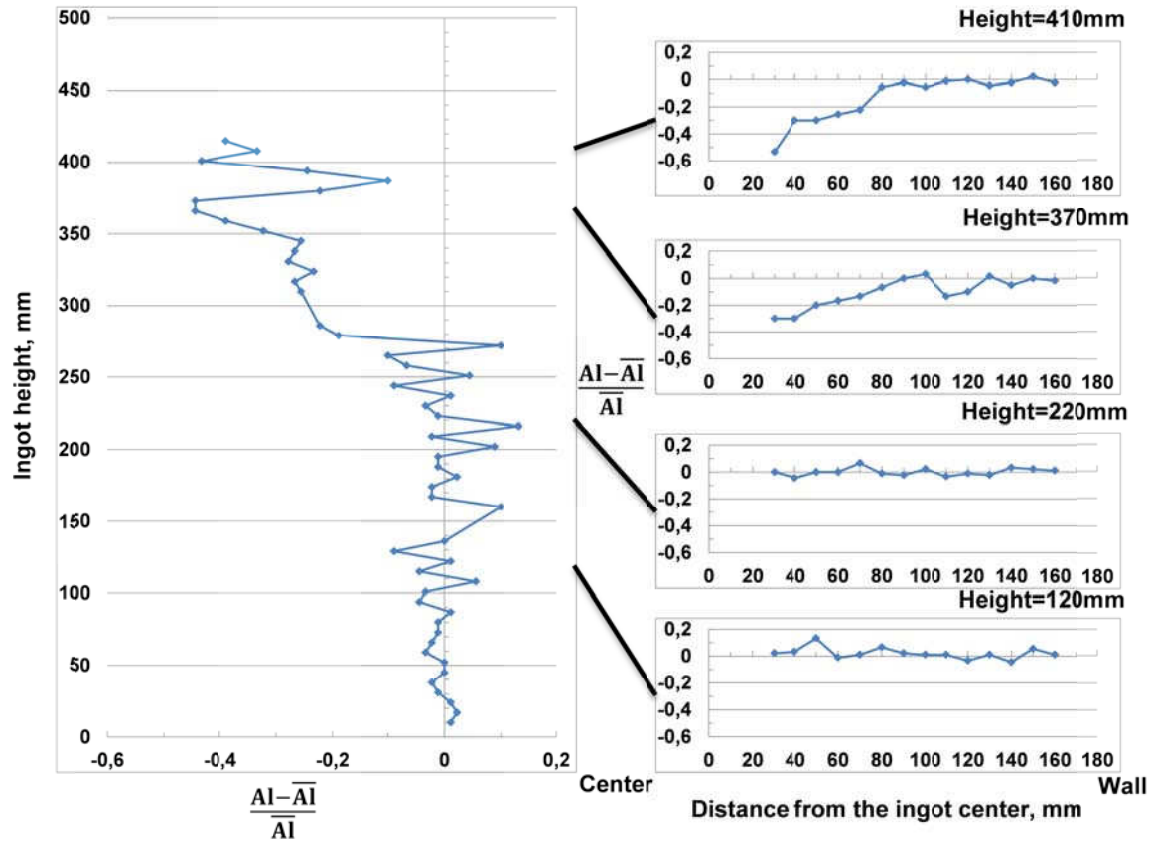
Fig. A11: Aluminum segregation index along the centerline and transverse directions of B2

Fig. A12: Carbon segregation index along the centerline and transverse directions of B1

Fig. A13: Manganese segregation index along the centerline and transverse directions of B1

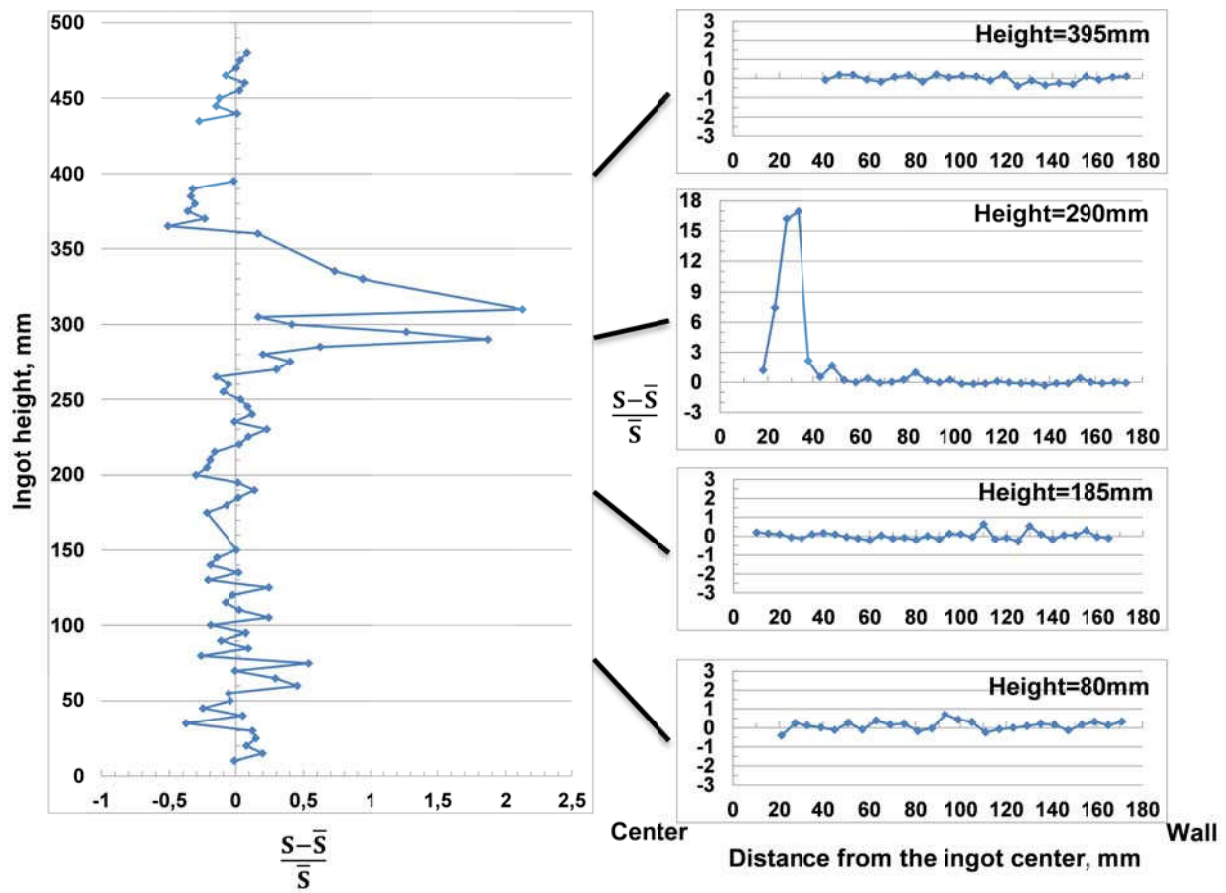Fig. A14: Silicon segregation index along the centerline and transverse directions of B1

Fig. A15: Sulfur segregation index along the centerline and transverse directions of B1
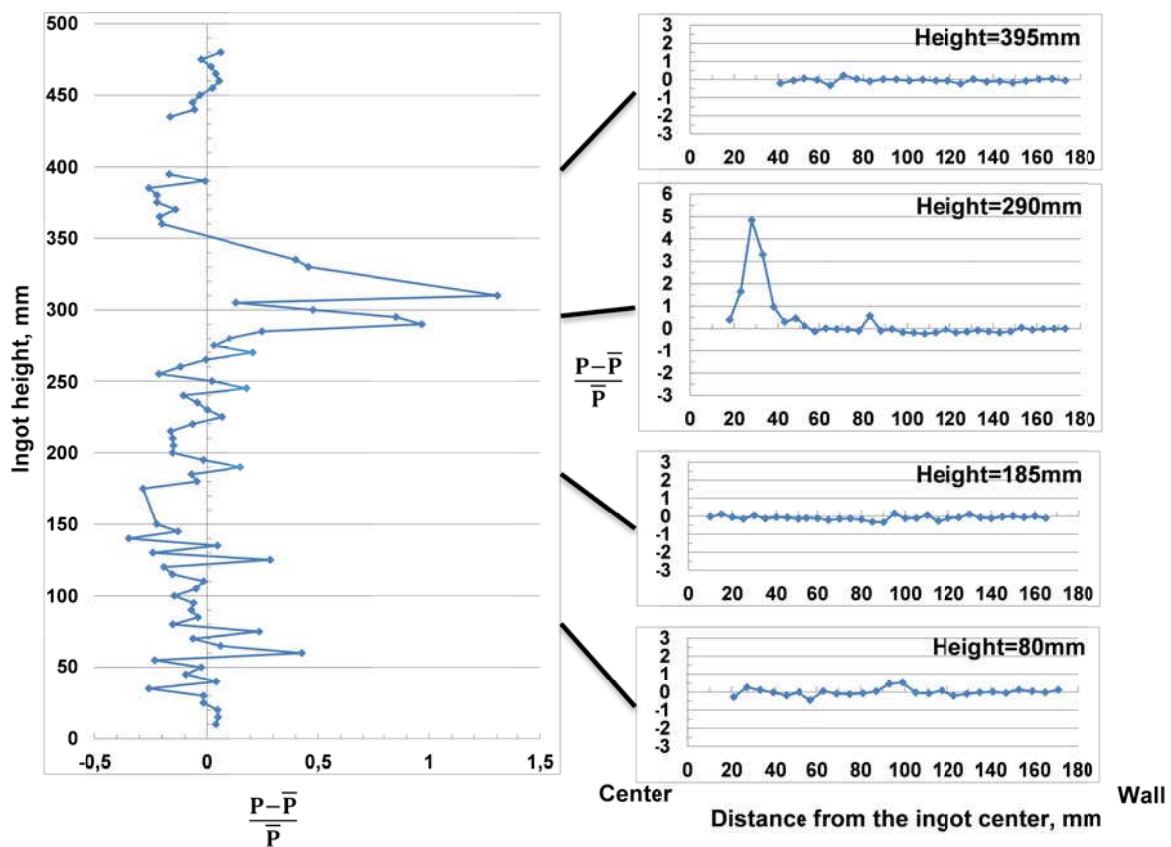

Fig. A16: Phosphorous segregation index along the centerline and transverse directions of B1
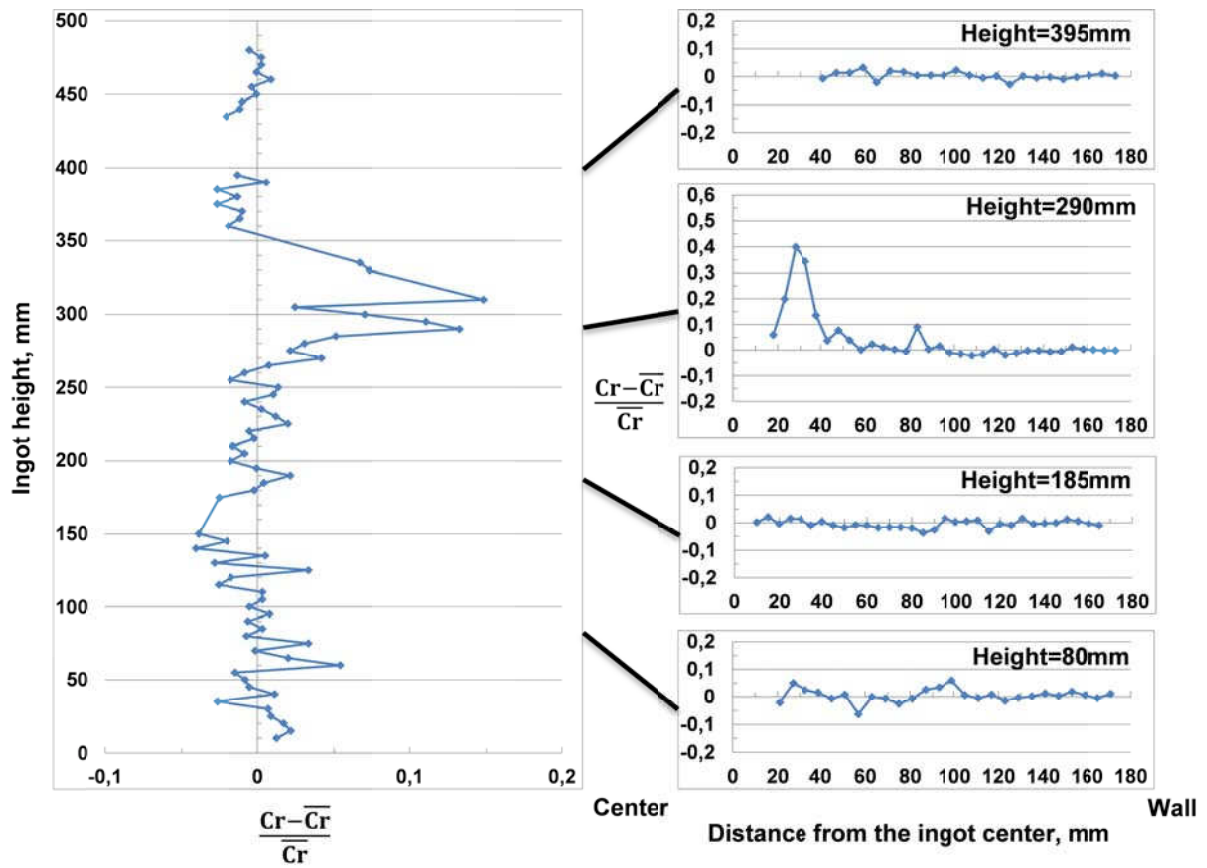
Fig. A17: Chromium segregation index along the centerline and transverse directions of B1
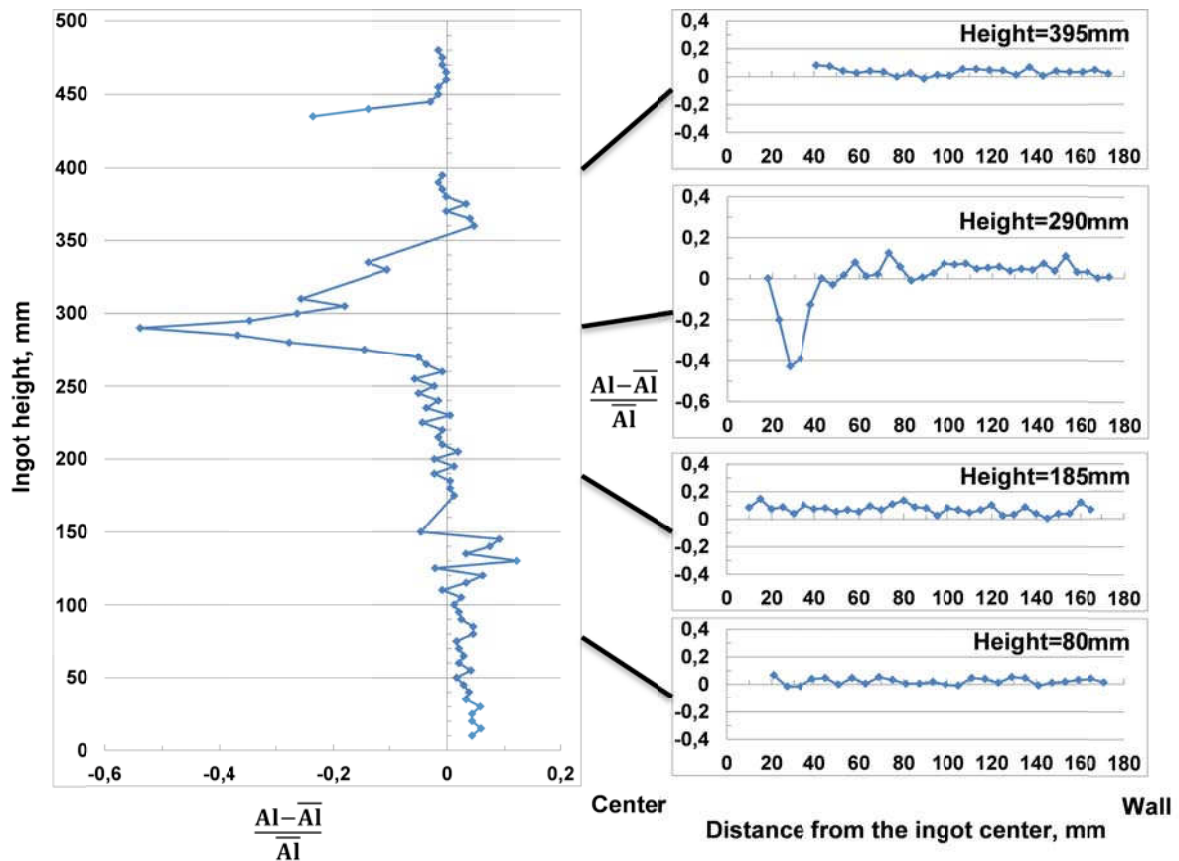

Fig. A18: Aluminum segregation index along the centerline and transverse directions of B1

Lebenslauf

Zur Person

Name:	Zhiye Chen
Geboren am:	25.03.1985 in Anhui, China
Familienstand:	verheiratet
Staatsangehörigkeit:	Chinesisch

Schulbildung

09/1991 – 07/1997	Grundschule in Huangshan, Anhui, China
09/1997 – 07/2000	1. Mittelschule in Tunxi, Huangshan, Anhui, China
09/2000 – 07/2003	1. Gymnasium in Tunxi, Huangshan, Anhui, China

Studium

09/2003 – 07/2007	University of Science & Technology Beijing, China Bachelor in Material Science and Technology Engineering
10/2007 – 02//2010	RWTH Aachen University, Aachen, Deutschland Master of Science in Metallurgical Engineering

Beruf

02/2009 - 05/2009	Praktikantin am Institut für Energieforschung, Forschungszentrum Jülich, Deutschland
03/2010 - 12/2013	Wissenschaftliche Mitarbeiterin am Institut für Eisenhüttenkunde der RWTH Aachen
seit 03/2014	Entwichlungsingenieurin, Buderus Guss, Breidenbach, Deutschland